Phased-Array Ultrasonic Residual Stress Measurement in Metal Additive Manufacturing: Development, Validation, and Microstructure-Aware Interpretation

Joseph Walker

Department of Electronic and Electrical Engineering

University of Strathclyde

A thesis submitted for the degree of

Doctor of Philosophy May 2026

Copyright

This thesis is the result of the author's original research. It has been composed by the author and has not been previously submitted for examination which has led to the award of a degree.

The copyright of this thesis belongs to the author under the terms of the United Kingdom Copyright Acts as qualified by University of Strathclyde Regulation 3.50. Due acknowledgement must always be made of the use of any material contained in, or derived from, this thesis.

Signed: 

Date: 03/09/2026

Contents

Copyright 2
Contents 3
Table of Figures 8
Table of Tables 11
Table of Equations 12
List of Publications 13
Journal Papers 13
Conferences 14
Terms and Abbreviations 16
Abstract 18
Chapter 1: Introduction 19
1.1 Background 19
1.2 Research Gaps 19
1.3 Aims & Objectives 20
1.4 Contribution to The Knowledge 20
1.4.1 PAURS in WAAM 20
1.4.2 PAURS+ 21
1.4.3 Basis for Future In-Situ Measurements 21
Chapter 2: Background 24
2.1 Introduction 24
2.2 Additive Manufacturing 24
2.2.1 Wire Arc Additive Manufacturing 24
2.3 RS Formation and Measurement Challenges 25
2.3.1 Context 25
2.3.2 RS in Additive Manufacturing 25
2.3.3 WAAM RS 26
2.3.4 RS Mitigation 26
2.4 Established RS Measurement Methods 26
2.4.1 Destructive Methods 27
2.4.1.1 CM 27
2.4.1.2 Incremental Hole Drilling 28
2.4.2 Non-Destructive 28
2.4.2.1 XRD 28
2.4.2.2 Neutron Diffraction (ND) 28
2.5 Ultrasonic Measurements 29

2.5.1 Conventional Ultrasonic RS 29
2.5.1.1 Principles 29
2.5.1.2 Snell's Law 29
2.5.1.3 LCR Waves 29
2.5.2 Phased-array Ultrasonic Measurements 30
2.5.2.1 Phased Array Ultrasonics for Defect Detection 30
2.6 Phased Array Ultrasonics for RS Measurement (PAURS) 31
2.6.1 Principles 31
2.6.2 Acoustoelasticity 31
2.7 Microstructure and PAURS+ 35
2.7.1 Observable-Based Interpretation of Phased-Array LCR Ultrasonics 36
2.7.1.1 Governing Elastodynamics and Microstructure–Stress Dependence 36
2.7.1.2 Stress Sensitivity of LCR ToF 36
2.7.1.3 Microstructural Sensitivity of Amplitude- and Frequency-Based Observables 37
2.7.2 Role of Phased-Array FMC 38
2.7.3 Observable-Level Separation Framework 38
2.7.4 Implications for Microstructure-Aware RS Measurement (PAURS+) 39
2.8 Key Insights 40
Chapter 3: Literature Review 41
3.1 Introduction and Scope 41
3.2 RS in Metal AM 41
3.2.1 RS Mitigation in WAAM 42
3.3 AM RS Measurements 43
3.3.1 RS WAAM Measurements 43
3.3.2 CM 44
3.3.3 XRD 44
3.3.4 RS Measurement Method Properties 45
3.3.5 Uncertainties in RS Measurement Methods 46
3.3.6 In-Situ Measurements 47
3.4 Ultrasonic RS Measurement 47
3.4.1 Acoustoelasticity 48
3.4.2 LCR Waves 49
3.4.3 Applications for AM 50
3.4.4 Single-Element LCR Limitations 51
3.4.5 LCR Wave Generation and Propagation 52
3.5 Phased-Array Ultrasonics 53

3.5.1 Principles 53
3.5.2 FMC 54
3.5.3 Phased Arrays for RS Measurement 55
3.5.4 Signal Processing and Reliability 55
3.6 Microstructural Effects on Measurements 56
3.6.1 Effects on ToF and Velocity 57
3.6.2 Effects on Attenuation, Backscatter and Frequency Response 58
3.6.3 Microstructure-Aware Interpretation 59
3.7 Summary and Research Gaps 60
Chapter 4: Methodology 62
4.1 Overview 62
4.1.1 Workflow 63
4.1.2 Facilities, Equipment and Contributions 64
4.1.3 Measured Components 65
4.2 Sample Manufacturing 65
4.2.1 Overview 65
4.2.2 WAAM Ti-6Al-4V 66
4.2.3 AFSD Aluminium 67
4.2.3.1 Manufacturing macroscopically-stress-relieved samples 67
4.3 Measurement Scanning Procedure 68
4.3.1 Identification of the HAZ 70
4.4 Validation RS Measurements 70
4.4.1 CM 70
4.4.2 XRD 73
4.5 PAURS 75
4.5.1 PAURS Process 75
4.5.2 Configuration 77
4.5.3 Wedge Design and Angle Optimisation 78
4.5.4 PAURS Experimental Setup 78
4.5.5 PAURS-ToF consistency 81
4.5.6 LCR wave propagation 82
4.5.7 Interpolation 83
4.5.8 Reduction of Couplant-Thickness Effects in ToF Measurements 85
4.5.9 Acoustoelastic constant 86
4.5.10 Automated ToF Extraction and Stress Calculation 89
4.6 PAURS+ 90
4.6.1 Stress-Free Reference State for Microstructure Isolation 91

4.6.2 Ultrasonic setup 91
4.7 Data Quality Assessment 94
4.8 Uncertainties 94
Chapter 5: Study 1: WAAM Ti-6Al-4V PAURS Feasibility Study 96
5.1 Introduction 96
5.1.1 Ultrasonic Phased Arrays for RS Measurement 96
5.2 Results and Discussion 97
5.3 Comparison of Results 105
5.4 Conclusions 107
Chapter 6: Study 2: WAAM Ti-6Al-4V Inter-pass Peening Study 108
6.1 Introduction 108
6.2 Results and Discussion 108
6.2.1 Microstructure Study 108
6.2.1.1 Material Preparation 108
6.2.2 CM 109
6.2.3 XRD 111
6.2.4 PAURS 112
6.2.4.1 Wedge Angle Testing 112
6.2.4.2 FMC 113
6.2.4.3 SNR 113
6.2.4.4 Acoustoelastic Constant 116
6.2.5 Final PAURS Measurements 119
6.2.6 Comparison of PAURS, CM, and XRD Results 126
6.3 Limitations and Extensions 128
6.4 Conclusions 129
Chapter 7: Study 3: PAURS+ Microstructural Effect Study 131
7.1 Introduction 131
7.1.1 RS and Microstructure in Advanced Manufacturing 131
7.1.2 Limitations of Conventional Characterisation Methods 131
7.1.3 Ultrasonics for Stress and Microstructure Characterisation 132
7.1.4 Observable-Level Characterisation for Decoupling Stress and Microstructure (PAURS+) 133
7.2 Results and Discussion 134
7.2.1 Microstructural Characterisation 134
7.2.1.1 EBSD Sample preparation 134
7.2.1.2 EBSD Characterisation 134
7.2.2 Assumptions and Scope of RS State 136

7.2.3 ToF: Pulse-Echo vs LCR 137
7.2.4 Pulse-Echo ToF (through-thickness averaging) 137
7.2.5 LCR ToF (near-surface, stress-dominated) 139
7.2.5.1 Identification of the LCR arrival 139
7.2.5.2 Waveform verification 140
7.2.5.3 FEG vs CEG LCR ToF 141
7.2.6 Attenuation 144
7.2.6.1 Definition of Attenuation in Pulse-Echo and LCR Measurements 144
7.2.6.2 Pulse-Echo Attenuation 145
7.2.6.3 LCR Attenuation 147
7.2.7 Backscattering 150
7.2.7.1 Pulse echo scattering 150
7.2.7.2 LCR scattering 151
7.2.8 FFT 154
7.2.8.1 Frequency-domain processing and spectral metrics 154
7.2.8.2 LCR FFT 155
7.3 Summary of Results: Microstructural Control of LCR Attenuation and Observable Separation 156
7.3.1 Microstructural Length Scale and LCR Attenuation 156
7.3.2 Effect of Morphology and Anisotropy Correlation 157
7.3.3 Observable-Level Separation and PAURS+ 157
7.4 Conclusions 160
Chapter 8: Discussion 162
8.1 Findings across the three studies 162
8.2 Validation 163
8.3 PAURS against diffraction and modelling 165
8.4 Limitations 165
8.5 Future Work 166
Chapter 9: Conclusions 168
References 172

Table of Figures

Figure 1 Flowchart showing the outline of the thesis chapters 22
Figure 2 Schematic of RS measurement using (a) single-element transducers versus (b) phased array ultrasonic approach [61] 35
Figure 3 The methodological progression of PAURS throughout the three stages 62
Figure 4 A flowchart showing an overview of the process of the methodology throughout the studies 63
Figure 5 The samples used in all studies show (a) the three WAAM Ti-6Al-4V samples used in studies 1 & 2, (b) the AFSD aluminium samples used in study 3 65
Figure 6 Schematic of the setup and dimensions for the manufactured experimental samples 66
Figure 7 Physical setup for the manufacturing and peening of the WAAM samples [66] 67
Figure 8. AFSD aluminium block and sectioned slices: (a) full block, (b) Sample #1 (EDM-only), (c) Sample #2 (heat-treated + EDM). [101] 68
Figure 9 The measurement methods used throughout all studies show (a) the three WAAM Ti-6Al-4V samples measured in studies 1 & 2, with PAURS, CM and XRD utilised, (b) the AFSD aluminium samples measured in study 3 with both LCR and pulse-echo PAURS measurements 69
Figure 10 A schematic showing the WAAM Ti-6Al-4V CM EDM setup using the Fanuc Robocut α-C600i 71
Figure 11 The cutting direction used for cutting the Ti-6Al-4V sample for CM and the resulting cut sample. [61] 71
Figure 12 A schematic of the Zeiss Contura g2 CMM setup 72
Figure 13 Method for data collection using XRD [66] 73
Figure 14 Full experimental setup for the XRD measurements [66] 74
Figure 15 PAURS process workflow 76
Figure 16 The PAURS measurement setup 77
Figure 17 Experimental setup for PAURS ToF measurements 79
Figure 18 (a) Schematic of WAAM Ti-6Al-4V scanning; (b) Top-down view of scan lines 79
Figure 19 PAURS measurement setup showing the PEAK MP6 using two 8-element 5MHz arrays acting as transmitter and receiver, connected to the laptop for ToF measurements, which were then calculated with acoustoelastic measurements for RS measurements. 80
Figure 20 An example signal showing how the zero crossing is found from the LCR wave. 81
Figure 21 Geometrical proof of ToF consistency [66] 81
Figure 22 (a) Single element LCR beam profile in a WAAM sample (b) 4-element phased array LCR beam profile [66] 82
Figure 23 Schematic of LCR paths using PAURS with two 8-element transducers [66] 83
Figure 24 Example LCR signal showing interpolation in Ti-6Al-4V [66] 84
Figure 25 8 example interpolated signals from Ti-6Al-4V [66] 84
Figure 26 Couplant-thickness influence and differential ToF procedure: (a) potential variation in the coupling layer between measurement positions and (b) use of adjacent receiver paths to reduce common coupling and system contributions 86
Figure 27 Close-up of the acoustoelastic constant testing setup 88
Figure 28. (a) Pulse-echo setup for Sample #1 using a 10 MHz, 16-element phased-array transducer; (b) LCR setup for Sample #2 using two 5 MHz, 8-element phased-array transducers and (c) Positioning of pulse-echo and LCR probes on the sliced AFSD samples [101] 92
Figure 29. Use of calibrated shims to maintain consistent couplant thickness during LCR measurements [101] 93
Figure 30 CM FE model with proposed scan lines for RS measurement in Ti-6Al-4V WAAM samples. [61] 97
Figure 31 CM RS measurement results. [61] 98
Figure 32 Cross-section of the WAAM sample. [61] 99

Figure 33 Loading/ascending acoustoelastic constant graphs [61] 100
Figure 34 Unloading/descending acoustoelastic constant graphs [61] 101
Figure 35 Calculated variance between each element's RS measurement and averaged results [61] 102
Figure 36 Per-element stress distribution across WAAM sample results [61] 103
Figure 37 Results of the RS measurement using the phased array ultrasonics method [61] 104
Figure 38 Comparison between phased array and CM RS measurements [61] 106
Figure 39 a) The cut section of the WAAM Ti-6Al-4V wall used for optical microscopy and b) Montaged optical macrographs of the deposited wall and the substrate [66] 109
Figure 40 CM RS measurements for as-deposited and post-peened samples [66] 110
Figure 41 FE analysis models for both the as-deposited and post-peened samples with back-calculated RS (in MPa) using CM [66] 111
Figure 42 XRD RS measurements of the as-deposited WAAM Ti-6Al-4V sample [66] 112
Figure 43 SNR calculation methodology and formula [66] 114
Figure 44 (a) SNR results across regions; (b) Sample positions [66] 115
Figure 45 Acoustoelastic constant graph during loading [66] 116
Figure 46 Acoustoelastic constant graph during unloading [66] 117
Figure 47 As-Deposited initial RS measurements [66] 119
Figure 48 Inter-pass Peened initial RS measurements [66] 120
Figure 49 As-deposited Standard Deviation results [66] 121
Figure 50 Inter-pass peened Standard Deviation results [66] 121
Figure 51 As-deposited RS measurements after outlier removal [66] 122
Figure 52 Inter-pass peened RS measurements after outlier removal [66] 123
Figure 53 Comparison of Mean RS before and after outlier removal [66] 124
Figure 54 Final Mean RS measurements for as-deposited and inter-pass peened samples [66] 125
Figure 55 (a) Final PAURS RS measurements, (b) XRD as-deposited RS, (c) CM RS for as-deposited and post-peened samples [66] 126
Figure 56. EBSD inverse pole figure (IPF) maps of the AFSD-deposited region of the AA7075 component: (a) as-deposited condition (Sample#1) and (b) heat-treated condition (Sample#2), showing a fine equiaxed grain structure. [101] 135
Figure 57. Grain size distribution derived from the EBSD maps for (a) as-deposited condition (Sample#1) and (b) heat-treated condition (Sample#2). [101] 135
Figure 58. EBSD inverse pole figure (IPF) maps of the substrate region of the AA7075 component: (a) as-deposited condition (Sample#1) and (b) heat-treated condition (Sample#2), showing a coarse and elongated grain structure. [101] 136
Figure 59. Pulse-echo ToF for Sample #1: (a) FEG, (b) CEG [101] 138
Figure 60. Pulse-echo ToF for Sample #2: (a) FEG, (b) CEG [101] 139
Figure 61. Rexolite wedge dimensions (a), A-scan (b) and LCR path geometry and critical angles (c) [101] 140
Figure 62. LCR arrival verification: (a) stable LCR waveform, (b) mode-converted arrival [101] 141
Figure 63. Fastest (T1R1) and slowest (T8R8) LCR path arrivals in FEG (a) and CEG (b) in Sample#1 [101] 142
Figure 64. Fastest (T1R1) and slowest (T8R8) LCR path arrivals in FEG (a) and CEG (b) in Sample#2 [101] 143
Figure 65. Pulse-echo attenuation in Sample #1 (a: FEG, b: CEG) [101] 145
Figure 66. Pulse-echo attenuation in Sample #2 (a: FEG, b: CEG) [101] 146
Figure 67. Attenuation of LCR wave propagated in FEG (a) and CEG (b) in Sample#1 [101] 147
Figure 68. Attenuation of LCR wave propagated in FEG (a) and CEG (b) in Sample#2 [101] 148
Figure 69. LCR attenuation in Sample #1 (a: FEG – b: CEG) [101] 149
Figure 70. LCR attenuation in Sample #2 (a: FEG – b: CEG) [101] 150
Figure 71. Pulse-echo backscatter RMS in Sample #1 [101] 151

Figure 72. Pulse-echo backscatter RMS in Sample #2 [101] 151
Figure 73: LCR backscatter windows evaluated (Regions A–D) [101] 152
Figure 74. LCR backscatter for Sample #1 (Region B) [101] 153
Figure 75. LCR backscatter for Sample #2 (Region B) [101] 154
Figure 76. LCR energy-normalised FFT spectra for Sample #1 (0–10 MHz), with extracted centre frequency and −6 dB bandwidth indicated [101] 155
Figure 77. LCR energy-normalised FFT spectra for Sample #2 (0–10 MHz), with extracted centre frequency and −6 dB bandwidth indicated [101] 156
Figure 78. Conceptual map of LCR observables and their roles within PAURS+. ToF (τ) encodes stress, whereas attenuation (α), backscatter (β) and frequency-domain metrics (Ψ) encode microstructure. [101] 159
Figure 79 The four main agreements between PAURS and validation methods 165

Table of Tables

Table 1. Dominant physical sensitivities of phased-array LCR ultrasonic observables to RS and microstructure..... 39
Table 2 The scan parameters used for XRD RS measurements 75
Table 3 Average difference in gain relative to Snell-calculated angle wedge vs. wedge angle for titanium. 100
Table 4 Loading acoustoelastic constant results 118
Table 5 Unloading acoustoelastic constant results..... 118
Table 6. LCR path-span ΔToF (T1R1–T8R8) measured across multiple frames in FEG and CEG regions for Sample #1 and Sample #2 143
Table 7 Backscatter analysis for sample#1. 152
Table 8. Backscatter analysis for sample#2. 152
Table 9. Summary of all results 158
Table 10 Comparison of RS measurement methods relevant to this thesis, summarised from the reviewed literature [6, 20–22, 25, 27–30, 36–40, 45–49, 53, 55, 63, 156, 157] and the three studies 164

Table of Equations

Equation 1 The formula for Snell's law 29
Equation 2 The shear modulus formula 32
Equation 3 Formula to calculate the ToF of longitudinal waves 32
Equation 4 The complete formula for the relationship between the ToFs of longitudinal waves and material stress 32
Equation 5 The formula for the relative sensitivity of velocity with strain 33
Equation 6 The equation for stress variation in terms of ToF variations (dt/t1). 33
Equation 7 Core formula to calculate US RS measurements 33
Equation 8 Formula to calculate the acoustoelastic constant 34
Equation 9 Phased array ultrasonics—direct approach 34
Equation 10 Phased array ultrasonics—FMC approach 34
Equation 11 Elastodynamic wave equation in a polycrystalline solid with RS 36
Equation 12 Decomposition of the effective stiffness tensor into a microstructure-dependent baseline term $\boldsymbol{C}0(M)$ and a residual-stress-dependent perturbation $\boldsymbol{C}\sigma(\boldsymbol{\sigma})$. 36
Equation 13 Acoustoelastic perturbation of LCR phase velocity, expressed as a microstructure-dependent baseline velocity $v0(M)$ plus a stress-dependent increment from the in-plane RS $\boldsymbol{\sigma}$ ‖. .. 36
Equation 14 LCR ToF along propagation path Γ, expressed as a path integral of the inverse local phase velocity incorporating microstructure-dependent baseline velocity $v0(M(s))$ and the acoustoelastic stress perturbation $\boldsymbol{L}$: $\boldsymbol{\sigma}$ ‖ (s). 37
Equation 15 Total attenuation expressed as intrinsic plus microstructure-dependent scattering contributions. 37
Equation 16 Backscatter heterogeneity metric defined by the RMS amplitude of the backscattered signal. 37
Equation 17 Frequency-dependent reduction in ultrasonic amplitude over propagation distance x. 37
Equation 18 FMC data structure for an N-element phased array, defined as the matrix of time-domain A-scans $sij(t)$ for all transmit element i and receive element j combinations. 38
Equation 19 LCR observable set used for stress and microstructure interpretation. 38
Equation 20 Decomposition of the measured ToF into couplant and material propagation contributions 85
Equation 21 Differential ToF calculated between adjacent receiver paths for a common transmitting element 85
Equation 22 Differential ToF variation between the WAAM measurement and the parent-material reference 86
Equation 23 Linear interpolation of the ultrasonic signal amplitude between adjacent time samples. 89
Equation 24 Formula used for calculating the variance between per-element results and the average of results at each point 102
Equation 25 Formula used to calculate SNR 113
Equation 26 Standard deviation formula used for calculating path outliers 121
Equation 27 Multi-echo pulse-echo attenuation estimate from successive backwall amplitude ratios 146
Equation 28 FMC-averaged multi-echo pulse-echo attenuation metric across all phased-array element pairs 146
Equation 29 Effective differential LCR attenuation per unit path length, computed from the amplitude ratio between two neighbouring transmit–receive paths. 148
Equation 30 Averaged adjacent-path amplitude gradient used to estimate phased-array LCR attenuation 149
Equation 31 Definition of the nondimensional scattering parameter ka, relating characteristic microstructural length scale a to ultrasonic wavelength λ. 156

List of Publications

Throughout my PhD, I have been the lead author on two published journal papers, with two still in preparation; the second author on one published journal paper; and a co-author on two submitted journal papers. For conferences, I have presented as the lead author at three and as a second author on one and have been a co-author on one submitted conference paper. These are detailed below:

Journal Papers

Lead author

Published

- Walker, J., Mills, B., Javadi, Y., MacLeod, C., Sun, Y., Ahmad, B., Williams, S., Ding, J., Tamimi, S.: Inter-pass peening for residual stress control in additive manufacturing: validation using ultrasonic, X-ray and contour method. Mater Des. 260, 115247 (2025). https://doi.org/10.1016/j.matdes.2025.115247
- Walker, J., Mills, B., Javadi, Y., MacLeod, C., Sun, Y., Taraphdar, P.K., Ahmad, B., Gurumurthy, S., Ding, J., Sillars, F.: Study of Residual Stress Using Phased Array Ultrasonics in Ti-6AL-4V Wire-Arc Additively Manufactured Components. Sensors. 24, 6372 (2024). https://doi.org/10.3390/s24196372

Unpublished

- Walker, J., Germano, E., Mills, B., Javadi, Y., Buffa, G., MacLeod, C., Gaghagan, A., Pierce, G., Mineo, C., Tamimi, S., Mohseni, E. and Lam, K.-H., n.d. Comparative Non-Destructive Evaluation of Additive Friction Stir Deposition Using Phased Array Ultrasonics and X-ray Computed Tomography. (Unpublished manuscript, in preparation)
- Walker, J., Mills, B., Javadi, Y., MacLeod, C., Sun, Y., Ding, J., Reid, M. and Paradowska, A., n.d. Residual Stress Characterisation of WAAM Ti-6Al-4V Using Phased Array Ultrasonics Validated by Neutron Diffraction. (Unpublished manuscript, in preparation)

Second author

Published

- Mills, B., Walker, J., Javadi, Y., MacLeod, C.N., Alipooramirabad, H., Reid, M., Paradowska, A.: Residual stress analysis in robotically welded plates using phased array ultrasonics with validation through neutron diffraction and hole-drilling methods. International Journal of

Pressure Vessels and Piping. 216, 105518 (2025). https://doi.org/10.1016/j.ijpvp.2025.105518

Co-author

Unpublished

- Mills, B., Serjeant, S., Javadi, Y., Tamimi, S., Walker, J., Showell, D., Samuel, J., MacLeod, C., Loukas, C., Mohseni, E., Rahimi, S. and Zhang, J., n.d. Phased Array Longitudinal Critically Refracted Waves for Microstructure Characterisation: Towards In-Process Characterisation. (Unpublished manuscript, submitted for publication)
- Javadi, Y., Mills, B., Samuel, J., Showell, D., Walker, J., Azam, S., Tamimi, S., Mohseni, E. and MacLeod, C., 2026. Toward Isolation of Microstructural and RSContributions in Phased-Array LCR Ultrasonics. (Unpublished manuscript, submitted for publication)

Conferences

Lead author

Published

- Walker, J, Mills, B, Javadi, Y, MacLeod, C, Sun, Y, Taraphdar, P, Ahmad, B, Gurumurthy, S & Ding, J (2025), 'The impact of peening on residual stress in wire-arc additive manufactured Ti-6Al-4V using contour method and phased array ultrasonics', 12th International Conference on Residual Stresses, Detroit, United States, 20/10/25 - 23/10/25.
- Walker, J, Mills, B, Javadi, Y, Sun, Y, Taraphdar, PK, Sillars, F, MacLeod, CN, Gachagan, A & Pierce, G (2024), 'Interpass peening impact on residual stress in wire-arc additive manufactured Ti 6Al-4V using phased-array ultrasonic testing', ASTM International Conference on Advanced Manufacturing 2024, Atlanta, United States, 27/10/24 - 1/11/24
- Walker, J, Mills, B, Germano, E, Javadi, Y, Buffa, G, MacLeod, CN, Gachagan, A, Pierce, G, Mineo, C & Tamimi, S (2024), 'Phased Array Ultrasonic Testing of Additively Friction Stir Deposited AA2024 Aluminum Alloy Samples', BINDT/61st Annual British Conference on Non-Destructive Testing 2024, Telford, United Kingdom, 3/09/24 - 5/09/24.

Second author

Published

- Germano, E, Walker, J, Mills, B, Javadi, Y, Buffa, G, MacLeod, C, Gachagan, A, Pierce, G, Mineo, C, Tamimi, S, Mohseni, E & Lam, KH 2024, 'Enhancing additive friction stir deposition through comprehensive ultrasonic defect detection and process optimisation', The UKRI EPSRC Centre for Doctoral Training in Future Ultrasonic Engineering Annual Scientific Meeting 2024, Glasgow, United Kingdom, 25/06/24 - 25/06/24.

Co-author

Unpublished

- Azam, S., Kalashnikov, K., Walker, J., Kerr, W., Javadi, Y., Buffa, G., Konkova, T., and Tamimi, S., 2026. Dissimilar Additive Friction Stir Deposition of AA6082-T6 on Low-Carbon Steel: Process Window Identification and Multi-Modal NDT Validation. (in preparation, unpublished manuscript)

Terms and Abbreviations

Manufacturing & Processes

WAAM	Wire Arc Additive Manufacturing
AM	Additive Manufacturing
AFSD	Additive Friction Stir Deposition
EDM	Electrical Discharge Machining

Materials & Microstructure

Ti-6Al-4V	Titanium Alloy (6% Al, 4% V)
HAZ	Heat-Affected Zone
FEG	Fine Equiaxed Grains
CEG	Coarse Elongated Grains
HCP	Hexagonal Close-Packed

Residual Stress (RS) Measurement Methods

RS	Residual Stress
CM	Contour Method
XRD	X-ray Diffraction

Ultrasonics & Acoustoelasticity

PAUT	Phased Array Ultrasonic Testing
PAURS	Phased Array Ultrasonics for Residual Stress Measurement
PAURS+	PAURS toward dual-field characterisation
LCR	Longitudinal Critically Refracted (wave)
ToF	Time-of-Flight
FMC	Full Matrix Capture
TFM	Total Focusing Method
SNR	Signal-to-Noise Ratio

FFT	Frequency-Domain Response
RMS	Root Mean Square
XEC	X-Ray Elastic Constants

Equipment / Hardware

CMM	Coordinate Measuring Machine
PEAK MP6	PEAK Micropulse 6 Phased Array Equipment

Software

FE	Finite Element
FEM	Finite Element Method

Variables / Constants / Units

σ	Stress
L_{11}	Acoustoelastic Constant
E	Elastic modulus
v	Poisson's ratio
ρ	Density
V	Velocity
λ / μ	First & second Lamé constants
A, B, C	Third-order elastic constants
MPa	Megapascal
GPa	Gigapascal
kN	Kilonewton
mm	Millimetre
Hz / MHz	Hertz / Megahertz
dB	Decibel

Abstract

Residual Stress (RS) remains a major challenge for metal Additive Manufacturing (AM), in large-scale processes such as Wire Arc Additive Manufacturing (WAAM). Steep thermal gradients and repeated thermal cycling can cause distortion, cracking and reduced structural performance. Existing RS measurement methods are often destructive, surface-limited or impractical for automated manufacturing. A non-destructive, subsurface-sensitive method is therefore required.

The thesis describes the development of Phased-Array Ultrasonics for Residual Stress measurement (PAURS). PAURS employs phased-array transducers to produce Longitudinal Critically Refracted (LCR) waves and makes use of acoustoelastic calibration in order to convert variations in Time-of-Flight (ToF) into RS measurements. Full Matrix Capture (FMC) allows averaging multiple paths and assessing the quality of each path, increasing measurement redundancy and reducing variability. PAURS+ is also examined as a microstructure-aware extension of PAURS

PAURS was assessed across three studies. Measurements from as-deposited and inter-pass-peened WAAM Ti-6Al-4V samples were compared with those obtained using the Contour Method (CM) and X-ray Diffraction (XRD); these methods differ in penetration depth and the gauge volumes. Additive Friction Stir Deposition aluminium was also investigated for variation in microstructure.

In the WAAM studies, PAURS identified central tensile RS peaks that decreased with distance from the Heat-Affected Zone, qualitatively agreeing with CM and XRD. PAURS indicated a reduction in peak tensile RS from approximately 660 MPa in the as-deposited specimen to 530 MPa following inter-pass peening. Quantitative differences were attributed partly to penetration depth, gauge volume and reference condition. FMC provided path redundancy and reduced variability following path-quality assessment.

The PAURS+ study found that LCR ToF exhibited limited sensitivity to the investigated microstructural transition, while attenuation and backscatter showed clearer microstructural contrast. Overall, PAURS demonstrates potential for non-destructive, repeatable and automated shallow-subsurface RS assessment. Further development is required before in-process deployment and quantitative separation of stress and microstructure.

Chapter 1: Introduction

1.1 Background

RS is a challenge in metal Additive Manufacturing (AM) because it can lead to distortion, cracking, and reduced structural performance in these manufactured components. As AM has become increasingly utilised for larger components and greater automation, a non-destructive, repeatable, and future-integrable RS measurement method is crucial. This thesis develops and validates a phased-array ultrasonic approach for RS measurements, focusing primarily on Wire Arc Additive Manufacturing (WAAM) Ti-6Al-4V.

1.2 Research Gaps

WAAM is favourable for large Ti-6Al-4V structures due to its high deposition rate and low material waste. Nevertheless, repeated thermal cycling and material contraction during cooling result in significant RS. Existing methods of RS assessment can provide useful validation. However, techniques based on non-destructive principles are limited in penetration depth, user-friendliness, and the facilities required, which limit their viability for in-situ RS assessment. The drawbacks of the techniques are discussed in Chapter 2, thereby demonstrating the need for an ultrasonic technique that can provide subsurface RS assessment while also being feasible for future in-situ RS measurements.

Despite progress in ultrasonic RS measurement, three main research gaps remain. These gaps are addressed sequentially through the three studies included in this thesis.

Gap 1, addressed in Chapter 5, concerns the validation of phased-array longitudinal critically refracted (LCR) ultrasonics for RS measurement in WAAM Ti-6Al-4V. Existing studies have demonstrated the sensitivity of ultrasonic Time-of-flight (ToF) to stress, but a repeatable methodology for using phased-array ToF data to calculate and validate RS measurements remains underdeveloped. This study addresses this gap by developing the phased-array LCR approach for WAAM Ti-6Al-4V, applying it to an as-deposited sample, and comparing the resulting RS distribution with that obtained using the Contour Method (CM).

Gap 2, addressed in Chapter 6, concerns the use of Full Matrix Capture (FMC), outlier removal, and Phased Array Ultrasonics for Residual Stress measurement (PAURS) to assess RS redistribution resulting from process-based mitigation strategies. Since acoustoelastic ToF changes are small, improved averaging, outlier detection, and acoustic path quality control are required to make ultrasonic RS measurements repeatable in heterogeneous AM materials. There is also limited evidence that ultrasonic RS measurement can assess RS redistribution resulting from strategies such as inter-pass peening. This study addresses this gap by applying PAURS with FMC to as-deposited and inter-

pass peened WAAM Ti-6Al-4V samples, using CM and X-Ray Diffraction (XRD) to assess whether the technique can identify stress redistribution after peening.

Gap 3, addressed in Chapter 7, concerns the influence of microstructural heterogeneity on ultrasonic RS measurements. Ultrasonic measurements in AM materials remain affected by microstructural variation because stress and microstructure can both affect ultrasonic signals. Therefore, it is necessary to distinguish stress-sensitive observables, such as ToF, from microstructure-sensitive observables, such as attenuation, backscatter, and frequency-domain response. This study addresses this gap by developing PAURS+, using AFSD aluminium samples to separate stress- and microstructure-dominated ultrasonic responses.

The three studies together address these gaps in a progressive structure. The feasibility of phased-array LCR RS measurement in WAAM Ti-6Al-4V is presented in Chapter 5. Chapter 6 demonstrates the application of PAURS with FMC to assess RS redistribution after inter-pass peening in WAAM Ti-6Al-4V. Chapter 7 extends PAURS+ to facilitate microstructure-informed interpretation of ultrasonic measurements. This progression connects the research gaps directly to the thesis structure. It shows the development of the method from feasibility to validation, to mitigation assessment and finally to microstructure-aware interpretation.

1.3 Aims & Objectives

The main objective of this work is to develop and demonstrate PAURS as a suitable and reliable non-destructive phased-array ultrasonic method for RS measurements in metal AM. The listed objectives describe how this aim will be addressed through method development, validation of a multi-technique approach, evaluation of RS mitigation and understanding of the microstructure of ultrasonic signals.

To achieve this aim, the research is carried out by considering the following four main objectives:

1. Develop a repeatable, phased-array ultrasonic measurement methodology for AM samples.
2. Evaluate PAURS through comparison with established RS measurement methods.
3. Assess whether PAURS can detect RS redistribution associated with mitigation strategies such as peening.
4. Extend PAURS to PAURS+ by separating stress-related and microstructure-related ultrasonic components.

1.4 Contribution to The Knowledge

1.4.1 PAURS in WAAM

This thesis develops and experimentally evaluates a phased-array LCR workflow for shallow-subsurface RS assessment in WAAM Ti 6Al 4V, evaluated through comparison with CM and XRD in Chapters 4 and 6. This process utilises phased-array LCR acquisition, ToF extraction, and acoustoelastic calibration to

calculate RS, which are then compared with reference RS measurements from CM and XRD in Chapters 4 and 6. It also demonstrates how FMC multi-path acquisition can be used in this method to support averaging, identify potentially anomalous paths and assess path-to-path variability.

1.4.2 PAURS+

This thesis also extends PAURS to PAURS+, an interpretation method that separates ultrasonic observables based on their primary sensitivity. In the AFSD aluminium samples studied in Chapter 7, LCR ToF was found to be most sensitive to RS variation. On the other hand, attenuation, backscatter, and frequency-domain features were demonstrated to be mainly sensitive to microstructural differences. This provides a basis for microstructure-aware interpretation of PAURS measurements in heterogeneous AM materials, where stress and microstructure effects may otherwise be coupled.

1.4.3 Basis for Future In-Situ Measurements

This thesis utilises PAURS to measure the redistribution of RS induced by inter-pass peening in a WAAM Ti-6Al-4V sample and compares these results with CM and XRD in Chapter 6. This demonstrated that PAURS could detect changes in RS distribution, supporting its ability to evaluate RS mitigation methods in WAAM Ti-6Al-4V. Although fully implementing in-situ methods is outside the scope of this thesis, PAURS provides experimental evidence supporting future development towards in-situ or automated RS inspections. Figure 1 shows a flowchart that outlines each chapter of the thesis.

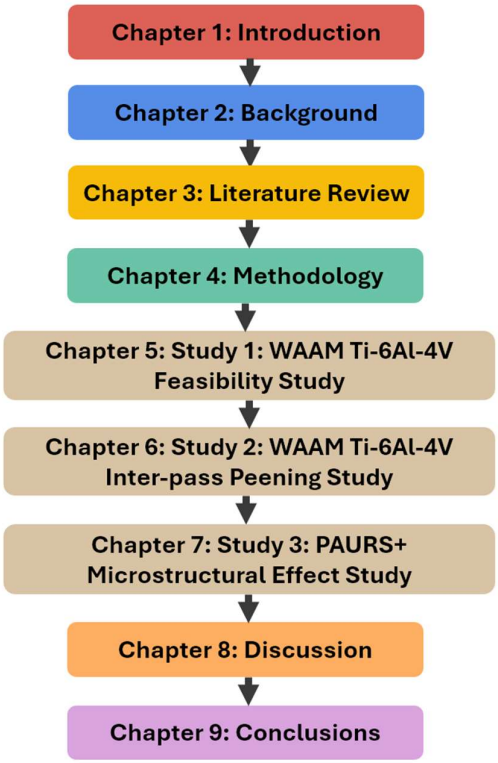


Figure 1 Flowchart showing the outline of the thesis chapters

Chapter 1 Introduction: introduces the research motivation, aims, objectives, contributions, and thesis structure.

Chapter 2 Background: introduces the technical foundations of WAAM RS, established measurement methods, ultrasonic LCR measurement, phased arrays, FMC, PAURS and PAURS+.

Chapter 3 Literature Review: evaluates previous research on these topics and identifies the limitations and research gaps addressed by PAURS and PAURS+.

Chapter 4 Methodology: outlines the process used throughout the thesis. It details the manufacture of the WAAM Ti-6Al-4V samples, the scanning strategies applied for ultrasonic inspection, and the phased-array LCR configuration developed for this research. The chapter also describes the acoustoelastic calibration process, the FMC strategy, and the data quality control procedures. Validation techniques, including CM and XRD are also outlined,

Chapter 5: Study 1: WAAM Ti-6Al-4V Feasibility Study: This chapter presents the initial development and feasibility of the phased-array LCR RS measurement approach for WAAM Ti-6Al-4V and compares the results with those from CM. It establishes the initial experimental and processing basis for PAURS.

Chapter 6: Study 2: WAAM Ti-6Al-4V Inter-pass Peening Study: This chapter applies PAURS to as-deposited and inter-pass peened WAAM Ti-6Al-4V samples. These results are then validated with CM, and XRD is used to assess whether PAURS can detect RS redistribution caused by peening.

Chapter 7: Study 3: PAURS+ Microstructural Effect Study: This chapter further develops PAURS+ by analysing how ToF, attenuation, backscatter, and frequency-domain features change with stress and microstructural variations in AFSD aluminium samples.

Chapter 8 Discussion: summarises the results from all three studies, offering a review of PAURS's advantages and limitations, as well as its future potential in industry. It draws upon insights from WAAM, inter-pass peening, and microstructure analysis to illustrate the progression of the PAURS methodology across various materials and applications. The chapter further examines the utilisation of PAURS for WAAM process optimisation, quality assurance, and future in-process monitoring. Chapter 8 provides a focused discussion of microstructure, explaining how microstructural changes influence ultrasonic observables and how findings from the PAURS+ study improve the interpretation of RS measurements throughout the thesis.

Chapter 9 Conclusions: summarises the thesis as well as the main contributions and findings, including results from all three studies. It also proposes future research directions, such as incorporating PAURS into automated WAAM systems, improving FMC analysis, and expanding the method to cover more materials and different component geometries.

Chapter 2: Background

2.1 Introduction

This chapter introduces the technical background required for the RS measurements presented in this thesis. It describes metal AM, WAAM, RS formation and the principal measurement methods relevant to the research. The chapter then introduces ultrasonic RS measurement, including acoustoelasticity, LCR waves, phased-array ultrasonics and FMC. These principles provide the basis for the PAURS methodology used in the subsequent chapters.

2.2 Additive Manufacturing

AM enables the manufacture of metallic components through successive material deposition, providing design freedom and part consolidation [1, 2]. For this thesis, the most relevant feature of AM is the repeated localised heating and cooling that occurs during metal deposition [2]. These thermal cycles generate non-uniform microstructures and RS fields, necessitating reliable measurement methods for AM components [1, 3].

Metal AM processes differ in their energy sources, feedstocks, build rates, and thermal histories. However, they share a common challenge which is that localised heat input and repeated reheating can generate non-uniform microstructures, defects, and RS [1, 2]. For this thesis, Directed Energy Deposition (DED) processes are most relevant because they include WAAM, in which large component size and repeated thermal cycling make RS measurements particularly important.

2.2.1 Wire Arc Additive Manufacturing

Within DED, WAAM has maintained a continued interest because it utilises arc-welding heat sources together with wire feedstock. This combination results in high deposition rates and relatively low material costs, which makes it ideal for large metallic components [1, 4]. WAAM is often considered a route for replacing machining of billet or large forgings for both low and high complexity parts, with prior studies highlighting its potential for titanium structural components [2, 4].

The WAAM thermal cycle influences the resulting microstructure and material properties. For Ti-6Al-4V, investigations report large columnar prior-β grains and Widmanstätten α morphologies that vary with height due to repeated heating and cooling cycles, with resulting mechanical performance generally comparable to that of conventional materials but still sensitive to defects such as porosity [4, 5]. These microstructural characteristics are essential for this thesis because they affect both the stress state and the propagation of ultrasonic waves, potentially coupling microstructure-related velocity changes with stress-related changes if not carefully managed in the measurement design.

2.3 RS Formation and Measurement Challenges

2.3.1 Context

RS is the internal stress retained in a material when external forces or thermal gradients are no longer present [6]. RS can occur because of the incompatibilities of different regions of assembly, material, or components. A simple occurrence of an RS field is caused by an oversized sphere within a spherical cavity inside a large homogeneous body made of the same material. This can occur due to cooling a body that contains a sphere with a smaller coefficient of thermal expansion but with the same elastic constants [7].

RS spans macroscopic fields that equilibrate over structural length-scales [8,9].

Type I: involves macro-RS that appear in the body of a component which is larger than the grain size of the material.

Type II: involves micro stresses which vary with the scale of individual grains; they generally arise in single-phase materials due to the anisotropy of each grain.

Type III: consists of micro-RS which are contained within a grain; these stresses arise due to dislocations and other crystalline defects. Both the Type II and Type III stresses are classified as micro stresses.

Examples of Type I stress are the stresses that result from the plastic bending of a bar, and which usually balance out over a length scale similar to that of the structure itself. Type II stresses are generally caused by differences in slip behaviour between grains. On the other hand, Type III stress is the result of point defects and of line defects caused by doping with atoms that have different amounts of radiation damage, damage which takes place at the atomic level.[7].

2.3.2 RS in Additive Manufacturing

In AM, RS arises primarily due to non-uniform thermal expansion and contraction during layer-by-layer deposition [7].

In WAAM, Type I RS is the main concern since it has a macroscopic scale and is capable of distorting the components as well as causing cracking and leading to a deterioration of fatigue performance [10]. Although Type II and Type III RS occur at smaller length scales, they are still important, especially in affecting phase stability and causing microcracks.

While Tensile RS is particularly detrimental, compressive RS is often beneficial and intentionally introduced through processes like peening [11].

2.3.3 WAAM RS

WAAM can generate RS and distortion through repeated heating, constrained cooling and contraction of the deposited material and substrate [4, 12]. The resulting stress field varies spatially and may change as additional layers are deposited.

In WAAM Ti-6Al-4V, repeated thermal cycling, temperature-dependent material properties and substrate restraint can produce spatially varying longitudinal, transverse and through-thickness stresses. High tensile stresses may occur near the deposited wall and deposit-substrate transition, balanced by compressive stresses elsewhere in the component [12, 13]. The stress state may also change following unclamping or substrate removal.

The distribution can be altered by mechanical and thermal treatments. Inter-pass rolling and peening cause local plastic deformation, whereas thermal stress relief leads to stress relaxation. The degree to which these treatments are effective varies according to the intensity of the treatment, the time at which it is carried out, and its position in relation to the deposited area [13, 14].

The same microstructural evolution that gives rise to thermal and mechanical effects may result in the presence of RS and microstructural gradients within the same areas, a fact which is especially relevant to ultrasonic measurement since both of these conditions can affect the acoustic response that is measured.

2.3.4 RS Mitigation

RS in WAAM can be modified through process control, thermal treatment and mechanical treatment. Thermal stress relief promotes material relaxation, while mechanical treatments such as inter-pass rolling and peening introduce local plastic deformation that can redistribute tensile RS and introduce compressive stress [15–18].

Machine hammer peening uses a controlled oscillating tool to deliver repeated impacts to the material surface. When applied between deposited layers, inter-pass peening becomes integrated into the WAAM process and modifies the evolving stress state before the build is complete. [16, 19, 20]

2.4 Established RS Measurement Methods

RS cannot be measured directly and must be inferred from a measurable response, such as elastic lattice strain, deformation following material removal or stress-dependent changes in a physical property. Each technique therefore represents a specific stress component, sampling depth and material [6, 20–22].

RS measurement methods are commonly classified as destructive, semi-destructive or non-destructive. Method selection depends on the component geometry, material condition, required

penetration depth, spatial resolution, gauge volume and whether repeated measurements are required.

The methods based on diffraction are used to determine the elastic lattice strain, whereas those based on mechanical relaxation calculate the stress by referring to the deformation that occurs after the controlled removal of material. The main techniques employed in this thesis are introduced below, and their relative suitability and uncertainty are assessed in Chapter 3.

2.4.1 Destructive Methods

2.4.1.1 CM

CM is a destructive method for the measurement of RS since it involves cutting a component and then measuring the deformation of the cut surfaces, after which the deformation profile is used to reconstruct the original RS distribution by means of finite element (FE) analysis [23].

The principle of superposition associated with Hans Bueckner [24], is an elastic one and says that when a cracked object is subjected to external loading and forces are also applied to the surface of the crack in order to close it, these forces must be equal to the stress distribution in an uncracked body of the same dimensions/geometry which is also being loaded externally.

This principle makes the calculations easier and enables us to determine the intensity of stress and deformation by means of the original stresses on the cut plane. In order to achieve this, it is necessary to understand how RS or applied stress can cause a crack to grow and thus redistribute the stress in the body. When a body is subjected to stress, whether it be applied or residual, a crack may grow, and as a result the stress is relieved on the face of the crack and the stress is redistributed throughout the body. Once the crack length increases, the redistributed stresses are then released rather than the original RS. It was at this point that Hans Bueckner developed a principle by which everything could be correctly calculated, and the redistribution of stress could be kept track of. This is the principle that is used in CM. [23].

CM determines a two-dimensional distribution of the stress component normal to a selected cut plane. Sectioning releases the original stress and produces deformation of the cut surfaces. The measured surface contour is reversed and applied to an FE model to reconstruct the stress that existed before cutting [25].

CM is particularly effective for mapping RS across large cross-sections and has been widely used in AM research [26]. CM measurements depend on cut quality, contour measurement, smoothing and finite-element reconstruction. Because the specimen is sectioned, its applicability in manufacturing is limited, and the method cannot be repeated at the same location.

2.4.1.2 Incremental Hole Drilling

IHD provides a near-surface depth profile while introducing only localised damage [27]. However, IHD is sensitive to strain measurement, drilling depth, hole geometry, and material constants, so its results must be interpreted with uncertainty [28–30].

2.4.2 Non-Destructive

2.4.2.1 XRD

XRD is a non-destructive method which determines RS by detecting the changes in the spacing of the crystal lattice planes caused by elastic strain [31]. It is most suitable for the analysis of surface and near-surface stresses, the penetration depth generally being limited to a few tens of microns. The technique is based on Bragg's law, which relates the shift in diffraction angle to strain; this strain then being converted into stress using the elastic constants. The principal limitations of the method are its surface sensitivity, texture, grain statistics and the need for access. Because of this, XRD is widely used for checking other RS measurement techniques and is appropriate for materials that have a fine, crystalline microstructure [32]. In this thesis, XRD is therefore used as a reference method with different depth sensitivity rather than as a direct replacement for PAURS.

Synchrotron XRD uses the same lattice-strain principle but employs a high-intensity, high-energy beam generated at a specialist synchrotron facility, providing greater penetration and spatial resolution [33]. The measurements in this thesis used a PROTO LXRD laboratory diffractometer with a conventional X-ray tube and the $\sin^2\psi$ multiple-exposure method. The PROTO LXRD is not a synchrotron system, and its measurements represent the surface or near-surface RS condition rather than the bulk through-thickness distribution.

2.4.2.2 Neutron Diffraction (ND)

Neutron Diffraction (ND) is a non-destructive technique used to measure RS within bulk crystalline materials. Neutrons penetrate more deeply into engineering metals than laboratory X-rays, allowing elastic lattice strain to be measured at selected locations within thick components. Measurements are normally taken in several orientations and converted into stress using an appropriate stress-free lattice spacing and diffraction elastic constants [34].

The measurement represents an average over a finite gauge volume defined by the incident and diffracted beams. The achievable penetration depth, spatial resolution and measurement uncertainty therefore depend on the material, specimen thickness, neutron wavelength, diffraction geometry and available beam intensity [34, 35].

ND is particularly valuable for mapping internal and through-thickness RS distributions without sectioning the component. Its main limitations are the need for a specialist neutron facility, relatively

long acquisition times, finite gauge volume, restricted equipment availability and uncertainty in determining the stress-free lattice spacing [36–38].

2.5 Ultrasonic Measurements

2.5.1 Conventional Ultrasonic RS

2.5.1.1 Principles

Ultrasonic RS measurement is based on the acoustoelastic effect, in which stress changes the ultrasonic velocity and, therefore, the ToF [39, 40]. Two major factors affect the velocity of US within a material; these are the elasticity and density of the material. Young's modulus represents the compressive and tensile stiffness of a material when a force is applied. The higher the value of Young's modulus is, the higher the velocity of sound propagating through it will be. For example, steel has a high Young's modulus value, and therefore, the velocity of sound travelling through it is typically high. On the other hand, the higher the density of the material is, the lower the velocity of sound travelling through it will be, so lead has a higher density than steel and, therefore, sound has a lower velocity when propagating through it. However, different waves have different velocities when travelling through materials. For instance, shear waves can travel through solids but do not have the same velocity as compression waves. This is caused by the modulus of rigidity of the solid, instead of Young's modulus, which affects the velocity, which is lower than the modulus of elasticity [41].

2.5.1.2 Snell's Law

Snell's law was discovered in 1621 and relates to the relationship between refraction and the angles of incidence for a light ray travelling through an interface of two isotropic media [42]**.** Snell's law is represented by the formula in Equation 1.

$$n_1 \sin\theta_1 = n_2 \sin\theta_2$$

Equation 1 The formula for Snell's law

Here, n_1 represents the refraction index of the first propagation media, n_2 represents the refraction index of the second propagation media, ϑ_1 represents the incident angle, and ϑ_2 represents the refracted angle. Despite being mainly discussed in terms of light rays, Snell's law also applies to ultrasound, and according to Snell's law, when an ultrasonic wave crosses an interface between two materials, with both materials having different indices of refraction, reflected and refracted waves are both generated, and these are altered depending on the angle of incidence [43]. This is crucial for understanding how LCR waves can be created and used for measuring RS.

2.5.1.3 LCR Waves

Ultrasonic waves can be split into four main types; these are transversal, longitudinal, Lamb and Rayleigh waves. Specifically looking at longitudinal waves, the particles oscillate in the direction of travel. When longitudinal waves interact with materials, several effects can alter the behaviour of the

waves. For example, when a wave travels through two different materials, refraction, transmission, and wave reflection occur. During refraction, the angle of wave propagation changes at the interface of the material. This is due to the difference in wave velocity for different materials, which is caused by different acoustic impedances. This phenomenon is expressed using Snell's law. When the wave incident angle increases, so does the wave propagation angle in the material volume. Using steel as an example, the first critical angle level is around 28°, and so before this, the longitudinal wave is transformed into a transversal wave and partially into an LCR wave, which travels parallel to the surface of the material [44].

LCR waves are generally used since they propagate near the surface and are sensitive to in-plane stress [45, 46]. As a result, they are appropriate for near-surface and subsurface RS measurements in AM components.

The measured ToF may also be influenced by environmental, coupling, geometric and material conditions. These influences require control or correction during calibration and measurement [40, 47–49].

Conventional LCR configurations commonly use one transmitter and one or two receivers, which provides limited data [45–49]. Its main limitations are restricted path redundancy and sensitivity to calibration, coupling, temperature, probe positioning and microstructure. This thesis addresses these limitations by using phased-array probes and FMC to increase the number of available acoustic paths, enabling averaging, outlier detection, and signal-quality control within the PAURS process.

2.5.2 Phased-array Ultrasonic Measurements

2.5.2.1 Phased Array Ultrasonics for Defect Detection

Phased-array probes contain multiple individually controlled elements. Applying timing delays across the active aperture allows the transmitted and received wavefields to be steered or focused. Beam behaviour depends on element dimensions, pitch, aperture, frequency and the applied delay law [50–53].

FMC records the time-domain response from every transmitter-receiver element combination, producing an $N \times N$matrix of A-scans [53]. The dataset can be processed using the Total Focusing Method (TFM) for imaging or analysed directly for ToF, amplitude and frequency characteristics. FMC is therefore the acquisition procedure, while TFM is one possible post-processing method [54, 55].

The application of FMC and phased-array post processing in the context of RS measurement is still in its infancy. It is generally aimed at the spatial localisation of reflectors. In contrast, PAURS requires highly repeatable ToF measurements along the propagation paths of LCR and the conversion of small timing changes into stress via acoustoelastic calibration. Thus, this thesis adapts phased-array and FMC

principles from NDT imaging to RS measurement. In the latter, outlier removal can be used for averaging and timing stability is prioritised over image formation.

2.6 Phased Array Ultrasonics for RS Measurement (PAURS)

2.6.1 Principles

Ultrasonics RS measurement typically uses LCR waves, and the traditional setup for this method is extremely sensitive to material temperature, which can affect the accuracy of the results [48]. Therefore, instead of single-element transducers, ultrasonic phased array transducers can be used in a setup provide additional measurements for averaging and consistency assessment. For PAURS , the two single-element transducers are replaced by two 8 element 5MHz arrays, with one acting as a transmitter and the other as a receiver, allowing for an increased amount of data over the traditional LCR RS setup.

2.6.2 Acoustoelasticity

Acoustoelastic constant increases because of tensile stress and decreases with compressive stress [56]. As mentioned, LCR waves have a higher sensitivity to stress when compared to other US wave types [46]. Based on this method, material stress can be determined using the ToF and the acoustoelastic coefficient measurements in both the material without stress and the material with either residual or applied stress. Using different US frequencies can also be used to penetrate a variety of materials with different thicknesses, which can be used to measure through-thickness RS. The transmitter and receiver transducers are placed into a wedge that can be moved over a material surface to extend the measurement coverage.

The acoustoelastic effect can only be shown by utilising extremely accurate measurements. For every MPa of stress applied to the material, only a 0.001% change in ultrasonic velocities is discovered [57]. Materials usually demonstrate substantial anisotropy and heterogeneity in their acoustic properties. The velocities of ultrasonic waves can be different in areas of the material that are free from stress. These limits of technological metals and the heterogeneity of acoustic properties are not entirely known [58].

The acoustoelasticity law states that material stress alters the ToF of US waves; therefore, Longitudinally Critically Refracted (LCR) waves are used due to their high sensitivity of stress when compared to other US waves.

Calculating US RS measurements relies on using both the ToF of the US waves and the acoustoelastic constant to find the RS in the sample. To do this, second-order elastic constants (Lamé constants) and third-order elastic constants are considered. When considering elasticity, the first Lamé constant is represented with λ and the second is represented by μ; this is the shear modulus of the material and

$$= \frac{\tau}{\gamma}$$

Equation 2 The shear modulus formula

is represented by Equation 2, where μ is the shear modulus, τ is the shear stress in the xy direction, and γ is the shear strain in the xy direction.

Along with the second-order elastic constants, the third-order elastic constants are also considered and are represented by A, B, and C.

The three principal strains within the homogeneous sample, categorised as ω1, ω2, and ω3, are combined and are represented by θ (a component of homogeneous triaxial principal strains). With these considered, the ToF of longitudinal waves, parallel to the stress direction, can be related to strain (ω) with Equation 3.

$$\rho_1 {V_{11}}^2 = \alpha + \beta$$

Equation 3 Formula to calculate the ToF of longitudinal waves

In this formula, ρ_1 represents the density of the material, V_{11} represents the velocity of the longitudinal wave, α represents the terms related to the properties of the material, and β represents the terms related to the strain. With this formula, the rest of the terms can be put into the formula to create Equation 4.

$$\rho_1 {V_{11}}^2 = \lambda + 2\mu + (2j + \lambda)\theta + (4k + 4\lambda + 10\mu)\omega_1$$

Equation 4 The complete formula for the relationship between the ToFs of longitudinal waves and material stress

For this formula, θ represents the combined strain and ω_1 represents the strain parallel to the stress. The relative sensitivity of velocity with strain then needs to be calculated to understand how the speed of the ultrasonic wave changes depending on the strain within the material. This is calculated using Equation 5.

$$\frac{L_{11}}{\rho_1 {V_{11}}^2} = 2 + (v\mu\varepsilon)\frac{\omega_1}{\theta}$$

Equation 5 The formula for the relative sensitivity of velocity with strain

L_{11} represents the acoustoelastic constant; in this equation, L_{11} is used to represent the fact that the acoustoelastic behaviour of the material is not dimensionless, unlike in other studies, such as that by Bray [59] where the authors use L_{11} as the dimensionless acoustoelastic constant. v represents the value of Poisson's ratio and ε represents the strain in the stress direction. The acoustoelastic constant is determined experimentally by recording ToF under known uniaxial stress. The specific tensile-test calibration procedure used in this thesis is described in the methodology chapter

For this testing, stress is increased in step intervals using the tensile testing machine while the ultrasonics equipment measures the ToF at each step [60]. Then, the stress variation in terms of ToF variations needs to be calculated to understand how changes in the ToF can relate to the variations in stress within the material. This is calculated using Equation 6.

$$\sigma = \frac{\left(\frac{L_{11}}{\rho_1 {V_{11}}^2}\right) \times \left(\frac{dt}{t_1}\right)}{\frac{\omega_1}{\theta}}$$

Equation 6 The equation for stress variation in terms of ToF variations (dt/t1).

Here, $d\sigma$ represents stress variation and (dt/t_1) represents ToF variation. Finally, the core formula for

$$\sigma = \frac{\left(\frac{L_{11}}{\rho_1 {V_{11}}^2}\right) \times (T_2 - T_1)}{T_1}$$

Equation 7 Core formula to calculate US RS measurements

ultrasonic stress measurement can be used with a combination of the previous equations, which is shown in Equation 7.

Here, σ represents the RS measurement, T_1 represents the ToF of the US wave in the stress-free material, and T_2 represents the ToF of the US wave in the material with applied stress or RS.

To find the acoustoelastic constant when considering all eight graphs, with each graph representing the ToF data of each array, Equation 7 is rearranged to create Equation 8.

$$L_{11} = \frac{\sigma T_1 \rho_1 V_{11}^2}{T_2 - T_1}$$

Equation 8 Formula to calculate the acoustoelastic constant

Equation 9 shows the formula used for the direct approach (σ_D) for phased array ultrasonics RS measurements, where only direct acoustic paths from one transmitter to the receiver are considered.

$$\sum \sigma_D = \frac{E}{L_{11}} \sum_{j=1}^{n} \left(\frac{T_j R_j \, WAAM - T_j R_j \, PARENT}{T_j R_j \, PARENT} \right) / n$$

Equation 9 Phased array ultrasonics—direct approach

Here, *E* represents the elastic modulus, *n* represents the number of points, *T* represents the transmitter data, *R* represents the receiver data, *WAAM* represents the *WAAM* Ti-6Al-4V sample measurement data, and *PARENT* represents the parent (stress-free) material measurement data.

If we use the Full Matrix Capturing (*FMC*) (σ_{FMC}) approach, Equation 10, can be used to generate results for all acoustic path possibilities instead. This allows for the acoustic path to transmit from any transmitter to any receiver and vice versa, generating more data than the direct approach.

$$\sum \sigma_{FMC} = \frac{E}{L_{11}} \sum_{j=1}^{n} \sum_{k=1}^{n} \left(\frac{T_j R_k \, WAAM - T_j R_k \, PARENT}{T_j R_k \, PARENT} \right) / n^2$$

Equation 10 Phased array ultrasonics—FMC approach

Figure 2 shows a schematic comparison of RS measurement using single-element transducers versus the phased array ultrasonics approach.

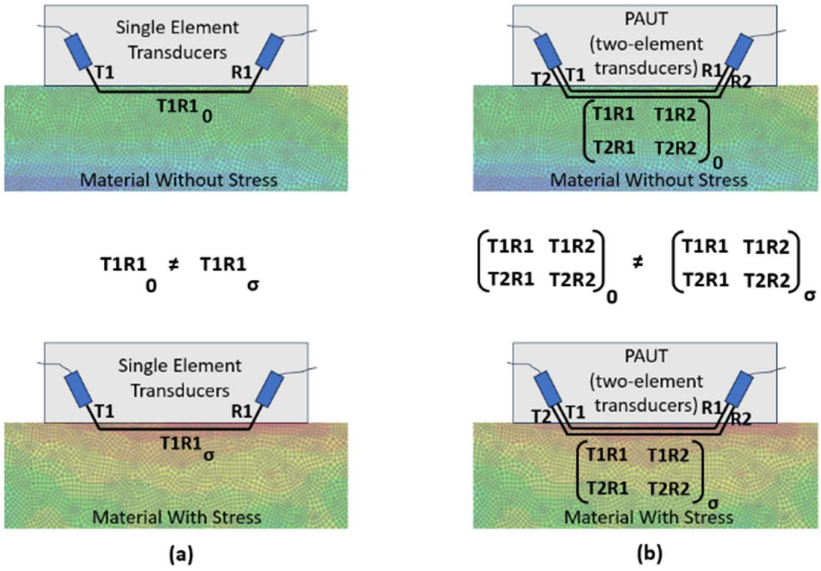


Figure 2 Schematic of RS measurement using (a) single-element transducers versus (b) phased array ultrasonic approach [61]

In the single-element method (Figure 2a), there is just one transmitter (T1) and one receiver (R1) transducer, and so the time of flight for the LCR wave is represented as T1R1. The value of T1R1 measured in a stressed material is different from that in an unstressed material because of acoustoelasticity (Equation 7). In the case of the phased array ultrasonics method (Figure 2b), there are two transmitter elements (T1 and T2) and two receiver elements (R1 and R2), which results in a 2 × 2 matrix for the measurements in both stressed and unstressed materials. None of the elements in this matrix is the same for the stressed material as they are for the unstressed material. When only T1R1 and T2R2 are considered, the method is known as the direct method (Equation 9). When all four elements of the matrix (that is, T1R1, T2R1, T1R2, and T2R2) are considered, the approach is referred to as the FMC method, as given in Equation 10.

2.7 Microstructure and PAURS+

WAAM and other AM processes can contain spatial variations in both RS and microstructure. Because microstructure can affect ultrasonic velocity, attenuation, backscatter and frequency response, multiple signal characteristics may be required to interpret LCR measurements in heterogeneous materials [62, 63]

PAURS+ is the microstructure-aware extension of PAURS developed in this thesis. The following sections introduce the mathematical description and ultrasonic observables used in this framework.

2.7.1 Observable-Based Interpretation of Phased-Array LCR Ultrasonics

2.7.1.1 Governing Elastodynamics and Microstructure–Stress Dependence

The relations given here are presented as first-order phenomenological approximations in order to aid in the interpretation at the observable level, not as a full constitutive description of wave propagation in stressed polycrystalline materials.

Ultrasonic wave propagation in polycrystalline media reflects both elastic heterogeneity and the macroscopic RS field. The elastodynamic equation can be written as:

$$\nabla \cdot C(M, \sigma) : \nabla u = \rho\, \ddot{u}$$

Equation 11 Elastodynamic wave equation in a polycrystalline solid with RS

where $\boldsymbol{u}$ is displacement, $\boldsymbol{\rho}$ is density, $\boldsymbol{\sigma}$ is the RS tensor, $\boldsymbol{M}$ represents the microstructural state, and $\boldsymbol{C}(\boldsymbol{M}, \boldsymbol{\sigma})$is the effective fourth-order stiffness tensor dependent on microstructure and RS. For interpretation, the stiffness is decomposed into a microstructure-dependent term and a stress-dependent perturbation:

$$C = C_0(M) + C_\sigma(\sigma)$$

Equation 12 Decomposition of the effective stiffness tensor into a microstructure-dependent baseline term $\boldsymbol{C}_0(M)$and a residual-stress-dependent perturbation $\boldsymbol{C}_\sigma(\boldsymbol{\sigma})$.

This decomposition is used here as an interpretive approximation to distinguish baseline microstructural contributions from stress-induced perturbations at the observable level.

2.7.1.2 Stress Sensitivity of LCR ToF

LCR waves propagate parallel to the surface at the first critical angle and sample a shallow near-surface depth. Their phase velocity is perturbed through the acoustoelastic effect:

$$v_{\mathrm{LCR}} = v_0(M) + L : \sigma_{\parallel}$$

Equation 13 Acoustoelastic perturbation of LCR phase velocity, expressed as a microstructure-dependent baseline velocity $v_0(M)$ plus a stress-dependent increment from the in-plane RS $\boldsymbol{\sigma}_{\parallel}$.

where $\boldsymbol{v}_{\mathbf{LCR}}$ is the LCR phase velocity, $\boldsymbol{v}_{\mathbf{0}}(\boldsymbol{M})$ is the stress-free baseline velocity, $\boldsymbol{L}$ is the acoustoelastic tensor, and $\boldsymbol{\sigma}_{\parallel}$ is the in-plane RS component parallel to the LCR propagation direction. The corresponding ToF along path Γ is:

$$\tau = \int_{\Gamma} \frac{ds}{v_0(M(s)) + L{:}\,\sigma_{\parallel}(s)}$$

Equation 14 LCR ToF along propagation path Γ, expressed as a path integral of the inverse local phase velocity incorporating microstructure-dependent baseline velocity $v_0(M(s))$and the acoustoelastic stress perturbation $\boldsymbol{L}{:}\,\boldsymbol{\sigma}_{\parallel}(s)$.

where $\boldsymbol{\tau}$ is the LCR ToF, $\boldsymbol{\Gamma}$ is the effective LCR propagation path, and $\boldsymbol{s}$ is the distance coordinate along $\boldsymbol{\Gamma}$. Under stress-relieved conditions, $\boldsymbol{\sigma}_{\parallel} \approx \mathbf{0}$ and microstructure-induced variations in $\boldsymbol{v_0}$ are small for aluminium, whose aggregate elastic anisotropy is modest even with texture. This indicates that LCR ToF should be regarded as an observable that is mainly sensitive to stress and has only a comparatively weak dependence on microstructure within PAURS+.

2.7.1.3 Microstructural Sensitivity of Amplitude- and Frequency-Based Observables

Microstructure strongly influences scattering, attenuation, and spectral redistribution.

Attenuation may be expressed as:

$$\alpha(f) = \alpha_{\text{int}}(f) + \alpha_{\text{scat}}(f, M)$$

Equation 15 Total attenuation expressed as intrinsic plus microstructure-dependent scattering contributions.

where $\boldsymbol{\alpha(f)}$ is the total attenuation at frequency $\boldsymbol{f}$, $\boldsymbol{\alpha_{\text{int}}(f)}$ is the intrinsic attenuation, and $\boldsymbol{\alpha_{\text{scat}}(f, M)}$ is the microstructure-dependent scattering attenuation.

Backscatter provides a scalar measure of heterogeneity:

$$\beta = \| s_{\text{back}}(t) \|_{\text{RMS}}$$

Equation 16 Backscatter heterogeneity metric defined by the RMS amplitude of the backscattered signal.

which increases with elongated grains, local texture, and elastic contrast. where $\boldsymbol{\beta}$ is the backscatter heterogeneity metric, and $\boldsymbol{s_{\text{back}}(t)}$ is the time-domain backscattered signal.

Spectral response follows:

$$S(f) = A(f)\exp[-\alpha(f)\,x]$$

Equation 17 Frequency-dependent reduction in ultrasonic amplitude over propagation distance x.

where $\mathbf{S(f)}$ is the received frequency-domain amplitude, $\mathbf{A(f)}$ is the initial frequency-domain amplitude, and $\mathbf{x}$ is the propagation distance.

- capturing preferential high-frequency damping in heterogeneous microstructures.
- Together, attenuation, backscatter and frequency-domain response (FFT) characteristics form microstructure-encoding observables.

2.7.2 Role of Phased-Array FMC

Phased-array operation with FMC provides a complete set of transmit–receive combinations,

$$\mathrm{S}_{\mathrm{FMC}} = (s_{ij}(t)), i, j = 1, \dots, N$$

Equation 18 FMC data structure for an N-element phased array, defined as the matrix of time-domain A-scans $s_{ij}(t)$for all transmit element $i$and receive element $j$combinations.

where $\boldsymbol{S_{\mathrm{FMC}}}$ is the complete FMC data matrix, $\boldsymbol{s_{ij}(t)}$ is the time-domain A-scan acquired using transmitting element $\boldsymbol{i}$ and receiving element $\boldsymbol{j}$, and $\boldsymbol{N}$ is the number of array elements.

FMC enables:

- averaging across multiple propagation paths [61, 64].
- improved stability in ToF estimation [65, 66].
- robust extraction of attenuation, backscatter, and spectral descriptors [67, 68].

It is necessary for there to be this redundancy if stress-dominated and microstructure-dominated observables are to be separated in practical measurements; in this study FMC is able to carry out robust ToF estimation for stress assessment and at the same time achieve a stable extraction of the attenuation/backscatter/FFT metrics for microstructure characterisation based on the same acquisition.

2.7.3 Observable-Level Separation Framework

Within the proposed framework, RS and microstructure are isolated through complementary ultrasonic observables extracted from the same LCR dataset:

- RS: primarily encoded in LCR ToF via Equation 14.
- Microstructure: encoded in attenuation, backscatter, and frequency-domain response via Equation 15 to Equation 17.

These observables are collected into a minimal descriptor set

$$\mathcal{O}_{\mathrm{LCR}} = (\tau, \alpha, \beta, \Psi)$$

Equation 19 LCR observable set used for stress and microstructure interpretation.

The LCR observable set is denoted by $\boldsymbol{O}_{\mathbf{LCR}}$, while the frequency-domain metrics derived from $\boldsymbol{S}(\boldsymbol{f})$**.** are represented by $\boldsymbol{\Psi}$. The main point is not that LCR is insensitive to microstructure, but rather that different physical mechanisms prevail for different observables.

enabling practical isolation within a unified measurement modality. This separation is evaluated under stress-free conditions to confirm ToF invariance alongside amplitude- and frequency-based microstructural contrast.

2.7.4 Implications for Microstructure-Aware RS Measurement (PAURS+)

In the PAURS+ interpretation proposed, ToF is mainly viewed as a stress-sensitive measure, whereas attenuation, backscatter and frequency characteristics are seen as possible indicators of microstructural variation. These are relative assignments of sensitivity rather than a full separation of stress and microstructure.

When these observables are interpreted together as part of a single phased-array LCR acquisition, it is possible to deal with the effects related to stress and microstructure without having to change the wave mode or the inspection geometry. *Table 1* gives a summary of the main mechanisms and the sensitivities expected.

Table 1. Dominant physical sensitivities of phased-array LCR ultrasonic observables to RS and microstructure

Ultrasonic observable	Primary physical mechanism	Sensitivity to RS	Sensitivity to microstructure	Interpretation within PA-LCR framework
ToF	Acoustoelastic velocity perturbation	High (dominant)	Low–moderate (baseline shift)	Direct indicator of in-plane macroscopic RS
Attenuation	Grain-scale scattering and internal friction	Low	High	Sensitive to grain morphology, size, and heterogeneity
Backscatter amplitude	Incoherent scattering from elastic contrast	Negligible	High	Qualitative measure of microstructural heterogeneity
FFT	Frequency-dependent scattering and absorption	Low	High	Is sensitive to texture, grain elongation, and spectral redistribution

2.8 Key Insights

Since WAAM causes overlapping changes in the thermal, mechanical, and microstructural aspects, the RS measurements have to be interpreted in light of the stress component, the sampling depth, and the material volume; consequently, techniques such as CM, XRD, ND, IHD and ultrasonics offer complementary rather than interchangeable information.

PAURS combines the use of LCR acoustoelastic measurement with phased-array acquisition in order to obtain multiple acoustic paths; PAURS+ goes a step further by considering both the ToF and attenuation, as well as backscatter and frequency characteristics. The method calls for calibration that is specific to the material and does not assume a complete separation between stress and microstructure.

Chapter 3: Literature Review

3.1 Introduction and Scope

Reliable RS measurement in metal AM is complicated by spatial variations in stress and by the different sampling characteristics of available measurement techniques. This is particularly relevant to WAAM Ti-6Al-4V, where stress gradients may coincide with variations in grain morphology, texture and phase distribution.

Even though existing methods offer complementary information, there are differences among them in terms of measurement depth, spatial resolution, and practical usefulness. Although ultrasonic methods enable a non-destructive examination of the subsurface, their response may be influenced by factors such as calibration, coupling, propagation conditions, and microstructure. Phased-array acquisition can provide extra data to evaluate the quality of the measurement, and further ultrasonic observables might help in the interpretation considering the microstructure. This review critically looks at the literature concerning these developments and points out the unresolved problems that are motivating PAURS and PAURS+.

3.2 RS in Metal AM

RS is inherent to many metal AM processes because localised energy input creates non-uniform heating, solidification and constrained cooling. When the resulting incompatible strains cannot be fully accommodated elastically or plastically, a self-equilibrating RS field remains after manufacture [69, 70].

In AM based on fusion, the newly deposited material expands against the cooler material surrounding it before later contracting as it solidifies and cools. The restraint exerted by the substrate and by the previously deposited layers usually results in tensile RS near the deposit, this being balanced by compressive stress elsewhere [69, 71]. Successive deposition cycles can accumulate, redistribute or partially relieve these stresses, meaning that the final distribution reflects the complete thermal and mechanical history of the component [70, 72].

These effects are particularly significant in WAAM, where high heat input and a relatively large melt pool create substantial temperature gradients. Reheating varies with position and build height, with lower layers experiencing more thermal cycles than later layers. The resulting RS distribution can therefore vary along the length, height and thickness of the component [69, 73].

High RS is frequently reported near the transition between wall and substrate. Mishurova et al. [16] for example, measured the highest RS within the transition region of a hybrid Ti-6Al-4V WAAM component and linked the overall RS distribution to the component's thermal history. This highlights the deposit-substrate interface as a critical region for RS assessment.

Substrate restraint, component geometry and deposition strategy affect RS development. Ahmad et al. [74] found that substrate removal substantially reduced RS in Ti-6Al-4V WAAM walls and that oscillation-path deposition produced lower RS than single-bead and parallel-path strategies. Interlayer temperature also affected the resulting distribution.

Material response must also be considered. Temperature-dependent elastic modulus, yield strength, thermal expansion, thermal conductivity and phase transformations govern how thermal strains develop and are accommodated. In Ti-6Al-4V, repeated WAAM thermal cycles also produce spatial variations in grain morphology and phase distribution [16, 73]. Stress and microstructural gradients may therefore coincide, complicating measurements that are sensitive to both mechanical and material properties.

RS can reduce accuracy through distortion following unclamping, substrate removal or machining. Tensile RS may also combine with service loads and influence fatigue and crack propagation. Because the final distribution depends on interacting thermal, geometric, mechanical and material factors, it cannot be reliably inferred from a single manufacturing parameter. Experimental measurement therefore remains important for component assessment and validation of numerical predictions [70, 74].

3.2.1 RS Mitigation in WAAM

Several methods have been investigated for controlling RS in WAAM. These include changes to deposition strategy, control of interlayer temperature, thermal stress relief, inter-pass rolling and peening [74, 75]. Mechanical treatments introduce local plastic deformation, which can redistribute tensile RS and, depending on the treatment conditions, introduce compressive stress.

Martina et al. [15] investigated high-pressure inter-pass rolling of Ti-6Al-4V WAAM components using rolling loads of 50 and 75 kN. CM measurements showed a substantial reduction in RS, particularly near the interface between the deposited material and the substrate. Inter-pass rolling has also been reported to refine the large columnar prior-β grains found in as-deposited Ti-6Al-4V and reduce mechanical-property anisotropy.

Peening offers another approach to RS redistribution and can be applied either between deposited layers or after the build is complete. The timing of treatment is important because inter-pass peening modifies the evolving stress state during deposition, whereas post-process peening acts on the completed component. Recent work on WAAM Ti-6Al-4V has shown that peening can introduce substantial compressive stress and alter the RS distribution measured using CM and phased-array ultrasonics.

Mitigation treatments can redistribute RS, although the measured response depends on the treatment parameters, application stage and measurement technique.

3.3 AM RS Measurements

The measurement methods introduced in Chapter 2 are evaluated here using the same comparison criteria: stress component, sampled region, spatial resolution, uncertainty, destructiveness and practical applicability. This provides the basis for interpreting agreement between PAURS, CM and XRD.

RS measurement in AM is complicated by spatial variation in stress across the surface, build height, substrate, and deposited region. Existing WAAM research shows that no single technique provides complete information across all these regions. The RS distribution depends partly on the measurement principle, stress component, spatial resolution and sampled material volume of the selected technique [69].

The AM studies usually combine a number of different techniques rather than depending on a single method as the definitive standard. While cross-sectional methods look at the wider distributions, diffraction methods give local measurements of elastic lattice strain. The two techniques thus offer complementary representations of the RS distribution. Boruah et al., [76] for example, compared RS results from Digital Image Correlation with CM and XRD in WAAM steel components. Their work illustrates the value of using independent techniques to evaluate common trends while recognising their different measurement characteristics.

The experimental work in this thesis uses CM and XRD as reference techniques. CM has been selected because it can provide a two-dimensional reconstruction across a selected section, while XRD provides a local, non-destructive assessment of near-surface stress.

3.3.1 RS WAAM Measurements

A suitable RS measurement method for WAAM must provide a defined stress direction, an appropriate sampling scale and sufficient sensitivity to distinguish relevant manufacturing conditions. Gurmesa et al. [69] showed that the range of experimental and numerical methods used in WAAM reflects the difficulty of characterising a spatially variable stress field with a single technique.

The directions for measurement must be aligned with a common component coordinate system, or apparently different values might be representing different tensor components rather than indicating a discrepancy between the techniques.

Published WAAM studies demonstrate that specimen preparation and component release can alter the stress state before measurement. Ahmad et al. [74] found that removing Ti-6Al-4V WAAM walls from their substrates substantially changed the RS distribution measured using CM. Their results show that the manufacturing and measurement sequence must be reported clearly because the measured condition may differ from the restrained state that existed during deposition.

Existing studies therefore indicate that a suitable WAAM measurement method must provide a defined stress direction, an appropriate sampling scale and sufficient sensitivity to distinguish relevant differences between manufacturing conditions. It must also be interpreted in relation to specimen restraint, preparation and measurement sequence. Practical requirements such as destructiveness, access, acquisition time and repeatability become increasingly important when moving from research validation towards manufacturing assessment.

3.3.2 CM

CM has been widely applied in WAAM research because it provides a two-dimensional representation of the stress component acting normal to a selected cut plane. This allows the broader stress distribution within a wall, substrate or transition region to be evaluated rather than inferred from isolated surface measurements. The method is particularly useful when comparing manufacturing strategies or utilising FE models.

CM results depend on cut quality, surface measurement and subsequent data processing. Hosseinzadeh et al. [77] showed that measurement spacing, smoothing and FE discretisation collectively determine the effective resolution. Consequently, CM maps must be interpreted in relation to the processing parameters used.

CM is therefore very useful as a reference for assessing the distribution of the broad cross-sectional stress and for comparing different processing conditions. Yet, since it is a destructive technique, the same specimen cannot be measured more than once. In this thesis, CM is used as a cross-sectional reference with a resolution and an uncertainty that are specific to the method, rather than as an absolute standard.

3.3.3 XRD

XRD is frequently used in AM research because it provides local, direction-specific measurements of near-surface RS without destruction of the component. Its applicability is particularly strong where the response of the accessible surface is of interest, including the evaluation of machining, surface treatments and near-surface stress redistribution.

Research on AM materials has nevertheless shown that XRD measurements are strongly affected by the condition of the surface being measured. Chen et al. [78] investigated Selective Laser Melted AlSi10Mg and found that RS measured on rough as-built surfaces were substantially different from those obtained after controlled surface finishing. The authors explained this behaviour by pointing to the uneven as-built surface and local stress relaxation, showing that surface preparation is more than just a step to improve measurement quality.

The shallow sampling depth of laboratory XRD is another important limitation. The effective penetration depth varies with the material, radiation source, diffraction plane and measurement geometry. Luo and Yang [79] showed that the measured RS can depend strongly on effective penetration depth. This means that a reported XRD value represents an average over a finite near-surface region rather than a stress value located at an ideal surface point.

Texture and grain statistics can also affect diffraction quality in AM materials, particularly where the microstructure is strongly directional or spatially non-uniform. These issues are relevant to AM because the microstructure may be directional and spatially non-uniform. The diffracting grains sampled at one position may not provide the same statistical response as those sampled elsewhere. Consequently, peak quality and the suitability of the selected X-ray elastic constants (XEC) must be considered alongside the stress values themselves.

NPL guidance highlights the importance of specimen condition, measurement geometry and appropriate XEC [80]. XRD is therefore valuable as a local near-surface reference, particularly when comparing signs, directions and relative changes in stress. Its results should not be treated as directly equivalent to cross-sectional or subsurface measurements without accounting for the substantial differences in sampling depth and material volume.

3.3.4 RS Measurement Method Properties

The studies currently available show that CM and XRD measure different aspects of the RS distribution. While CM reconstructs the stress component that is normal to the selected cut plane within a two-dimensional section, XRD measures a component determined by the diffraction geometry in a shallow illuminated area. It is therefore possible for their results to differ even if both methods function properly.

The depth at which measurement is made is the most clear-cut difference; with CM it is possible to observe the variations over the chosen section, whereas conventional laboratory XRD is mainly responsive to the near-surface area. It is for this reason that a sharp stress gradient can result in different magnitudes since the two techniques do not sample the same depth. Luo and Yang [79]showed that even in the case of XRD analysis, changing the effective penetration depth can lead to a change in the measured value.

Gauge volume also raises a similar problem. The effective resolution of CM relies on the surface measurement density, the smoothing procedure, and the FE discretisation, while XRD averages over both the illuminated area and the penetration depth. Hosseinzadeh et al. [77] showed that CM gauge size cannot be attributed to the FE mesh alone because the preceding measurement and smoothing stages already impose spatial length scales.

The measured stress directions must also be aligned; the longitudinal values obtained from XRD should be compared with the corresponding longitudinal component from the reference method. If the CM cut gives a different normal component, the values cannot be directly compared even if the positions are aligned. This is especially important in WAAM, since the deposition direction provides a natural material and stress coordinate system.

Boruah et al. [76] used CM and XRD alongside Digital Image Correlation to validate RS in WAAM steel walls. Their multi-method approach illustrates the value of comparing independent results while recognising that the techniques provide different forms of spatial information.

A comparison that is to be effective must therefore look at the degree of agreement step by step. The stress component, the spatial distribution, the positions of the tensile and compressive regions, the location of the peak, and the response to processing can all be examined before comparing the absolute magnitude. Quantitative agreement can only be claimed in cases where the coordinate system, the stress component, and the sampling region are sufficiently compatible.

3.3.5 Uncertainties in RS Measurement Methods

The uncertainty estimates published in relation to CM and XRD cannot be directly transferred from one study to another since they vary according to the component, material, equipment, processing method and stress distribution; instead, the literature recommends identifying the main sources of uncertainty and assessing how these contribute to each measurement chain.

For CM, cut quality, released-surface measurement, alignment, smoothing and FE reconstruction all contribute to the final uncertainty. Hosseinzadeh et al. [77] emphasised the importance of controlling each of these stages, while Olson et al. [81] demonstrated that displacement noise and smoothing can be propagated to obtain a spatially varying uncertainty map.

The kind of spatial variation found by Olson et al. [81] is of particular significance. In their experiment, the uncertainty was about 5 MPa over a large part of the section but increased locally to about 10 MPa, being even higher near the perimeter. These figures apply only to the aluminium specimen that was tested and must not be taken as general limits for CM uncertainty. The wider meaning is that uncertainty varies with the position of the measurement and with the local response of the specimen.

For XRD, uncertainty arises from equipment alignment, peak fitting, measurement geometry, surface condition, texture, grain statistics, penetration depth and XEC. Luo and Yang [79] demonstrated that diffraction parameters and effective penetration depth can alter calculated stresses. At the same time, the NPL guidance identifies specimen preparation and elastic-constant selection as important parts of the wider uncertainty evaluation.

The fitting uncertainty reported by analysis software represents only one component of the total XRD uncertainty. A well-fitted peak does not rule out systematic effects caused by unsuitable material constants, texture, or surface preparation. Chen et al. [78] demonstrated this distinction by showing that the as-built surface condition systematically altered the measured stress, even though the measurements could still be processed numerically.

Differences between CM and XRD must also be distinguished from measurement uncertainty. Where the methods sample different depths, components or material volumes, disagreement may represent genuine variation in the stress field. Method compatibility must therefore be assessed before using the difference between two measurements as an error estimate.

3.3.6 In-Situ Measurements

CM is unsuitable for repeated in-situ assessment because sectioning irreversibly changes the specimen. Its main role in AM research is detailed post-processed characterisation, validation of numerical models and comparison between equivalent samples. However, using separate specimens introduces sample-to-sample variability, and the results represent the stress state immediately before cutting rather than the state that existed earlier during deposition.

It is possible to carry out XRD on accessible surfaces without having to remove any material, which is an advantage when it comes to comparing the near-surface stress before and after a manufacturing or treatment process. Yet, its practical use is limited by factors such as access, the need for surface preparation, alignment, acquisition time, and the shallow sampling depth. Because of these limitations, conventional XRD is better suited to controlled near-surface evaluations than to the continuous monitoring of a WAAM build.

The review by Gurmesa et al. [69] concluded that WAAM RS research continues to rely on multiple experimental and numerical approaches because the available techniques have different strengths and restrictions. The selection of a method therefore depends on whether the objective is detailed post-process mapping, local surface assessment, model validation, or manufacturing-stage inspection.

Although CM and XRD are still useful reference techniques, their limitations mean that it is not possible to carry out repeated assessments of the subsurface structure during manufacturing, which is why ultrasonic methods should be considered.

3.4 Ultrasonic RS Measurement

Ultrasonic RS measurement has been looked into as a non-destructive alternative to the existing methods of RS measurement. Instead of measuring stress directly, ultrasonic techniques calculate the stress from the changes in wave propagation that result from the material's acoustoelastic response. Although this allows for portable and repeatable measurements it also makes the results sensitive to

material and experimental factors which may influence the ultrasonic response independently of the stress.

Acevedo et al. [82] reviewed the application of ultrasonic techniques to metal AM and identified their potential for measurements both during and after manufacture. The authors nevertheless concluded that AM introduces particular challenges through surface condition, anisotropy, complex geometry and different material properties. These factors make it difficult to convert an ultrasonic response into an accurate RS measurement and hinder the direct transfer of calibration data across different material regions or components.

Bastola and others [10] did the same thing and placed ultrasound within a wider group of techniques for measuring RS in metal AM. They pointed out that the choice of method depends on the AM process, the condition of the material and the pattern of stress distribution. Although ultrasonics has some practical benefits for non-destructive evaluation, its interpretation necessitates a clear understanding of the volume being sampled and of the factors that influence acoustic velocity.

Experimental studies outside AM provide important evidence regarding the reliability and limitations of the technique. Hwang et al. [45] demonstrated that changes in LCR wave arrival time followed changes in applied tensile stress in rail steel. After experimentally determining the acoustoelastic coefficient, the researchers used the measured ToF to calculate RS measurements.

The current studies show that ultrasonic RS measurement is feasible, but ToF cannot be attributed solely to stress. The sections that follow look at influences other than stress, with the microstructural effects to be examined separately later.

3.4.1 Acoustoelasticity

The method based on the acoustoelastic relationship between stress and time of flight, as described in Chapter 2, involves a focus in the relevant literature on the transferability of the calibration coefficient and the effects of material condition and measurement configuration.

Dos Santos and Bray [83] compared acoustoelastic approaches for evaluating stress in steel plates and bars. Their work showed that the sensitivity of an ultrasonic measurement depends on the wave mode, propagation direction and relationship between the acoustic path and the applied stress. This means an acoustoelastic coefficient is specific to the selected measurement arrangement rather than a single, universally transferable property.

Zhu et al. [84] determined the acoustoelastic constants by recording the LCR ToF while subjecting Q345 steel to known uniaxial loads. Within the elastic range that was investigated, the measured relationship was found to be approximately linear, which supports the use of a calibration gradient in order to convert changes in ToF into stress. The study also looked at couplant thickness and temperature,

showing that the calibrated stress-ToF relationship can be influenced by conditions that are not related to changes in material stress.

Hwang et al. [85] employed an approach similar to that used for rail steel. When a tensile stress was applied, there was a systematic variation in the arrival time of the LCR, from which an acoustoelastic coefficient was calculated. The coefficient was then used to determine the RS in sections of used rail. This method shows the importance of obtaining the coefficient from a material and propagation configuration that is representative rather than depending entirely on published constants.

The crystallographic texture has a significant effect on simple calibration transfer. Man [86] created a constitutive model for textured polycrystals and demonstrated that the acoustoelastic coefficients depend on both the material constants and the texture coefficients. As a result, two specimens which have the same nominal composition can show different velocity-stress relationships if their crystallographic textures are different. This point is relevant to AM since calibration may not be transferable between areas that have different textures or grain morphologies.

The ToF sample also introduces an element of uncertainty. Even though the value obtained from the nominal parent material provides practical information, it cannot be assumed that the reference area is stress-free. The calculated result shows stress in relation to the selected reference unless the reference condition has been verified independently. Although annealing or some other kind of stress-relief treatment might support this assumption, it could also alter the microstructure and therefore the baseline acoustic velocity.

3.4.2 LCR Waves

LCR waves are used for ultrasonic stress measurement since they give a longitudinal response which is relatively sensitive to stress in a shallow area beneath the surface. Yet the literature does not justify the idea that they travel at one particular depth; instead, the response covers a certain acoustic field, and the area over which it effectively samples varies with frequency, material velocity, transducer shape and propagation distance.

Hwang et al. [45] used LCR probes to measure stress distributions in rail specimens and demonstrated that the arrival-time response changed systematically with applied stress. The resulting measurements distinguished differences between rail regions exposed to different service conditions, supporting the use of LCR waves for non-destructive comparative stress measurement.

In a later study, Hwang et al. [85] used probes with different centre frequencies to investigate RS at different effective depths. They measured distinct stress measurements for unused and serviced rails and concluded that frequency selection could provide depth-dependent information. The study also confirms that the resulting values remain averages over frequency-dependent interrogation regions rather than discrete point measurements.

Chen et al. [87] applied a one-transmitter, double-receiver LCR arrangement to rotary-forged aluminium plates. Their measurements reproduced the broad tensile-centre and compressive-edge distribution predicted by FE analysis, although the maximum difference between the ultrasonic and numerical results reached 61 MPa. The study demonstrates both the value of differential LCR measurement and the remaining quantitative uncertainty when applied to formed components.

Effective penetration depth usually decreases as the frequency increases. While this enables a study of stress that varies with depth, it also makes it more difficult to compare the results with those from XRD and CM. If one is to regard an LCR result as equivalent to an XRD surface measurement or to a single point taken from a complete cross-sectional map, then the differences in sampling depth and spatial averaging must be considered.

Lai et al. [49] examined practical influences on LCR stress measurement, including surface roughness, temperature, mechanical vibration and surface paint. Surface roughness reduced signal intensity without producing a corresponding ToF shift in their specimens, whereas increasing temperature produced an approximately linear increase in transition time. Surface paint also increased the measured transition time, while external mechanical vibration had little effect on either ToF or amplitude under the investigated conditions.

It shows that different practical influences do not have the same effect on all the ultrasonic characteristics. One condition may cause a reduction in amplitude and a deterioration of signal quality without altering the ToF, while another might affect the timing measurement. It is important to take this difference into account when choosing criteria for path quality and when interpreting changes in the calculated stress.

3.4.3 Applications for AM

Published applications of ultrasonic RS measurement to metal AM remain limited compared with measurements on rails, plates and conventionally manufactured components. Acevedo et al. [82] identified this as an emerging research area, noting that ultrasound offers potential for non-destructive assessment during and after manufacture. Still, surface roughness, anisotropy and heterogeneous microstructure complicate quantitative interpretation.

AM research contains a wider range of ultrasonic work on defect detection and material characterisation than on quantitative RS measurements. Acoustic and ultrasonic methods have been used to identify porosity, lack of fusion, elastic-property variation and microstructural changes, but few studies convert stress-sensitive ToF measurements into validated RS measurements. Acevedo et al. [82] concluded that additional calibration and validation are required before ultrasonic stress methods can be applied routinely across different AM processes and alloys.

Difficulty arises partly because the acoustic response of AM material is not spatially uniform. The parent material, deposited region and thermally affected zone may differ in texture, grain morphology, porosity and surface condition. Man's analysis of textured polycrystals indicates that these variations can affect the acoustoelastic coefficient, while Lai et al.'s work shows that temperature and surface condition can independently influence the measured signal [49, 86].

Evidence from conventionally manufactured components supports the technical basis of LCR measurement but transfer to AM requires material-specific calibration and validation [84, 85, 87].

A key gap is therefore not whether ultrasonic waves respond to stress, but whether stress-related changes can be distinguished reliably from AM-specific material variation. Quantitative application requires calibration, knowledge of the sampled depth, stable ToF extraction and validation against established methods.

3.4.4 Single-Element LCR Limitations

Standard LCR systems usually have one transmitter and one or two receivers placed at fixed distances apart. With two receivers, the differential travel time between two propagation distances can be measured, thus reducing the effects of common timing errors and eliminating the need for an absolute system delay. Chen et al. [87] successfully applied this setup to aluminium plates, showing how useful it is for practical RS measurement. However, the small number of paths means that spatial interpretation is limited when there are significant changes in stress or microstructure within the area being investigated.

The small timing shift caused by stress makes the method very sensitive to systematic effects. Zhu et al. [84] found that couplant thickness and temperature were important factors during their experimental calibration, and Lai et al. [49] showed that both temperature and surface coatings could affect the measured transition time. However, the effects cannot be eliminated merely by averaging the repeated values when the bias is the same in all the measurements.

Probe spacing and alignment create further uncertainty because the calculated stress depends on a defined propagation distance. Changes in wedge seating, local curvature or surface distortion can change the effective path length. This is particularly relevant to AM components, which may have rough or distorted surfaces and may require measurements at several locations with different contact conditions.

Conventional LCR measurements also average the acoustic response along the propagation path and over an effective depth. When the path crosses a steep stress or microstructural gradient, the measurement cannot be assigned unambiguously to one spatial point. Hwang et al.'s [85] frequency-dependent rail measurements demonstrate that different probes can sample different effective depths, but each remains a path-averaged response.

Texture and microstructure are also a fundamental limitation. Man [86] showed that texture has an effect on acoustoelastic coefficients, which means that a single calibration cannot be used to represent acoustically different sections of the same component. This kind of uncertainty cannot be eliminated by improving the timing resolution alone since it alters the physical relationship between stress and velocity.

Conventional single-element systems are therefore at their most reliable when the material, surface, coupling and propagation geometry are well controlled, since their limited path redundancy hampers anomaly detection and path-quality assessment, and systematic effects due to calibration, temperature and the heterogeneous response of the material still persist. It is for these reasons that phased-array and FMC approaches have been developed.

3.4.5 LCR Wave Generation and Propagation

The first critical-angle condition was introduced in Chapter 2. Previous research shows that the usable LCR response also depends on the finite angular spectrum, wedge material, aperture, frequency and interface condition.

The theoretical approach typically relies on Snell's law, which uses nominal velocities and assumes an ideal, flat interface with a single incident direction. However, actual transducers generate a limited angular spectrum, and the measured response can be influenced by uncertainties in material properties, manufacturing tolerances in the wedge, and interface conditions.

Chaki et al. [88] found that LCR energy was generated across a range of incident angles around the calculated critical condition, although its amplitude varied with angle. They therefore optimised angle selection using the measured and simulated energy distribution rather than relying solely on the theoretical value.

Djerir et al. [89] similarly identified incident angle as a principal control on beam directivity and main-lobe position. Transducer aperture and centre frequency also affected the resulting beam, indicating that the wedge angle cannot be optimised independently of the probe characteristics.

The literature thus indicates that a two-stage selection procedure should be followed. First, Snell's law must be used to establish a range of possible angles, after which angles in the neighbourhood of these should be examined experimentally by means of LCR amplitude, the required gain, waveform stability and separation from other arrivals. Although numerical modelling can aid in the interpretation of the wavefield, it is not able to fully replicate practical effects such as imperfect coupling, material anisotropy and transducer response.

Interface conditions also affect performance. Lai et al. [49] found that surface roughness reduced signal amplitude without significantly changing ToF in the specimens investigated, whereas surface paint

increased the measured transition time. Temperature also produced an approximately linear change in ToF. Liu et al. [90] further showed that wedge material influenced the estimated LCR propagation depth, confirming that both material and geometry should be reported when describing a wedge configuration.

An angle should therefore be described as optimal for a specific transducer-wedge-specimen configuration and evaluation criterion, rather than as a universal angle for the material. For this thesis, existing studies support using the Snell's law estimate to define the test range and selecting the practical angle that provides the most stable LCR response with the lowest required gain.

3.5 Phased-Array Ultrasonics

Drinkwater and Wilcox [53] looked at ultrasonic arrays for use in NDE and pointed out electronic beam steering, dynamic focusing, better coverage, and greater post-processing flexibility as their main advantages. They also noted that performance is influenced by element spacing, aperture, frequency, and the firing strategy chosen, which means that increasing the number of elements does not inherently lead to improvements in every measurement.

Xu and Wang [91] then reviewed phased-array sound-field modelling and imaging methods. Their analysis highlighted the importance of modelling element directivity, interference, aperture and propagation when designing an array inspection. These considerations are relevant to RS measurement because different transmitter-receiver combinations may not have identical amplitudes, beam profiles or sampled regions, even when their nominal propagation paths appear similar.

Although most phased-array research concerns imaging, element-wise acquisition also provides a basis for multi-path LCR measurement. Its applicability to RS assessment is discussed later.

3.5.1 Principles

Phased-array operation relies on the constructive and destructive interference of waves generated by individual elements. Controlled time delays can be applied during transmission and reception to steer or focus the acoustic field. The active group of elements defines the aperture, while element width, pitch, frequency and delay law determine beam directivity and the occurrence of side or grating lobes.

Drinkwater and Wilcox [53] pointed out that array probes are able to carry out a number of inspections without needing the physical reconfiguration that is required by multiple single-element transducers. This flexibility is useful in cases where it is necessary to examine different propagation directions or focal positions. Yet the acoustic field still relies on the array geometry and on the individual element responses.

Xu and Wang [91] compared a range of analytical and numerical approaches for modelling phased-array fields, including ray tracing, angular-spectrum methods, multi-Gaussian beams, finite-element

modelling and distributed point-source methods. The review showed that no single model is optimal for every geometry and that model complexity should reflect the measurement objective.

For LCR measurement, phased arrays may be used differently from conventional imaging applications. Rather than applying delay laws to focus at points within the specimen, individual transmitter-receiver element pairs can be treated as separate ToF measurement paths. The array then provides several observations of the near-surface response from one probe placement.

This distinction is important because measurements from different paths should not be assumed to be statistically or physically identical. Outer and inner elements may have different directivity, propagation distance, coupling conditions and signal amplitude. Path averaging is therefore defensible only after waveform consistency and signal quality have been evaluated.

3.5.2 FMC

Holmes, Drinkwater and Wilcox [55] established FMC as an alternative to conventional phased-array acquisition, where delays are applied directly during transmission to generate a predefined beam. By recording the complete matrix first, different processing strategies can be applied after acquisition. Their experiments showed good agreement with modelled performance and demonstrated focusing in both transmission and reception throughout a target region,

Holmes et al. later [92] extended full-matrix post-processing to scanned inspections. The authors showed that FMC could increase the effective aperture and available probing angles and could support inspection modes that would be difficult to implement through conventional hardware firing alone. They also identified data transfer, storage and processing time as practical constraints.

FMC is frequently associated with the TFM, but the two terms are not the same. FMC describes the acquisition of all transmitter-receiver signals, whereas TFM is one possible imaging method applied to those signals. FMC data can instead be processed for ToF, amplitude, attenuation, backscatter or frequency-domain analysis without generating a focused image.

For RS measurements, the principal value of FMC is therefore not necessarily image formation. The complete matrix provides multiple LCR paths that can be compared for waveform consistency, timing stability and signal quality. It may also expose paths affected by poor coupling, mode interference or element directivity.

However, the paths within an FMC dataset are correlated because they share transducers, coupling interfaces and overlapping material regions. Increasing the number of signals does not produce an equivalent number of independent stress measurements. FMC should therefore be described as providing better data redundancy and diagnostic information, rather than automatically increasing measurement accuracy.

3.5.3 Phased Arrays for RS Measurement

Research on phased-array RS measurements is scarce compared to the well-developed literature on array imaging. Most ultrasonic stress studies typically employ a single transmitter with one or two receivers. For instance, Chen et al. [87] utilised a setup with one transmitter and two receivers in an LCR configuration to assess RS in rotary-forged aluminium plates. Their ultrasonic findings matched the general pattern of tensile-centre and compressive-edge distribution predicted by FE analysis, although there were some quantitative discrepancies.

Hwang et al. [85] used dedicated LCR probes with different centre frequencies to map RS in rails at different effective depths. Their results demonstrated the value of acquiring several depth-sensitive measurements, but each probe remained a conventional fixed-path arrangement rather than a full phased-array acquisition,

These studies establish the underlying value of multiple propagation paths or frequencies, but do not fully exploit element-wise phased-array acquisition.

Extending LCR measurement to arrays enables element-wise acquisition without repeated transducer repositioning. The unresolved issue is how these correlated paths should be selected, corrected and combined for quantitative RS assessment. The additional paths cannot remove systematic effects shared across the dataset, including calibration error, reference-state uncertainty, temperature variation and microstructural velocity differences.

The main gap in the independent literature is therefore not the feasibility of phased-array acquisition, which is well established in NDE, nor the stress sensitivity of LCR waves, which is supported by conventional probe studies. The gap concerns how element-wise and FMC measurements should be selected, corrected, averaged and validated for RS measurements.

3.5.4 Signal Processing and Reliability

Since stress-induced differences in the time of flight are possibly smaller than the raw sampling interval, RS measurement places more stringent timing requirements on the data from phased arrays than does conventional defect detection. Reliability in this case is therefore based on the consistent selection of arrival times, the use of interpolation, the assessment of path quality and the correction of timing variations not related to stress.

ToF can be identified using threshold crossing, zero crossing, envelope peaks, cross-correlation or phase-based methods. Threshold and peak approaches are relatively simple but can shift when amplitude or waveform shape changes. Cross-correlation uses a larger portion of the waveform and may be more reliable where signals retain a consistent shape, but it can also be biased by dispersion, mode interference or changes in frequency content.

Svilainis and Dumbrava [93] examined interpolation methods for ultrasonic ToF estimation and showed that interpolation can reduce sampling-related timing error. The authors compared linear zero-crossing interpolation, correlation-based interpolation and parabolic peak estimation. Their analysis also demonstrated that interpolation does not remove errors arising from waveform variation or incorrect feature selection.

Yang et al. [94] Conducted a comparison of ultrasonic NDE's automated ToF methods and developed a feature-tracking approach that utilizes signals processed through the Hilbert transform and subsequent denoising. Their study shows how important it is to keep the same feature selection when the waveform includes a number of possible peak responses or arrivals. In the case of measuring LCR stress, a zero crossing is of value only if the same oscillation cycle and wave mode are chosen for all paths and at all scan positions. A transition from one crossing to another may result in an apparent timing shift that is much greater than the acoustoelastic response. Automated processing must therefore make use of a temporal gate that is based on physical principles and check waveform similarity rather than simply selecting the nearest crossing without first carrying out any contextual verification.

3.6 Microstructural Effects on Measurements

The material's microstructure causes changes in the elastic response, scattering and modification of the waveform, and this has an effect on a number of ultrasonic measurements. In the case of RS assessment, ambiguity results since the variation that is measured may not be due to stress alone.

Park et al. [95] investigated AM metallic samples produced under different processing conditions and compared ultrasonic velocity, attenuation and nonlinear parameters with microscopy and EBSD measurements. The authors found that ultrasonic characteristics changed with grain size, texture, lack of fusion, and porosity, showing that several material features can contribute to the measured response simultaneously.

Yeoh et al. [96] examined the effect of microtextured regions, or macrozones, in Ti-6Al-4V using FE modelling and experimental measurements. Changes in macrozone size, shape and crystallographic orientation produced measurable differences in ultrasonic velocity, attenuation and backscatter. The study showed that propagation direction relative to microstructural orientation is important and that equal grain dimensions do not necessarily produce equal ultrasonic responses when texture differs.

Microstructural sensitivity is therefore both specific to the observable and dependent on the configuration. The ToF and velocity mainly indicate the coherent propagation response, whereas attenuation, backscatter and frequency measurements relate to energy redistribution and waveform modification. Although these quantities give complementary information, none of them can generally

be attributed to a single material property without considering defects, coupling, geometry, and the direction of measurement.

3.6.1 Effects on ToF and Velocity

The effective phase or group velocity involved in ultrasonic ToF reflects the directional elastic response of the grains that are being sampled in a polycrystalline material; it is therefore possible for changes in crystallographic texture, phase composition or grain morphology to cause a change in the reference ToF even if the overall stress state remains unaltered.

Man [86] showed that crystallographic texture affects the acoustoelastic coefficients of polycrystals. The analysis demonstrated that ultrasonic velocity and its stress sensitivity depend on texture coefficients as well as the constituent elastic constants. Consequently, an acoustoelastic calibration obtained from one material condition may not transfer directly to another region with a different crystallographic orientation distribution.

Yeoh et al. [96] similarly reported that Ti-6Al-4V macrozones affected ultrasonic velocity according to their orientation relative to the propagation direction. The authors found correlations between macrozone characteristics and the resulting velocity, attenuation and backscatter responses. This indicates that a measured ToF difference may reflect directional microstructural variation as well as stress.

Park et al. [95] identified relationships between ultrasonic velocity and microstructural conditions in AM metals. However, the samples also contained variations in porosity and lack of fusion, making it difficult to assign velocity changes exclusively to grain structure.

The effect of grain size on coherent velocity is generally less direct than its effect on scattering in cases where the grain dimensions are small compared to the wavelength. But in situations where the grains are elongated, or a strong texture is present, the velocity can become more and more dependent on direction. Comparisons based on travel time therefore need to use a fixed propagation direction and must distinguish between changes in the absolute travel time and those caused by variations in path length or coupling.

This does not prove that ToF is independent of microstructure in general when assessing RS, since the particular microstructural transition in question caused only a relatively small response under the chosen frequency, propagation direction and sampling depth. Calibration transfer cannot be established when there are substantial differences between the reference and the area being inspected in terms of texture, grain morphology or phase distribution.

3.6.2 Effects on Attenuation, Backscatter and Frequency Response

The decrease in amplitude of coherent ultrasonic waves as they move away from the source is known as attenuation. This occurs due to energy losses caused by various mechanisms, including scattering, absorption, mode conversion, and other types of beam losses. In polycrystalline metals, scattering takes place mainly as a result of grain-scale elastic anisotropy, since adjacent crystals have different directional stiffnesses and this affects the wave that is propagating.

Wan et al. [97] investigated grain-size effects on ultrasonic attenuation in 316L stainless steel. The authors found that attenuation depended strongly on the relationship between ultrasonic wavelength and grain size. Exceptionally large grains along the propagation path could dominate the measured attenuation, showing that an average grain size may not fully represent the acoustic response.

The ratio of wavelength to grain size determines the scattering regime; when the grains are much finer than the wavelength, the scattering is weak, and the material may be regarded as behaving like an effective homogeneous medium. However, as the size of the grains becomes a larger part of the wavelength, scattering increases and there is a greater loss of coherent amplitude. This is the reason why coarse-grained areas may exhibit higher attenuation even though the fine-grained areas have more grain boundaries.

The shape and texture of the grains also affect attenuation. Yeoh et al. [96] discovered that the orientation and shape of the macrozones had an effect on attenuation in Ti-6Al-4V, proving that directional correlation can be just as important as the average grain size. Zhang et al. [68] compared the various ultrasonic techniques for determining grain size in aluminium, steel and copper and found that attenuation and backscatter give complementary information; backscatter worked well in materials which scattered weakly, whereas attenuation was more effective in the case of the coarsely grained steel and copper specimens.

Backscatter represents the portion of scattered energy returning towards the receiver. Its amplitude and variability depend on grain dimensions, crystallographic contrast, morphology and spatial distribution. Dobrovolskij and Schladitz [98] modelled backscatter from polycrystalline microstructures and demonstrated that the grain-size distribution and inspection frequency influence the resulting microstructural noise. Their work also showed that multiple statistically equivalent microstructures can produce different individual backscatter responses, supporting the use of averaged or statistical descriptors rather than a single waveform amplitude.

Frequency-domain characteristics offer another way of describing how propagation is influenced by microstructure. When higher-frequency components are preferentially scattered or damped, this can lead to a decrease in the centre frequency, a reduction in bandwidth, or a steeper high-frequency roll-off. According to Markja et al. [99], changes in ultrasonic attenuation and frequency behaviour were

observed in steels having different grain structures, which supports the idea of using spectral changes as indicators of microstructural evolution.

Frequency measurements have to be interpreted with care since the spectrum that is observed also varies with the transducer bandwidth, the coupling, the propagation distance, the window chosen and the normalisation. An apparent shift in the centre frequency might be due to decisions made during signal processing or to a decrease in the signal-to-noise ratio (SNR) rather than being caused solely by the microstructure. Spectral comparisons must therefore make use of the same acquisition conditions, identical temporal windows and the same normalisation procedures.

Attenuation, backscatter and frequency characteristics are consequently sensitive to microstructure, but they do not provide unique measurements of grain size or morphology without calibration. Their strongest value lies in identifying relative changes and supporting interpretation alongside microscopy, EBSD or another independent characterisation.

3.6.3 Microstructure-Aware Interpretation

Microstructure-aware interpretation combines ultrasonic quantities with different relative sensitivities rather than assigning any measurement exclusively to stress or microstructure. Park et al. [95] and Yeoh et al. [96] showed that velocity, attenuation and backscatter provide complementary information about microstructure and defects.

The relative response has to be determined by experiment for both the material and the method of inspection. A ToF measurement might show only a small variation between two microstructures that have undergone stress relief, whereas attenuation and backscatter would change considerably. This outcome lends support to the view that ToF is less sensitive to that particular microstructural transition, but it does not prove a general distinction between stress and microstructure.

A suitable experimental design should therefore control one field while investigating the other. Stress-relieved samples with distinct microstructures can examine microstructural sensitivity, while mechanically loaded specimens with a consistent microstructure can establish stress sensitivity. Complete quantitative separation requires both forms of experiment and an uncertainty assessment covering acquisition, processing and material variability.

FMC is able to support this interpretation by offering a number of transmitter-receiver paths obtained from the same probe position. The path-wise arrival times, attenuation, backscatter and spectral measurements can be checked for consistency and for directional dependence. Nevertheless, the paths are not completely independent since they have common coupling interfaces and involve overlapping material volumes. Although multi-path acquisition enhances the diagnostic information, it does not in itself separate stress from microstructure.

The existing studies thus advocate a careful approach that involves the use of multiple measurement methods. ToF should mainly be employed for assessing stress since its sensitivity to microstructure is relatively low. Meanwhile, attenuation, backscatter and frequency characteristics can show if the material being examined differs from the calibration condition. This enables the microstructural information to help qualify the interpretation of the stress without implying that both stress and microstructure have been independently quantified from a single acquisition.

This thesis presents PAURS+ as a microstructure-aware interpretation of phased-array LCR data and not as a fully validated dual-field inversion method; support from the literature indicates that the dominant sensitivities of the available measurements can be assessed, but further work on controlled loading, microstructural calibration and uncertainty propagation is needed before independent quantitative values for both stress and microstructure can be obtained.

3.7 Summary and Research Gaps

Research currently available indicates that in order to mitigate RS in WAAM, it is necessary to use measurement methods which are capable of detecting the spatial redistribution under various manufacturing conditions. Although CM and XRD offer complementary reference data, direct quantitative comparison is limited because of the differences in measurement depth, gauge volume, stress component and uncertainty.

Ultrasonic LCR measurements provide a non-destructive and repeatable method of assessing the shallow subsurface RS. Yet, their reliability relies on carrying out material-specific acoustoelastic calibration, making a choice of reference state, ensuring stable wave generation, and obtaining consistent ToF values. Since conventional single-element systems have only limited acoustic-path redundancy, it is difficult to detect abnormal measurements and variations due to coupling. Phased arrays and FMC can offer extra paths which allow averaging and the assessment of measurement quality, though they do not automatically eliminate systematic errors.

The microstructure poses an additional problem since grain size, morphology and texture can affect ToF, attenuation, backscatter and frequency response. It is difficult to tell these effects apart from those related to stress without carrying out controlled experiments and making use of further ultrasonic measurements.

The literature therefore points out three main research gaps. The first is that a complete and validated phased-array LCR workflow for measuring RS in WAAM Ti-6Al-4V is still underdeveloped. The second lies in the need for further investigation into the use of FMC for assessing the quality of the path and for detecting RS redistribution after peening. The third is that the relative sensitivity of LCR ToF, attenuation, backscatter, and frequency response to microstructural variation has not been adequately

established. It is these gaps that lead to the development, validation and microstructure-aware interpretation of PAURS which is presented in the following chapters.

Chapter 4: Methodology

4.1 Overview

Figure 3 presents the methodological progression followed throughout this thesis. The thesis is structured around three research studies, each developing a different part of the PAURS methodology. The purpose of this chapter is not to repeat the full experimental process, but to explain the common experimental framework that links the three studies and to clarify why specific parameters, validation methods and scanning strategies differ between studies.

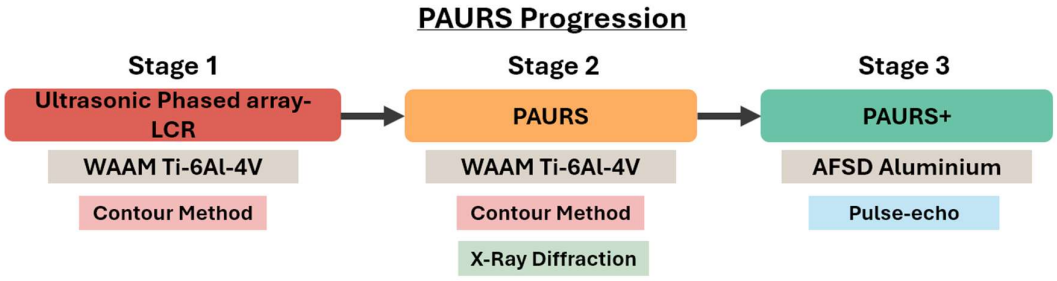


Figure 3 The methodological progression of PAURS throughout the three stages

The methodology progresses in three stages. In the first stage, the phased-array LCR concept is introduced and tested on a WAAM Ti-6Al-4V component to determine whether phased-array ultrasonic measurements can be used to assess RS in an AM Ti-6Al-4V component. This includes wedge selection, phased-array configuration, acoustoelastic calibration, ToF extraction and comparison with CM. This stage assessed whether phased-array LCR measurements could reproduce the principal features of the RS distribution in WAAM Ti-6Al-4V.

The second stage studies WAAM Ti-6Al-4V again and applies PAURS to assess the effectiveness of RS mitigation. In this study, PAURS is used to compare as-deposited and inter-pass peened WAAM samples. FMC is incorporated to increase the number of available acoustic paths, improve averaging and enable more systematic outlier rejection. This stage extended PAURS from initial feasibility to the detection of RS redistribution following inter-pass peening.

The third stage extends the method into PAURS+. Rather than focusing solely on RS measurements, this stage examines how ultrasound responds to stress and microstructure. AFSD aluminium samples are used because they contain distinct fine and coarse-grain regions. These samples allow ToF, attenuation, backscatter and frequency-domain behaviour to be compared across controlled microstructural conditions. This stage provided the basis for microstructure-aware interpretation within PAURS+.

Across all stages, the same phased-array LCR acquisition principle was retained. A material-specific wedge configuration was selected, ultrasonic signals were acquired using phased-array transducers, and the resulting observables were processed according to the purpose of each study. In the WAAM studies, ToF variation was converted into RS using acoustoelastic calibration. In the PAURS+ study, ToF, attenuation, backscatter and frequency-domain characteristics were compared between microstructural regions.

4.1.1 Workflow

Figure 4 summarises the workflow used throughout the thesis. The figure shows that PAURS is not evaluated against a single RS method. Instead, it is compared with destructive and non-destructive methods, each of which samples a different part of the RS field. This is necessary because no individual RS measurement method provides a complete benchmark for PAURS.

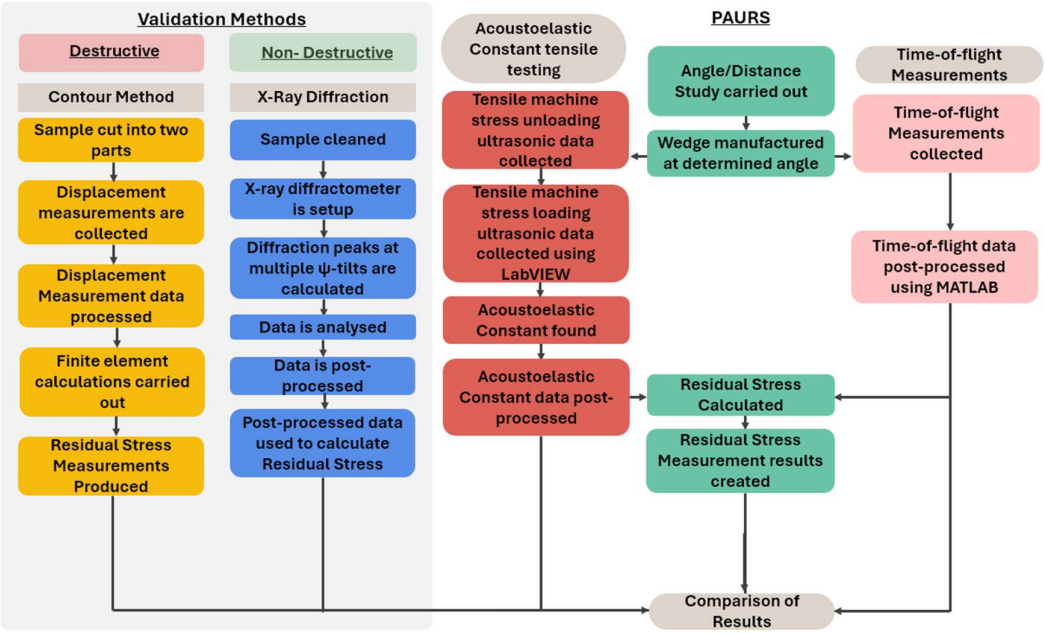


Figure 4 A flowchart showing an overview of the process of the methodology throughout the studies

Validation was based on complementary evidence rather than pointwise equivalence. Agreement was assessed using the measured stress component, overall distribution, peak location and response to processing. Differences in measurement depth, gauge volume and spatial resolution were considered when interpreting stress magnitude.

4.1.2 Facilities, Equipment and Contributions

The experiments were carried out with the help of facilities and expertise provided by a number of collaborating organisations. In this section the location and ownership of the main equipment are explained and the author's contribution to each part of the methodology is stated.

The ultrasonic measurements known as PAURS and PAURS+ were carried out at the Centre for Ultrasonic Engineering (CU) at The University of Strathclyde, with the PEAK NDT MicroPulse 6 controller and commercial IMASONIC phased-array transducers being used. The equipment was supplied by The University of Strathclyde. The author set up the ultrasonic measurement system, obtained and processed the data, and prepared the methods employed for calculating and interpreting the PAURS and PAURS+ results. He also designed the wedge configurations and performed the experimental study of the wedge angle that was used to choose the practical LCR measurement setup.

The acoustoelastic calibration tests were carried out using tensile-testing equipment in the Advanced Materials Research Laboratory (AMRL) at the University of Strathclyde; the author took the ultrasonic measurements while the material was being loaded and dealt with the stress and ToF data that corresponded to this. The technical staff of the AMRL provided support for the running of the mechanical-testing equipment.

The specimens of WAAM Ti-6Al-4V were made at Cranfield University and were then provided for the measurement programme. The AFSD aluminium specimens were manufactured by MELD Manufacturing Corporation as part of the AFRC CORE programme and were supplied by the Advanced Forming Research Centre (AFRC). The author was not involved in the production of either set of specimens but carried out the ultrasonic measurements and the related analysis.

The XRD measurements were carried out at the National Manufacturing Institute Scotland (NMIS) with the use of a PROTO LXRD laboratory diffractometer; the positions at which the measurements were made, and the direction of stress were chosen in order to allow comparison with PAURS, and the resulting XRD data were provided for analysis and interpretation in this thesis.

The CM measurements were carried out at Coventry University; this involved wire-EDM sectioning, the measurement of the exposed cut surfaces and the reconstruction of the cross-sectional stress maps. The author used the provided results to define the corresponding comparison profiles and to assess the agreement with PAURS.

The main contribution of the author was the design of the wedge arrangement, the determination of its configuration and calibration of the PAURS system, the collection of ultrasonic data, the signal processing, the calculation of the RS, and the interpretation of both the PAURS and PAURS+ measurements; the production of the samples and the carrying out of the specialist reference measurements were carried out by the organisations that were involved in the collaboration.

4.1.3 Measured Components

PAURS measured the longitudinal component of the stress in the direction of the path average since the LCR waves travelled parallel to the direction of deposition. The PAURS value given therefore represents the stress component along the ultrasonic propagation path in the effective near-surface inspection area.

CM reconstructed the RS component normal to the wire-EDM cut plane perpendicular to the longitudinal direction. XRD measured the near-surface stress component defined by the diffraction measurement direction. For the measurements aligned parallel to the deposition path, the reported value corresponds to the longitudinal component.

CM and XRD provide complementary reference measurements of different RS components and sampling regions. A future component-by-component comparison could align the longitudinal stress measured by XRD with the corresponding component reconstructed by CM, while accounting for their different measurement depths, spatial resolutions and gauge volumes. This was outside the scope of the present work, which focused on comparison with PAURS.

4.2 Sample Manufacturing

4.2.1 Overview

Figure 5 shows the two types of samples used throughout the thesis. The WAAM Ti-6Al-4V samples provide the main AM RS case study. Meanwhile, the AFSD aluminium samples provide controlled microstructural variation for the PAURS+ study.

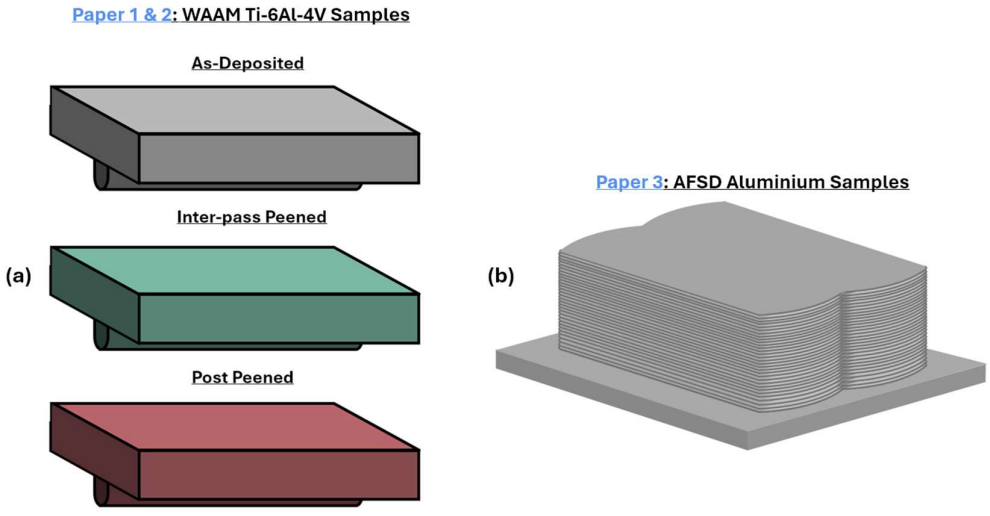


Figure 5 The samples used in all studies show (a) the three WAAM Ti-6Al-4V samples used in studies 1 & 2, (b) the AFSD aluminium samples used in study 3

The WAAM Ti-6Al-4V samples shown in Figure 5a were used in studies 1 and 2. Three WAAM Ti-6Al-4V specimens were manufactured at Cranfield University using a robotic plasma-transferred-arc system. The specimens had identical nominal dimensions of 250 mm × 60 mm × 7.3 mm, and each contained ten deposited layers. The three conditions were as-deposited, inter-pass peened and post-peened.

The as-deposited sample was analysed with PAURS and verified with CM and XRD. The inter-pass peened sample was measured with PAURS only, and the post-peened sample was analysed with CM for comparison. This configuration was chosen as it is an RS mitigation method that can be implemented in an automated WAAM process.

4.2.2 WAAM Ti-6Al-4V

Figure 6 and Figure 7 shows a schematic of the WAAM sample manufacturing and the physical setup, respectively. A 1.2 mm diameter Ti-6Al-4V wire was used as the feedstock. Deposition was performed using a PTA system, with a wire feed speed of 2.2 m/min and a current of 180 A. The travel speed was varied: the first layer was deposited at 4 mm/s, the second at 4.5 mm/s, and the remaining layers at 5 mm/s. The average layer height was approximately 0.98 mm, and the wall width was 9.2 mm.

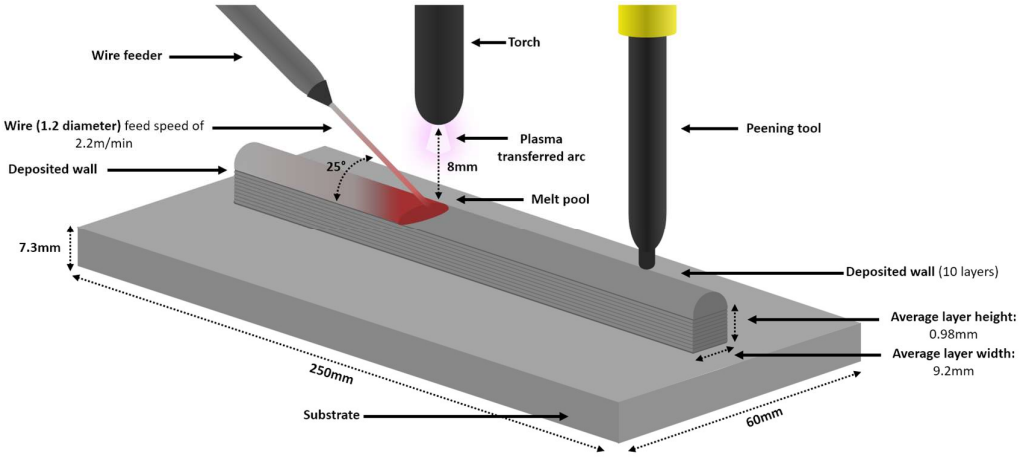


Figure 6 Schematic of the setup and dimensions for the manufactured experimental samples

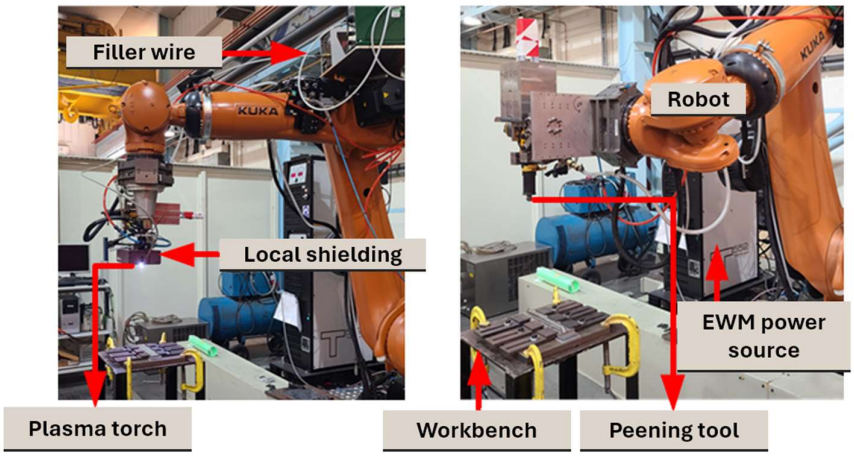


Figure 7 Physical setup for the manufacturing and peening of the WAAM samples [66]

A hammer peening tool (Atlas RRH06P) was integrated into the deposition setup for the inter-pass peened sample. The pneumatic tool was mounted with the robot and provided an energy per blow of 6 J (7 bar air pressure). The peening head had a diameter of 10 mm, operated at a frequency of 36 Hz, and travelled at 10 mm/s.

The substrate was clamped using six evenly spaced clamps to minimise distortion during deposition. Shielding was provided by pure argon gas, with flow rates of 0.8 L/min for the plasma gas, 8 L/min for the shielding gas, and 68 L/min for the local shielding device. All samples were built using a 6-axis KUKA robotic arm, which controlled the deposition path in an alternating travel direction to ensure uniform heat distribution.

4.2.3 AFSD Aluminium

4.2.3.1 Manufacturing macroscopically-stress-relieved samples

The PAURS+ study used an AA7075 component produced by AFSD onto an AA7075 substrate. The solid-state deposition process produced a fine equiaxed microstructure within the deposited region, while the rolled substrate retained a coarse elongated grain structure. These contrasting regions provided the controlled microstructural conditions required for ultrasonic comparison.

To tailor the mechanical properties of the deposited material to industrial requirements, a heat treatment comprising solution treatment followed by artificial ageing was applied. Each deposited part was sectioned into two halves to assess the influence of the AFSD process and the subsequent heat treatment. One half was characterised in the as-deposited condition, while the other was characterised after heat treatment. In accordance with the AMS 2770H for AA7075 aluminium alloy, solution treatment was carried out at 466 °C for 2 h, followed by water quenching within 15 s of furnace removal [100]. Artificial ageing was then performed in two steps (107 °C for 6 h followed by 177 °C for 6 h). Ageing was conducted immediately after quenching to minimise natural ageing. The extended ageing

treatment also promotes stress relaxation, thereby reducing RS introduced during the AFSD deposition process.

The component investigated in this study is shown in *Figure 8*. Two slices, each approximately 8 mm in thickness, were extracted from the AFSD blocks using electrical discharge machining (EDM): one from the as-deposited condition (denoted as Sample #1 in *Figure 8*b) and the other from the heat-treated condition (Sample #2, shown in *Figure 8*c). In this context, macroscopically stress-relieved refers to the reduction of Type I RS through specimen sectioning and, where applicable, post-processing heat treatment. It is well established that sectioning processes such as EDM, when applied under controlled conditions, release macroscopic RS through elastic redistribution, forming the basis of the CM for RS measurement [77]. While microstructurally-driven stresses at smaller length scales (Type II/III) may persist, these are intrinsic to the material state and form part of the microstructural contribution investigated in this work.

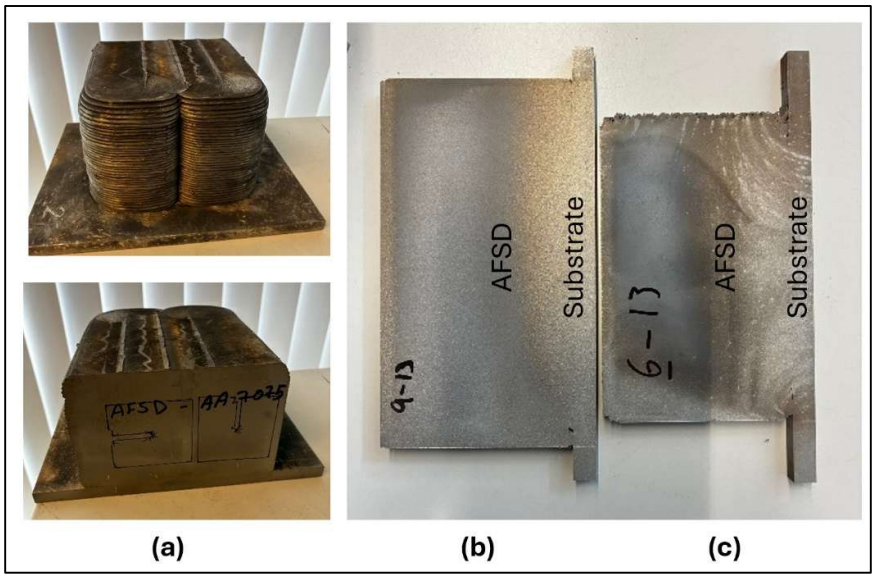


Figure 8. AFSD aluminium block and sectioned slices: (a) full block, (b) Sample #1 (EDM-only), (c) Sample #2 (heat-treated + EDM). [101]

4.3 Measurement Scanning Procedure

Figure 9 summarises the measurement methods applied to each sample type. The figure is used here to clarify how the scanning strategy changed between studies. In Chapters 5 and 6, scanning was designed primarily to resolve RS gradients. In Chapter 7, scanning was designed primarily to compare ultrasonic responses across different microstructural regions.

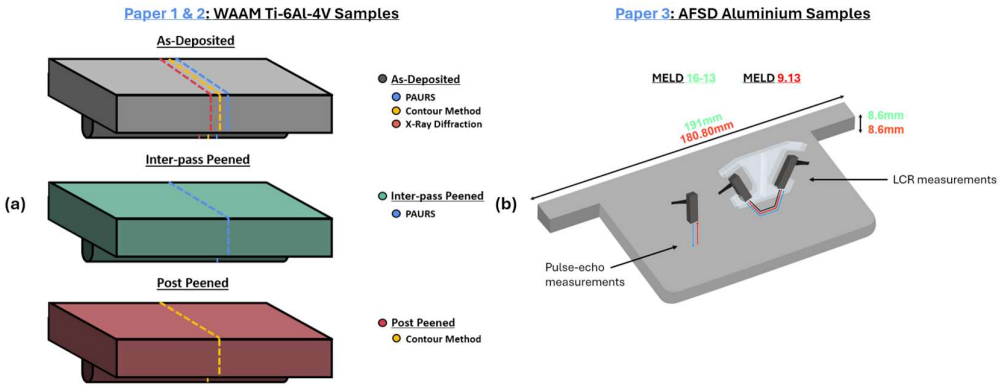


Figure 9 The measurement methods used throughout all studies show (a) the three WAAM Ti-6Al-4V samples measured in studies 1 & 2, with PAURS, CM and XRD utilised, (b) the AFSD aluminium samples measured in study 3 with both LCR and pulse-echo PAURS measurements

For the WAAM Ti-6Al-4V samples in Chapters 5 and 6, the scan coordinate system was defined relative to the centreline beneath the deposited wall. This position was set to 0 mm because it corresponds to the region most affected by repeated thermal cycling and is expected to contain the highest tensile RS. Scan positions were then taken on either side of this centreline. Fine spacing was used within and around the HAZ, where steep stress gradients were expected, while wider spacing was used outside this region, where stress was expected to vary more gradually.

For the AFSD aluminium samples in Chapter 7, the scan strategy was different because the main objective was to separate stress-sensitive and microstructure-sensitive ultrasonic responses. Scan paths were therefore selected to cross fine equiaxed and coarse elongated grain regions. The scan spacing was chosen to ensure that each microstructural region was sampled sufficiently to enable comparison of ToF, attenuation, backscatter, and frequency-domain behaviour.

This thesis identified that the depth of the LCR in the subsurface lies between 1.2 and 1.5 mm, the variations being due to differences in acoustic velocities. The fact that this depth is so small shows that PAURS is a method which is used in the shallow subsurface region and therefore comparisons with more deeply situated volumetric techniques should be made with caution.

Where possible, data at a similar depth to the PAURS penetration depth were considered. For CM, FE reconstructions yielded stress profiles along scan lines near the estimated LCR depth. The comparison for XRD included considerations of differences in measurement depth and gauge volume.

Therefore, the scan spacing and measurement depth varied among the studies. They were chosen based on the specific feature being analysed: RS gradients in WAAM samples, and microstructural transitions in AFSD aluminium.

4.3.1 Identification of the HAZ

The HAZ measurement region was identified using an initial coarse PAURS scan across the bottom surface of the WAAM specimen. ToF measurements were taken at wider intervals on both sides of the deposited-wall centreline to identify the lateral extent over which the ultrasonic response differed from the surrounding parent material. The outer positions at which the response returned to the parent-material baseline were treated as the preliminary HAZ boundaries.

The boundaries were compared with the corresponding CM stress distribution, and the CM map was used to check whether the area detected from the first PAURS measurements matched the greater stress concentration located underneath and around the deposited wall. The joint PAURS and CM evaluation was then employed to establish the final scan area.

In the last PAURS scan, finer spacing was used in the designated HAZ since steeper stress gradients were expected there, and wider spacing was used elsewhere where the response changed more gradually. The boundary of the HAZ was therefore not defined merely on the basis of the nominal wall width or the deposition geometry. Rather, it was determined through experimental ultrasonic measurements and then checked against the CM results.

4.4 Validation RS Measurements

4.4.1 CM

CM was utilised as the primary reference method for studies of WAAM Ti-6Al-4V, as it provides a two-dimensional map of RS across a cut plane

Stress profiles along scan lines from the CM reconstruction that best matched the PAURS measurement locations and the LCR interrogation depth were extracted for comparison with PAURS. This depth alignment was needed because PAURS does not measure the full cut plane, but rather a shallow-subsurface, path-averaged response.

CM was used to measure RS in the as-deposited and post-peened samples. Both samples were sectioned vertically using a Fanuc Robocut α-C600i wire electro-discharge machine (EDM) with a 0.25 mm brass wire. The cut was initiated from the top of the deposit and progressed downward through the substrate. Both samples were clamped symmetrically, and low electrical power parameters were used for better surface finish, and fewer wire EDM cutting errors at the cut perimeter. A schematic of this setup is shown in Figure 10. The red line represents the wire-EDM cut plane from which the cut-surface displacement and corresponding RS distribution were reconstructed.

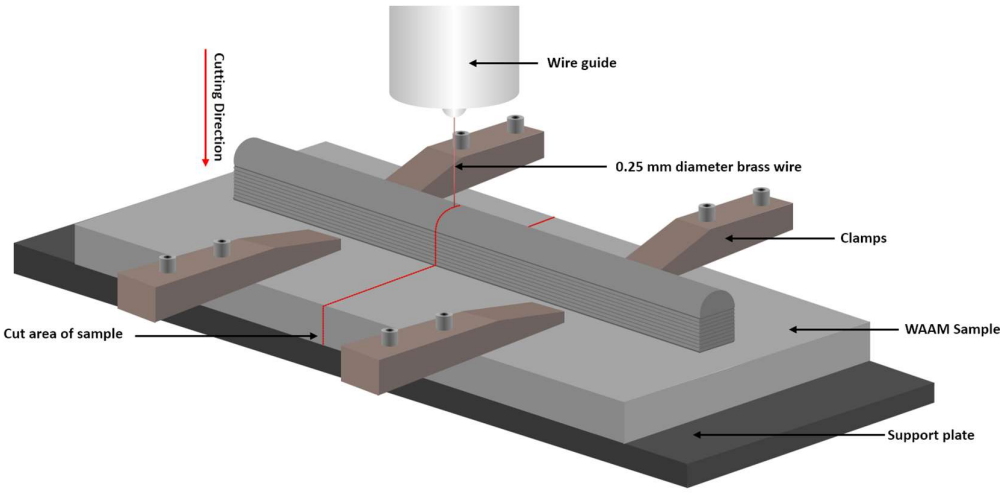


Figure 10 A schematic showing the WAAM Ti-6Al-4V CM EDM setup using the Fanuc Robocut α-C600i

Figure 11 shows the cutting direction used for CM and the resulting as-deposited cut sample. This was then used to produce the CM stress map and data for RS measurements.

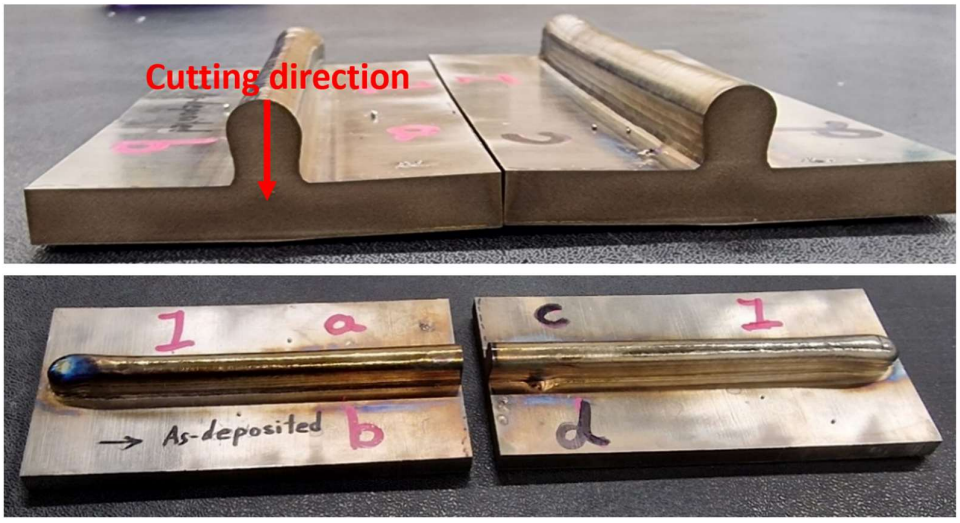


Figure 11 The cutting direction used for cutting the Ti-6Al-4V sample for CM and the resulting cut sample. [61]

The wire-EDM cut progressed from the top of the deposited wall towards the substrate. This direction was selected to initiate sectioning in the thinner wall and progressively release the RS as the cut advanced into the more highly constrained deposit-substrate interface and substrate. Beginning at the wall also reduced the length of the initially unsupported cut surfaces and allowed the critical wall-to-substrate region to remain restrained until later in the cut. This was intended to limit premature cut-

face movement, wire deflection and cutting-induced artefacts that could affect the measured contour [77, 102].

A cutting speed of approximately 0.25 mm/min was used, and displacement profiles of the cut surfaces were measured using a Zeiss Contura g2 coordinate measuring machine (CMM) with a 3 mm drag probe. Measurement points were spaced at 0.2 mm intervals in both directions from the sample perimeter. A schematic of the CMM setup is shown in Figure 12.

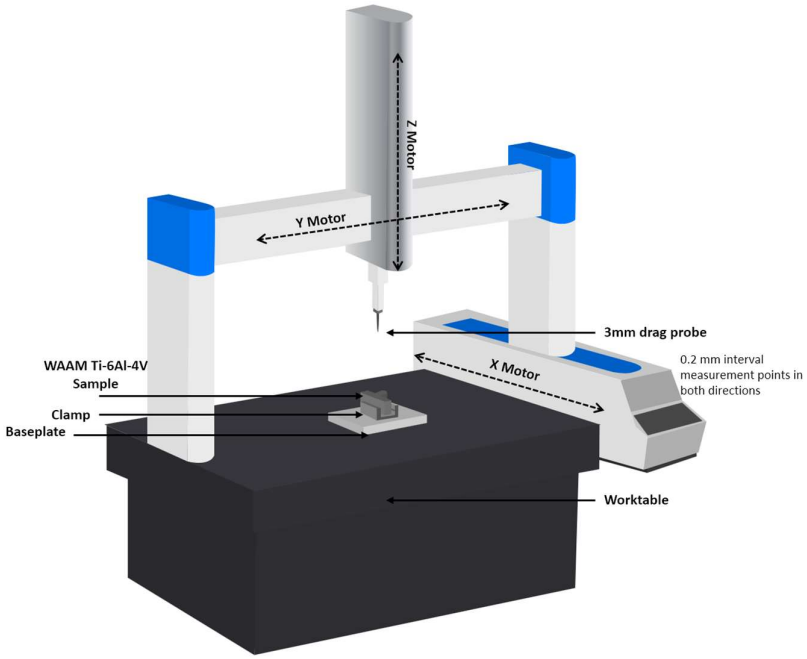


Figure 12 A schematic of the Zeiss Contura g2 CMM setup

Post-processing of the displacement data from both cut surfaces of each sample involved aligning, cleaning, flattening, and smoothing using MATLAB analysis. Smoothing was achieved with a cubic spline knot spacing of 2.5 mm in both X and Y directions. An FE model of one cut half of the samples was developed, using the Abaqus software 2021, using an eight-node brick element (C3D8R). Constraints were applied to the model to prevent rigid body motion and the measured contour's reverse was used as the displacement boundary condition. A linear elastic FE analysis was carried out to obtain the stress results with the following material properties: modulus of elasticity [E] = 113.8 GPa and Poisson's ratio [v] = 0.342.

The FE mesh influences the spatial detail and peak-stress magnitude obtained from the CM reconstruction. However, the effective resolution is governed collectively by the surface-measurement spacing, displacement-data smoothing and FE element size. The mesh should therefore be sufficiently fine to represent the variations retained in the smoothed contour, but additional refinement below this experimental resolution does not provide meaningful spatial information. In this study, the

reconstructed maps were interpreted at the length scale supported by the measured and smoothed displacement data, with emphasis placed on the broader stress distribution and extracted profiles rather than element-scale fluctuations or isolated peak values [103].

4.4.2 XRD

In WAAM Ti-6Al-4V studies, XRD was used as a non-destructive, surface-sensitive reference method. The measurements on the bottom surface were performed with the sin2ψ method. The stress values obtained provided an independent comparison of near-surface PAURS trends.

Figure 13 illustrates the procedure used for collecting XRD data. As XRD was selected to validate both CM and PAURS as RS measurement methods, measurements were taken along the bottom of the sample for direct comparison. Only the as-deposited sample was analysed, as the purpose was validation rather than comparison with the inter-pass peened condition. Fifteen measurement points were taken along the bottom surface to provide a representative RS distribution for comparison with CM and PAURS results.

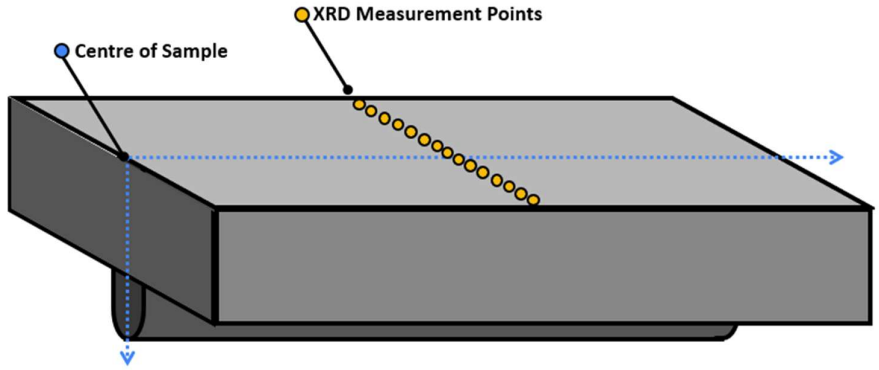


Figure 13 Method for data collection using XRD [66]

Figure 14 shows the full experimental setup for the XRD measurements on the as-deposited Ti-6Al-4V WAAM sample. RS measurements were performed using a PROTO LXRD diffractometer, applying the $\sin^2\psi$ method, which is widely used for stress analysis in polycrystalline materials. This technique involves tilting the sample at various ψ angles to detect changes in lattice spacing, from which strain and stress are calculated. Due to the limited penetration depth of X-rays (typically a few tens of microns), the method is ideal for surface and near-surface stress evaluation in additively manufactured parts.

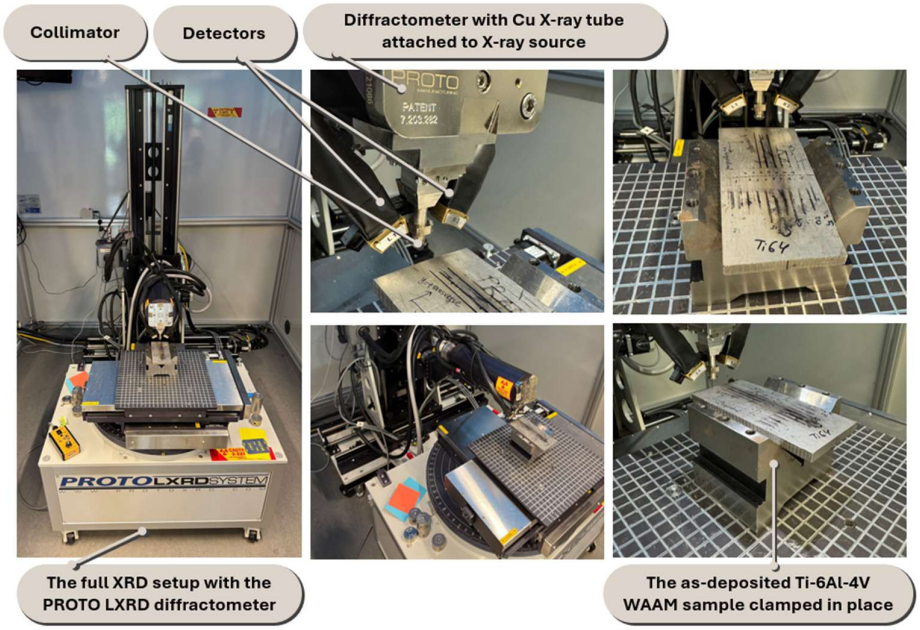


Figure 14 Full experimental setup for the XRD measurements [66]

The analysis was carried out using PROTO XRDWin 2.0 software. The terms "longitudinal" and "transverse" refer to directions that are parallel and perpendicular to the WAAM build path, respectively, since they are used to measure how stress varies with different orientations. The XEC specific to the material were retrieved from the software's internal database. The peak positions were fitted using a 75% Gaussian curve, and the peak shifts were calculated by means of the Absolute Peak method in order to ensure a reliable assessment of the stress. The scan parameters, such as the tilt angles, the exposure times, and the choice of diffraction plane, are given in Table 2.

Table 2 The scan parameters used for XRD RS measurements

Parameter	
Diffraction plane (h,k,l)	**213**
Crystal structure	**HCP**
Tube	**Cu Kα**
Wavelength, nm	**1.541838**
Aperture (round), mm	**1**
Acceleration voltage, kV	**30**
Current, mA	**30**
½ S2, MPa^{-1}	**$11.89 * 10^{-8}$**
-S1, MPa^{-1}	**$2.97 * 10^{-8}$**
Bragg Angle, deg.	**142.0**

Because XRD samples a much shallower region than the LCR waves used in PAURS, the XRD results were not treated as a direct quantitative equivalent. Instead, they were used to assess whether the same general stress distribution and relative changes were observed near the surface.

4.5 PAURS

4.5.1 PAURS Process

Figure 15 illustrates a clear process : (1) choose the appropriate LCR wedge configuration for the material, (2) calibrate the acoustoelastic constant with a representative tensile specimen, (3) gather phased-array LCR ToF data, (4) perform interpolation, (5) apply correction and path-quality filtering, (6) transform ToF variations into RS measurements, and (7) compare the RS distribution with the most suitable reference method.

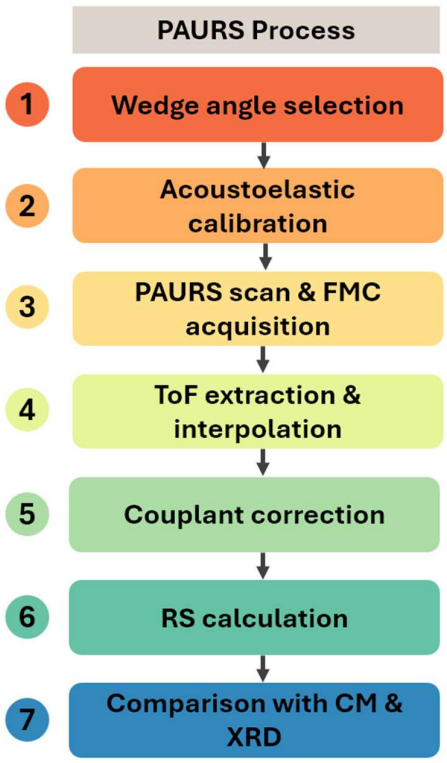


Figure 15 PAURS process workflow

For each PAURS measurement, a wedge-specific LCR wave was excited and recorded by phased-array transducers in a transmitter-receiver configuration. The LCR arrival was detected in the received A-scan, and a consistent zero-crossing point was used as the ToF marker. The obtained ToF values were then compared with a stress-free reference and converted into RS using the calculated acoustoelastic constant for the material of interest.

LCR waves were selected since the time of flight is influenced by the stress component in the direction of propagation through the acoustoelastic effect; furthermore, they investigate a shallow subsurface layer and provide greater sensitivity than laboratory XRD, all without being destructive and with the ability for repeated measurements.

The key methodological point is that the same measurement principle was retained across all studies, while the material changed. Ti-6Al-4V and aluminium have different acoustic velocities, microstructures and geometries, so their wedge angles, validation methods and requirements differ. These differences are accounted for within the PAURS workflow rather than treated as separate methods.

Two PAURS acquisition approaches were used. The first was the direct-element approach, in which corresponding transmitter and receiver elements were used to generate multiple element-wise ToF

measurements. This approach was used in the initial WAAM Ti-6Al-4V feasibility study because it allowed each element response to be inspected individually. Element-wise comparison enabled the identification of outlier measurements before averaging. FMC extends the direct-element approach by acquiring the complete transmitter-receiver matrix.

The transition from direct element-to-element measurements to the utilisation of FMC represents an important advancement in this thesis. The direct approach establishes feasibility and potential, whereas FMC provides additional data for evaluating path consistency and reducing sensitivity to individual anomalous measurements.

4.5.2 Configuration

As shown in Figure 16, the PAURS system consists of two 5 MHz phased-array transducers, each with 8 elements. One transducer is a transmitter, and the other is a receiver. The arrays are mounted in an acrylic wedge to generate LCR waves in the material under test. A-scan acquisition and ToF measurements were carried out using a PEAK Micropulse 6 phased-array device with LabVIEW-based data acquisition routines.

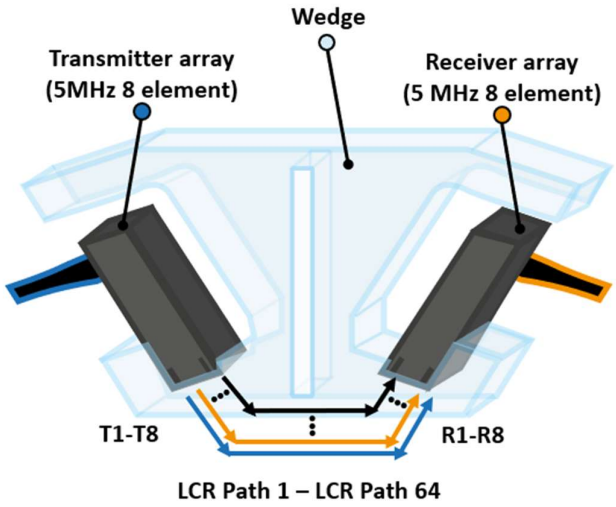


Figure 16 The PAURS measurement setup

Traditional LCR setups generate only two wave paths, limiting their ability to mitigate interference from material texture and microstructure. The PAURS setup, by contrast, can generate at least 8 acoustic paths and up to 64 paths using FMC.

This configuration was selected because it provides multiple acoustic paths in a compact inspection arrangement. In the direct-element approach, matched transmitter–receiver element pairs provide repeated ToF measurements at each scan position. In the FMC approach, each transmitter element is pulsed sequentially, and all receiver elements record the response, producing an 8 × 8 dataset with 64

possible acoustic paths per scan position. This increased path data is central to the PAURS methodology because it supports averaging, outlier detection and signal-quality assessment.

4.5.3 Wedge Design and Angle Optimisation

The wedge angle was selected separately for each material because LCR-wave generation depends on refraction at the wedge-specimen interface and, therefore, on the acoustic velocities of both materials. For the WAAM Ti-6Al-4V studies, Snell's law was first used to estimate the first critical angle and define a suitable range for experimental evaluation. Candidate wedge angles between **22.2° and 23.2°** were then assessed by comparing the signal amplitude, waveform stability and separation of the LCR arrival from competing wave modes. This procedure identified **22.7°** as producing the clearest and most consistent LCR response for the phased-array transducer, wedge and Ti-6Al-4V configuration used in this thesis.

A different wedge configuration was required for the AFSD aluminium investigation because the longitudinal-wave velocity of aluminium differs from that of Ti-6Al-4V. The corresponding refraction condition and practical LCR response therefore differed from those of the WAAM measurements.

The wedge angle that was selected was determined according to the specific material and measurement arrangement, rather than following a general standard. However, the method used for choosing it was the same throughout the thesis: it began with an initial estimate derived from Snell's law, after which experimental tests were carried out to obtain a stable and clearly distinguishable LCR response in the material being tested.

4.5.4 PAURS Experimental Setup

Figure 17 shows a schematic of the PAURS ToF measurement setup, which utilises a PEAK Micropulse 6 phased array instrument in combination with LabVIEW. Scans were carried out along the bottom surfaces of both the as-deposited and inter-pass peened WAAM Ti-6Al-4V samples. The bottom surface was selected because it provided a flat and accessible inspection surface for repeatable wedge positioning. Although this arrangement did not directly interrogate the top of the deposited wall, it remained relevant to the manufacturing process because the substrate restrained the deposit during WAAM and contained stress redistributed during deposition, cooling, peening and component release. The measurements therefore characterised the longitudinal RS distribution beneath the deposited wall and across the substrate region.

To ensure consistent spacing, a ruler was used to guide the scanning process, with measurements taken at 5 mm intervals outside the HAZ and at 1 mm intervals within it.

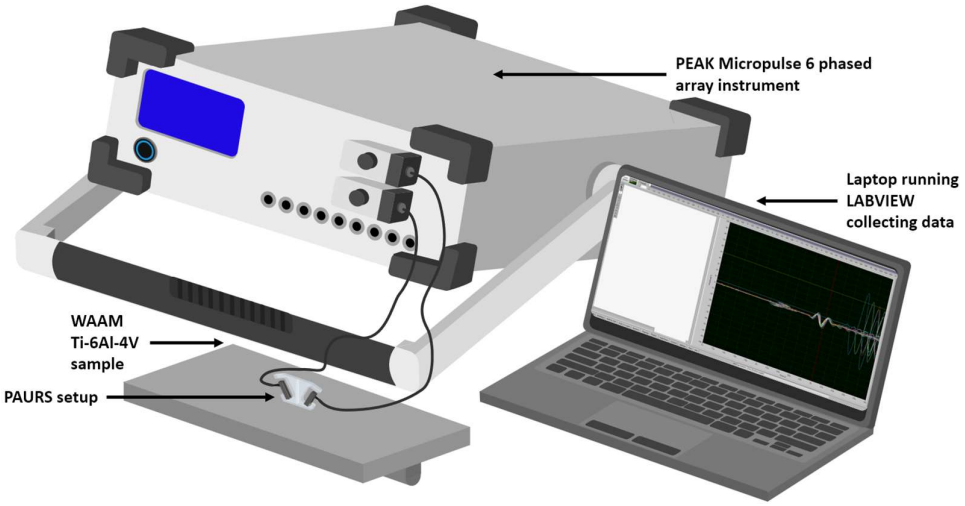


Figure 17 Experimental setup for PAURS ToF measurements

To perform ultrasonic ToF RS measurements effectively, the sample was divided into multiple scan lines, as shown in Figure 18. The centre of the sample wall is defined as 0 mm, with scan lines extending to ±25 mm. Because RS is expected to peak within the HAZ due to thermal cycling, that region was scanned more extensively.

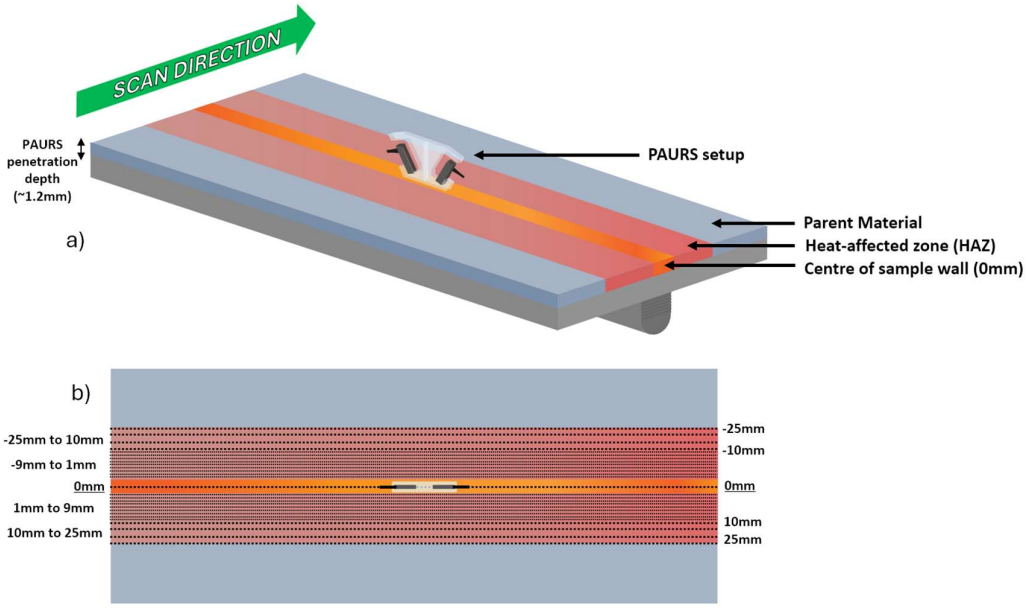


Figure 18 (a) Schematic of WAAM Ti-6Al-4V scanning; (b) Top-down view of scan lines

Outside the HAZ, 8 measurements were taken at 5 mm intervals: -25, -20, -15, -10 mm on one side, and 10, 15, 20, 25 mm on the other. Within the HAZ, 18 measurements were taken at 1 mm intervals from -9 mm to 9 mm. This increased sampling improves RS resolution in the HAZ.

The physical PAURS ToF setup is shown in Figure 19. A ruler was placed onto the bottom of the WAAM sample, and the 20 mm point was aligned with the 0 mm measurement point. Using the ruler as a basis to understand where the scan lines were, RS measurements could be taken from −10 to 10 mm for the data points used in the results graph. This allowed for an easy comparison of the data between the RS measurement methods and demonstrates how robotic scanning would be carried out in an automated in-situ setup.

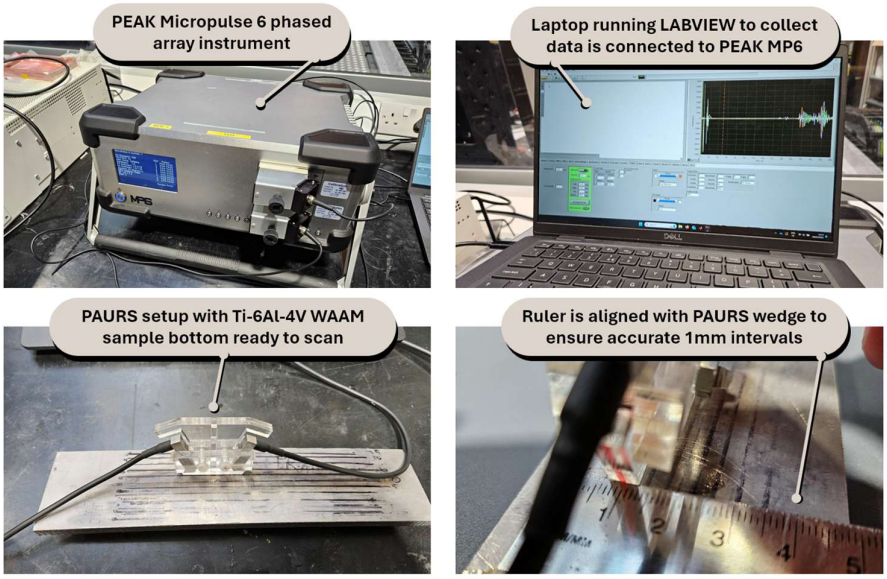


Figure 19 PAURS measurement setup showing the PEAK MP6 using two 8-element 5MHz arrays acting as transmitter and receiver, connected to the laptop for ToF measurements, which were then calculated with acoustoelastic measurements for RS measurements.

The important data to collect from the ToF measurements is the zero-crossing point. The zero crossing needs to be taken from every signal for the data collected. For example, if using the direct approach, it needs to be taken from each of the 8 signals, but with FMC, this increases to 64, so it will need to be taken from each of the 64 signals. These zero crossing values are then later used alongside the acoustoelastic constant data to produce the RS measurements.

Figure 20 shows the LCR waveform feature used for ToF measurement. The automated zero-crossing extraction and stress-calculation procedure is described later.

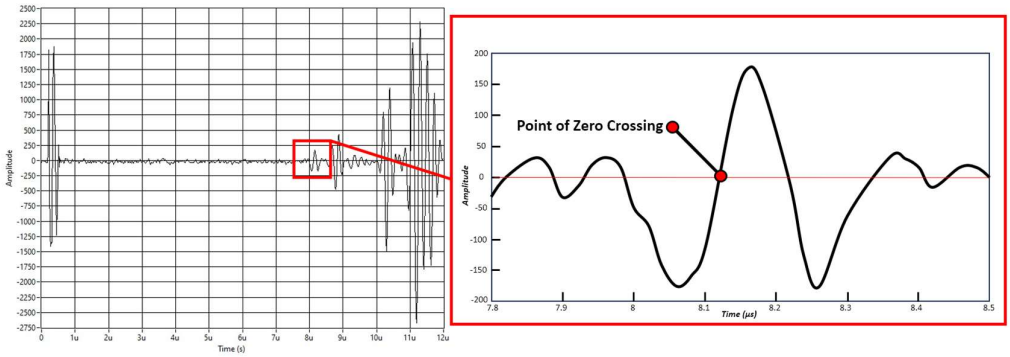


Figure 20 An example signal showing how the zero crossing is found from the LCR wave.

4.5.5 PAURS-ToF consistency

It is important to note that the ToF for LCR waves remains consistent regardless of the LCR path or the number of transmitter and receiver elements. This consistency was demonstrated by Javadi et al in their feasibility study of the PAURS method [104].

Figure 21 provides geometrical proof showing that ToF remains unchanged whether Element n transmits a wave travelling distance A1 in the wedge and T + B2 in the Ti-6Al-4V sample, or Element m transmits a wave travelling distance A2 in the wedge. This confirms that all elements in the transducer yield the same ToF, regardless of the LCR wave path between transducers.

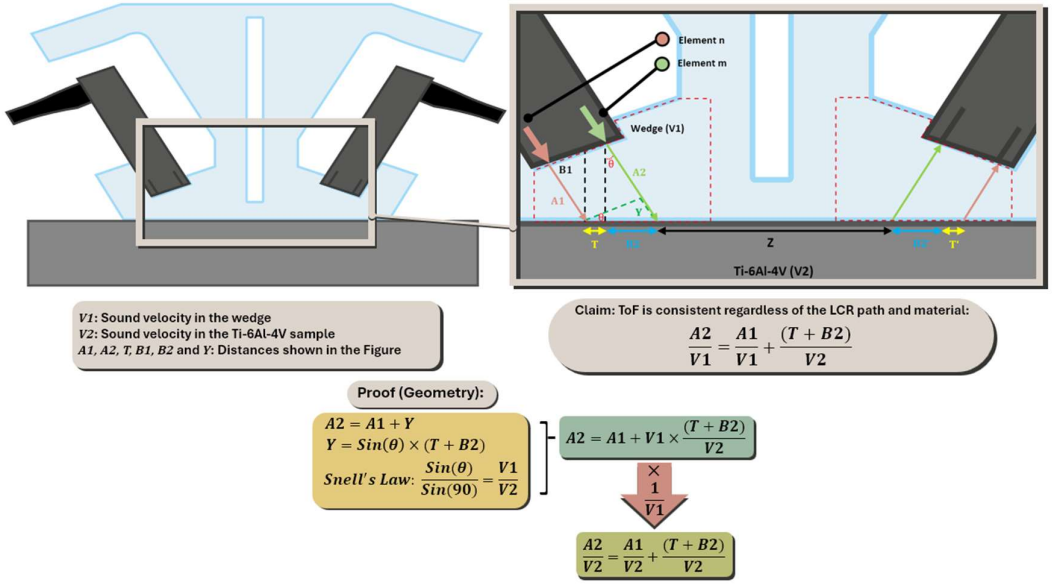


Figure 21 Geometrical proof of ToF consistency [66]

4.5.6 LCR wave propagation

It is also crucial to understand that ultrasonic waves do not travel in straight lines. LCR waves exhibit specific beam profiles upon refraction in the sample. Figure 22 (a) illustrates how a single element generates an LCR wave, showing its beam profile and refraction angles. The principal lobe, containing most of the energy, refracts at 84°, while a stronger side lobe appears at 67° [105].

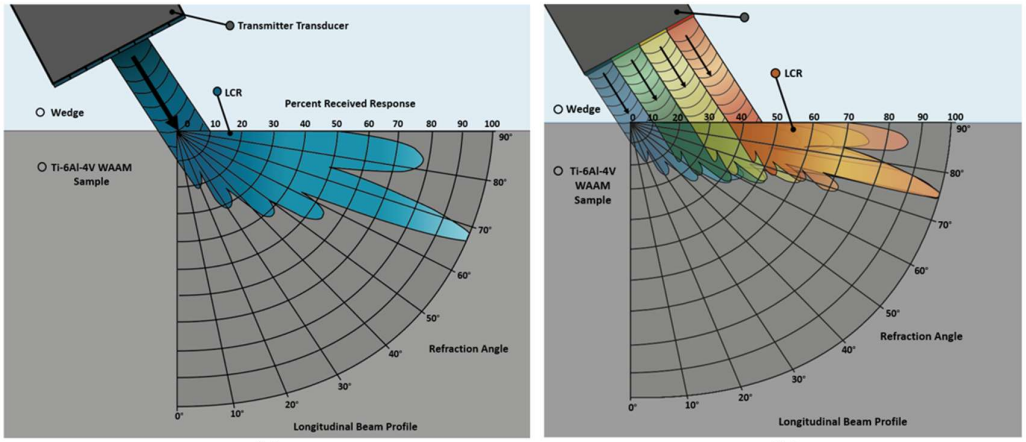


Figure 22 (a) Single element LCR beam profile in a WAAM sample (b) 4-element phased array LCR beam profile [66]

Figure 22 (a) Single element LCR beam profile in a WAAM sample (b) 4-element phased array LCR beam profile. (b) illustrates an example of how a 4-element phased array transmitter generates an LCR beam profile as it propagates through the sample. At first glance, the overlapping wavefronts may suggest potential interference or signal crosstalk between elements. However, this is effectively managed in two ways: spatially, by maintaining appropriate spacing (element pitch) between the array elements, and temporally, through the use of delay laws that control the timing of each transmitted signal. These measures ensure that the main LCR waves remain well-defined and travel toward the receiving elements without significant interference, preserving the integrity of the received signals. It is important to note that these assumptions are supported by experimental results presented in this study. LCR waves exhibit distinct characteristics, such as the fastest wave arriving at the receiver confirming their near-surface propagation, as observed by Mills et al [65] and Walker et al [61], which help distinguish them from other wave modes or noise caused by interference.

While Figure 22 shows a more realistic depiction of LCR paths, capturing the spread and shape of the ultrasonic energy lobes as they propagate through the material, Figure 23 simplifies this by representing each path as a straight line. It illustrates how each of the 8 transmitter elements sends LCR waves to all 8 receiver elements, resulting in 64 unique transmit-receive combinations, compared to just 2 in a traditional single-element setup.

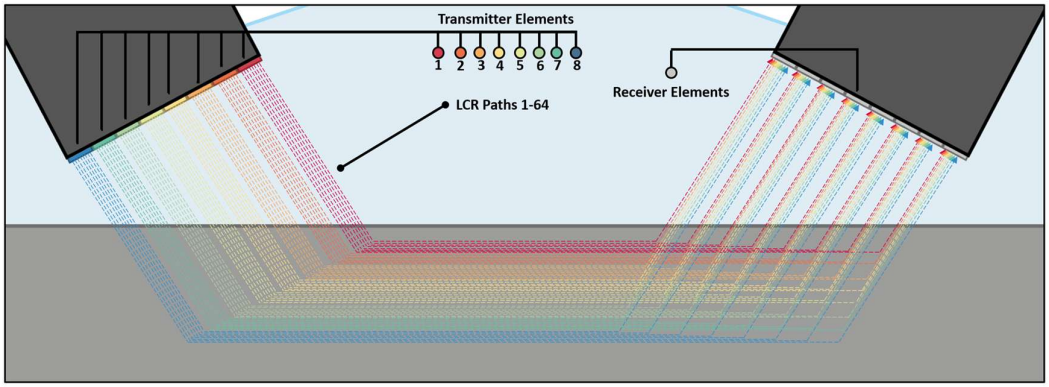


Figure 23 Schematic of LCR paths using PAURS with two 8-element transducers [66]

Although the straight-line paths in Figure 23 do not reflect the actual wavefront shapes or energy distribution shown in Figure 22, they help clarify the FMC process. This schematic highlights how each receiver element captures individual LCR waves from each transmitter, making the inspection coverage and data acquisition strategy easier to interpret. This simplified line representation will be used throughout this study to discuss the PAURS results.

4.5.7 Interpolation

A key advantage of the PAURS method is its ability to overcome the limitations imposed by conventional ultrasonic sampling rates, which typically restrict time resolution to around 10 to 20 ns. This resolution is insufficient for accurately identifying the zero-crossing point of LCR signals for reliable RS calculations. PAURS addresses this challenge by utilising FMC and interpolation across multiple acoustic paths and reducing timing errors, without the need for expensive high-speed analogue-to-digital converter (ADC) hardware.

Standard ultrasonic equipment typically samples at rates up to 100 MHz, which corresponds to a time resolution of 10 ns or more. However, RS measurements often require much finer resolution, around 1 ns, to accurately determine the zero-crossing point of the LCR signal. To overcome this, interpolation is used to estimate values between sampled points. Javadi et al. demonstrated this approach using synchronised 100 MHz equipment to achieve precise ToF measurements in austenitic stainless steel. [106]

Figure 24 shows an example of an interpolated LCR signal, where there is a 10 ns gap (using a 100 MHz sample rate) between two sampled points (from 8.05 µs to 8.06 µs). A 100 MHz sampling rate was selected as a practical compromise between hardware capability, data size, and cost. In single-element transducer setups, interpolation is based on only two points, which can introduce significant error, up to 10 ns in this case, when estimating the zero-crossing. While this may be acceptable for general defect detection, it can significantly affect the accuracy of RS measurements.

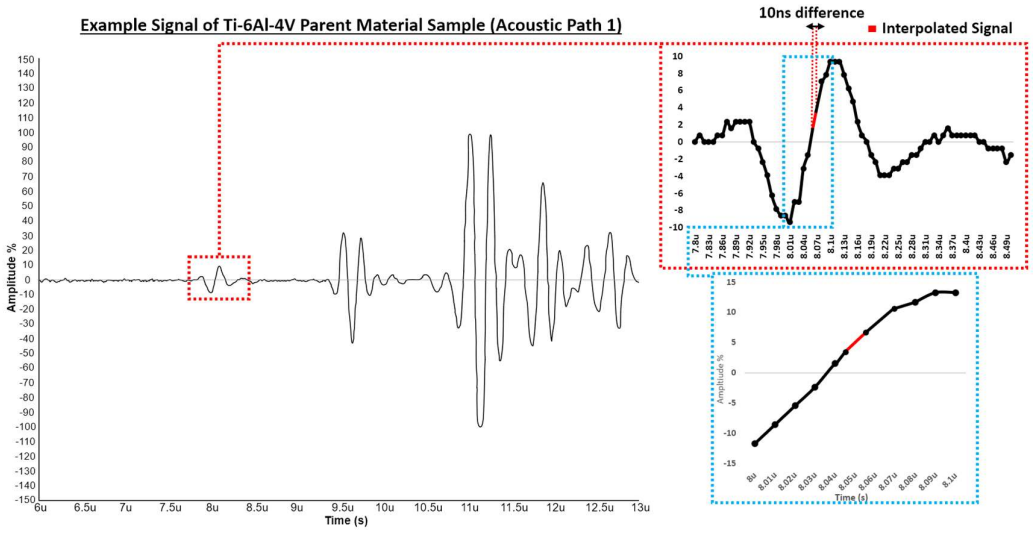


Figure 24 Example LCR signal showing interpolation in Ti-6Al-4V [66]

Interpolation was applied separately to each FMC path before path assessment and averaging. This allows interpolation to be performed 64 times, once for each acoustic path, and the results can then be averaged to reduce random error. Figure 25 presents 8 of these 64 interpolated signals, with zero-crossing times of 8.04, 8.03, 8.035, 8.03, 8.02, 8.01, 8.01, and 8.01 µs for paths 8, 16, 24, 32, 40, 48, 56, and 64, respectively. When all 64 paths are averaged, the resulting interpolated zero-crossing time is 8.023 µs. This averaging process smooths out individual interpolation errors and improves the precision of the ToF measurement. Since the theoretical ToF is identical across all paths, the averaged value provides a more accurate and reliable estimate, something that would be difficult to achieve with a single-element setup.

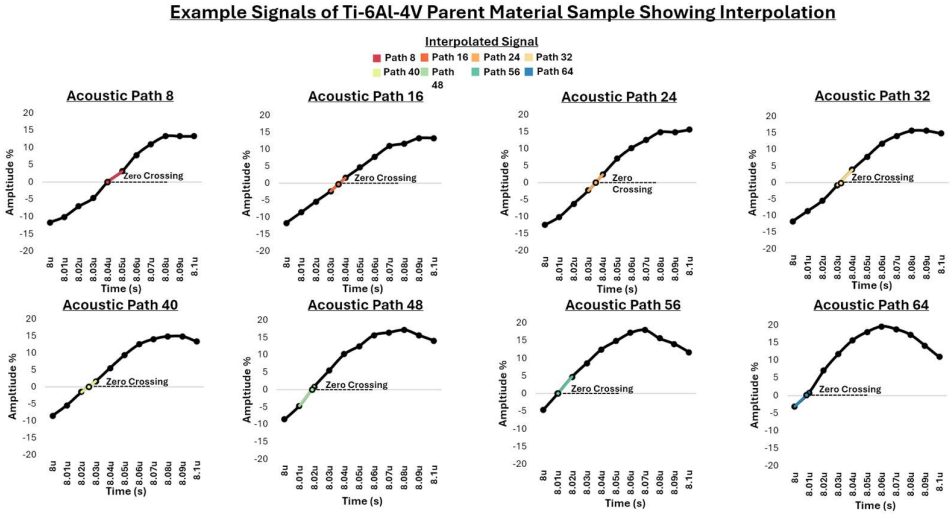


Figure 25 8 example interpolated signals from Ti-6Al-4V [66]

4.5.8 Reduction of Couplant-Thickness Effects in ToF Measurements

In order to eliminate the air gap and enable the transmission of ultrasonic energy across the interface, couplant was placed between the wedge and the specimen. The ToF that was measured includes the times taken for the ultrasonic waves to propagate through the wedge, the couplant and the specimen. Since the acoustic velocity in the couplant is different from that in the wedge and the specimen, variations in the thickness of the couplant layer can cause changes in the measured ToF even when there is no corresponding change in material stress.

The importance of this effect lies in the small amount of ToF variation caused by stress. As a result, differences in the amount of couplant, probe pressure or the way the wedge is seated between scans may be wrongly taken to indicate changes in RS. Since couplant variation is a systematic measurement effect, it cannot always be eliminated by averaging several paths. Earlier modelling and experimental studies showed that uncoupled couplant variation could lead to an RS error of about 36 MPa for the PAURS configuration under investigation. [107].

The measured ToF can be represented as the combination of contributions from the couplant and material:

$$\mathrm{ToF}_{\mathrm{meas}} = \mathrm{ToF}_{\mathrm{C}} + \mathrm{ToF}_{\mathrm{M}}$$

Equation 20 Decomposition of the measured ToF into couplant and material propagation contributions

where $\mathrm{ToF}_{\mathrm{meas}}$ is the measured ToF, $\mathrm{ToF}_{\mathrm{C}}$is the contribution associated with the coupling interfaces, and $\mathrm{ToF}_{\mathrm{M}}$is the propagation time associated with the material path. Fixed contributions from the wedge and instrumentation are omitted from Equation 20 because they remain common when the same system configuration is used.

A differential receiver approach was applied to reduce the common coupling and system contributions. For a fixed transmitting element, ToF values from two receiving elements were subtracted:

$$\Delta\mathrm{ToF}_{i,j} = \mathrm{ToF}_{i,j+1} - \mathrm{ToF}_{i,j}$$

Equation 21 Differential ToF calculated between adjacent receiver paths for a common transmitting element

where $\Delta\mathrm{ToF}_{i,j}$ is the differential ToF, i identifies the transmitting element, and $j$and $j+1$ identify adjacent receiving elements. Contributions common to the two measurements are reduced through subtraction, while the remaining value primarily represents the difference between the corresponding propagation paths in the specimen.

The same calculation was applied to the parent-material reference and the WAAM measurement. The change relative to the reference was then determined from:

$$\Delta \mathrm{ToF}_{\mathrm{rel}} = \Delta \mathrm{ToF}_{\mathrm{WAAM}} - \Delta \mathrm{ToF}_{\mathrm{REF}}$$

Equation 22 Differential ToF variation between the WAAM measurement and the parent-material reference

This procedure was applied to all the available combinations of FMC transmitters and receivers. The path-wise values thus obtained were then used in conjunction with the acoustoelastic calibration which had been determined in the experiments to calculate the RS. This procedure is demonstrated in Figure 26.

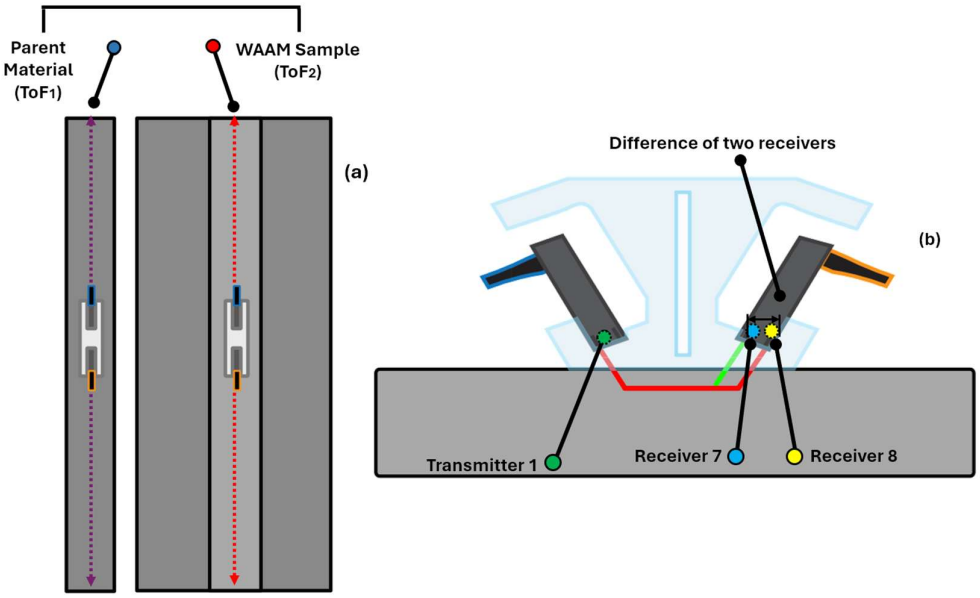


Figure 26 Couplant-thickness influence and differential ToF procedure: (a) potential variation in the coupling layer between measurement positions and (b) use of adjacent receiver paths to reduce common coupling and system contributions

During the acquisition, it was also necessary to keep a consistent application of the couplant and a steady pressure on the probe. Although the differential method reduces the effects that are common to the paired paths, it cannot ensure complete cancellation since the coupling layer may differ in various areas of the wedge. Residual variation in coupling was therefore left as a source of measurement uncertainty.

4.5.9 Acoustoelastic constant

A material-specific acoustoelastic calibration was required to convert ToF variation into stress. Calibration was performed using a representative specimen and the same ultrasonic configuration used for the corresponding measurements.

The acoustoelastic coefficient was determined experimentally because the relationship between stress and ultrasonic ToF depends on the material condition, wave mode, propagation direction, frequency

and measurement configuration. Published studies commonly determine this coefficient by applying known mechanical loads and measuring the corresponding change in LCR travel time before using the resulting relationship for stress evaluation [45, 85],

Published acoustoelastic coefficients are available for several materials and conventional ultrasonic configurations. However, no directly comparable value was identified for the specific Ti-6Al-4V phased-array LCR system used in this thesis. Values reported for other materials, frequencies, propagation directions or single-element probe arrangements were not considered directly transferable. Crystallographic texture can also affect the baseline ultrasonic velocity and acoustoelastic coefficient, further supporting calibration using a representative specimen and the same phased-array configuration used for the component measurements [86, 108].

The coefficient was therefore obtained by applying known uniaxial loads to a representative Ti-6Al-4V specimen while recording the corresponding phased-array LCR ToF. The gradient of the stress-ToF relationship provided the calibration used to convert subsequent ToF changes into stress. This experimental approach incorporated the combined response of the material, phased-array transducers, wedges, propagation direction and signal-processing procedure within a single configuration-specific calibration.

For the initial feasibility study, the parent-material region outside the deposited wall was used as the reference datum for the component measurements. This region was selected because it provided a repeatable measurement location away from the principal deposited and thermally affected regions, allowing corresponding acoustic paths to be compared using the same probe arrangement and processing workflow. However, the parent-material reference was not annealed or independently verified as having zero RS. It should therefore not be described as an experimentally confirmed stress-free condition.

An annealed reference specimen could have provided a closer approximation to a null-stress acoustic state. However, an annealing stage was not included in the initial study because the work focused on establishing the feasibility of the developing phased-array LCR technique. Consequently, the calculated PAURS values represent stress relative to the selected parent-material datum and may contain an unknown common offset if RS was present in the reference region. Differences in microstructure between the parent material and inspected regions may also contribute to the measured ToF variation.

The parent-material datum remains suitable for evaluating the relative spatial distribution of RS because it provides a consistent baseline across the component. The results from the initial study should therefore be interpreted primarily through the shape of the stress profile, the locations of tensile and compressive regions, and agreement with the distributions obtained using the reference

methods. Later stages of the methodology introduced more controlled treatment of the reference condition as PAURS and PAURS+ developed.

Absolute stress referencing would require either independent measurement of the RS in the parent-material datum or a representative specimen prepared in a verified stress-relieved condition. This limitation should be considered when interpreting the absolute PAURS stress magnitudes reported in the initial feasibility study.

Figure 27 presents a close-up schematic of the acoustoelastic testing setup, which mirrors the configuration used for the ToF measurements. The PAURS system, previously shown in Figure 22, is used identically here and clamped directly onto the sample to collect measurements at each loading interval.

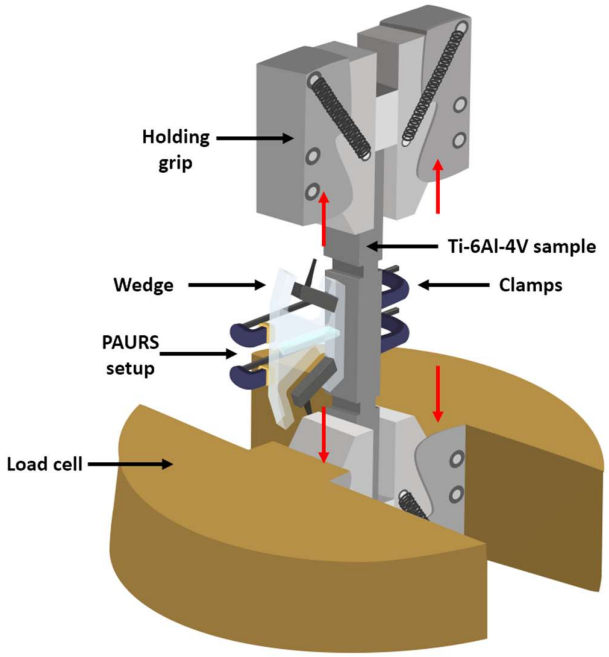


Figure 27 Close-up of the acoustoelastic constant testing setup

Similar to the ToF measurements, a PEAK MP6 system connected to a laptop running LabVIEW was used to collect the data. Initial testing was conducted to verify system functionality, applying load increments of 10 kN up to 240 kN, followed by unloading back to 0 kN. Once confirmed, the main test was performed using smaller 2 kN increments up to 250 kN, then unloaded to 0 kN. This procedure enabled analysis of how ultrasonic wave propagation through the material varied with applied stress.

Although a maximum stress of 578.7 MPa could be achieved with 250 kN, a maximum load of 200 kN was ultimately selected. This decision was based on the slotted section of the sample being only 7 mm thick, and because 200 kN was sufficient to gather the necessary data for determining the

acoustoelastic constant. During tensile testing, the machine paused at each load interval for 10 seconds to allow the PEAK MP6 to collect A-scan data.

Two eight-element phased array transducers were used, resulting in 16 data points per load step for both loading and unloading. Each data point was acquired using FMC, producing 64 acoustic paths from the 8×8 transducer matrix. Due to the large volume of data generated, the results were averaged to obtain a reliable value for the acoustoelastic constant.

Calibration is also a major step in controlling uncertainty. Because stress-induced ToF changes are small, individual ToF measurements can be affected by coupling, triggering and signal-quality variation. The phased-array configuration reduces this sensitivity by producing multiple ToF measurements at each load step, allowing the calibration response to be averaged across paths and elements.

4.5.10 Automated ToF Extraction and Stress Calculation

An automated MATLAB workflow was developed to extract the LCR ToF and calculate RS from the phased-array data. Measurement files were first ordered according to scan position. Each file contained alternating time and amplitude data for the available transmitter-receiver paths, which were processed individually before averaging.

For each acoustic path, the measured waveform was resampled onto a common time vector using linear interpolation, as expressed in Equation 23. This provided a finer numerical grid for locating the selected zero crossing but did not add new physical information to the measured signal.

$$y(t) = y_1 + \frac{y_2 - y_1}{t_2 - t_1}(t - t_1)$$

Equation 23 Linear interpolation of the ultrasonic signal amplitude between adjacent time samples.

where $y(t)$is the interpolated amplitude at time t, and $(t_1, y_1)$and $(t_2, y_2)$are adjacent measured time-amplitude samples.

The expected LCR response was isolated using a predefined temporal window selected for the material and inspection configuration. Within this window, the algorithm detected changes in signal polarity and selected the second valid zero crossing as the ToF marker. A small amplitude tolerance was applied to reduce false detections caused by low-amplitude fluctuations around zero. The same temporal window and zero-crossing number were used across corresponding paths and scan positions to ensure that the same LCR waveform cycle was selected consistently.

If fewer than two valid zero crossings were detected within the temporal window, the path was flagged as invalid and excluded from subsequent averaging. The automated procedure therefore returned a ToF value and validity status for each available acoustic path.

For the FMC analysis, adjacent receiver paths were paired for each transmitting element. Differential ToF values were calculated using the receiver-difference procedure described in Equation 21 and Equation 22 . This reduced contributions shared by the paired paths, including common wedge, system and couplant delays. A corresponding differential ToF was calculated for the selected reference condition, allowing the relative timing change at each measurement position to be determined.

The differential ToF variation was converted into a path-wise RS value using the material-specific acoustoelastic relationship introduced in Equation 7, and extended to the FMC configuration in Equation 10. The relevant elastic properties, reference condition and acoustoelastic calibration were selected for the material and experimental configuration under investigation.

The final RS value at each scan position was obtained by averaging the valid path-wise results after signal-quality assessment. Individual path values were retained to assess path-to-path variability and identify anomalous measurements before averaging. The interpolation length, temporal-window limits, path combinations and reference condition were adapted to the requirements of each study and are reported in the relevant research chapters.

4.6 PAURS+

Although PAURS is mainly designed for RS measurement, microstructure effects have to be considered because ultrasonic propagation is influenced by grain morphology, texture, phase distribution and scattering. This is particularly important in the case of AM materials, where microstructural gradients and RS gradients can coexist in the same regions.

For the WAAM Ti-6Al-4V studies, metallographic characterisation was used to relate the LCR interrogation region to the local microstructure. A transverse section of the WAAM wall and substrate was prepared using EDM sectioning, grinding, polishing and etching. Optical microscopy and montaged macrographs were then used to identify microstructural transitions through the wall and substrate. This supported interpretation of PAURS signal quality and helped assess whether the LCR path was sampling a relatively consistent microstructural region.

In Chapter 7, the characterisation of microstructures was extended using the PAURS+ framework. AFSD aluminium samples containing fine equiaxed and coarse elongated grain regions were examined using EBSD, optical microscopy and hardness mapping. These measurements confirmed the microstructural differences between regions and enabled more systematic interpretation of ultrasonic observables.

The PAURS+ framework classifies ultrasonic observables by their dominant physical sensitivity. LCR ToF was evaluated as a predominantly stress-sensitive observable, while attenuation, backscatter and frequency-domain characteristics were evaluated for their relative sensitivity to microstructural

variation. This distinction is important for future PAURS measurements in heterogeneous AM materials, where stress and microstructure may otherwise produce coupled ultrasonic effects.

4.6.1 Stress-Free Reference State for Microstructure Isolation

Sample #1, obtained by EDM sectioning alone, may be treated as macroscopically stress-relieved, as the removal of global constraint eliminates long-range Type-I RS. Although grain-scale incompatibility stresses (Type II and Type III) may persist at the intergranular and intragranular levels [6, 20, 109], such stresses do not generate a significant macroscopic stress gradient after sectioning and therefore do not influence the acoustoelastic component of LCR ToF at the scales considered here.

Sample #2 underwent EDM sectioning followed by solution treatment and artificial ageing in accordance with AMS 2770H, a process known to relax Type-I and the majority of Type-II/III RS in aluminium alloys through recovery and recrystallisation mechanisms [6, 20, 109]. As a result, Sample #2 may be regarded as macroscopically stress relieved, with significantly reduced microstructural (Type II/III) RS.

Importantly, aluminium does not exhibit solid-state phase transformations during heating or cooling, in contrast to ferritic steels where fcc–bcc/bct transformations generate transformation strains that dominate the RS field [109]. Because phase-transformation misfit does not occur in aluminium, and neither sample experienced significant thermal gradients after sectioning nor heat treatment, both samples constitute macroscopically-stress-relieved states for isolating microstructural influences on ultrasonic observables. At the near-surface LCR sampling depth, any remaining Type-II/III stresses operate over length scales far smaller than the ultrasonic wavelength and therefore are expected to contribute negligibly to LCR ToF, which is governed primarily by macroscopic acoustoelastic effects.

The specimens used in this study were extracted using EDM following procedures consistent with CM sample preparation, ensuring minimal introduction of additional plastic deformation [77]. For the annealed condition, a stress-relief heat treatment was applied in accordance with established practice for aluminium alloys [100], providing further reduction of macroscopic RS. CM measurements performed as part of the broader study (not included here due to scope constraints) confirm low RS in the as-cut condition and negligible macroscopic stress following heat treatment.

4.6.2 Ultrasonic setup

Ultrasonic measurements were conducted on two distinct microstructures, FEG and CEG, using Phased-array LCR ultrasonics, and phased-array pulse-echo ultrasonics. ToF was evaluated in both modes to verify the absence of macroscopic residual-stress-induced velocity changes. Additional observables (attenuation, backscatter, and frequency-domain response) were extracted to characterise microstructural influences under nominally stress-free conditions.

*Figure 28*a illustrates the pulse-echo inspection arrangement used for Sample #1. A 10 MHz, 16-element phased-array transducer with an element pitch of 0.25 mm (Imasonic, France) was driven by a phased-array controller (PEAK NDT, UK), with all data acquisition performed in LabVIEW. Measurement locations consisted of nine points across the AFSD deposit and eight points across the substrate. All measurements were acquired in side-inspection through-thickness mode, where waves travel through the full 8 mm thickness and reflect from the backwall (*Figure 28*c). Successive backwall echoes were compared to minimise variability in coupling conditions, a standard practice for pulse-echo attenuation and backscatter evaluation.

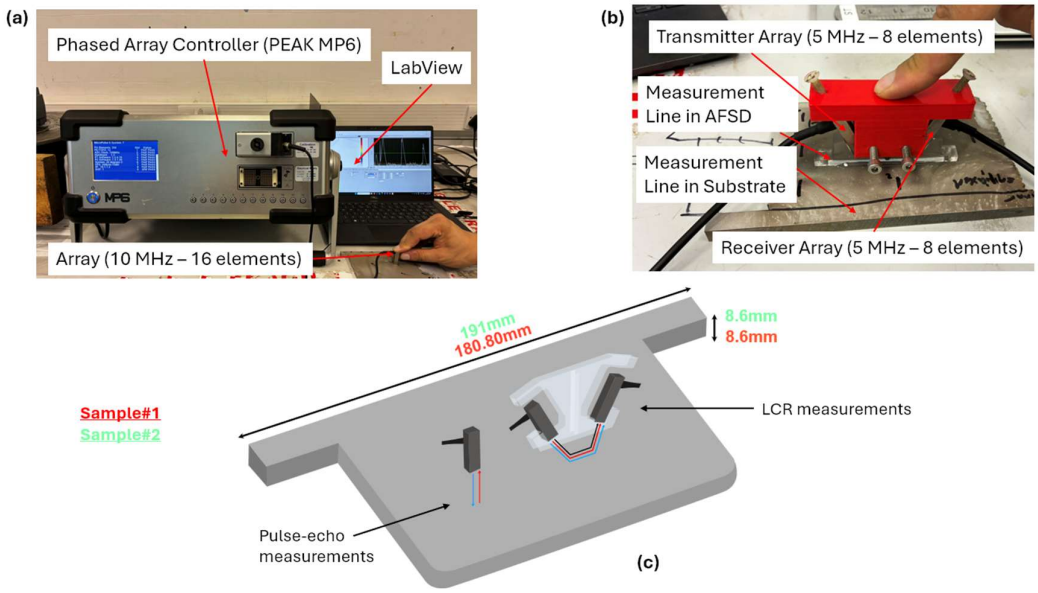


Figure 28. (a) Pulse-echo setup for Sample #1 using a 10 MHz, 16-element phased-array transducer; (b) LCR setup for Sample #2 using two 5 MHz, 8-element phased-array transducers and (c) Positioning of pulse-echo and LCR probes on the sliced AFSD samples [101]

*Figure 28*b shows the LCR testing arrangement for Sample #2 (and equally applies to Sample #1). The LCR arrangement exploits the first critical angle to produce a critically refracted longitudinal wave propagating parallel to the surface. In the present study, the same PAURS configuration used by Mills et al [65] is employed for microstructure characterisation. LCR waves were generated and received using two 5 MHz, 8-element phased-array transducers, with an element pitch of 0.5 mm, mounted in a side-inspection configuration (*Figure 28*c). The effective near-surface LCR sampling depth is approximately 1.2 mm, as experimentally quantified by Mills et al [65] for the same transducer frequency, wedge geometry, and inspection configuration. Because the present work employs an identical PAURS setup, the same sampling depth applies. While the experimental arrangement is identical to that used for RS measurement, the analysis here focuses on attenuation, backscatter, and frequency-domain observables.

- Pulse-echo and LCR modalities interrogate different effective depths (*Figure 28*c):
- Pulse-echo averages the response through the full thickness (8 mm).
- LCR samples a near-surface depth of approximately 1.2 mm, making it more sensitive to microstructure in that region.
- This difference in sampling volume complements the observable-level separation between ToF (stress-sensitive) and amplitude/FFT metrics (microstructure-sensitive).

Sequential measurements on AFSD and substrate regions introduce couplant variability, particularly affecting amplitude-based observables such as attenuation and backscatter. To mitigate this, two calibrated shims were used during LCR measurements to maintain a consistent couplant thickness across all acquisitions (Figure 29). Each measurement location was acquired with a minimum of three repeated FMC acquisitions under identical gain and delay-law settings to assess repeatability and suppress coupling-related variability. For pulse-echo measurements, couplant effects were suppressed by normalising successive backwall echoes, which reduces sensitivity to coupling-layer variations. The arrival time was measured between two successive backwall echoes within the same A-scan rather than from the initial interface echo. This intra-signal differential ToF suppresses the influence of couplant layer thickness and wedge/interface delay because these contributions are common to both echoes and cancel. In the LCR configuration, no equivalent second LCR arrival is available within the same A-scan; therefore, to reduce sensitivity to common coupling and wedge delay, the analysis compares the path-span difference between the earliest and latest phased-array LCR arrivals (T1R1 and T8R8) within each acquisition and then compares that path-span metric between FEG and CEG under the same delay law.

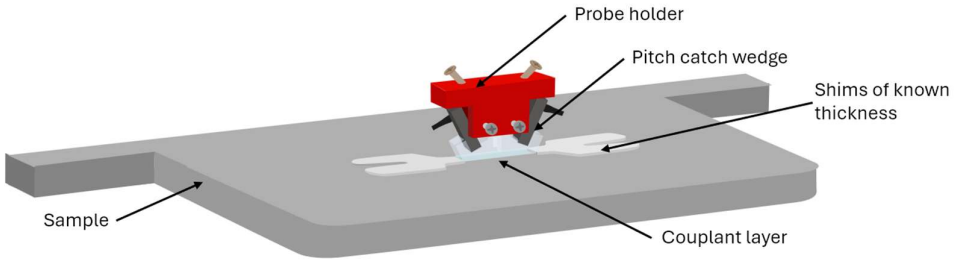


Figure 29. Use of calibrated shims to maintain consistent couplant thickness during LCR measurements [101]

The AFSD aluminium samples shown in Figure 5 were used in Chapter 7. These samples were not selected primarily for high RS, but for their controlled microstructural variation. The AFSD process produced regions of fine, equiaxed grains and coarse, elongated grains, enabling comparison of ultrasonic ToF, attenuation, backscatter, and frequency response across distinct microstructural zones. These samples, therefore, provided the basis for developing the PAURS+ interpretation framework.

Samples were typically selected to test PAURS across two manufacturing methods and contexts. Firstly, RS measurement in WAAM Ti-6Al-4V, followed by microstructure-aware ultrasonic interpretation in AFSD aluminium. Detailed manufacturing procedures are given in the respective chapters of the study; here, only the essential information is given to understand the common experimental framework.

4.7 Data Quality Assessment

Data quality assessment was built into the PAURS workflow because the acoustoelastic effect produces small ToF changes, making it sensitive to experimental error. The main sources of PAURS measurement variability are coupling variation, triggering instability, surface condition, wedge positioning, low SNR, mode interference and microstructural heterogeneity.

In the direct-element approach, stress was calculated for each element pair and compared with the element-averaged result. Outliers were found in the case of the measurements that deviated significantly from the overall trend. This element-wise comparison was important in Chapter 5, because it showed that individual paths or elements could produce anomalous values, but phased-array averaging could diminish their effect on the final RS profile.

In the FMC-based implementation, the number of acoustic paths increased to 64 per scan position. This provided a broader basis for assessing path-to-path consistency because path-to-path consistency could be assessed statistically. SNR was calculated within defined time windows to assess the reliability of the LCR signal relative to background noise or interfering arrivals. paths meeting the defined exclusion criteria were flagged and excluded before averaging.

This is especially true in the HAZ and weld regions, where surface conditions, geometry, and microstructure can all degrade signal quality. Therefore, the final PAURS stress profiles were calculated on corrected and filtered path sets and not on raw paths without differentiation.

The use of FMC also provided a quantitative basis for uncertainty reduction. In the FMC implementation, each scan position contained up to 64 transmit–receive paths rather than only matched element pairs. This allowed the spread of path-wise ToF or stress values to be assessed at each location. In addition, interpolation was required because the 100 MHz acquisition rate corresponds to a raw sampling interval of approximately 10 ns, which is larger than some stress-induced ToF changes. These numerical checks were used before the final uncertainty interpretation.

4.8 Uncertainties

Measurement uncertainties vary across the RS evaluation techniques used in this study. For the CM, uncertainty primarily arises from surface displacement measurement and FE reconstruction, with typical values reported as ±20-30MPa for titanium and high-strength alloys [81,26]. For XRD, using the $\sin^2\psi$ method, errors are generally ±10-20MPa, influenced by peak fitting and elastic constant accuracy

[79,110]. For PAURS, uncertainty depends on ToF resolution and acoustoelastic constant determination; studies on Ti-6Al-4V WAAM components report values of approximately ±25-40MPa after FMC averaging and outlier removal [61,65].

The elastic modulus, E, and Poisson's ratio, ν, used in the CM reconstruction are bulk elastic properties assigned to the linear-elastic FE model. XRD also requires elastic parameters to convert measured lattice strain into stress; however, XRD uses diffraction elastic constants associated with the selected crystallographic plane. These may differ from the bulk properties used in CM because the diffraction measurement represents grains satisfying a specific diffraction condition and can be influenced by crystallographic anisotropy and texture. Differences between the elastic parameters used by CM and XRD may therefore contribute to discrepancies in the calculated stress magnitudes. A systematic assessment of this effect was outside the scope of the thesis, but it was considered when interpreting comparisons between the two methods.

Uncertainty is treated through both experimental design and interpretation of results. ToF extraction, acoustoelastic calibration, couplant thickness variation, wedge positioning, signal quality, microstructure and the finite LCR interrogation depth are the main sources of uncertainty for PAURS. These factors affect the accuracy of the calculated stress values and should be considered when comparing PAURS with reference methods.

Several procedures reduced the uncertainty of the PAURS. First, phased-array acquisition provided multiple acoustic paths, instead of a single LCR measurement. Second, the number of acoustic paths available was increased to 64 per scan position, allowing for averaging and outlier rejection. Third , the accuracy of the ToF was improved by interpolation over the raw sampling interval. Fourth, differential ToF correction was applied to minimise the timing variation due to the couplant. Finally, unreliable signals were filtered by means of SNR and path-consistency checks before the final stress calculation.

Thus, the comparisons in this thesis are interpreted in terms of measurement compatibility. A quantitative comparison is more meaningful when the PAURS and reference methods sample similar depths and stress components. If the methods differ considerably in either depth or gauge volume, the comparison is made in terms of stress trends, peak locations and relative changes between processing conditions.

Chapter 5: Study 1: WAAM Ti-6Al-4V PAURS Feasibility Study

5.1 Introduction

5.1.1 Ultrasonic Phased Arrays for RS Measurement

In their paper on the development of a PAUT-LCR system for RS measurement, Javadi et al. carried out a feasibility study for measuring RS in WAAM samples [111]. In their method, the Longitudinally Critically Refracted (LCR) ultrasonic technique was used as the goal was to measure stress in the bulk areas of the samples. However, this study extends the previous feasibility study by applying phased-array ultrasonics to calculate RS in WAAM samples and comparing the results with CM.

Although PAUT RS measurements were introduced by Javadi et al. [111], they did not go further than a feasibility study, and results were not produced as only ToF variations caused by RS were discussed, not final RS measurements. While Javadi et al. [112] and Mills et al. [113] used similar principles for the measurement of bolt stress using phased array ultrasonics, they did not use them for RS measurement in WAAM components. The microstructures of the weld and WAAM, as well as the HAZ, bring more challenges in RS measurement than in the stress measurement of bolted connections. In this study, phased-array ultrasonic testing is applied to RS measurement in WAAM components, extending previous feasibility work from ToF variation toward calculated RS profiles.

In the feasibility study carried out by Javadi et al. [111], they anticipated that the increase in the number of acoustic paths generated from their setup would therefore increase the measurement accuracy when compared to a traditional setup that generates two acoustic paths from three single-element transducers. As this was only a feasibility study, a comparison between the two methods was not made, but this increased data redundancy and measurement consistency was one of the focus areas of this study.

However, one of the main disadvantages of PAUT RS measurement, described by Javadi et al., is the issue of average data measurement. The average of the RS affected by the wave travel path, rather than point-based measurements, is measured. Therefore, when measuring RS at specific depths, it can include both bulk and surface stress data, and due to the rapid change in RS in WAAM components, the overall measurements are affected. Increasing the number of measurement frequencies in the method is one way to mitigate this issue. Another important factor to consider is the size of the probe. Larger arrays, due to the averaging issue, have problems measuring RS due to the sharp gradients within WAAM components. As a result, small-footprint arrays are the best alternative for WAAM RS measurements using PAUT.

In their paper on the development of the PAUT RS measurement system [111], Javadi et al. describe that another one of the main disadvantages of the ultrasonics method is that the ultrasonic wave is influenced by both the material texture as well as RS, making it difficult to differentiate between them. Also, in comparison to other RS measurement methods, only the average of RS is measurable using the ultrasonics method, limiting the method's selectivity.

5.2 Results and Discussion

As described previously, RS measurements were collected using the CM and PAUT methods as seen in the FE model in Figure 30, which was created using the CM. Scan lines were determined that can be used to measure the RS in specific areas of the sample using the phased array ultrasonics method. As the purpose of this study was to demonstrate the ability for WAAM RS measurement using the phased array setup, the scan area for the comparison of data for these results was focused on the Lc scan line. In the figure showing the FE model, the Lc scan line at the bottom of the sample can be seen to contain a high amount of RS. Therefore, by choosing this area, an easy comparison can be made between the phased array and CM results. The Lc scan line was also chosen as the penetration depth of the 5MHz transducers used was measured to be 1.2 mm, which was equivalent to the Lc line in the CM results, as that line also showed the data at 1.2 mm.

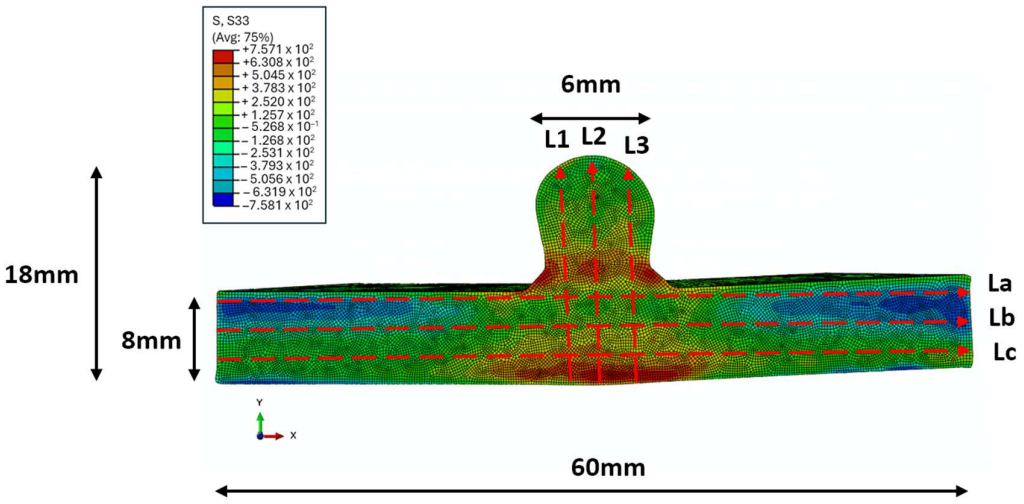


Figure 30 CM FE model with proposed scan lines for RS measurement in Ti-6Al-4V WAAM samples. [61]

Towards the centre of the bottom of the sample, the highest amount of RS was present where RS remained high but was slightly lower within *Zone 2*. As seen in the CM results shown in Figure 31, the stress gradually increased to a peak of 400 MPa at 30 mm along the substrate. The stress then began a gradual decline to the lowest point of −150 MPa at 55 mm along the substrate and then increased again to 100 MPa between 55 and 60 mm.

There were a few anomalies found in the CM data. As seen in Figure 31, between 0 mm and 1 mm there was a slight spike in stress from −200 MPa to −150 MPa, which then decreased again to −200 MPa before increasing gradually along the substrate as mentioned before. A similar occurrence happened between 45 and 60 mm, where stress increased and decreased several times towards the end of the substrate.

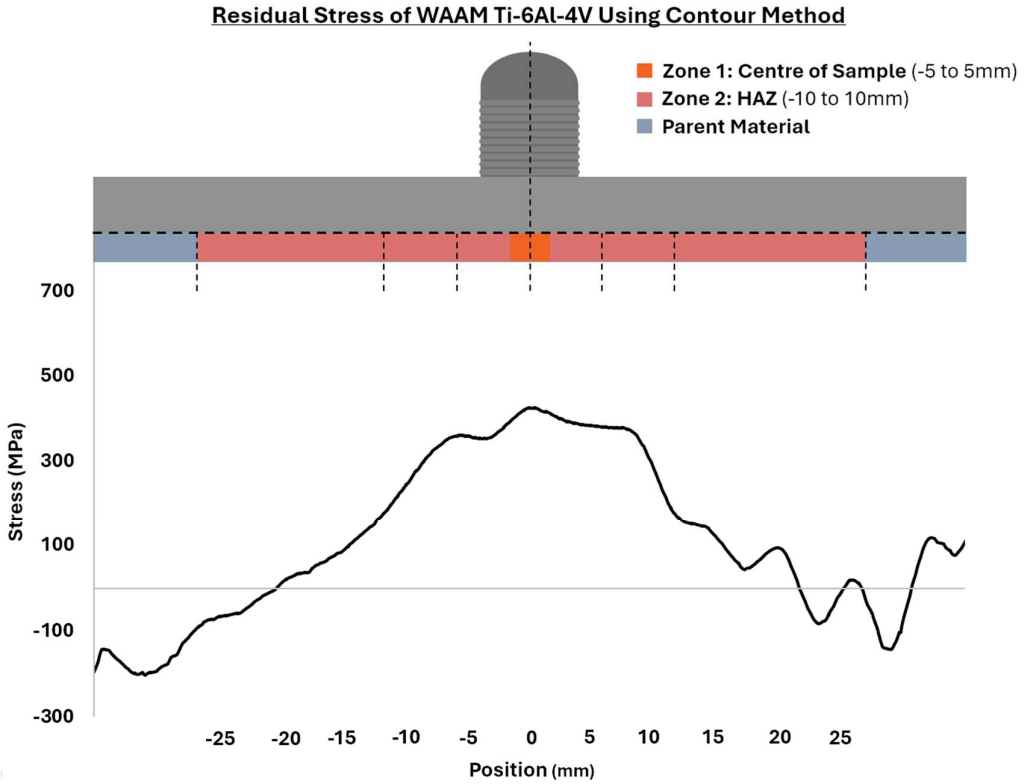


Figure 31 CM RS measurement results. [61]

Another factor that stood out from the CM results was the overall shape of the data. We would expect, from RS measurements carried out on the WAAM sample, that the shape of the graph would be symmetric due to the overall manufactured shape of the sample. There were a few possibilities to explain this unexpected graph shape. One was that the shapes of the WAAM samples that were being tested had a slight bow to them and were not completely flat; a visual representation of this bowed shape can be seen in the cross-sectional geometry in Figure 32, created using a laser scan where the bottom of the WAAM sample can be seen to not be flat. The slight distortion during the production process was due to the stress on the sample during the manufacturing process, and this could have affected the stress values as the distortion of the sample relieved some stress. It is believed that this distortion did not interfere with the ToF measurement for two reasons. (I) the distortion resembled angular shrinkage rather than buckling, which could have affected surface flatness. This was studied

by Satarri-Far and Javadi [106], who found that distortion on welded pipers did not affect the final RS measurements when comparing the FE results and the experimental data. It should be noted that surface flatness can influence ToF measurement, especially if the width of the PAUT wedge is too wide to account for surface deformations. (II) The width of the PAUT wedge was 8 mm, which made it significantly narrower than any potential surface deformation on this sample.

Efforts were carried out to prevent the distortion of the sample as much as possible. The substrate was flat before deposition and six clamps were used with each side of the substrate having three clamps placed evenly in the longitudinal direction, creating a symmetrical clamping condition.

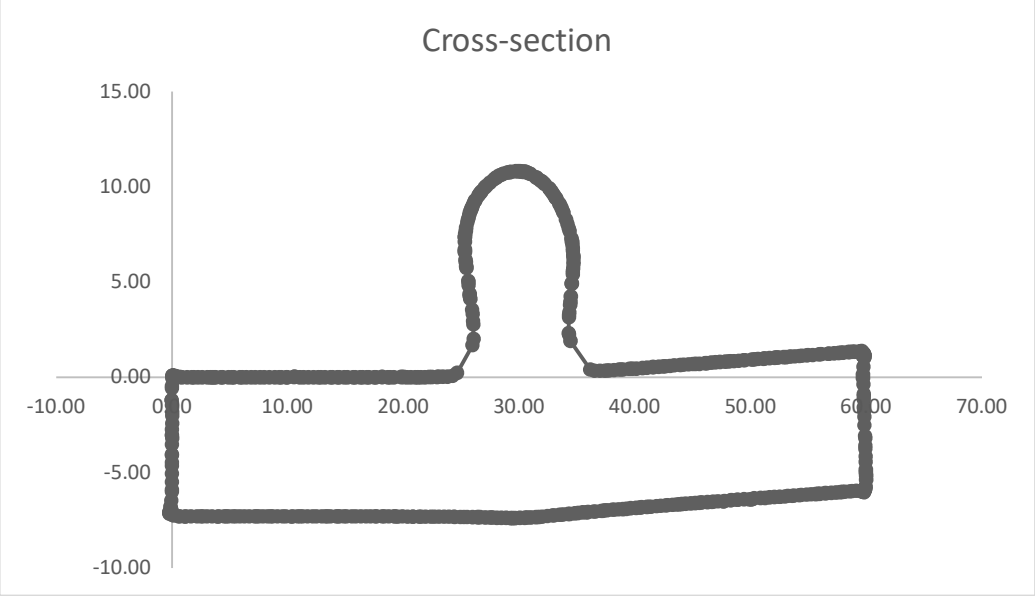


Figure 32 Cross-section of the WAAM sample. [61]

Shown in Table 3 are the results from the Snell's-law experiment to find the correct angle for the wedge for use with Ti-6Al-4V when collecting phase array ultrasonics measurements. From these results, the average difference in gain from the Snell calculated angle wedge could be compared against the wedge angle for titanium. These wedge angles were tested between 22.2 and 23.2 degrees as these are the approximate angles for the first critical angle level when using LCR waves with titanium alloys as a material. Therefore, by measuring within this area, a specific wedge angle degree could be found that was most suitable for the RS measurements.

From these results, the most important thing to consider is that the lower the average difference in gain is, the more suitable the wedge is for titanium, as less gain is required to reach the required amplitude necessary to collect the ToF measurements, ensuring that they are accurate.

As seen in Table 3, the lowest values were found at 22.6 and 22.7 degrees, and therefore, both wedge angles were suitable for ultrasonic phased array testing in Ti-6Al-4V samples; ultimately, a 22.7-degree wedge was chosen for this study.

Table 3 Average difference in gain relative to Snell-calculated angle wedge vs. wedge angle for titanium.

Wedge Angle (Deg)	Average Difference in Gain from Snell Calculated Angle vs. Wedge Angle for Titanium (dB)
22.2	14
22.3	8.5
22.4	1
22.5	5.5
22.6	0
22.7	0
22.8	11
22.9	4.5
23	4
23.1	14.5
23.2	11.5

To measure the acoustoelastic constant, tensile testing was carried out, with stress increments in both loading and unloading modes, and the results are shown in Figure 33 and Figure 34, respectively. Since two eight-element arrays were used, the results have been presented per element. For example, Element 4 shows the ToF is measured for the acoustic path between Element 4 of the transmitter array and Element 4 of the receiver array. Although there are a total of eight graphs produced (per element), a selection of three notable graphs are chosen here, along with the mean.

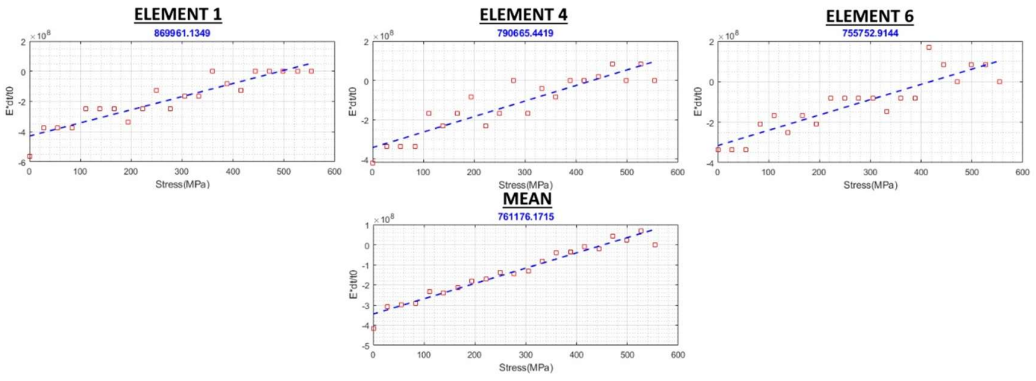


Figure 33 Loading/ascending acoustoelastic constant graphs [61]

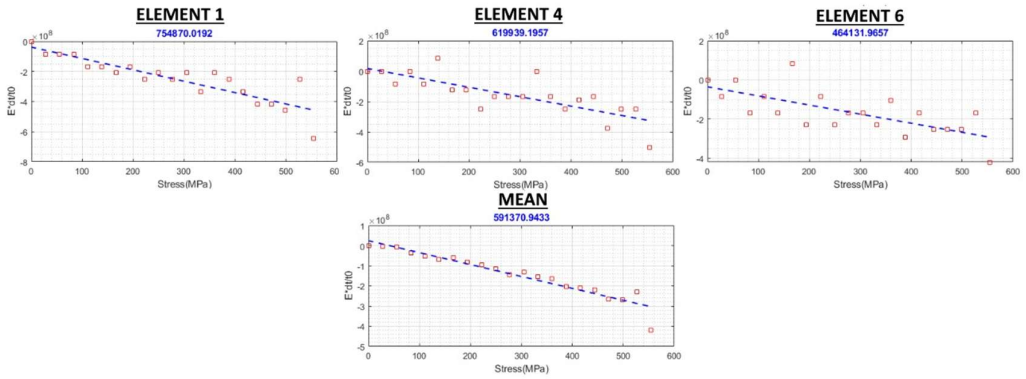


Figure 34 Unloading/descending acoustoelastic constant graphs [61]

The vertical axis shows the Exdt/t0, so the slope of each of these graphs represents the acoustoelastic constant, L_{11}, in Equation 7. However, the final acoustoelastic constant can be calculated by considering all 16 graphs presented in Figure 33 and Figure 34 using Equation 8. Since it increases with increasing stress and decreases with decreasing stress, the loading and unloading graphs are ascending and descending, respectively. However, several points do not follow this general trend. For instance, in Element 6 in Figure 33, there is a spike at around 350 MPa, followed by an unexpected decrease at the next point. This issue can be attributed to one of the ultrasonic RS measurement system errors discussed by Javadi et al. [111] such as in the couplant film thickness, a triggering error, or a tensile-testing machine error. However, it is important to note that the acoustoelastic constant would have been measured using all 200 (the number of data points in each graph) × 16 data points collected during the tensile testing process, which reduces the influence of individual anomalous measurements, although systematic errors may remain. This is one of the main advantages of a phased array over a single-element ultrasonic system, where only one of these graphs (instead of sixteen) would have been generated. Although a single averaged graph can be generated by using the ultrasonic phased array system, by generating 16 individual graphs, any anomalies/errors can be spotted and considered for the final RS results. However, with a single-element ultrasonic system, the singular graph could potentially contain errors without the ability to compare them to the average trend of the results to spot them.

Using the acoustoelastic constants, the final phased-array WAAM RS measurements could be created. Once the RS measurements were collected for each element of the phased array transducer, these measurements could then be averaged to produce a single set of RS measurements. it was important to assess the consistency of the path-wise results. To find these outliers, the variance between the RS measurements of each element and the averaged results were calculated using Equation 24.

$$Variance = \frac{(Element\ \sigma\ Measurement - Averaged\ \sigma\ Measurement)}{Averaged\ \sigma\ Measurement}$$

Equation 24 Formula used for calculating the variance between per-element results and the average of results at each point

This formula was carried out for each of the eight elements, however for the purpose of demonstrating how the outliers were calculated and chosen, the four most notable elements are shown in Figure 35.

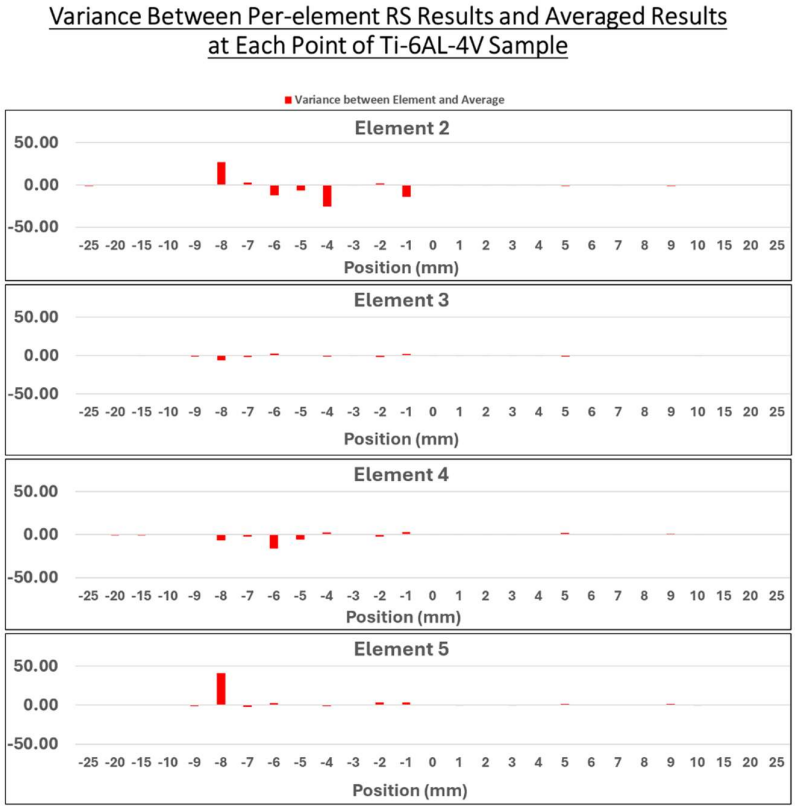


Figure 35 Calculated variance between each element's RS measurement and averaged results [61]

Any drastic difference between the RS measurements of each element and the averaged results could be visually seen and removed to flag for assessment before calculating the average. To ensure the consistency of the chosen outliers, measurements with a variance of 5 or above were flagged as potential outliers using the selected empirical criterion, as can be seen at −8 mm on Element 3. Element 2 most notably had the most outliers, with five measurements identified as outliers, indicating that this element showed greater deviation from the element-averaged trend. Element 4 also had numerous outliers, with three identified. These outliers for the individual element results could be attributed to the normal ultrasonic stress measurement errors that were reported by Javadi et al. [111] when using the conventional single-element technique for LCR RS measurements.

Figure 36 presents the RS measurements obtained from each transmitter-receiver element pair at a depth of 1.2mm. The red markers identify measurements flagged as outliers using the variance criterion described above. These points were excluded when calculating the filtered average because they showed unusually large deviations from the corresponding element-averaged values. However, their exclusion does not materially alter the overall RS distribution or the location of the central tensile-stress peak. The main benefit of the filtering is therefore the removal of isolated anomalous measurements rather than a substantial change in the interpreted stress profile.

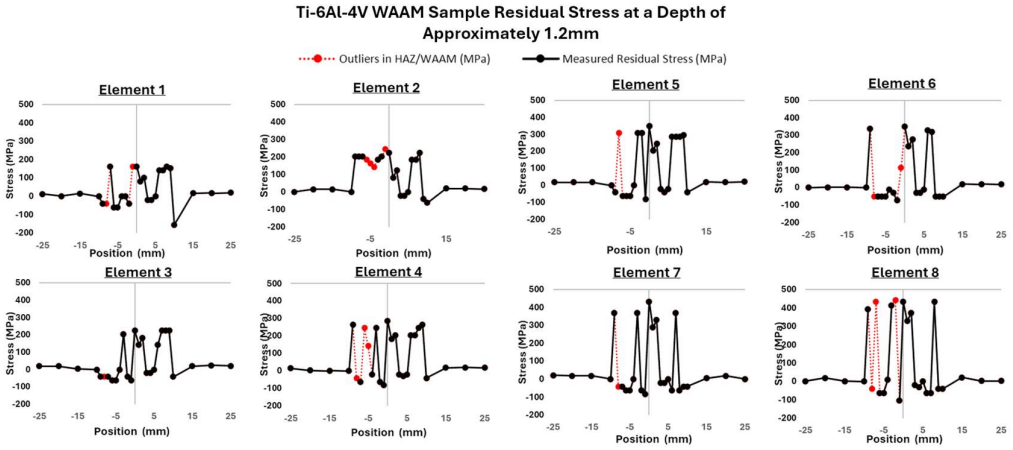


Figure 36 Per-element stress distribution across WAAM sample results [61]

When considering the outliers and overall shape of the results of each element, Element 2 is most noteworthy as it displayed a very different RS distribution when compared to the rest of the elements. Elements 3 and 7 showed the closest agreement with the element-averaged trend and contained relatively few flagged points. In all the measurements, the overall RS distribution was as expected as represented by the zones illustrated in Figure 18. Outside of the HAZ (−10 to 10 mm), a low RS was measured at ~0 to 20 MPa, and when measured at the start of the HAZ, the RS spiked and was measured at ~200 to 300 MPa in all elements, which occurred on both sides of the HAZ. In all elements, peak RS was measured at 0 mm, which had been expected. However, within the HAZ, all the elements displayed a similar drastic drop in the RS at both sides of the HAZ from ~0 to −150 MPa.

These drops in the RS and other outliers could have been due to similar issues during the measurement process mentioned previously for the acoustoelastic results discussed by Javadi et al. [111] such as the triggering of errors, the couplant film thickness, or small angle variances with the array wedge. These factors are difficult to control during an experimental process, but future work can be controlled to mitigate their impacts. For example, a phased array experiment using arrays with higher numbers of elements allows for better control and reassurance in identifying the potential outliers.

To create the final averaged results for the RS of the WAAM Ti-6Al-4V sample using the phased array ultrasonics method, ToF measurements were used alongside the calculated acoustoelastic constant, and these results are shown in Figure 37.

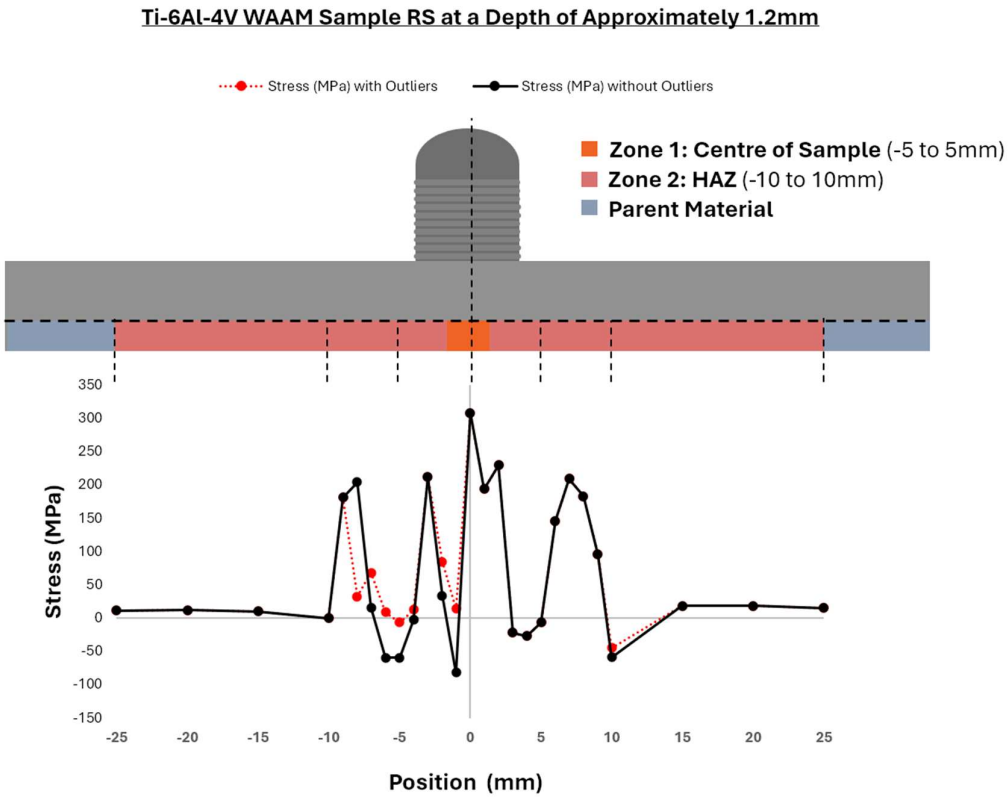


Figure 37 Results of the RS measurement using the phased array ultrasonics method [61]

These measurements have been shown at a depth of 1.2 mm due to the effective depth of the phased array ultrasonics equipment. These results are averages of the per-element results taken from each of the eight elements in the phased array transducers. The red line represents the actual stress measured and includes the outliers that were previously identified in the per-element results in Figure 36, and the black line removes these outliers. As can be seen, excluding the flagged points produced a slightly more symmetric profile, although the overall RS distribution remained largely unchanged.

These results follow a similar trend to the per-element results, as expected, with lower RS measurements outside of both Zone 1 and Zone 2, where less heat is present during the manufacturing of a sample. However, the RS increased from −10 mm until Zone 1, where the sample was most affected by heat, and there was a vast increase in the RS. From −5 mm, RS increased to ~220 MPa and peaked at 0 mm to ~310 MPa, where heat was most prevalent during fabrication. As discussed previously for the per-element results, there was a drop in RS measured on both sides of the HAZ at both between −7 and −4 mm, where RS dropped to ~60 MPa, and between 3 and 5 mm, where RS dropped to -27

MPa. Another significant drop in RS was measured at −2 mm at ~−80 MPa. These drops in RS in the HAZ could sometimes be expected within this area of the sample or could be attributed to the issues during the measurement process discussed for the per-element results. Also, the overall trend of the data was not perfectly symmetric. However, this had been expected, as the shape of the sample was slightly distorted, as shown in Figure 32.

To create the averaged phased array results from the per-element measurements, it was important to consider the outliers found in the per-element measurements. To average correctly, we needed to divide the sum of the black points (measured RS) by the number of points as shown in Equation 9. However, instead of simply considering the number of elements used, we needed to consider the number of elements minus the red points shown in the per-element results (outliers in HAZ) for the specific point being considered. For example, some of the measurements only had a single outlier/red point, such as Elements (3), (5), and (7), so we summed the black points and divided the resulting value by seven.

Doing this allowed for the averaging of the measurements rather than relying on single-element measurements. Javadi et al. [111] anticipated that the increased acoustic paths from the LCR approach with phased arrays would increase the measurement accuracy when compared to using just two acoustic paths from the three single-element transducers in the traditional method. Although not used in this study, this phased array ultrasonic setup can also be utilised with FMC to create many more data. By using the two eight-element arrays for this study, a potential 8 × 8 matrix of 64 LCR wave paths could be generated, increasing measurement accuracy. Also, with the ability to produce eight sets of RS measurements, the amount of data was increased, and if arrays with a higher number of elements were used, this same setup could be used to produce even more data. This is especially important if problematic elements, such as Element 2, are identified, which would have affected the accuracy of the averaged results. With a higher-element array, the impact of these problematic elements would be reduced.

5.3 Comparison of Results

Figure 38 shows a comparison between the CM results and the phased array ultrasonic results. Comparing the averaged phased array ultrasonics results in Figure 37 with the CM results in Figure 31, shown in Figure 37.

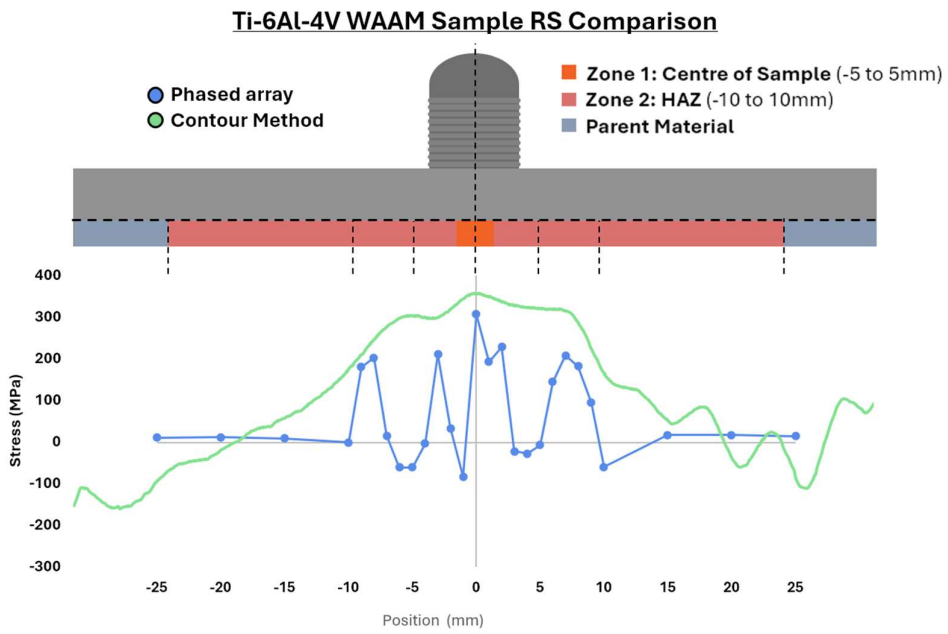


Figure 38 Comparison between phased array and CM RS measurements [61]

The phased-array data provided element-wise redundancy for identifying anomalous ultrasonic measurements. CM involves different processing and uncertainty considerations. The CM results showed a measurement of −200 MPa on one end of the sample at 0 mm and 100 MPa on the other end of the sample, showing that there was a large disparity in the measured RS outside of the HAZ. On the other hand, the phased array ultrasonics results showed a more symmetrical distribution of stress with RS measured similarly on both ends of the HAZ at ~20 MPa on each side. Both the averaged phased array and the CM results measured a similar peak RS at 0 mm, with the CM measuring it at ~420 MPa and the phased array measuring it at ~310 MPa.

Within the HAZ, the stress distributions were similar in both results, with a slightly lower RS on one side of the area. These low RS measurements were flipped for the averaged results; however, this was due to the CM being scanned the opposite way. Although both results displayed a slightly asymmetric trend due to the shape of the WAAM sample, the non-symmetry was much more apparent in the CM results.

Set side by side, the averaged phased-array profile showed closer qualitative agreement with the broad CM distribution. As previously discussed, the CM results represent a clear increase in RS at the HAZ between −10 and 10 mm with the highest RS expected to be between −5 and 5 mm. When comparing the shapes of the RS distributions, the phased array ultrasonics results align well with this increase in RS, which can be presumed to provide support for the qualitative consistency of the measured distribution.

Comparing the per-element results with the averaged phased array ultrasonics results, the averaged profile shows reduced sensitivity to individual anomalous element measurements. By having the ability to compare the RS measurement of each element with the averaged results, potentially anomalous measurements can be flagged before averaging, reducing the influence of individual path deviations. Problematic elements, such as Element 2 in Figure 35 and Figure 36, can also be recognised when one is able to compare the RS measurements of the element with an averaged set of data. These findings motivated the implementation of FMC in the subsequent study.

5.4 Conclusions

In this study, an investigation for a phased array ultrasonic system for the RS measurement of WAAM Ti-6Al-4V samples, compared with the CM, was carried out. Tensile testing was also conducted for both loading and unloading with 200 load increments to measure the acoustoelastic coefficients of WAAM Ti-6Al-4V as the parent material for calibration to use for the discussed ultrasonics method.

The initial study established the feasibility of phased-array LCR measurement for identifying the principal RS distribution in WAAM Ti-6Al-4V. However, it did not independently quantify the contribution of microstructure to the measured ToF. Further work is therefore required to determine whether changes in grain morphology and texture could be distinguished from stress-induced velocity changes.

From the results, the following can be concluded:

- A Snell's-law-based study identified 22.7° as the optimum wedge angle for generating LCR waves in Ti-6Al-4V.
- Phased-array ultrasonics demonstrated potential for non-destructive and repeatable assessment of the RS distribution
- Element-wise measurements enabled anomalous points to be identified. However, excluding these points had only a minor effect on the overall averaged RS profile.
- The direct phased-array approach produced eight measurement sets, providing greater data redundancy than a single-element setup.
- Quantitative agreement with CM was limited, with peak stresses of approximately 310 MPa from ultrasonics and 420 MPa from CM. Nevertheless, both methods showed a similar RS distribution, including elevated tensile stress near the centre of the HAZ.
- Overall, phased-array ultrasonics is a promising approach for non-destructive, repeatable RS assessment in WAAM Ti-6Al-4V, although further validation and FMC implementation are required.

Chapter 6: Study 2: WAAM Ti-6Al-4V Inter-pass Peening Study

6.1 Introduction

The main aim of this study is to build upon the studies carried out by Javadi et al [114], Walker et al [61], and Mills et al [65], and to assess the feasibility and reliability of PAURS for RS measurement in WAAM Ti-6Al-4V components. To validate PAURS, its results are compared against those obtained from CM and XRD. Three samples were measured: an as-deposited sample, an inter-pass peened sample, and a post-peened sample. This allows for both the evaluation of inter-pass peening as a RS mitigation method and the validation of PAURS as a RS measurement technique. The findings contribute to the goal of enabling in-process RS inspection in metal AM.

6.2 Results and Discussion

6.2.1 Microstructure Study

6.2.1.1 Material Preparation

Although the focus of this study is RS rather than microstructure engineering, ultrasonic interpretation is influenced by grain morphology, texture, and α/β distribution. Extensive literature has shown that elongated or textured microstructures increase ultrasonic scattering and attenuation, while equiaxed regions exhibit weaker backscatter and lower frequency-dependent loss ,[68, 115–118]. To confirm that the WAAM-built Ti-6Al-4V wall used in this study exhibits a representative microstructure, a cross-section was prepared and examined under an optical microscope. A transverse section of the WAAM-built Ti-6Al-4V wall and substrate was prepared for optical microscopy. The sample was cut perpendicular to the build direction using EDM to avoid introducing cutting damage, as shown in Figure 39 a) and Figure 39 b) presents montaged optical macrographs of the deposited wall and the substrate.

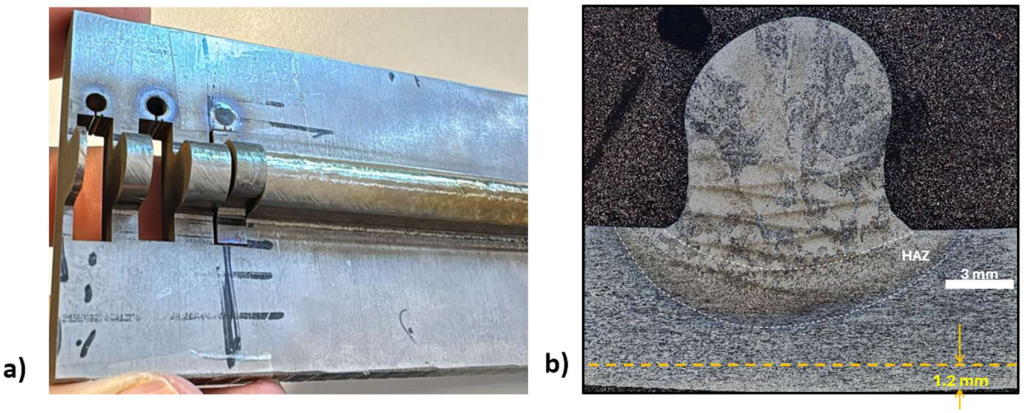


Figure 39 a) The cut section of the WAAM Ti-6Al-4V wall used for optical microscopy and b) Montaged optical macrographs of the deposited wall and the substrate [66]

The mounted specimen was ground sequentially with P240, P400, P800, P1200, and P2500 SiC papers, followed by final polishing on a micro cloth using 0.02 µm colloidal silica to achieve a scratch-free finish. The polished surface was etched in Kroll's reagent (ASTM E407 No. 187) by immersion for 10–20 s, rinsed, and dried to reveal the microstructure features.

No apparent macroscopic porosity was observed in the etched section. At the substrate–wall interface, the prior-β grains were largely equiaxed, sizing approximately 0.5 ± 0.3 mm at the base and increasing to roughly 3 ± 1 mm within the first few millimetres of build height, reflecting the accumulation of thermal energy during deposition. Further up the wall, the structure transitioned to columnar prior-β grains oriented along the build direction, extending across several layers and frequently exceeding 3 mm in length until the point where deposition was interrupted. In the HAZ, close to the fusion boundary, a slight increase in grain size relative to the bulk substrate was visible, suggesting local exposure to temperatures near or above the β-transus during deposition. This observation is in line with prior reports for WAAM-processed Ti-6Al-4V [119,120].

It is also worth highlighting that the LCR ultrasonic technique used here penetrates approximately 1-1.2 mm from the bottom surface of the substrate, as indicated by the dashed line in Figure 39 b). This depth lies well below the HAZ and therefore remains unaffected by the thermal cycles associated with WAAM deposition. As a result, the region interrogated during LCR measurements retains a uniform microstructure across the width of the examined section.

6.2.2 CM

Figure 40 shows the CM RS results for both the as-deposited and post-peened WAAM Ti-6Al-4V samples, alongside a schematic indicating the expected zones within the WAAM samples, aligned with the measurement results.

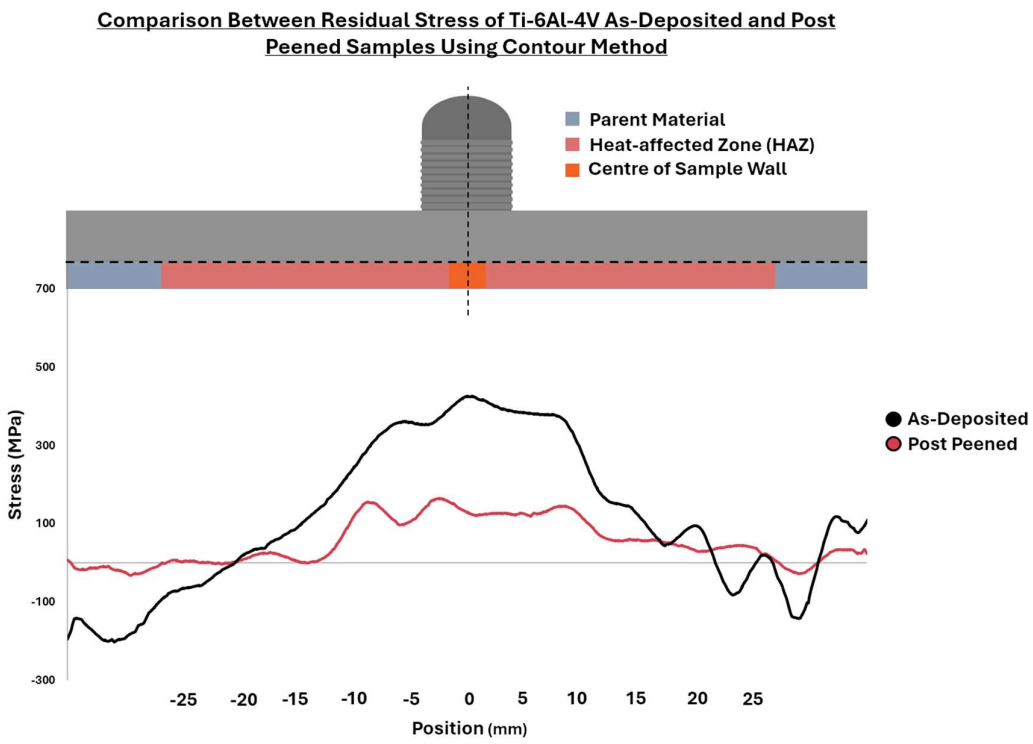


Figure 40 CM RS measurements for as-deposited and post-peened samples [66]

In the as-deposited sample, RS begins at a minimum of ~-150MPa at -35mm, and increases steadily toward the centre, peaking at ~410 MPa at 0mm, which aligns with the sample wall's centre, where RS is typically highest. Beyond this point, RS remains relatively constant until 9mm, after which it gradually decreases to ~-90MPa at -30mm, before slightly rising again to ~100 MPa after 25mm.

In the post-peened sample, a clear reduction in the overall RS is examined. While the general trend remains similar with lower RS values further from the centre, there is still a noticeable increase in RS between -10mm and 10mm, closely mirroring the peak observed in the as-deposited condition. However, the magnitude of this peak is significantly reduced, with a maximum RS of ~130 MPa at 3mm. Notably, the RS values further from the centre are higher in the post-peened sample compared to the as-deposited one. For instance, at 25mm, the RS is ~-200 MPa in the as-deposited sample, whereas it is ~0MPa in the post-peened sample. Similarly, at 30mm, the RS is about -125 MPa in the as-deposited condition and only -10 MPa after peening. This is expected, as peening does not eliminate RS but rather redistributes it, reducing tensile stress and introducing beneficial compressive stresses to enhance the structural integrity of the sample.

Several anomalies are observed in the CM RS measurements. At the furthest end of the sample at 35mm, there is a small spike in RS from approximately -200 MPa to -150 MPa, which then returns to -

200 MPa. A similar pattern of sharp fluctuations is seen between 17 and 20mm, where the stress increases and decreases abruptly.

Additionally, the RS distribution is not perfectly symmetrical. This asymmetry is expected due to slight distortions at the bottom of the WAAM Ti-6Al-4V samples, which are not completely flat. This is more clearly illustrated in the CM FE model shown in Figure 41. Such distortion is a result of stress on the samples during the manufacturing process, which is then relieved, and can potentially influence the measured RS. To minimise this effect, all samples were flat before deposition, and symmetrical clamping was applied using six clamps, with three evenly spaced along each side in the longitudinal direction.

Despite the presence of distortion, it is unlikely to affect the ToF measurements, as the deformation resembles angular shrinkage rather than buckling, which would impact surface flatness. This phenomenon has been discussed in previous studies, such as the work by Sattari-Far and Javadi [106], who found that distortion in welded pipes did not significantly affect RS measurements when comparing FE model predictions with experimental data.

The resulting CM FE models, along with the back-calculated RS distributions, are shown in Figure 41.

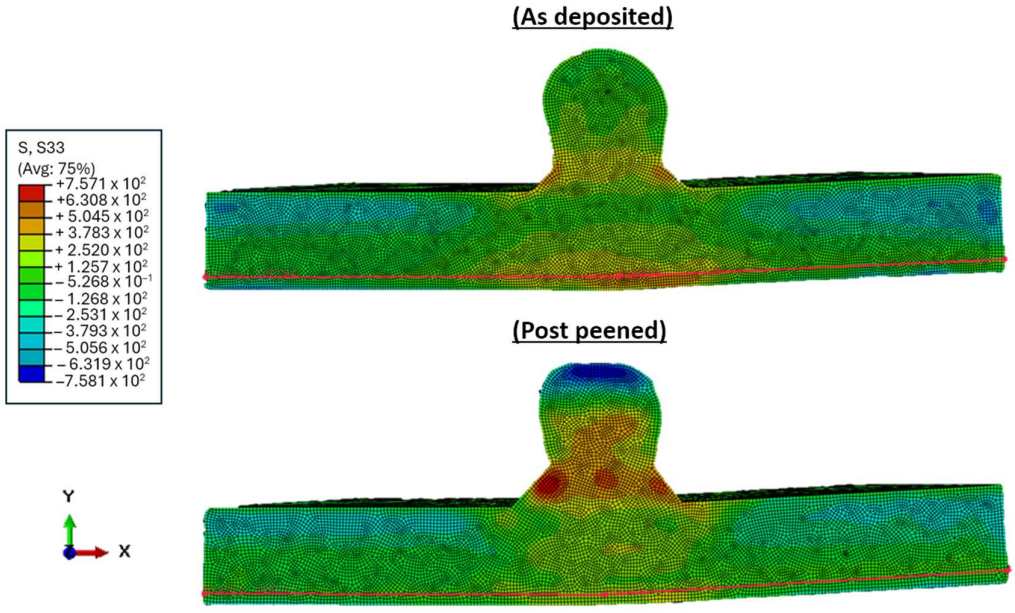


Figure 41 FE analysis models for both the as-deposited and post-peened samples with back-calculated RS (in MPa) using CM [66]

6.2.3 XRD

Figure 42 shows the XRD RS measurements of the as-deposited Ti-6Al-4V WAAM sample. Only an as-deposited sample was chosen for this measurement method to provide further validation of the RS

measurements of the PAURS measurements. The results presented only consider the longitudinal stress measurements, as this is the main direction in which tensile RS occurs and where it is highest, so is the area mainly considered for RS measurements. As previously described, measurements were taken at 15 different points on the bottom of the sample, which are shown in the results.

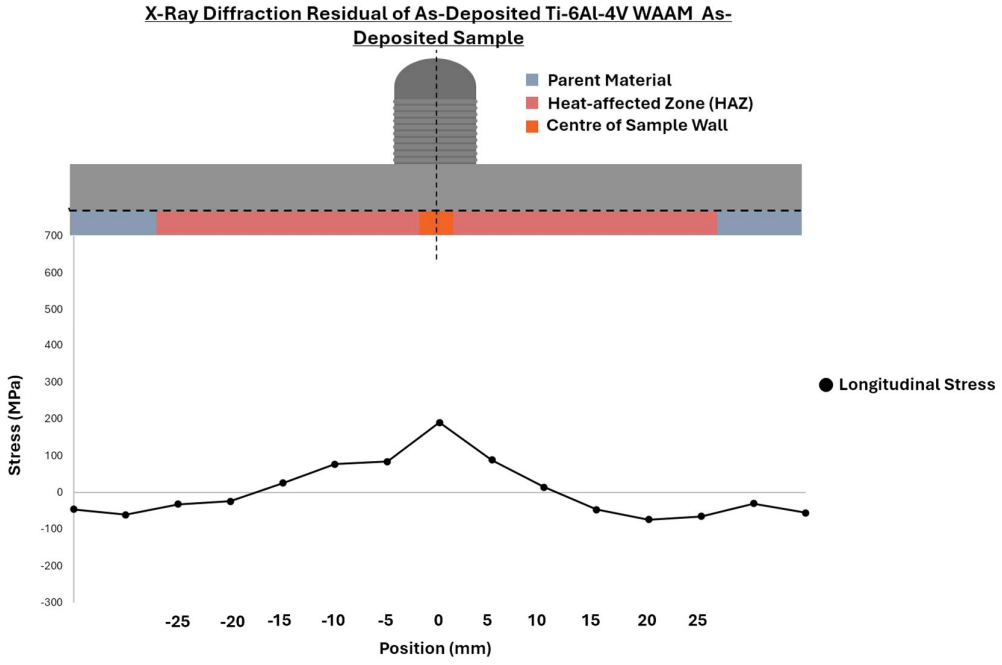


Figure 42 XRD RS measurements of the as-deposited WAAM Ti-6Al-4V sample [66]

As shown in the results, the RS distribution from the XRD measurements of the as-deposited WAAM Ti-6Al-4V sample aligns well with the expected stress zones. The RS reaches a peak of approximately 190 MPa at the centre of the sample wall, as expected. Within the HAZ, particularly between -10 and 5mm, the RS remains relatively high, ranging from around 80 MPa to 90 MPa.

Further from the HAZ, particularly between 15 to 25mm, the RS values are significantly lower, ranging from approximately ~-60 MPa to ~-30 MPa, and remain below zero in these outer regions.

Overall, the RS distribution follows the expected profile and appears relatively symmetrical. However, similar to CM results, a slight asymmetry is present. This is attributed to the same distortion on one side of the as-deposited WAAM sample, as previously discussed.

6.2.4 PAURS

6.2.4.1 Wedge Angle Testing

The optimal wedge angle for ultrasonic RS measurements in Ti-6Al-4V was determined following the Snell's law-based approach described[61]. A set of acrylic wedges with angles near the first critical

angle for LCR waves in titanium alloys, ranging from 22.2° to 23.2°, was tested. The angle requiring the least gain adjustment for accurate ToF measurements was selected, resulting in an optimal wedge angle of 22.7° for the PAURS setup.

6.2.4.2 FMC

FMC extends PAURS by increasing the number of available transmitter-receiver paths, supporting averaging, path-quality assessment and identification of anomalous measurements. FMC enhances data redundancy, enables outlier removal, and improves RS accuracy by generating 64 LCR paths [55].

6.2.4.3 SNR

Although the PAURS setup is capable of generating 64 LCR wave paths, not all of these paths are usable. In WAAM samples, the strength of LCR signals can be affected due to various factors, including noise and interference from other ultrasonic wave modes, such as shear waves. To assess the quality of the LCR signals and determine their reliability, it is essential to calculate the SNR.

The SNR calculation used here is a non-conventional, comparative signal-quality metric rather than a standard SNR measurement. Four representative noise peaks were isolated within a consistent pre-arrival window, and their RMS amplitude was used as the noise reference. This was compared with the LCR signal amplitude to assess the relative quality of the 64 FMC paths and identify paths in which noise could affect zero-crossing detection. The metric was applied consistently across all measurements and was not intended as an absolute SNR value.

SNR was calculated for each of the 64 LCR paths in the as-deposited Ti-6Al-4V sample across three distinct regions: the parent material, the -25 mm scan line, and the centre of the sample wall (0 mm), as shown in Figure 18. This was carried out using the SNR formula in Equation 25.

$$SNR(dB) = 20x\ log10(\frac{SA}{NA})$$

Equation 25 Formula used to calculate SNR

To ensure consistency and repeatability in the SNR evaluation, a standardised methodology was developed. This methodology was applied across all sample locations and LCR paths and is shown in Figure 43.

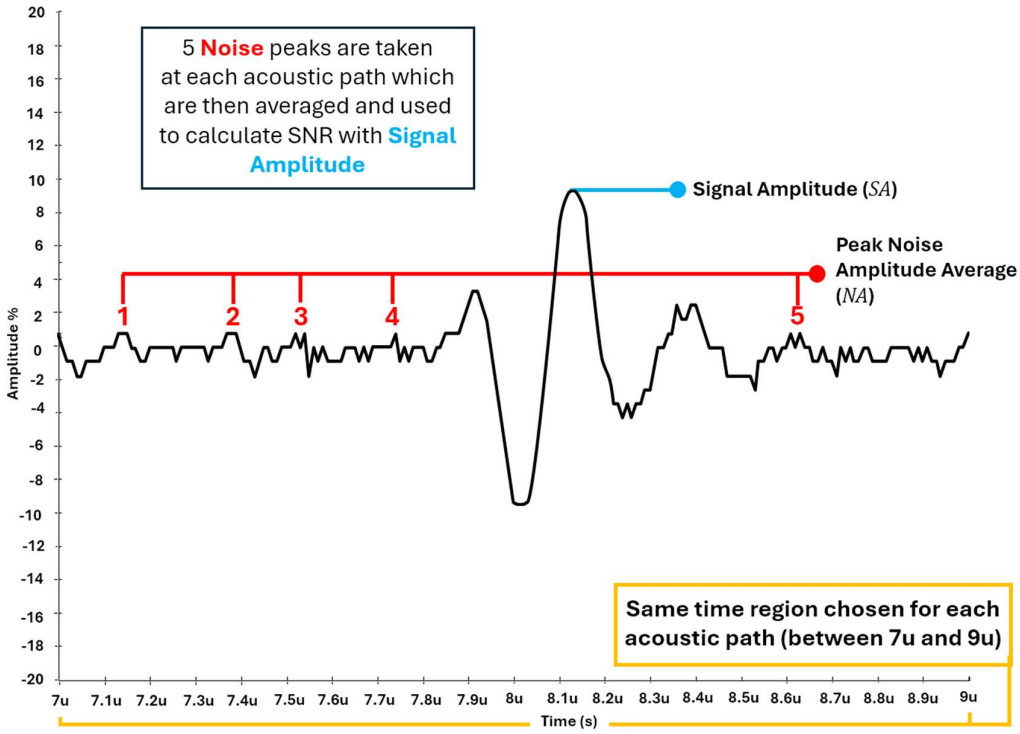


Figure 43 SNR calculation methodology and formula [66]

As part of the methodology, an example signal from the Ti-6Al-4V parent material is used to demonstrate how the SNR is calculated. The time window between 7 µs and 9 µs was selected for all acoustic paths and samples, as this region consistently contains both the LCR signal and the peak noise, allowing for a good comparison.

It is important to consider the results across all acoustic paths and regions to fully understand the signal quality. These results are shown in Figure 44.

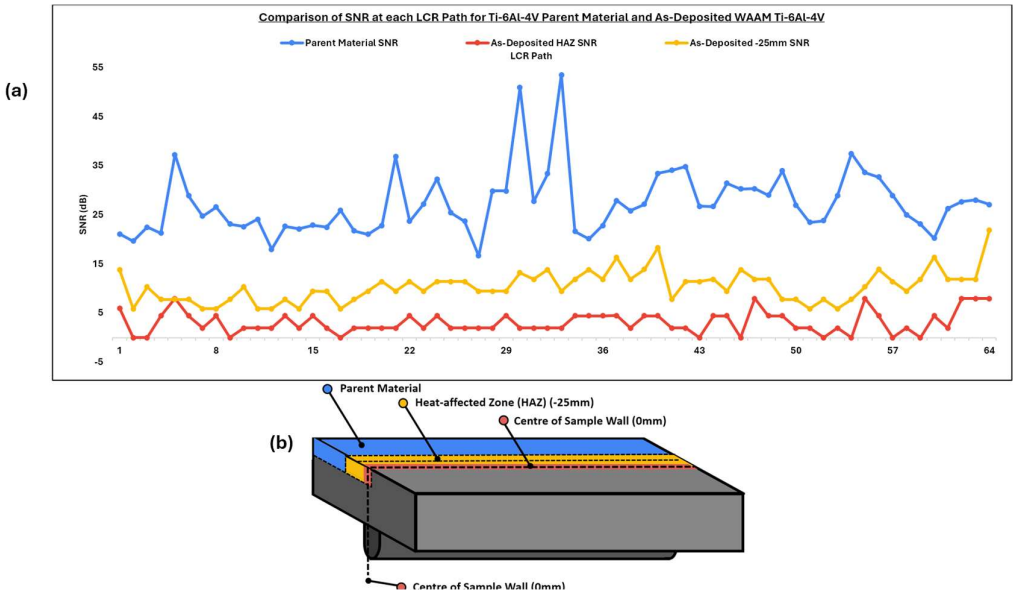


Figure 44 (a) SNR results across regions; (b) Sample positions [66]

Although the variability decreases towards the sample centre, this does not necessarily indicate improved measurement consistency. The low SNR in this region suggests that the response may be dominated by stochastic noise, making the extracted ToF values less reliable.

The calculated SNR values are generally consistent across all acoustic paths and regions, ranging from approximately 0 dB to 53 dB, with a few significant anomalies. Among the three regions, the parent material shows the most consistent SNR and the lowest overall noise levels. The -25 mm scan line, located at the edge of the measurement area, shows higher SNR values than the HAZ region, which is expected due to reduced interference.

Across all positions, the SNR follows a repeating pattern. It tends to remain stable or gradually increase, peaking at every eighth path before decreasing again. This pattern is observed consistently from path 8 through to path 64 and is likely related to the way ultrasound propagates using FMC, as shown in Figure 23. As the acoustic paths progress from the first transmitter through each set of eight receivers, the SNR appears to increase across the receiver group before resetting with the next transmitter.

Interestingly, the SNR results are not entirely consistent with expectations. The parent material, which should exhibit minimal variation, show more fluctuation than anticipate. Notable spikes occur at path 30 with 51 dB and path 33 with 53 dB, followed by a return to the previous SNR range. In contrast, the WAAM sample shows slightly more stable SNR values than expected. This improved consistency may be due to the WAAM measurements being retaken later using an updated method to enhance RS accuracy, which was not carried out for the parent material.

The SNR results in Figure 44 indicate a clear correlation between signal quality and measurement reliability. Paths with SNR above ~40 dB, such as those observed in the parent material, consistently produced stable RS profiles without unrealistic peaks. In contrast, paths within the HAZ, where SNR was typically below 10 dB, were more prone to interpolation errors and generated extreme outliers during initial PAURS calculations. This supports the expectation that higher SNR improves zero-crossing detection and reduces timing uncertainty. Therefore, SNR serves as a practical criterion for identifying unreliable paths and guiding outlier removal during FMC-based averaging.

6.2.4.4 Acoustoelastic Constant

The results from this experiment were previously discussed in the study by Walker et al. [61]. During the experiment, stress increments were applied through both loading and unloading cycles, allowing acoustoelastic constant measurements to be obtained separately for each mode. Since the PAURS setup uses two eight-element arrays, results can be presented individually for each element. This means that a total of 16 sets of data are produced when using the direct approach, with eight sets of data for loading and eight for unloading.

Figure 45 and Figure 46 show the acoustoelastic constant results for both loading and unloading, respectively. Each set of data corresponds to a specific array element, with data points collected using FMC. For example, "Element 3" refers to the ToF measurement between transmitter element 3 and receiver element 3.

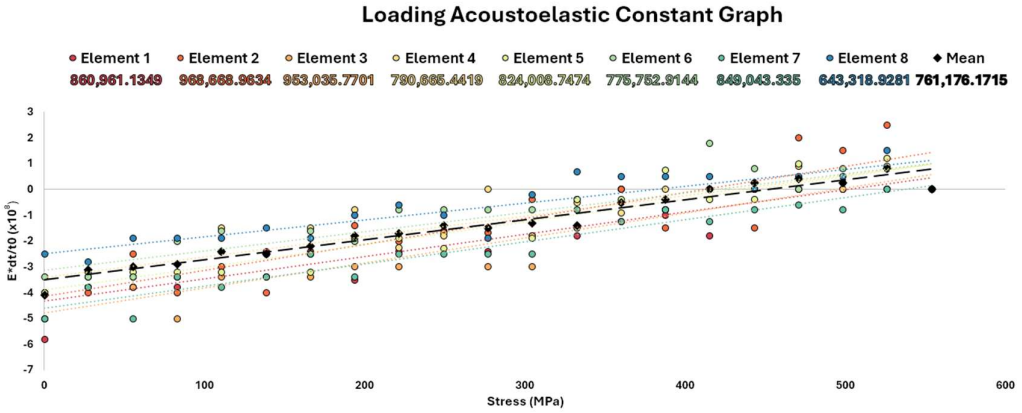


Figure 45 Acoustoelastic constant graph during loading [66]

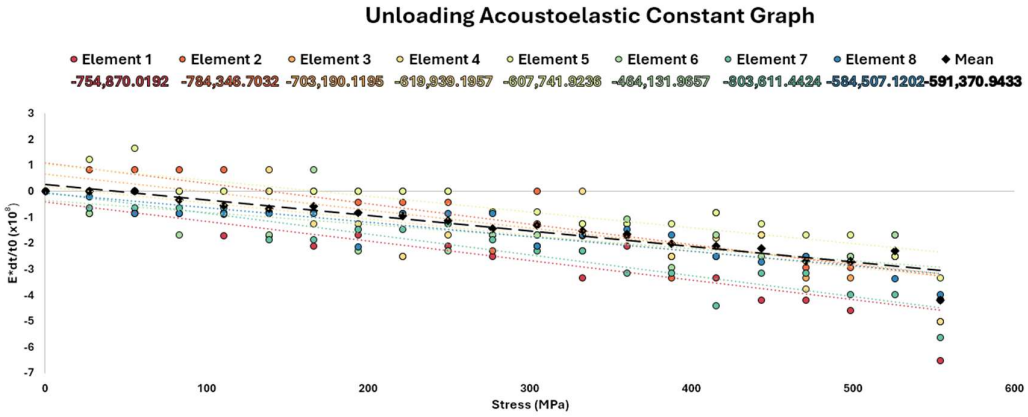


Figure 46 Acoustoelastic constant graph during unloading [66]

The vertical axis of each graph represents the value of Exdt/t0, where the slope of the graph corresponds to the acoustoelastic constant. This constant is calculated by plotting the known stress applied by the tensile testing machine against the effective Young's modulus of the material. The acoustoelastic constant is then extracted from the best-fit line through the data points, which is shown in red on each graph.

As expected, the loading graph shows an upward trend, with increasing stress resulting in higher values of Exdt/t0, while the unloading graph displays the opposite pattern. However, a few outliers deviate from this trend. For instance, in the loading data, Element 6 shows an unexpected spike just after 400 MPa, followed by a gradual decrease. A similar anomaly appears in the unloading data at approximately 150 MPa for both Elements 4 and 6. Additionally, there are instances where the Exdt/t0 value remains constant over a wide stress range, despite a significant increase in applied stress.

These irregularities may be attributed to known sources of error discussed in previous studies by Javadi et al. [114] and Walker et al. [61], such as triggering issues or inconsistencies in the tensile testing machine. However, the impact of these errors is largely mitigated in the PAURS setup. Unlike traditional single-element ultrasonic methods, which rely on a single measurement and are more vulnerable to such anomalies, PAURS collects hundreds of data points across multi-paths. These are averaged to produce more reliable acoustoelastic constant measurements, allowing for greater confidence in the results and easier identification of outliers.

The Exdt/t0 values for each element are shown in Table *4* and for loading and unloading, respectively.

Table 4 Loading acoustoelastic constant results

Element	**Exdt/t0**
1	860,961.1349
2	968,668.9634
3	953,035.7701
4	790,665.4419
5	824,008.7474
6	775,752.9144
7	849,043.335
8	643,318.9281
Mean	761,176.1715

Table 5 Unloading acoustoelastic constant results

Element	**Exdt/t0**
1	-754,870.0192
2	-784,346.7032
3	-703,190.1195
4	-619,939.1957
5	-607,641.9236
6	-464,131.9657
7	-803,611.4424
8	-584,507.1202
Mean	-591,370.9433

The loading and unloading results have opposite signs because the stress increased during loading and decreased during unloading. However, their mean absolute values also differ by approximately 169,805, indicating hysteresis or experimental variability between the two cycles. Possible contributors include coupling changes, probe seating, tensile-machine compliance, and uncertainty in zero-crossing extraction. The difference is therefore treated as a calibration uncertainty rather than evidence of a material effect, and it should be considered when interpreting the calculated RS magnitudes.

6.2.5 Final PAURS Measurements

The PAURS measurement method was applied to both the as-deposited and inter-pass peened WAAM Ti-6Al-4V samples. This allowed for a direct comparison between the two conditions, as well as with the CM results, providing insight into both the effectiveness of inter-pass peening and the suitability of phased array ultrasound for RS evaluation in WAAM components. All RS measurements are measured with a penetration depth of 1.2mm, as discussed previously from the macrographs. This depth is below the HAZ, so it is unaffected by WAAM thermal cycles and retains a uniform microstructure across the section.

The initial results from these measurements are presented in Figure 47 and Figure *48* for as-deposited and inter-pass peened samples, respectively. These were obtained using the path difference method illustrated in Figure 19, where adjacent ToF values are subtracted to reduce the influence of couplant thickness on the RS measurements. Therefore, 56 acoustic paths are shown due to subtracting adjacent ToF to mitigate the effect of couplant thickness on the RS measurements.

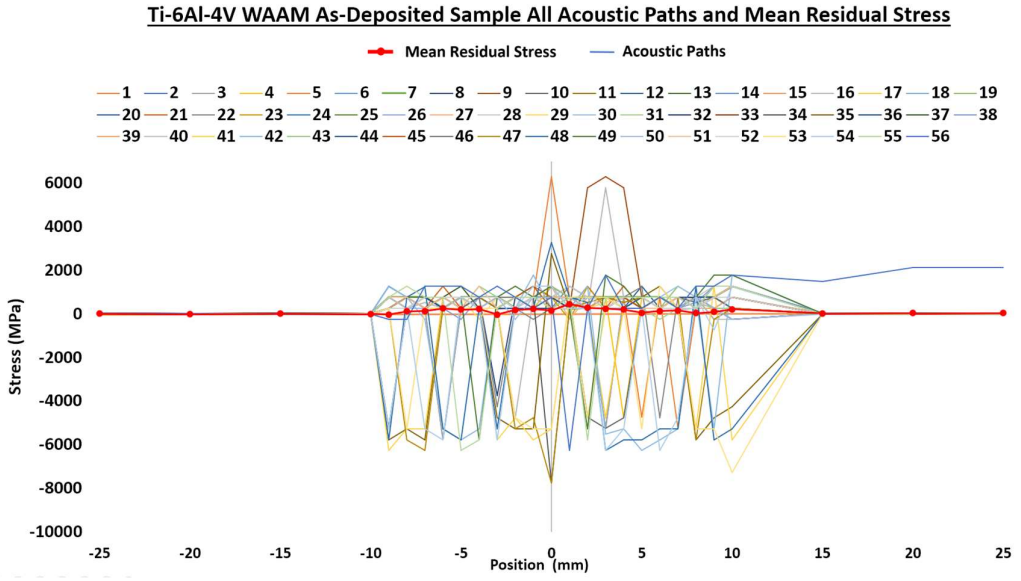


Figure 47 As-Deposited initial RS measurements [66]

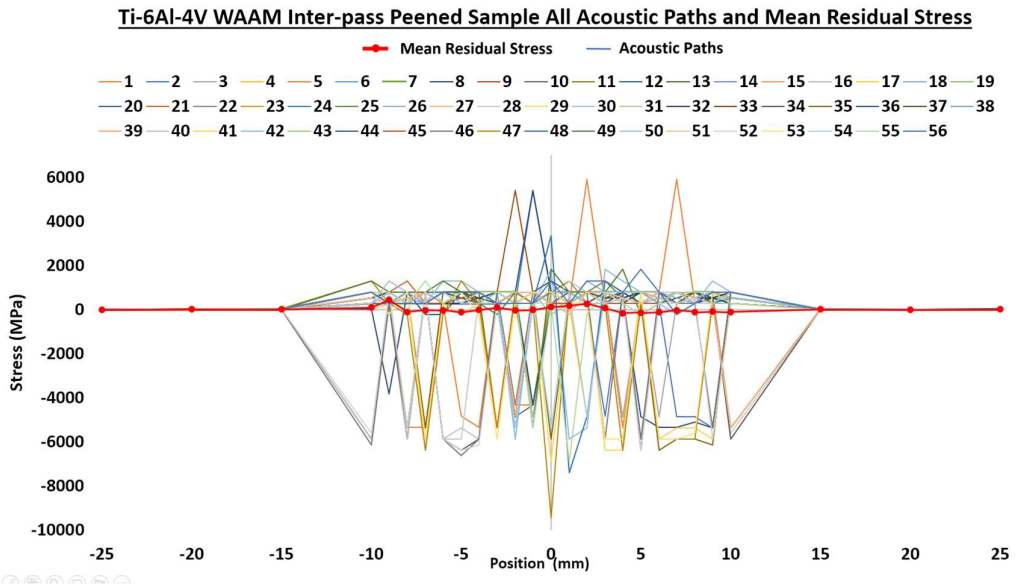


Figure 48 Inter-pass Peened initial RS measurements [66]

The initial RS measurements obtained using the PAURS method show several noticeable outliers that significantly affect the overall results for both the as-deposited and inter-pass peened WAAM Ti-6Al-4V samples. In both datasets, the red line represents the mean RS across all acoustic paths. However, in many cases, individual RS measurements deviate substantially from this mean, indicating the presence of outliers.

For the as-deposited sample, several acoustic paths between 0 mm and 5 mm show RS values as high as approximately 6000 MPa, which is far above the expected range. Additionally, between -10 mm and 10 mm, some paths report RS values between -6000 MPa and -8000 MPa. Outside the HAZ, path 56 shows a clear anomaly between 10 mm and 25 mm, where RS spikes to around 2000 MPa.

Similarly, the inter-pass peened sample contains outliers, with several paths showing peak RS values between 4000 MPa and 6000 MPa. In the same central region between -10 mm and 10 mm, some paths report extremely low RS values, ranging from -6000 MPa to -10,000 MPa.

These extreme values were flagged for assessment because they were physically implausible and strongly influenced the path-averaged result. One advantage of the PAURS method is that it generates 56 acoustic path measurements, allowing for a mean RS to be calculated and compared against individual paths. This makes it easier to identify and isolate outliers. Therefore, standard deviation can be used in order to identify these outliers using Equation 26.

$$Standard\ Deviation = \sqrt{\frac{\Sigma \text{Path } \sigma \text{ measurement} - \text{Mean } \sigma \text{ measurement})^2}{Total\ number\ of\ acoustic\ paths}}$$

Equation 26 Standard deviation formula used for calculating path outliers

Figure 49 and Figure 50 present the standard deviation results for the as-deposited and inter-pass peened samples, respectively. Although standard deviation was calculated for all 56 paths, a set of 8 paths from each sample is shown to demonstrate how this method helps identify and remove outliers

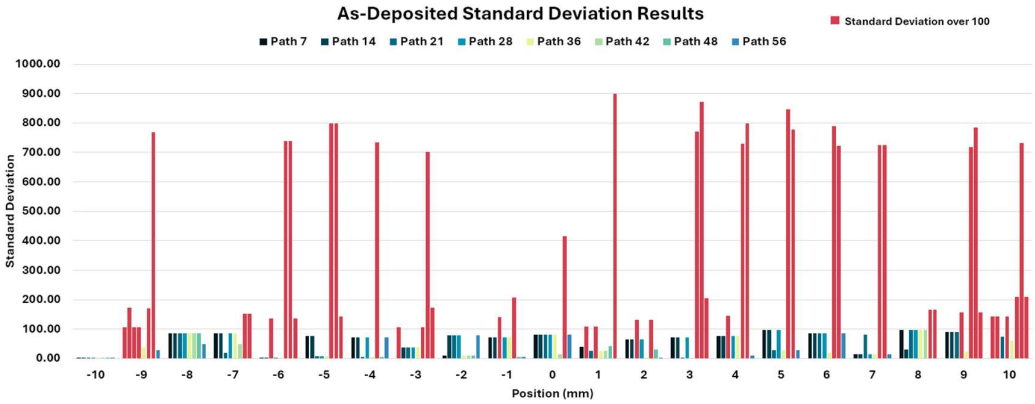


Figure 49 As-deposited Standard Deviation results [66]

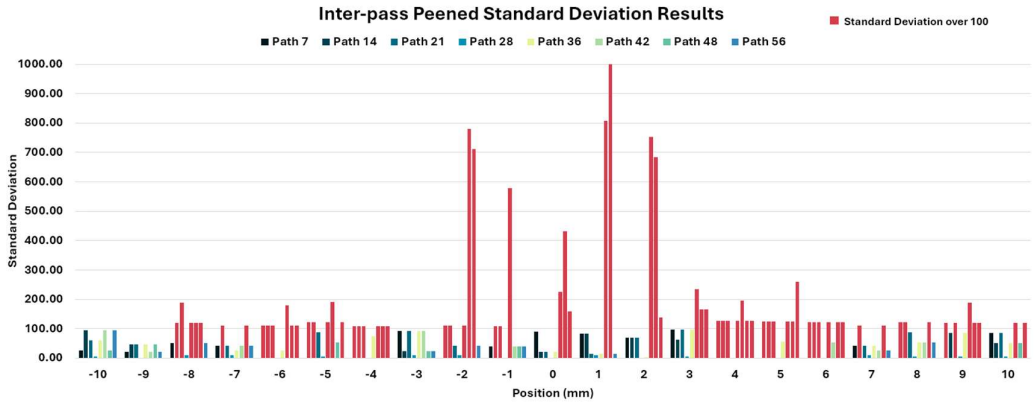


Figure 50 Inter-pass peened Standard Deviation results [66]

Outliers were identified with a threshold of 100 MPa. This value was chosen based on two factors:

(i) Material yield strength: Ti-6Al-4V typically exhibits a yield strength of 850–950 MPa [121]. Even under extreme conditions, RS exceeding ~120% of the yield strength of 1100 MPa is highly unlikely. Therefore, any calculated RS values in the range of several thousand MPa are physically unrealistic and indicative of measurement or interpolation errors.

(ii) Statistical consistency and prior studies: Previous ultrasonic RS studies [122,65,123] have shown that outlier rejection based on statistical dispersion, such as standard deviation, is effective for mitigating noise and coupling inconsistencies. A 100MPa threshold is small relative to the material's yield strength yet large enough to accommodate naturally occurring variability in ultrasonic measurements, ensuring that genuine stress variations are preserved while extreme anomalies are removed.

A trend was observed in both samples where paths between 42 and 56 showed significantly more deviation from the mean. These paths correspond to combinations involving the outer elements of the phased array (particularly Elements 6 to 8), which are more affected by poor coupling and uneven contact with the sample surface. This issue is common in array setups because the ends of the transducer often experience less consistent pressure compared to the elements at the centre. While a single-element transducer can also suffer from coupling inconsistencies, the impact is more pronounced in phased arrays due to the larger number of elements and the reliance on multiple transmit–receive combinations. However, PAURS mitigates this by averaging results across 56 acoustic paths, reducing the influence of any single unreliable path on the final RS measurement.

After removing the identified outliers, the final as-deposited and inter-pass peened RS measurements were produced and are shown in Figure 51 and Figure 52, respectively. As illustrated, the individual acoustic paths now align much more closely with the mean RS values, and the RS measurements fall within the expected range for both the as-deposited and inter-pass peened samples. A clear reduction in RS is observed in the inter-pass peened sample, confirming the effectiveness of the peening process in reducing tensile stress within the WAAM Ti-6Al-4V structure.

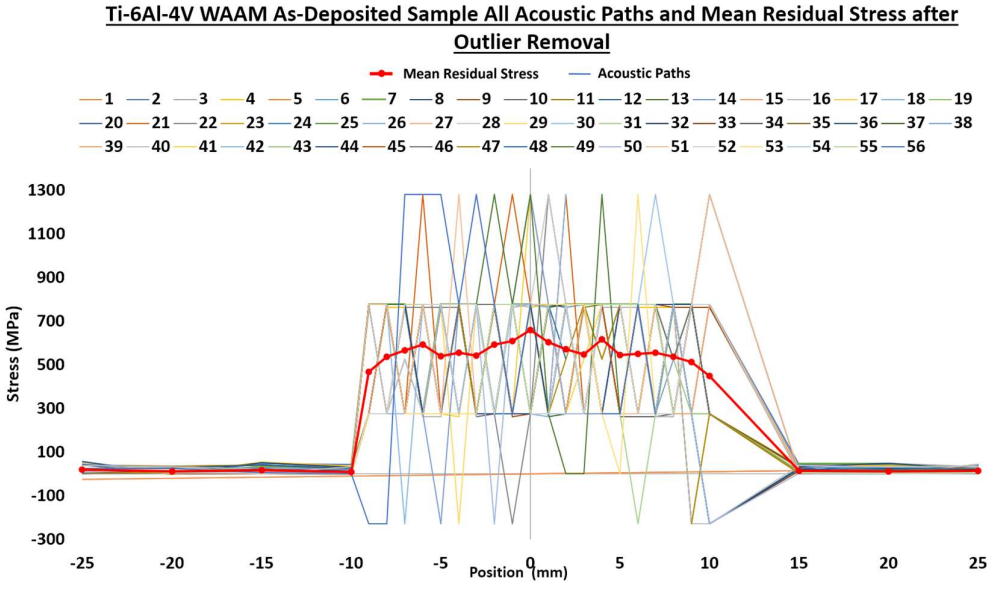


Figure 51 As-deposited RS measurements after outlier removal [66]

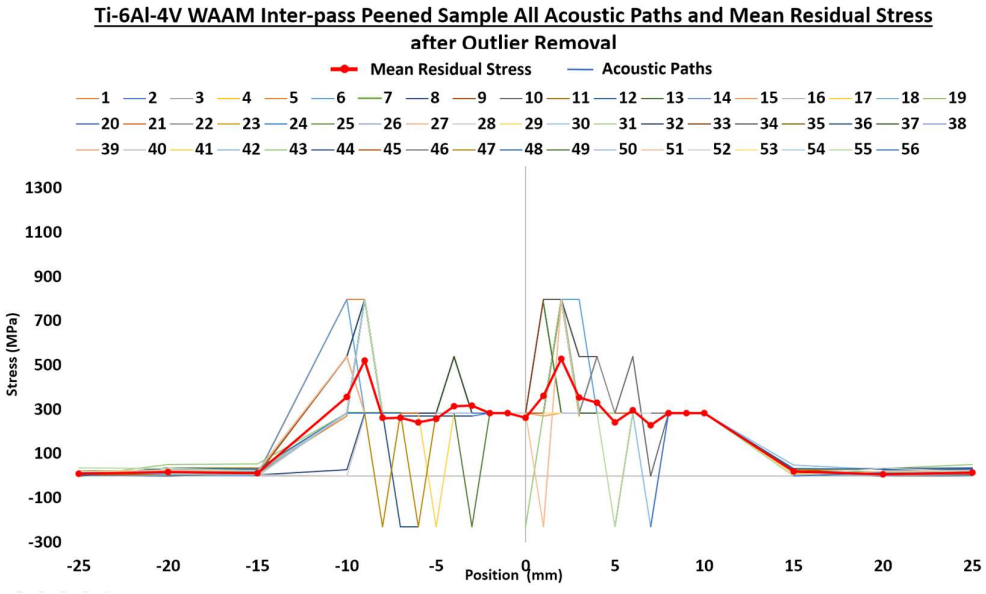


Figure 52 Inter-pass peened RS measurements after outlier removal [66]

It is important to note that RS values up to 1300 MPa were not considered outliers in this study. This decision was based on the yield strength of Ti-6Al-4V, which typically ranges between 850 MPa and 950 MPa depending on processing conditions [124]. Assuming a threshold of 120% of yield strength, values up to approximately 1140 MPa [125] could still be considered in regions of high RS. The 1300 MPa measurements, whilst much higher than the mean, were consistent with surrounding data and did not exhibit the behaviour typical of true outliers, such as the extreme values exceeding 6000 MPa.

The comparison between the mean RS values before and after outlier removal is shown further in Figure 53, the filtered profiles show reduced variability and greater consistency with the expected broad RS distribution. One of the most notable observations is the higher concentration of outliers within the HAZ, particularly between -10 mm and 10 mm in both samples. Outside the HAZ, the removal of outliers has had a lesser effect, except for the region beyond 15 mm in the as-deposited sample. This corresponds to previously identified errors in path 56, which showed abnormal RS values between 10 mm and 25 mm. Removing this path led to a clear improvement in that area.

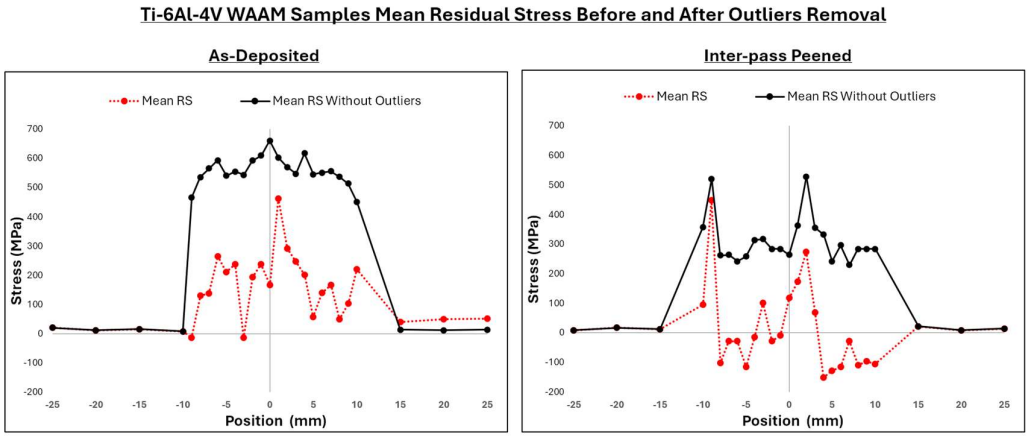


Figure 53 Comparison of Mean RS before and after outlier removal [66]

In the as-deposited sample, the overall RS distribution remains largely unchanged in shape after outlier removal. However, the RS values are significantly higher, with the peak increasing from ~480 MPa to ~660 MPa. The removal of outliers also greatly reduced fluctuations within the HAZ, resulting in a smoother and more natural RS curve between -10 mm and 10 mm. The peak RS now occurs at the centre of the sample wall (0 mm), as expected. These fluctuations were previously caused by extremely low RS values, with some acoustic paths measuring as low as -6000 MPa.

For the inter-pass peened sample, the overall RS shape also remains mostly consistent, but the RS values increase across the sample after outlier removal. This is due to similar issues as in the as-deposited sample, where several acoustic paths showed unrealistically low RS values between -6000 MPa and -10,000 MPa. Interestingly, the location of the peak RS shifts. Initially, the peak RS was observed at -10 mm with a value of ~450 MPa. After outlier removal, this increases slightly to ~520 MPa. However, a more significant change occurs at 2 mm, where the RS increases from ~280 MPa to ~530 MPa, indicating that this region was heavily affected by outliers. Outside the HAZ, the RS remains close to 0 MPa on both sides of the sample.

Figure 54 presents the final mean RS measurements for both the as-deposited and inter-pass peened WAAM Ti-6Al-4V samples. Alongside the RS data, a schematic of a WAAM sample is included to illustrate the specific regions where measurements were taken, as previously shown in Figure 18.

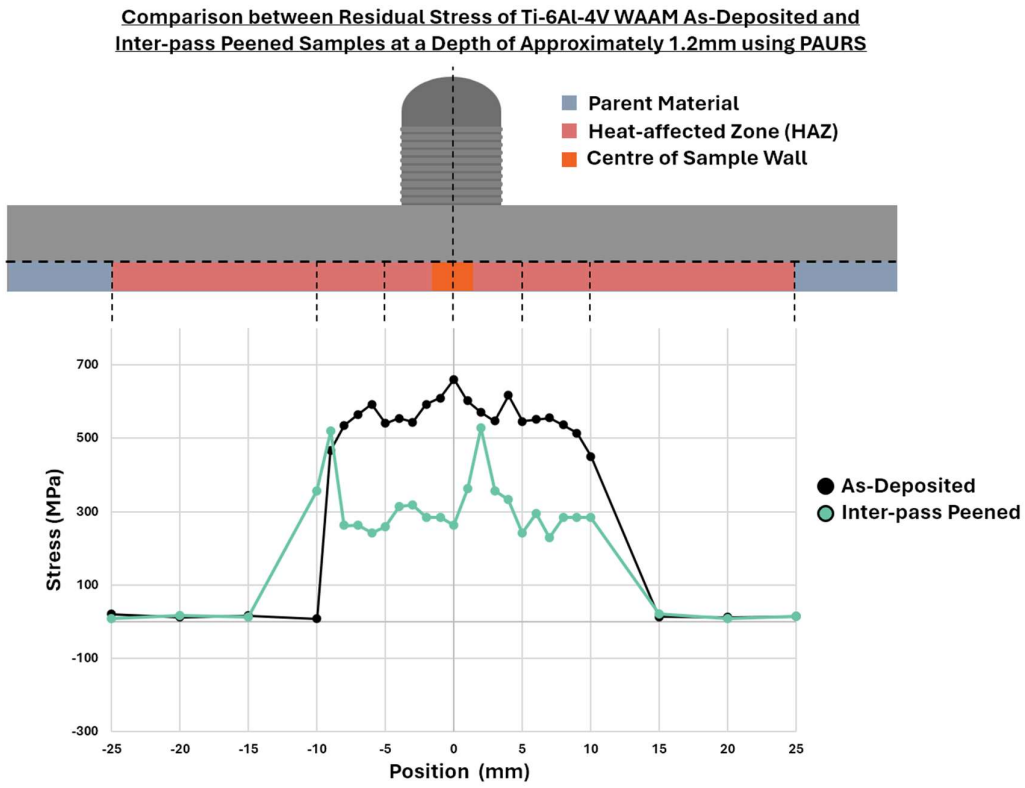


Figure 54 Final Mean RS measurements for as-deposited and inter-pass peened samples [66]

Figure 54 shows that both the as-deposited and inter-pass peened samples show the expected RS distribution, with higher RS values concentrated near the centre of the sample, between -10 mm and 10 mm. This region corresponds to the area most affected by heat during the WAAM process. Outside of this central zone, RS values drop significantly, with both samples measuring approximately 0 MPa, as expected.

The overall RS profile of the inter-pass peened sample closely resembles that of the as-deposited sample, but with noticeably lower RS values in the central region. Excluding the peak RS values, the average RS between -10 mm and 10 mm decreases from ~500–600 MPa in the as-deposited sample to around 250–300 MPa in the inter-pass peened sample. This reduction demonstrates the effectiveness of inter-pass peening in lowering overall RS.

However, two significant RS spikes remain in the inter-pass peened sample at -10 mm, -9 mm, and 2 mm, where RS values reach ~350 MPa, 520 MPa, and 530 MPa, respectively. Notably, the RS at -10 mm and -9 mm is higher in the inter-pass peened sample than in the as-deposited one, increasing from 0 MPa to 360 MPa at -10 mm and from 480 MPa to 520 MPa at -9 mm. While this may suggest that peening increased RS at these points, it is more likely that the process redistributed stress within the

HAZ. The reduction in RS across the rest of the HAZ may have concentrated stress at these specific locations. Additionally, inter-pass peening may have replaced harmful tensile stress with beneficial compressive stress, improving the overall structural integrity of the sample.

Overall, the comparison between both samples and their respective scan areas confirms that PAURS reproduced the principal features of the expected RS distribution in the investigated WAAM Ti-6Al-4V specimens. For example, the peak RS of approximately 680 MPa occurs precisely at 0 mm, aligning with the centre of the sample wall where the highest thermal input is expected. The similarity in RS distribution between the two samples, along with the clear reduction in RS in the inter-pass peened sample, further supports the reliability of the PAURS method.

6.2.6 Comparison of PAURS, CM, and XRD Results

Figure 55 shows a comparison of RS results across multiple measurement methods and sample conditions. It includes CM results for both the as-deposited and post-peened samples, PAURS results for the as-deposited and inter-pass peened samples, and XRD results for the as-deposited sample.

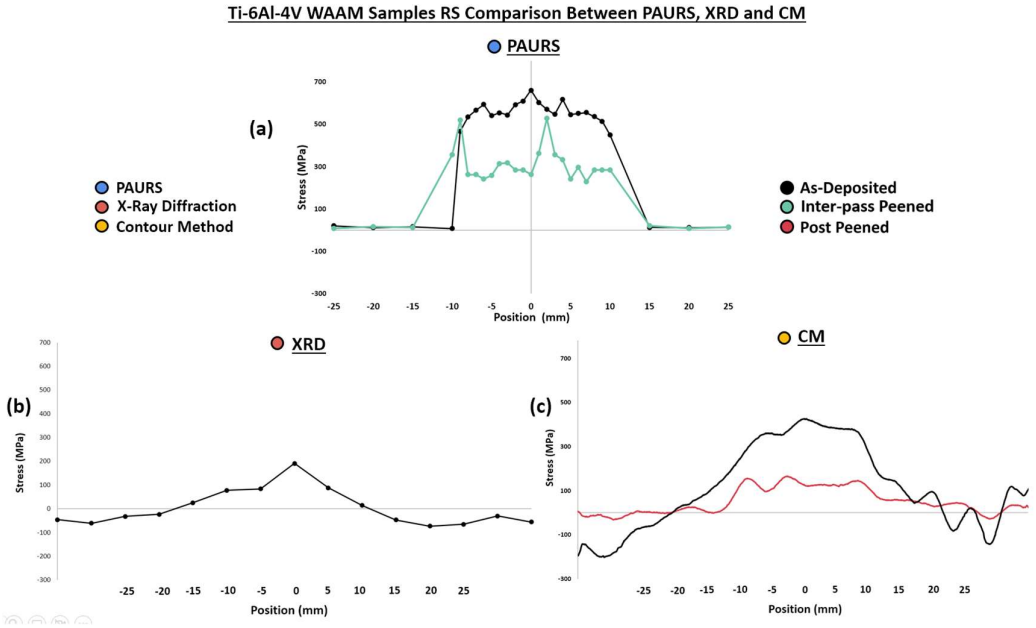


Figure 55 (a) Final PAURS RS measurements, (b) XRD as-deposited RS, (c) CM RS for as-deposited and post-peened samples [66]

Despite differences in measurement principles and data acquisition techniques, all three methods show qualitative agreement in the broad RS distribution and central peak location. In each case, the peak RS occurs at the centre of the sample wall (0 mm), where thermal input during WAAM is most concentrated in the HAZ, and RS decreases as it is measured further from the HAZ.

The PAURS results are notably smoother than those obtained using CM and show significantly less fluctuation, particularly in regions such as 0–5 mm and 45–60 mm, where CM shows notable instability. XRD results are similarly smooth, and PAURS FMC supports path-quality assessment and reduces the influence of selected anomalous paths.

For the as-deposited Ti-6Al-4V samples, the PAURS method recorded the highest peak at ~680 MPa, followed by CM at around 410 MPa. XRD measured the lowest peak RS, with ~190 MPa.

The quantitative differences in peak RS values can be attributed to the inherent characteristics of each technique. PAURS measures near-surface stress over a depth of approximately 1-1.2 mm and uses ultrasonic velocity changes, which are highly sensitive to local stress variations [61]. The use of FMC and interpolation enhances resolution, allowing detection of sharper stress gradients and higher peak values [65]. In contrast, CM provides an averaged stress distribution across the entire cross-section after material removal, which tends to smooth out localised peaks [26]. XRD measures only the top few microns of the surface, where stress relaxation and microstructural effects can reduce tensile stress compared to subsurface regions [79]. Additionally, differences in spatial resolution, penetration depth, and data processing, such as FE reconstruction using CM against LCR path averaging using PAURS, contribute to these discrepancies [126]. These variations are consistent with prior comparative studies of RS measurement techniques and highlight the importance of considering method-specific sensitivities when interpreting RS data [127].

The very small penetration depth of XRD means that it is not the best to study the effect of peening on the peened surface directly. However, this was out of the scope of this study, in which the bottom surface was studied, but the potential of using PAURS and XRD for RS measurement on the WAAM wall is in the vision of the work.

Both inter-pass peening (measured using PAURS) and post-peening (measured using CM) demonstrate clear effectiveness in reducing RS. PAURS shows a reduction of approximately 200–250 MPa in peak RS in the inter-pass peened sample compared to the as-deposited sample. Similarly, CM shows a reduction of around 300 MPa in the post-peened sample. Although the inter-pass peened sample shows a higher peak RS (~500 MPa) than the post-peened sample (~130 MPa), this difference is likely due to the measurement method rather than the peening process itself. The elevated values in PAURS may result from differences in depth sensitivity, reference condition and path filtering, and from the nature of inter-pass peening, which may redistribute stress and replace tensile RS with beneficial compressive RS.

Among the three methods compared in this study, PAURS has particular potential for future in-process RS assessment because it is non-destructive and compatible with automated scanning. Further development could enable manufacturing-stage evaluation, and a future automated implementation

could allow PAURS measurements to be acquired at selected stages of deposition or between processing steps. PAURS has the potential to be adapted for in-situ use, although in-process operation was not demonstrated in this thesis. This means the sample does not need to be unclamped or transferred to another measurement setup. This is particularly advantageous for both inter-pass and post-process evaluation, as it avoids stress redistribution that may occur during handling. In contrast, while XRD is also non-destructive, it requires specialised facilities and is not suitable for in-process or in-situ applications. CM, although capable of providing full FE RS modelling, is destructive and requires the sample to be cut, making it unsuitable for iterative or real-time evaluation.

Based on these findings, PAURS demonstrates strong potential as a method for RS measurements in WAAM components. Although each investigated method has unique advantages and limitations, PAURS has potential for future in-process and in-situ RS measurements, unlike CM and XRD in the configurations used here. Both PAURS and XRD are non-destructive, while CM is destructive but provides comprehensive RS measurements and modelling. The ability of PAURS to support real-time decision-making during manufacturing, combined with its adaptability and depth of measurement, makes it a highly effective tool for RS evaluation in WAAM Ti-6Al-4V components.

6.3 Limitations and Extensions

While this study has demonstrated the capability of PAURS for RS evaluation, it also has several limitations, which highlight directions for future work. First, PAURS measurements were limited to the bottom surface of the WAAM samples. Due to the use of 5 MHz arrays with limited penetration depth, the current setup cannot directly access RS within the WAAM wall. This constraint will be addressed in future developments by integrating phased array probes into a roller-probe configuration developed for in-process defect-detection of the wall [128]. Such an approach represents a key justification for PAURS, as it is among the methods that have the potential to evolve into a practical in-process RS measurement tool [65].

A second limitation arises from coupling effects. Although techniques such as path-difference analysis and FMC averaging were used to mitigate couplant thickness variation and edge-element inconsistencies, these factors remain sources of error and point to the need for further refinement in transducer design and coupling methods.

The influence of microstructure on both RS evaluation and ultrasonic propagation was also not directly characterised in this work. Variations in grain morphology, such as columnar-equiaxed transitions, and anisotropy effects could affect CM accuracy and ultrasonic velocity [6,6, 105]. Prior work has shown that ultrasonics can detect gross changes in anisotropy and grain aspect ratio [114,65, 114], suggesting that combining PAURS with complementary microstructural characterisation would provide a more comprehensive framework for process control and structural integrity in WAAM components.

Finally, while both inter-pass and post-peening strategies demonstrated measurable reductions in RS, a direct comparison of their effectiveness is restricted by the use of different measurement techniques, with PAURS for inter-pass peening and CM for post-peening. This introduces variability due to differences in penetration depth and spatial resolution [61]. Nevertheless, qualitative trends remain consistent, and both methods significantly reduce tensile RS in the HAZ compared to the as-deposited condition [129].

From a practical standpoint, inter-pass peening offers the advantage of being integrated into the WAAM process, enabling real-time mitigation of stress accumulation without removing the component from the setup. This reduces the risk of distortion during handling and opens the possibility for in-process monitoring when combined with PAURS [65]. However, its effectiveness may be influenced by process parameters such as peening frequency and energy per blow, and it requires careful synchronisation with deposition to avoid surface defects [130].

Conversely, post-peening provides greater flexibility in applying higher-intensity treatments after the component has cooled, which can lead to more uniform stress redistribution [131]. It is less constrained by deposition timing but introduces additional manufacturing steps and handling, which may allow partial stress relaxation before treatment [132]. Furthermore, post-peening cannot prevent distortion during the build, whereas inter-pass peening can mitigate these effects progressively [133].

In summary, inter-pass peening is advantageous for large, complex WAAM components where in-process stress control is critical, while post-peening remains valuable for achieving deeper and more uniform stress redistribution when process integration is less feasible [133]. Future work should include applying the same measurement method to both conditions or combining PAURS and CM on identical samples to enable a fully quantitative comparison [61].

6.4 Conclusions

This study investigated the use of PAURS measurements on WAAM Ti-6Al-4V samples in both as-deposited and inter-pass peened conditions. The results were compared with CM and XRD measurements to evaluate the feasibility of PAURS and the effectiveness of inter-pass peening as a RS mitigation strategy. The following conclusions were drawn:

PAURS demonstrated potential for RS assessment in the investigated specimens, with FMC providing increased path redundancy and supporting reduced variability after path filtering.

PAURS and XRD as-deposited results displayed more stable results with significantly less fluctuations than the CM results. While PAURS and CM differed quantitatively, with PAURS showing RS peaks of ~500–650 MPa and CM showing ~400–450 MPa, they remained within a comparable range. XRD showed lower peak RS (~190 MPa) but followed a similar distribution.

Qualitatively, all three methods agreed, with PAURS producing a comparatively smooth filtered profile under the processing procedure used and significantly reduced fluctuation compared to CM, especially outside the HAZ.

Differential ToF processing and FMC-based path assessment reduced selected sources of variability, although systematic uncertainties remained.

Inter-pass peening effectively reduced RS in WAAM Ti-6Al-4V. When comparing the PAURS-measured inter-pass peened sample with the CM-measured post-peened sample, both showed RS reductions in the HAZ—~250 MPa for inter-pass peening and ~300 MPa for post-peening. The differences in peak RS are likely due to the measurement methods rather than the peening processes themselves.

Based on the findings, PAURS is considered a promising method for non-destructive, repeatable RS assessment in WAAM Ti-6Al-4V, subject to further validation and uncertainty quantification. Additionally, inter-pass peening is validated as an effective RS mitigation technique, offering practical benefits during the manufacturing process.

Chapter 7: Study 3: PAURS+ Microstructural Effect Study

7.1 Introduction

7.1.1 RS and Microstructure in Advanced Manufacturing

The mechanical performance, dimensional stability, and service life of metallic engineering components depend not only on geometry and defect population, but critically on RS and microstructure [134]. Microstructural attributes such as grain size, morphology, and crystallographic texture influence elastic anisotropy, fatigue resistance, crack propagation, and damage tolerance [135]. RS, introduced through non-uniform thermal cycles and plastic deformation, further modify these behaviours and may accelerate crack initiation, distortion, or premature failure [136]. RS fields are inherently multiscale, comprising Type I (macroscopic), Type II (intergranular), and Type III (intragranular) components, each arising from different mechanisms and operating over distinct length scales [6, 20]. This behaviour can be understood in terms of eigenstrain-driven incompatibility and constraint, where spatially non-uniform plastic strain, phase transformation, or thermal contraction generates self-equilibrating stress fields [137]. The magnitude and distribution of these stresses depend on process history, boundary conditions, and material constitutive response, and are therefore inherently coupled to microstructural evolution.

Advanced manufacturing processes, including robotic welding, WAAM, and AFSD, produce steep spatial gradients in both RS and microstructure, often concentrated within the near-surface region [70, 138]. For these processes, there is a growing demand for non-destructive, scalable, and in-process capable techniques that can interrogate both fields with sufficient spatial resolution [65].

Predictive understanding of these coupled fields has been pursued through thermo-mechanical and microstructure-informed modelling approaches, which have demonstrated sensitivity of RS distributions to phase evolution and transformation kinetics in welds and additively manufactured materials [109].

7.1.2 Limitations of Conventional Characterisation Methods

Established characterisation techniques such as electron backscatter diffraction, optical microscopy, XRD, neutron diffraction, and CM provide high-fidelity information on microstructure and RS. However, these methods are typically destructive, laboratory-bound, time-consuming, or incompatible with in-process deployment [7, 65, 139]. As a result, they are poorly suited to real-time monitoring or large-

area mapping in industrial manufacturing environments. Furthermore, many of these techniques provide either stress or microstructure information in isolation, requiring separate measurements and co-registration, which introduces additional uncertainty when correlating the two fields in heterogeneous materials [6, 139].

Ultrasonic methods offer an attractive alternative, combining non-destructive operation, penetration depth control, and compatibility with harsh environments and robotic integration. However, a persistent challenge lies in disentangling the coupled influences of RS and microstructure on ultrasonic wave propagation [61, 65].

7.1.3 Ultrasonics for Stress and Microstructure Characterisation

Ultrasonic wave propagation in polycrystalline media is affected by both elastic moduli perturbations and wave–microstructure interactions. RS influences wave velocity through the acoustoelastic effect, forming the basis of ultrasonic stress measurement [140]. Microstructure, by contrast, modifies wave attenuation, scattering, and frequency content through grain-scale elastic mismatch and anisotropy [67]. These interactions are governed by elastic inhomogeneity at the grain scale and have been described through scattering frameworks such as the unified theory of Stanke and Kino and subsequent extensions accounting for grain size distributions and anisotropy [141, 142]. Both analytical and FE studies have shown that backscatter amplitude and attenuation scale with grain size, morphology, and crystallographic contrast [143, 144].

LCR waves are particularly well suited to RS measurement due to their strong sensitivity to in-plane stress components and confinement to the near-surface region [145]. Since their introduction, LCR-based methods have been shown to provide the highest stress sensitivity among conventional ultrasonic wave modes [146, 147]. The transition from single-element probes to phased-array implementations has further improved robustness, repeatability, and suitability for automated inspection [61, 65, 66, 114]. Beyond stress measurement, phased-array ultrasonic datasets have increasingly been exploited for microstructural characterisation, including grain size estimation from attenuation and backscatter statistics, and discrimination between equiaxed and columnar morphologies [67, 148–150]. More recent studies have also demonstrated sensitivity to macrozones and texture-induced anisotropy in additively manufactured alloys [96].

LCR waves are also sensitive to microstructure. Grain morphology, texture, and heterogeneity influence LCR attenuation, backscatter, and spectral response, particularly within the shallow penetration depth where advanced manufacturing processes exhibit the strongest microstructural gradients [66]. Despite this, microstructural effects are often treated as a source of uncertainty or noise in RS measurements, rather than as a complementary source of information [66]. Recent developments in phased-array implementations of LCR waves have further highlighted the broader sensitivity of these measurements beyond RS alone. Luo et al [151] introduced a phased-array-based LCR strategy (PA-LCR) that relaxes

the strict dependence on the first critical angle, enabling robust excitation across a range of incident angles and material wave velocities through beam steering and focusing. This improves adaptability of LCR measurements in heterogeneous and variable materials. In subsequent work [152], the same framework was extended to anisotropic fibre-reinforced composites, where LCR wave amplitude was shown to correlate with microstructural degradation during hygrothermal ageing, with the ultrasonic response interpreted in terms of evolving material anisotropy and internal structure. These studies demonstrate that phased-array LCR measurements inherently contain microstructure-sensitive information, although they do not explicitly address the separation of stress and microstructural contributions within a unified measurement framework.

LCR waves exhibit high sensitivity to RS, with ToF between transmitter and receiver commonly used for stress evaluation [140]. Bringing LCR and phased-array ultrasonics together was originally introduced by Javadi et al [114] and subsequently termed PAURS [65, 66]. The development of PAURS represented an improvement over conventional single-element LCR techniques, enabling increased measurement redundancy, improved signal stability, and practical deployment in automated and robotic inspection environments [61, 65, 66, 114]. While PAURS has demonstrated robustness for residual-stress mapping, its accuracy across heterogeneous microstructures remains limited. The present study focuses not on further validation of stress recovery, but on identifying how different LCR observables respond to stress and microstructure independently.

Recent PA-LCR and PAURS studies have demonstrated sensitivity of LCR measurements to both RS and microstructural state, including grain morphology, texture, and damage evolution. However, these studies typically treat such sensitivities either implicitly or as sources of uncertainty, without explicitly assigning dominant physical roles to individual ultrasonic observables extracted from the same dataset. As a consequence, while sensitivity is established, it remains unclear which LCR observables can be reliably interpreted as stress-dominated and which primarily encode microstructural information under controlled conditions. This unresolved ambiguity limits both quantitative stress evaluation and the systematic use of phased-array LCR data for multi-field characterisation. The present study directly addresses this gap by establishing an observable-level interpretation framework under stress-relieved conditions.

7.1.4 Observable-Level Characterisation for Decoupling Stress and Microstructure (PAURS+)

Ultrasonic measurements contain multiple observables, such as ToF, attenuation, backscattered energy, and frequency-domain behaviour, each governed by different physical mechanisms. In phased-array LCR ultrasonics, the measured observables arise from different stress- and microstructure-dependent mechanisms. Their relative sensitivities are therefore examined within a single ultrasonic acquisition.

This study adopts this perspective as the conceptual foundation for PAURS+, denoting a microstructure-aware extension of PAURS based on observable-level interpretation. To examine these sensitivities clearly, a stress-relieved AFSD aluminium specimen with distinct equiaxed and elongated microstructures is used. Suppressing macroscopic RS allows the microstructural contributions to attenuation, backscatter, and spectral content to be assessed directly, while verifying that LCR ToF remains comparatively stable under macroscopically stress-relieved conditions.

This work establishes an experimental foundation for observable-level interpretation of phased-array LCR ultrasonics by identifying which LCR observables exhibit strong sensitivity to microstructural variation, and which show comparatively weak microstructural dependence under the present conditions. This clarification supports future efforts to isolate stress- and microstructure-related contributions from the same phased-array LCR dataset.

7.2 Results and Discussion

7.2.1 Microstructural Characterisation

7.2.1.1 EBSD Sample preparation

Samples for EBSD analysis were sectioned and warm mounted in a conductive copper-based resin. Surface preparation was performed by sequential grinding using SiC papers (P240–P4000), followed by polishing with 3 µm and 1 µm diamond suspensions. Final surface preparation was carried out using colloidal silica (OPS Non-Dry) to remove residual deformation and obtain a surface suitable for EBSD analysis.

7.2.1.2 EBSD Characterisation

The EBSD areas were chosen to correspond to the ultrasonic inspection locations so that the microstructural observations could be directly related to the ultrasonic measurements. EBSD was performed using an AZtec HKL Advanced (C5 Premium) Nordlys Max 2 detector installed on a FEI Quanta 650 field-emission gun SEM at the AFRC. An indexing rate of at least 90% was obtained across the mapped regions. The working distance was 27.5 mm, and the accelerating voltage was 20 kV for all scans. Grain boundary analysis was carried out using a misorientation criterion greater than 10°, taken to represent high-angle grain boundaries.

*Figure 56*a and *Figure 56*b show the EBSD inverse pole figure (IPF) maps of the deposited Al within the AFSD region in the as-deposited and heat-treated conditions, respectively. In both cases, the microstructure is characterised by fine, equiaxed grains with a relatively uniform distribution across the analysed region. The area weighted mean grain size (*Figure 57*) is approximately 3-4 µm, indicating a refined grain structure. Such refinement is typical of the AFSD process, where high friction and intense shear deformation at elevated temperatures promote dynamic recrystallisation. During this process, deformation of the original grains leads to the formation of new recrystallised grains and

subgrain structures, resulting in the observed equiaxed/fine morphology [153]. EBSD was used to characterise grain morphology and crystallographic orientation in the deposited and substrate regions. The results are presented as Inverse Pole Figure maps with superimposed Grain Boundaries (IPF + GB). In each map, the colour within a grain represents its crystallographic orientation relative to the selected sample reference direction, according to the accompanying IPF colour key. The boundary-line colours indicate the grain-boundary classifications defined by their misorientation-angle ranges. The IPF key, boundary legend, sample direction and scale bar are included in each figure.

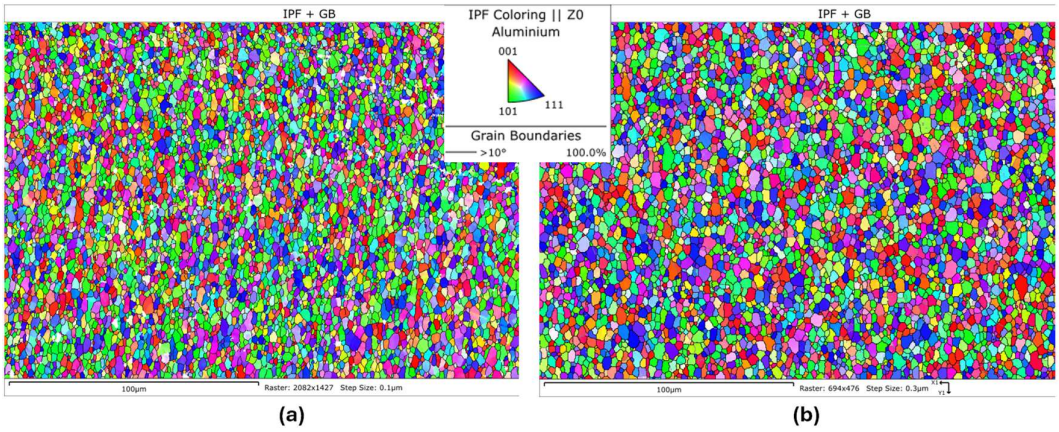


Figure 56. EBSD inverse pole figure (IPF) maps of the AFSD-deposited region of the AA7075 component: (a) as-deposited condition (Sample#1) and (b) heat-treated condition (Sample#2), showing a fine equiaxed grain structure. [101]

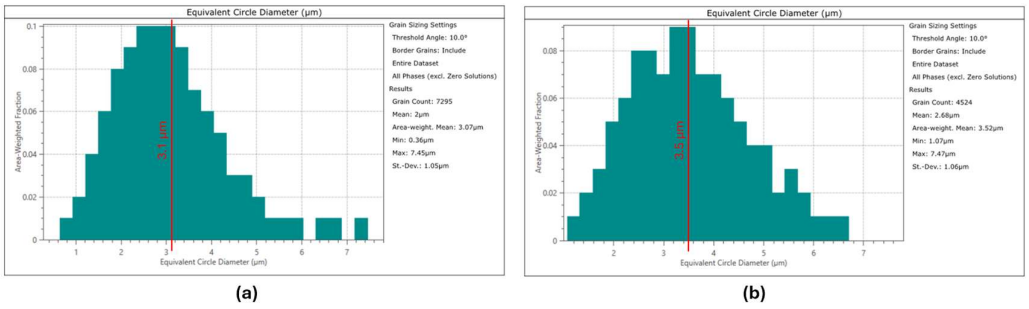


Figure 57. Grain size distribution derived from the EBSD maps for (a) as-deposited condition (Sample#1) and (b) heat-treated condition (Sample#2). [101]

*Figure 58*a and *Figure 58*b show the microstructures of the substrate in the as-deposited and heat-treated conditions, respectively. In contrast to the FEG observed in the deposited AFSD region, the substrate exhibits coarse and significantly elongated grains. The average grain width is approximately 10 µm and 14 µm for the as-deposited and heat-treated conditions, respectively, while the grain length

extends to several hundred micrometres. This pronounced grain elongation indicates that the substrate material was originally processed by rolling.

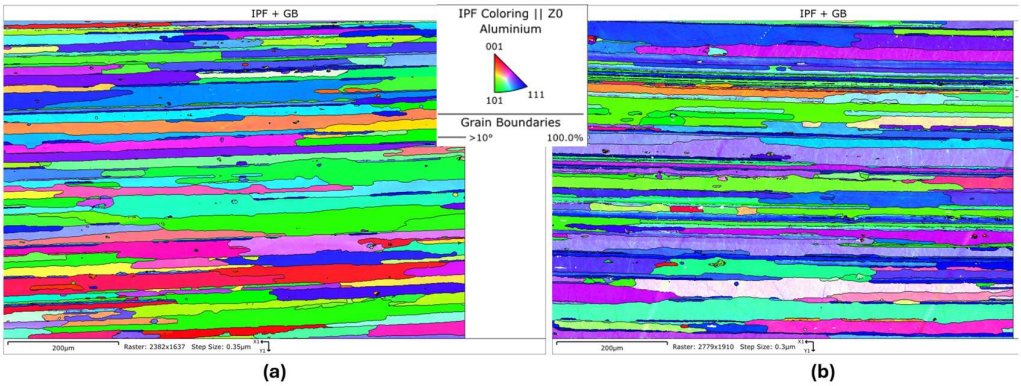


Figure 58. EBSD inverse pole figure (IPF) maps of the substrate region of the AA7075 component: (a) as-deposited condition (Sample#1) and (b) heat-treated condition (Sample#2), showing a coarse and elongated grain structure. [101]

For clarity, different EBSD-derived length measures are reported here to reflect the distinct grain morphologies present in the two regions. In the AFSD-deposited material, grains are fine and approximately equiaxed, such that an area-weighted mean grain size provides an appropriate characteristic measure. In contrast, the substrate exhibits strongly elongated grains resulting from rolling, for which grain width and grain length represent distinct microstructural dimensions. In subsequent ultrasonic analysis, these measures are interpreted in relation to wave propagation direction and wavelength, rather than as a single scalar grain size common to both regions.

Based on these EBSD results, the AFSD region can be confidently classified as FEG, while the substrate can be classified as CEG. These two microstructural conditions serve as the reference states for interpreting the ultrasonic attenuation, backscatter, and spectral differences presented later in the Results and Discussion section.

7.2.2 Assumptions and Scope of RS State

The following analysis is conducted under the assumption of negligible macroscopic (Type I) RS, with remaining ultrasonic variations interpreted primarily in terms of microstructural effects. It is important to note that this study does not quantify RS directly. Instead, it establishes a controlled condition in which macroscopic stress is minimised, enabling isolation of microstructural influences on LCR observables. Full decoupling of stress and microstructure, including quantitative reconstruction of both fields, requires combined experimental campaigns and is the subject of ongoing work.

This assumption is supported by the specimen preparation methodology, including EDM sectioning and stress-relief heat treatment, which are widely used to minimise macroscopic RS in RS

measurement practice. Any remaining stress state is expected to be dominated by microstructural-scale (Type II/III) effects, which operate over length scales significantly smaller than the ultrasonic wavelength and therefore have a negligible influence on the acoustoelastic component of LCR ToF. These microstructural-scale effects are intrinsic to the material and form part of the ultrasonic response investigated here.

The analysis presented here focuses on identifying consistent observable-level trends between distinct microstructural states rather than on statistical generalisation; representative plots are therefore used to illustrate repeatable behaviour confirmed across multiple acquisitions, with full statistical characterisation reserved for future work.

7.2.3 ToF: Pulse-Echo vs LCR

Absolute ToF was initially considered for comparing the FEG and CEG regions. However, absolute arrival time includes contributions from coupling-layer thickness, interface transmission, wedge propagation and fixed instrumentation delay, in addition to propagation within the material. Differential measurements were therefore adopted to reduce these common timing contributions and improve the reliability of the microstructural comparison.

The differential measurement was defined differently for the two ultrasonic modes because their waveforms contain different reference features. For pulse-echo measurements, two successive backwall echoes were available within the same A-scan. The time interval between these echoes was therefore used, allowing the shared coupling, interface and instrumentation delays to cancel to first order. For LCR measurements, no equivalent second LCR arrival was available within the same A-scan. A path-span metric was therefore introduced using the ToF difference between the selected earliest and latest phased-array LCR paths acquired under the same delay law.

The pulse-echo backwall interval and LCR path-span are therefore not equivalent physical quantities. The pulse-echo metric represents repeated through-thickness propagation, whereas the LCR metric represents the timing spread between selected near-surface phased-array paths. Both were adopted to provide internally referenced measurements with reduced sensitivity to common timing offsets, but their magnitudes should not be compared directly without normalisation.

7.2.4 Pulse-Echo ToF (through-thickness averaging)

In practice, repeatable pulse-echo measurements required consistent probe alignment, contact pressure and coupling at each inspection position. These factors affected the amplitude and shape of the backwall echoes, particularly when measurements were moved between the FEG and CEG regions. Surface condition and local specimen geometry also influenced probe seating, while the stronger attenuation in the CEG region reduced the number and clarity of the later backwall echoes available for analysis.

The selection of a consistent echo pair presented an additional practical constraint. Later echoes provide a longer material propagation path and potentially greater sensitivity to velocity differences, but their amplitudes decrease through repeated propagation and reflection. This effect was more pronounced in the CEG region, where scattering and attenuation caused the backwall echoes to deteriorate more rapidly. The same identifiable pair of successive echoes was therefore selected for the FEG and CEG measurements, rather than selecting different echoes according to their individual signal strengths.

Couplant and interface delays were reduced by calculating ToF between two backwall echoes within the same A-scan. This differential approach removed timing contributions common to both echoes to first order. However, changes in coupling could still modify waveform amplitude and shape, potentially affecting the identification of the echo position. Repeated acquisitions, consistent equipment settings and verification of the selected echo pair were therefore used to assess measurement stability.

Pulse-echo ToF measurements for Sample #1 and Sample #2 are presented in *Figure 59* and *Figure 60*, respectively. For each location, the full FMC dataset (64 paths) was analysed. These paths are shown collectively, with the mean signal highlighted. ToF was extracted between the same pair of successive backwall echoes in the FEG and CEG regions. This backwall-to-backwall interval follows the differential strategy and primarily represents the through-thickness material transit time. The resulting differences were therefore interpreted in terms of effective longitudinal velocity rather than absolute arrival time.

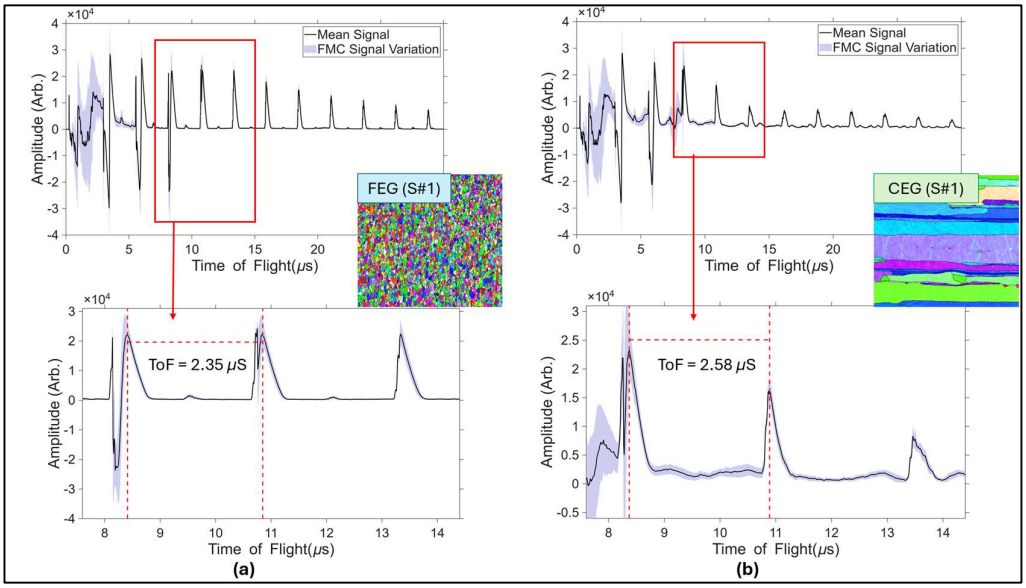


Figure 59. Pulse-echo ToF for Sample #1: (a) FEG, (b) CEG [101]

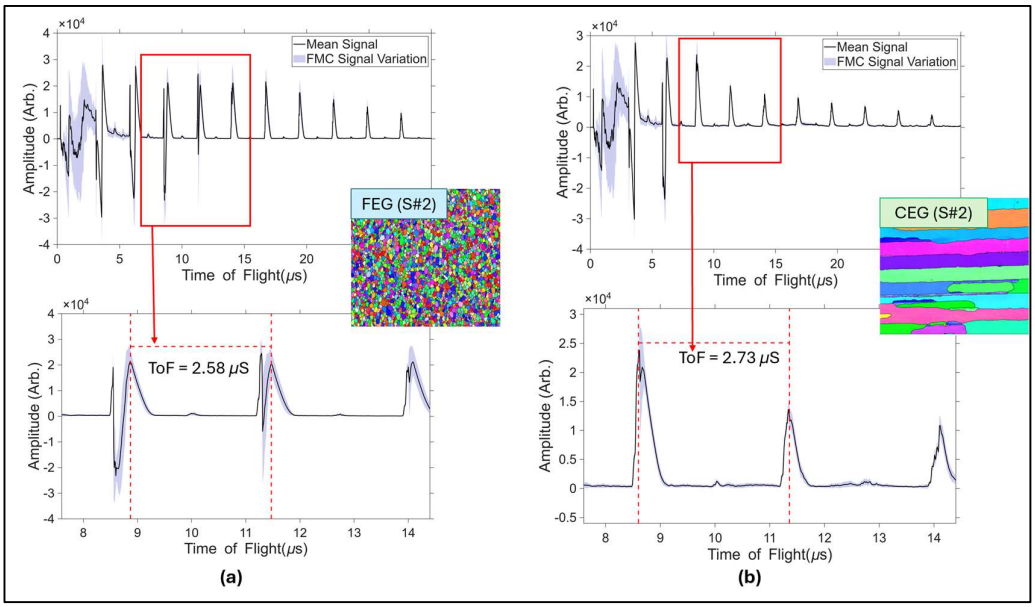


Figure 60. Pulse-echo ToF for Sample #2: (a) FEG, (b) CEG [101]

The longer pulse-echo ToF in the CEG region is consistent with the coarse elongated grain morphology identified by EBSD. Unlike the fine equiaxed AFSD region, the rolled substrate contains elongated grains and a direction-dependent crystallographic structure. The through-thickness pulse-echo wave therefore samples a different effective elastic response in the CEG region, producing a lower average longitudinal velocity and a corresponding increase in ToF. The smaller FEG–CEG difference following heat treatment suggests that heat treatment reduced, but did not remove, the acoustic contrast between the two microstructural regions. Because the specimens were treated as macroscopically stress relieved, these ToF differences are interpreted primarily as microstructure-related rather than as evidence of Type I RS. However, pulse-echo ToF alone cannot distinguish the individual contributions of grain morphology, texture and local material properties.

Using the consistently selected backwall-echo pair, Sample #1 exhibited a CEG ToF of 2.58 µs (*Figure 59*b) which is approximately 230 ns longer than 2.35 µs measured in the FEG deposit (*Figure 59*a); *ΔToF* = 230 ns. In Sample #2, *ΔToF* is smaller, because Sample #2 had heat treatment, at around 150 ns (*Figure 60*). These differences arise from microstructure-induced variations in effective through-thickness longitudinal velocity rather than RS, as both samples were treated to minimise macroscopic stress.

7.2.5 LCR ToF (near-surface, stress-dominated)

7.2.5.1 Identification of the LCR arrival

Correct identification of the LCR mode is a prerequisite for reliable ToF analysis. Figure 61 summarises the wave propagation paths generated at different incident angles. When the wedge angle satisfies the

first critical condition (≈22° in the present Rexolite–aluminium configuration, see Figure 61a), the incident longitudinal wave becomes critically refracted and propagates parallel to the specimen surface, forming the LCR mode (path A). At higher angles, refraction produces shear waves, while at lower angles longitudinal waves reflect from the backwall. Consequently, multiple wave modes coexist in the A-scan, making discrimination of the true LCR arrival essential.

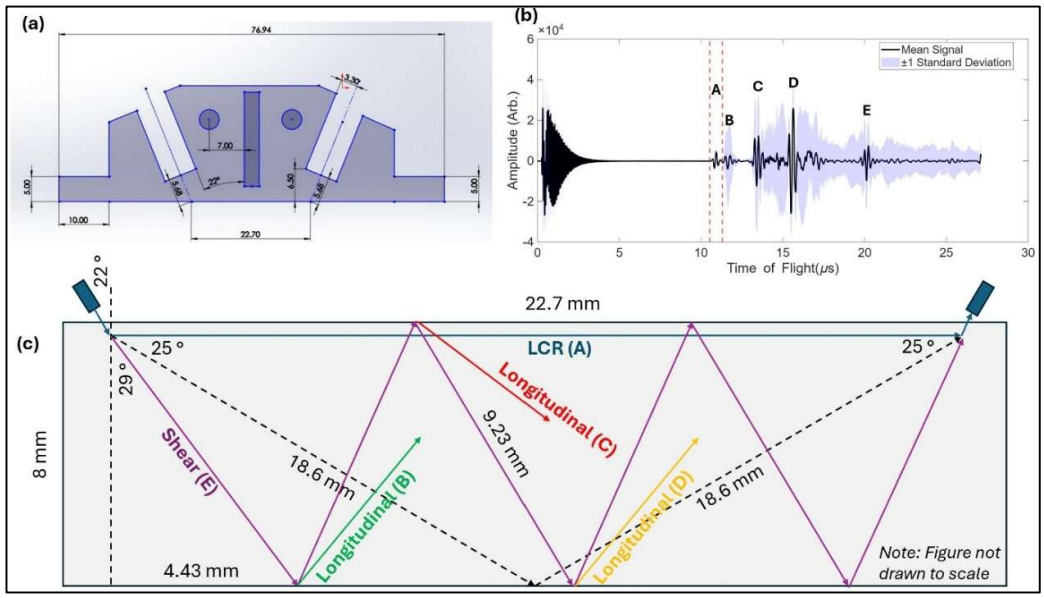


Figure 61. Rexolite wedge dimensions (a), A-scan (b) and LCR path geometry and critical angles (c) [101]

Using the measured bulk longitudinal velocity (~6400 m/s) and the LCR surface path length (22.7 mm), the expected LCR arrival is ~11 µs after accounting for wedge transit and electronic delay, consistent with region A in *Figure 61*b. The later ~14.9 µs arrival corresponds to the shear path (region E). Therefore, region A is identified as the purely longitudinal wave (LCR), region E as the pure shear wave, while the intermediate regions (B–D) arise from mode-converted longitudinal and mixed-mode components.

7.2.5.2 Waveform verification

Figure 62 verifies the LCR identification by contrasting the temporal coherence and path-to-path synchrony of the earliest arrival against later, mixed-mode packets. *Figure 62*a shows the first, most coherent packet with (i) a common zero-crossing and (ii) minimal phase dispersion across all transmit–receive pairs; behaviours characteristic of phased-array LCR reception [65, 66]. In LCR stress measurements, the earliest-arrival criterion in combination with such across-path synchrony is widely used to discriminate the LCR mode from later shear or mode-converted components, whose longer or refracted trajectories yield delayed, more variable waveforms.

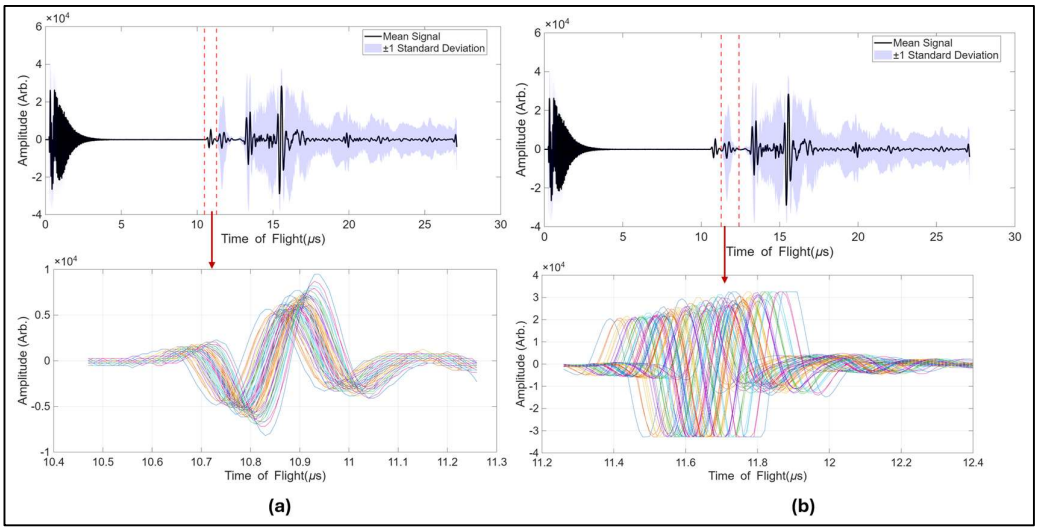


Figure 62. LCR arrival verification: (a) stable LCR waveform, (b) mode-converted arrival [101]

*Figure 62*b exhibits the expected increase in arrival-time spread, envelope variability, and phase inconsistency associated with later mode-converted and scattered wave components, which are more sensitive to local anisotropy and microstructural heterogeneity. The coexistence of an early, tightly clustered waveform packet and later, more variable arrivals supports the interpretation that the earliest stable arrival corresponds to the dominant LCR mode used for ToF analysis in RS applications.

In an idealised geometric LCR framework, the material transit component is expected to remain constant for element pairs spanning the same effective surface-parallel propagation path, such that identical LCR arrival times would be obtained after excluding wedge and system delays. This idealised ToF invariance has been discussed previously for geometrically equivalent LCR paths [66]. However, in the practical phased-array implementation used here, the recorded arrival time also includes imposed delay-law offsets, wedge transit contributions, element-dependent coupling variations, and fixed instrumentation timing. As a result, small path-dependent differences remain in the measured absolute ToF, even when the nominal LCR propagation distance is comparable. Accordingly, the present study does not interpret absolute inter-path ToF equality as a requirement; instead, it evaluates the relative ToF spread across paths acquired under identical delay-law and coupling conditions and uses this path-consistent differential behaviour as the basis for comparing FEG and CEG regions. In practice, the earliest stable arrival is defined as the first waveform packet exhibiting consistent arrival time, phase, and zero-crossing across all transmit–receive pairs within the FMC dataset. Repeat acquisitions confirmed frame-to-frame ToF variation within a few nanoseconds.

7.2.5.3 FEG vs CEG LCR ToF

Following the differential strategy introduced previously, the LCR analysis required a different internal reference from the pulse-echo measurement. Because the LCR waveform did not contain a second

equivalent in-material arrival, a same-trace backwall-to-backwall interval could not be calculated. The ToF span between T1R1 and T8R8 was therefore used as a within-frame differential metric under the same phased-array delay law. This reduced sensitivity to timing contributions common to the selected paths and avoided interpreting absolute arrival-time offsets as microstructural differences.

Figure 63 and Figure 64 therefore present the LCR path-span comparison rather than absolute LCR ToF. This change in metric was necessary because the differential backwall method used for pulse echo could not be transferred directly to the LCR waveform.

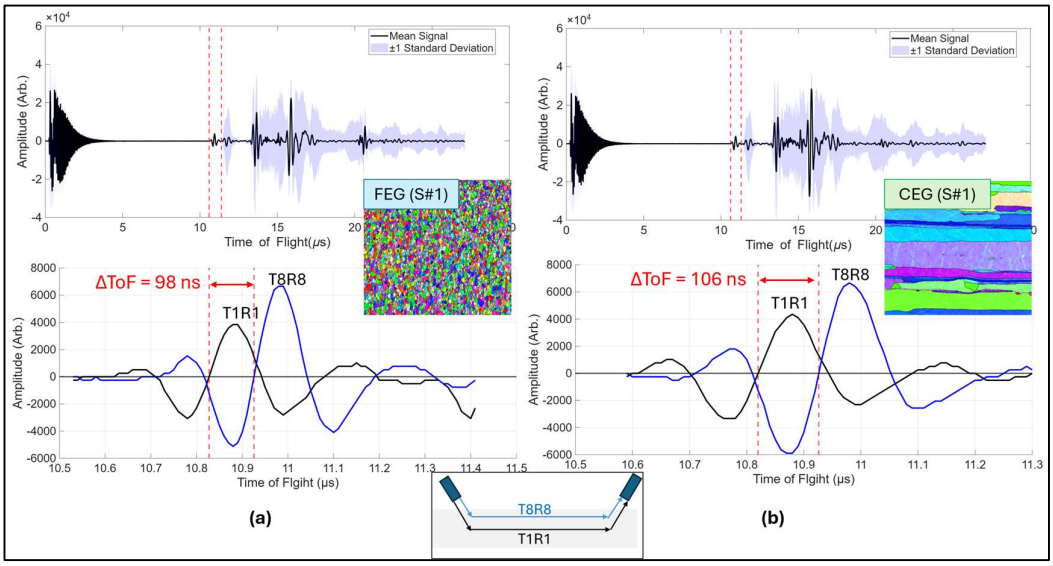


Figure 63. Fastest (T1R1) and slowest (T8R8) LCR path arrivals in FEG (a) and CEG (b) in Sample#1 [101]

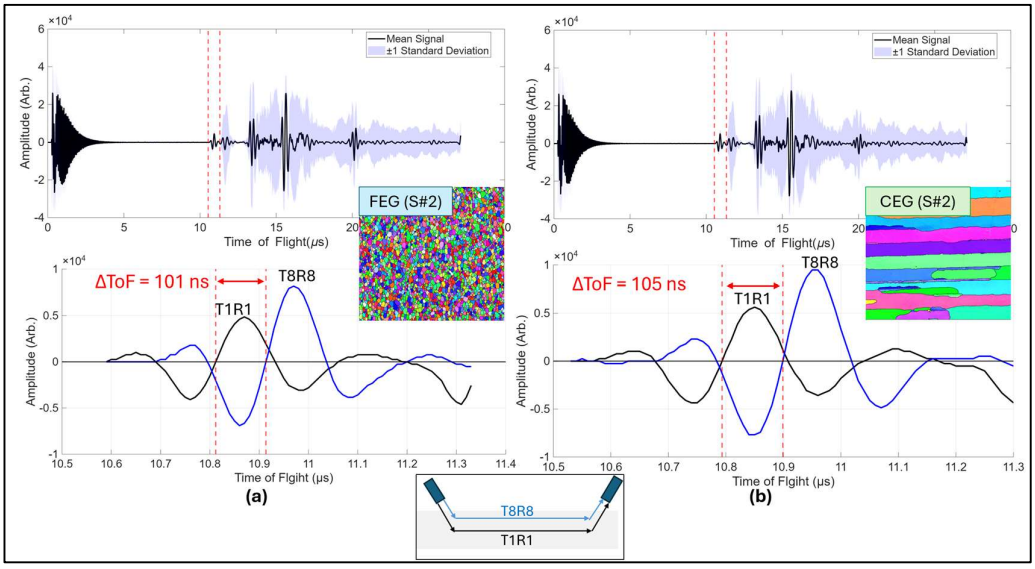


Figure 64. Fastest (T1R1) and slowest (T8R8) LCR path arrivals in FEG (a) and CEG (b) in Sample#2 [101]

As discussed, the relevant comparison is not whether all paths exhibit identical absolute ToF, but whether the within-frame T1R1–T8R8 ToF span changes between FEG and CEG under identical acquisition settings. Because the same delay law was applied in both regions, this *ΔToF* metric would be expected to remain nominally unchanged unless the FEG–CEG microstructural transition introduces an additional perturbation to LCR propagation. In Sample #1, the FEG region (*Figure 63*a) exhibits a *ΔToF* of 98 ns, while the CEG region (*Figure 63*b) shows a *ΔToF* of 106 ns, corresponding to a difference of only 8 ns. This variation is even smaller in Sample #2: the FEG region (*Figure 64*a) has a *ΔToF* of 101 ns, and the CEG region (*Figure 64*b) has a *ΔToF* of 105 ns, giving a difference of just 4 ns. These results indicate that the FEG–CEG transition produces only a minor change in the LCR path-span ToF metric compared with the much stronger microstructure sensitivity observed in attenuation, backscatter, and frequency-domain indicators.

Given the small differences observed, four additional independent frames were acquired in each region to assess repeatability and quantify frame-to-frame variation in the T1R1–T8R8 *ΔToF* metric. The frame-averaged *ΔToF* values are summarised in *Table 6*, showing mean *ΔToF* of ~4 ns (Sample #1) and ~2 ns (Sample #2).

Table 6. LCR path-span ΔToF (T1R1–T8R8) measured across multiple frames in FEG and CEG regions for Sample #1 and Sample #2

Sample	**Frame**	**FEG path-span *ΔToF* (T1R1–T8R8, µs)**	**CEG path-span *ΔToF* (T1R1–T8R8, µs)**	**Absolute difference (ns)**
1	1	0.098	0.106	8
1	2	0.102	0.099	3
1	3	0.103	0.102	1
1	4	0.097	0.101	4
1	Mean			4
2	1	0.099	0.099	0
2	2	0.101	0.101	0
2	3	0.101	0.105	4
2	4	0.100	0.104	4
2	Mean			2
**Note: ΔToF denotes the within-frame arrival-time span between the earliest and latest phased-array LCR paths under an identical delay law.*				

The pulse-echo ToF differences and their relationship to the elongated CEG microstructure were discussed alongside Figures 59 and 60. In comparison, the LCR path-span metric varied by only a few nanoseconds between the FEG and CEG regions. Although the pulse-echo and LCR metrics represent different propagation paths and sampling volumes, their order-of-magnitude difference indicates that LCR path-span ToF was comparatively less sensitive to the investigated microstructural transition under the present conditions. This supports its use as the predominantly stress-sensitive observable within PAURS+, without implying that LCR ToF is intrinsically independent of microstructure.

The T1R1–T8R8 ΔToF metric is used as an upper-bound sensitivity measure rather than a statistical descriptor of the 64-path distribution. It captures the maximum observable differential delay within the fixed delay-law aperture. Because LCR ToF variations in this configuration are primarily governed by stress-dependent velocity changes, any microstructure-induced effect would manifest within this bound. The small ΔToF differences observed between FEG and CEG (4–8 ns range across frames) indicate that travel-time variations are below experimental resolution, whereas attenuation and spectral features show clear microstructural sensitivity and are therefore more appropriate for ensemble analysis.

As established, the pulse-echo backwall interval and LCR path-span are not directly commensurate because they represent different propagation paths and sampling volumes. The comparison presented here is therefore intended to provide order-of-magnitude context for microstructure-induced travel-time variation, rather than a normalized or dimensionless equivalence between the two metrics. A rigorous quantitative comparison would require normalization using velocity- or length-based measures (e.g. $\Delta\tau/\tau$ or $\Delta v/v$), which is beyond the scope of the present exploratory study.

7.2.6 Attenuation

7.2.6.1 Definition of Attenuation in Pulse-Echo and LCR Measurements

In this study, attenuation is treated as an observable-level metric describing amplitude reduction associated with material-induced scattering and absorption, rather than as an intrinsic material constant. Its practical definition and normalisation depend on the ultrasonic configuration and propagation geometry.

For pulse-echo measurements, attenuation is evaluated from the decay of successive backwall echoes within the same A-scan and is normalised by the known through-thickness propagation distance. This differential, intra-signal formulation suppresses the influence of coupling conditions, interface losses, and fixed system gain that are common to both echoes.

For LCR measurements, attenuation is evaluated from differential amplitude changes between phased-array LCR propagation paths along the surface-parallel direction. Because no equivalent

second LCR arrival exists within the same A-scan, a path-to-path differential formulation is used to provide internal normalisation and to reduce sensitivity to absolute amplitude scaling, coupling variations, and fixed system delays.

Attenuation can also be evaluated in the frequency domain using a spectral-ratio method, in which the logarithmic ratio of spectra measured over two propagation distances is calculated as a function of frequency. This approach can provide frequency-dependent attenuation and may be less sensitive than a single peak-amplitude measurement to local waveform fluctuations. However, reliable application requires comparable acoustic paths, consistent beam behaviour, adequate spectral SNR and correction for diffraction and interface effects. In the present study, time-domain amplitude ratios were used as practical attenuation metrics, while the energy-normalised FFT analysis was used separately to examine spectral redistribution. A calibrated frequency-domain attenuation measurement would provide a useful extension for future work.

7.2.6.2 Pulse-Echo Attenuation

Pulse-echo attenuation for Sample #1 and Sample #2 is shown in *Figure 65* and *Figure 66*, respectively. In both samples, the attenuation behaviour differs markedly between the two microstructural regions. The CEG consistently exhibits higher attenuation, while the FEG region shows lower loss and more sustained echo visibility. In Sample #1 and Sample #2 alike, backwall echoes in the FEG region remain clearly identifiable for up to approximately 40 µs, whereas echoes in the CEG deteriorate much more rapidly, typically within 20–30 µs. The elongated grains and strong directional texture in the CEG produce greater scattering and absorption, leading to faster signal decay, while the equiaxed FEG microstructure supports more uniform propagation with reduced scattering.

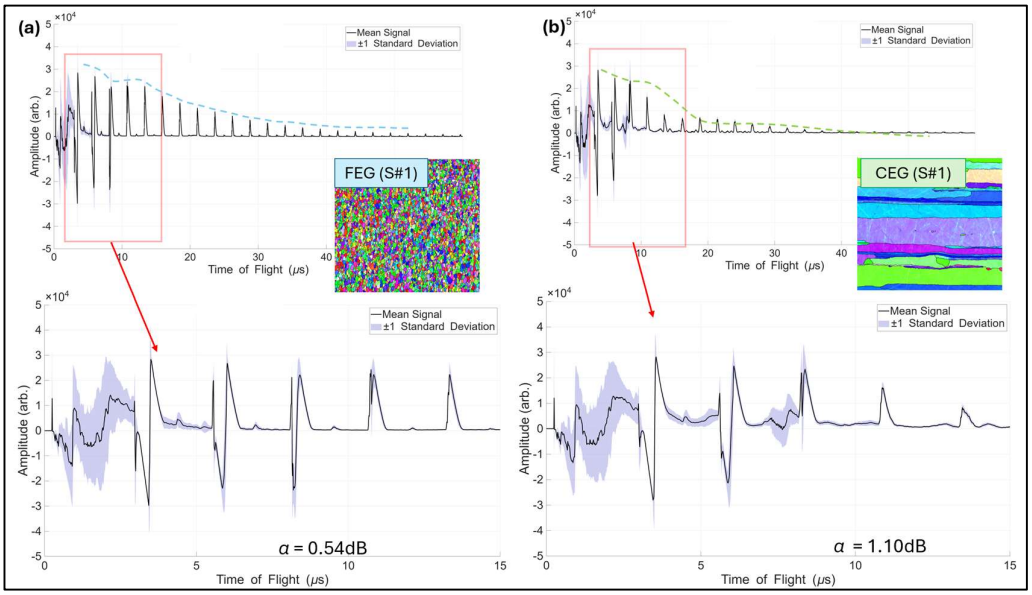


Figure 65. Pulse-echo attenuation in Sample #1 (a: FEG, b: CEG) [101]

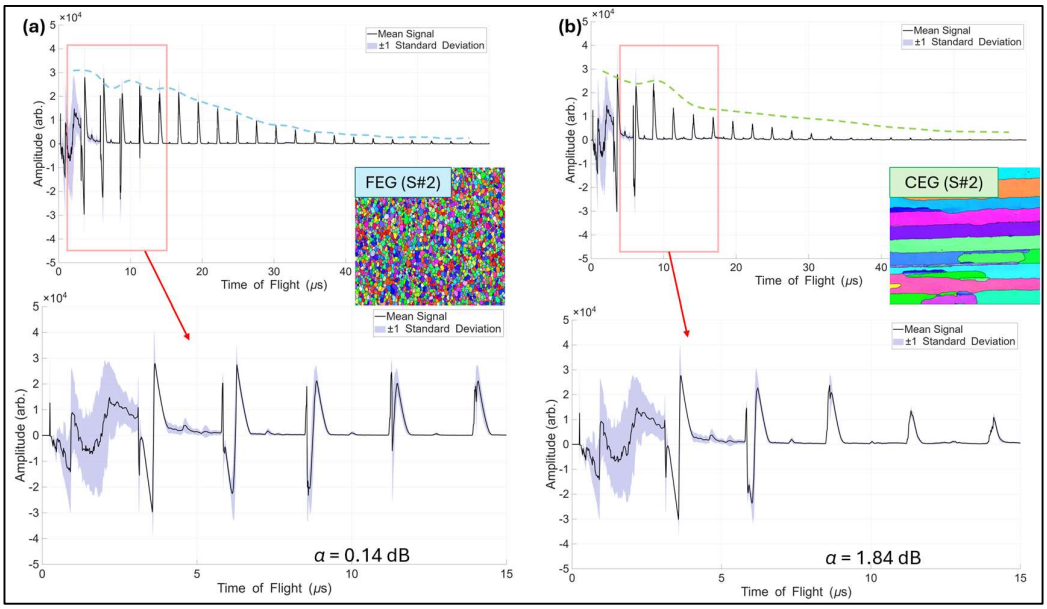


Figure 66. Pulse-echo attenuation in Sample #2 (a: FEG, b: CEG) [101]

Although only the first five echoes are shown, attenuation was calculated using all measurable echoes. Attenuation is quantified by examining the amplitude reduction across successive backwall reflections. To suppress noise effects, multiple echoes are included in the calculation. If $\boldsymbol{A_1, A_2, \ldots, A_n}$ denote the amplitudes of successive backwall peaks, an effective attenuation metric is defined as:

$$\alpha = \frac{20}{2L(n-1)} \sum_{k=1}^{n-1} \log_{10}\left(\frac{A_k}{A_{k+1}}\right) \qquad (10)$$

Equation 27 Multi-echo pulse-echo attenuation estimate from successive backwall amplitude ratios

For phased-array measurements, where FMC provides multiple transmitter–receiver combinations $(\boldsymbol{i}, \boldsymbol{j})$, this expression is extended by averaging over all $\boldsymbol{N}$ array elements:

$$\alpha_{\mathrm{PA}} = \frac{1}{N^2} \sum_{i=1}^{N} \sum_{j=1}^{N} \left[\frac{20}{2L(n-1)} \sum_{k=1}^{n-1} \log_{10}\left(\frac{A_k^{(i,j)}}{A_{k+1}^{(i,j)}}\right) \right] \qquad (11)$$

Equation 28 FMC-averaged multi-echo pulse-echo attenuation metric across all phased-array element pairs

Using this effective attenuation metric, the pulse-echo attenuation in Sample #1 is 0.54 dB in the FEG region (*Figure 65*a) and 1.10 dB in the CEG (*Figure 65*b). In Sample #2, the corresponding values are 0.14 dB and 1.84 dB (*Figure 66*). In both samples, the elongated CEG exhibits noticeably lower successive echo amplitudes compared with the equiaxed FEG region, consistent with classical

observations in polycrystalline materials where elongated grains and strong texture enhance scattering and absorption [148, 154].

7.2.6.3 LCR Attenuation

The LCR attenuation results for Sample #1 and Sample #2 are shown in *Figure 67* and *Figure 68*, respectively. For clarity, only the T1R1 and T8R8 paths are compared. In Sample #1, the amplitude change, ΔA, is 2,816 in the fine equiaxed grain (FEG) region (*Figure 67*a) and 3,840 in the coarse elongated grain (CEG) region (*Figure 67*b). Similarly, in Sample #2, ΔA is 2,048 in the FEG region (*Figure 68*a) and again 3,840 in the CEG region (*Figure 68*b). CEG exhibits higher attenuation than FEG in both samples. It is also noted that the T8R8 path consistently displays higher amplitude than T1R1. This is expected because T1R1 corresponds to a longer propagation distance within the material and is therefore more strongly affected by scattering and attenuation along the LCR path.

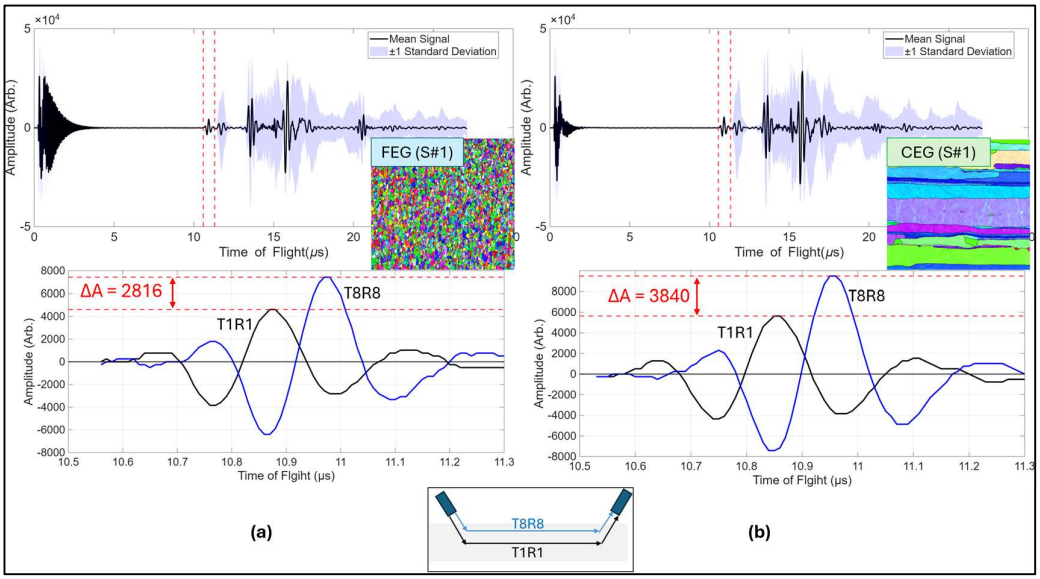


Figure 67. Attenuation of LCR wave propagated in FEG (a) and CEG (b) in Sample#1 [101]

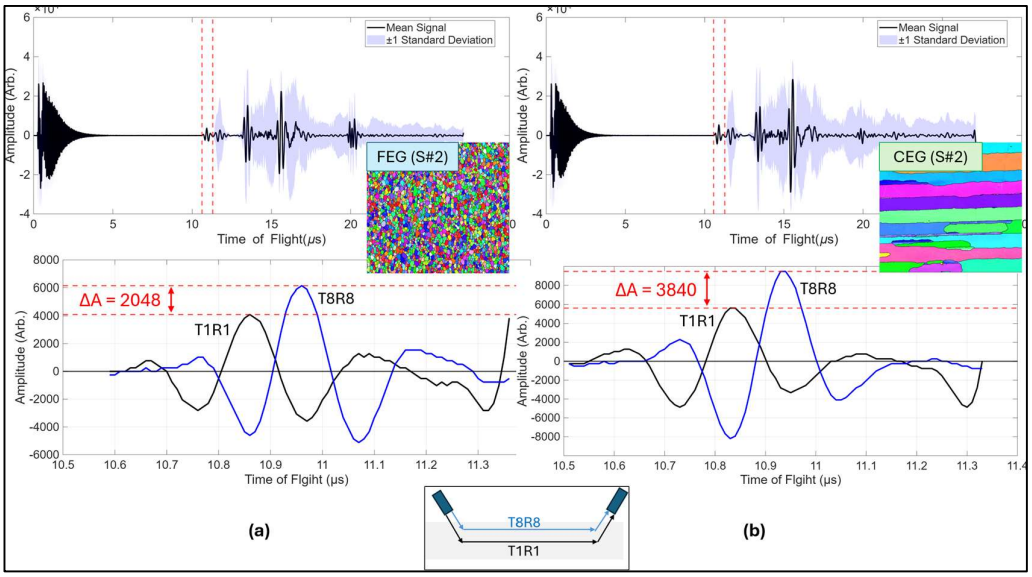


Figure 68. Attenuation of LCR wave propagated in FEG (a) and CEG (b) in Sample#2 [101]

Similar to the pulse-echo case (Sec. 0), LCR attenuation must also be extended across all phased-array transmit–receive paths. Because LCR waves are generated and received using phased-array transducers, amplitude reduction should be evaluated for all available acoustic paths. For a single LCR path, an effective differential attenuation between adjacent transmitter–receiver combinations can be defined as:

$$\alpha = \frac{20\log_{10}\left(\frac{A_{T_iR_j}}{A_{T_mR_n}}\right)}{x} \qquad (12)$$

Equation 29 Effective differential LCR attenuation per unit path length, computed from the amplitude ratio between two neighbouring transmit–receive paths.

where $\boldsymbol{A_{T_iR_j}}$ and $\boldsymbol{A_{T_mR_n}}$ are the peak amplitudes associated with two LCR paths, and $\boldsymbol{x}$ is the additional propagation distance between these paths. Unlike pulse-echo, where distance is determined by backwall thickness, here $\boldsymbol{x}$corresponds to multiples of the array pitch $\boldsymbol{p}$, because LCR signals propagate parallel to the surface.

For a full phased-array acquisition, this expression may be generalised by averaging across all transmitter ($\boldsymbol{N_t}$) and receiver ($\boldsymbol{N_r}$) elements:

$$\alpha_{\mathrm{PA,LCR}} = \frac{1}{N_t N_r} \sum_{i=1}^{N_t} \sum_{j=1}^{N_r - 1} \left[\frac{20}{p} \log_{10} \left(\frac{A_{T_i R_j}}{A_{T_i R_{j+1}}} \right) \right] \qquad (13)$$

Equation 30 Averaged adjacent-path amplitude gradient used to estimate phased-array LCR attenuation

Here, $\boldsymbol{p}$ is the element pitch, and successive pairs $(\boldsymbol{R_j}, \boldsymbol{R_{j+1}})$ represent adjacent LCR propagation paths separated by one pitch increment. Because LCR travel time is effectively invariant across element pairs, this formulation isolates amplitude-based effects that arise from microstructure rather than changes in ToF. This formulation assumes that relative amplitude differences between adjacent LCR paths are dominated by material attenuation and scattering, while beam spreading, diffraction losses, and near-field effects are treated as second-order and common across paths under identical inspection conditions.

Using the attenuation definition in Equation 30, the mean LCR attenuation was computed for all transmitter–receiver combinations, and the results are presented in *Figure 69* and *Figure 70*. In Sample #1, FEG region exhibits a mean attenuation of 1.49 dB, whereas CEG region shows a higher mean attenuation of 2.09 dB (*Figure 69*). A similar trend is observed in Sample #2, where the mean attenuation values are 1.62 dB in the FEG region and 2.38 dB in the CEG region (*Figure 70*).

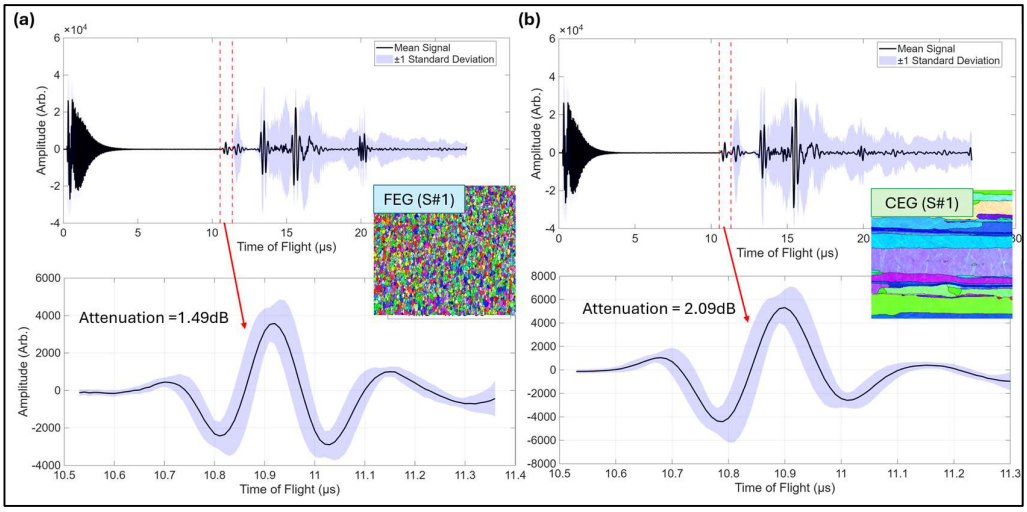


Figure 69. LCR attenuation in Sample #1 (a: FEG – b: CEG) [101]

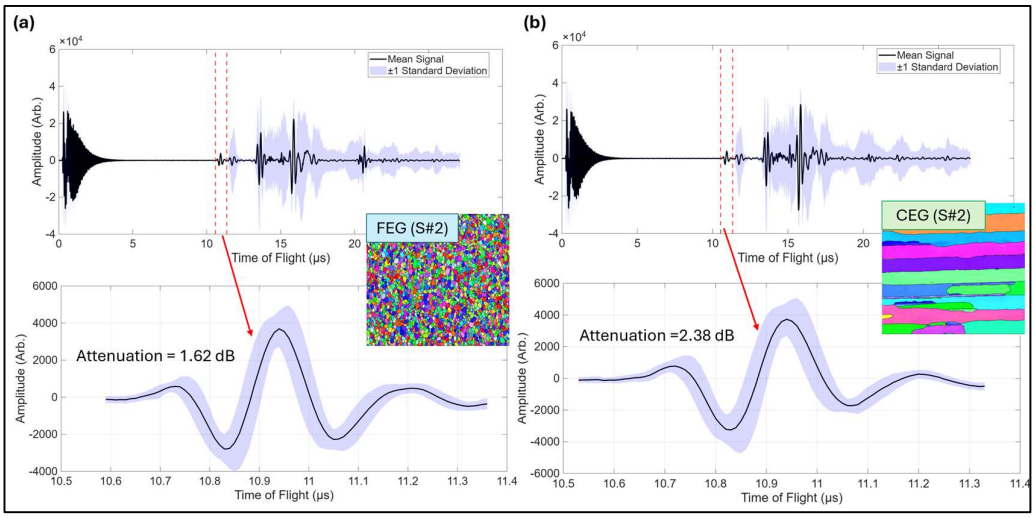


Figure 70. LCR attenuation in Sample #2 (a: FEG – b: CEG) [101]

7.2.7 Backscattering

7.2.7.1 Pulse echo scattering

Pulse-echo backscatter RMS values are presented in *Figure 71* and *Figure 72* for Sample #1 and Sample #2, respectively. In Sample #1, the FEG region yields an RMS of 2230, whereas the CEG region produces a markedly higher RMS of 2370 (*Figure 71*). In Sample #2, the same trend is observed but with increased contrast: the FEG region records an RMS of 2580 and the CEG region 4830 (*Figure 72*). These observations align with expectations for polycrystalline media in which elongated grains and directional texture enhance impedance fluctuations at the grain scale, increasing backscatter energy relative to equiaxed microstructures. The consistently higher RMS in the CEG regions of both samples indicates that the pulse echo backscatter metric is sensitive to the underlying microstructural state.

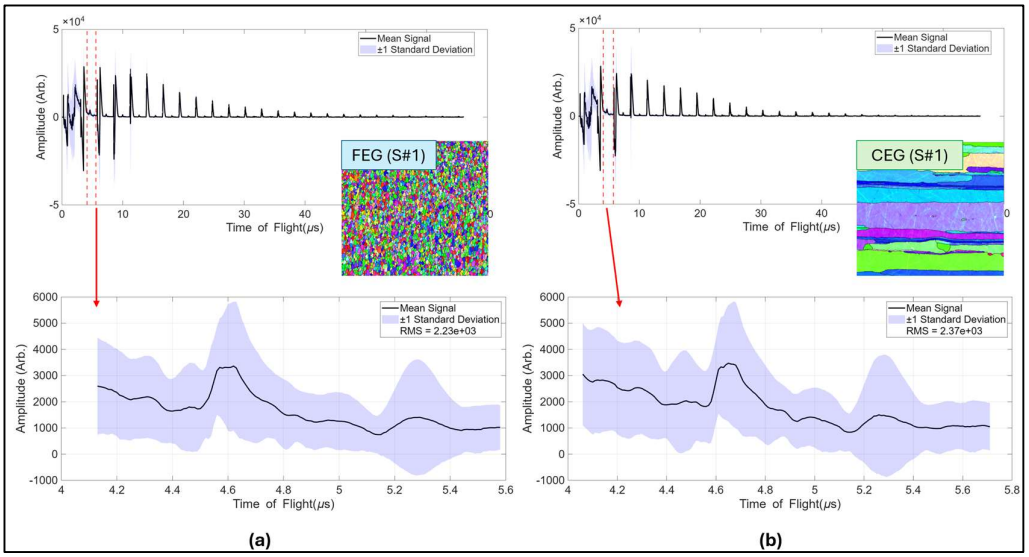


Figure 71. Pulse-echo backscatter RMS in Sample #1 [101]

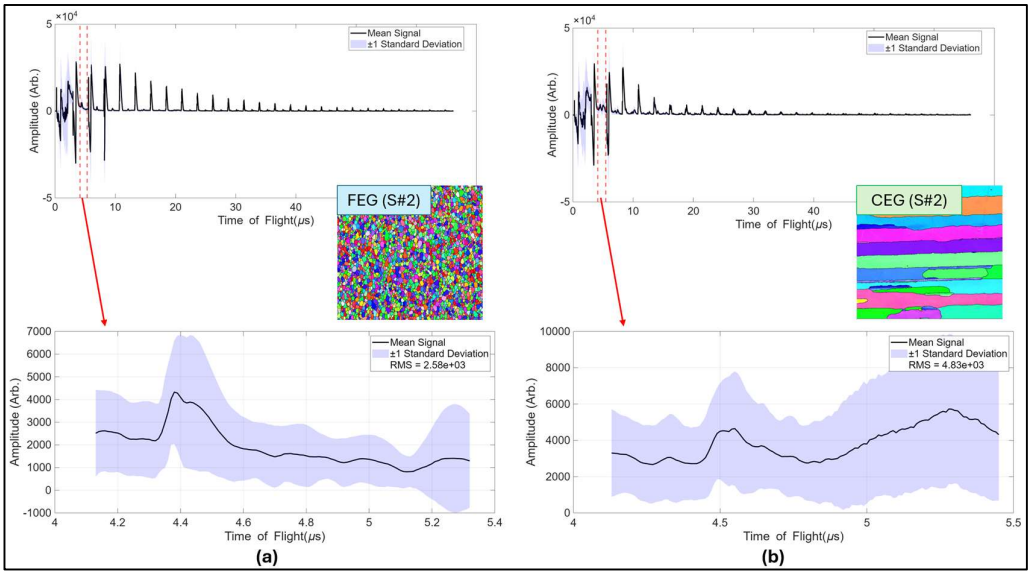


Figure 72. Pulse-echo backscatter RMS in Sample #2 [101]

7.2.7.2 LCR scattering

Backscatter was evaluated within the four post-arrival windows shown in Figure 73. The windows were defined from the observed wave packets rather than selected solely to maximise the FEG–CEG difference. Region A contains the principal coherent LCR arrival and was therefore not expected to provide a direct measure of incoherent backscatter. Regions B and D produced the greatest FEG–CEG contrast, but they represent different parts of the received wavefield. Region B follows the principal LCR arrival and provides a comparatively long window in which scattered energy remains influenced by near-surface LCR propagation. Region D occurs later and provides stronger numerical contrast, but its shorter duration and greater likelihood of containing mode-converted or multipath contributions make its physical interpretation less certain. Region B was therefore selected as the principal comparison window because it provided the more stable and physically relevant measure of LCR-associated backscatter across repeated acquisitions.

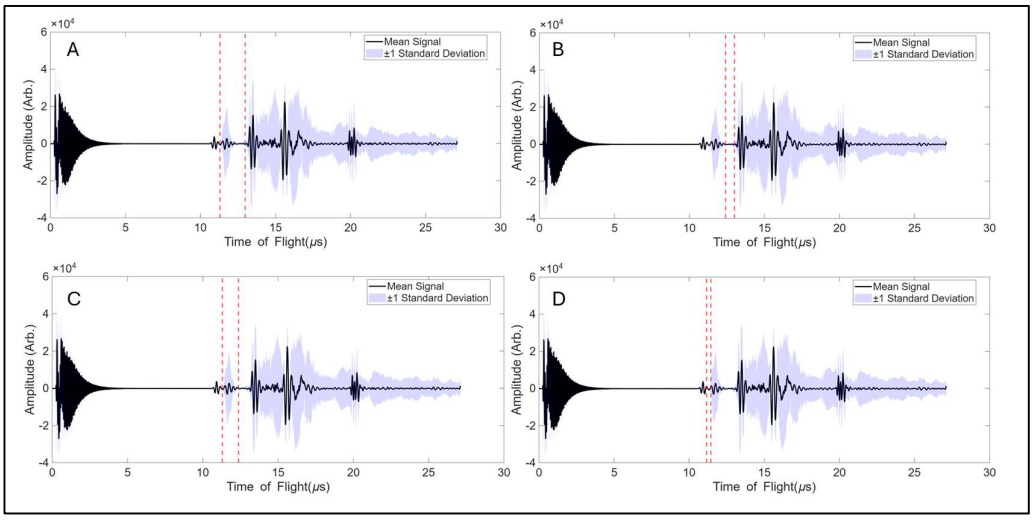


Figure 73: LCR backscatter windows evaluated (Regions A–D) [101]

The comparative analysis in

Table 7 and *Table 8* identifies Regions B and D as the most discriminative for FEG–CEG contrast, with Region B preferred due to its longer usable ToF range and correspondingly greater repeatability across frames, while remaining within a predominantly LCR-influenced interval.

Table 7 Backscatter analysis for sample#1.

Region	FEG Backscatter RMS	FEG ToF Range (µs)	CEG Backscatter RMS	CEG ToF Range (µs)	Percentage Difference
A	6650	1.80	7010	1.80	5.27
B	729	0.65	863	0.60	16.83
C	8430	1.10	8680	1.15	2.92
D	1420	0.35	2030	0.30	35.36

Table 8. Backscatter analysis for sample#2.

Region	FEG Backscatter RMS	FEG ToF Range (µs)	CEG Backscatter RMS	CEG ToF Range (µs)	Percentage Difference
A	7190	1.65	9090	1.75	23.34
B	653	0.60	916	0.55	33.52
C	8910	1.05	11500	1.05	25.38

D	1110	0.25	1950	0.25	54.90

The higher percentage difference obtained from Region D should not be interpreted automatically as evidence that it is the most reliable measurement region. RMS amplitude depends on the position and duration of the selected window, while later arrivals may contain overlapping shear, mode-converted and multiply scattered components. The Region D result is therefore retained as supporting evidence of microstructural contrast, whereas Region B is used for the principal comparison because its location relative to the LCR arrival and its longer usable duration provide greater repeatability.

Representative Region B backscatter results are presented in *Figure 74* and *Figure 75*. In Sample #1, the FEG region exhibits an RMS value of 729, while the CEG region exhibits 863, corresponding to a +16.8% increase. In Sample #2, the FEG region records 653 and the CEG region 916, a +33.5% increase. Across both samples, the CEG region consistently produces higher and more variable LCR backscatter than the FEG region. This behaviour is consistent with elongated, textured microstructures, which introduce stronger elastic contrast and increased orientation-dependent scattering, thereby elevating incoherent backscatter energy relative to equiaxed microstructures.

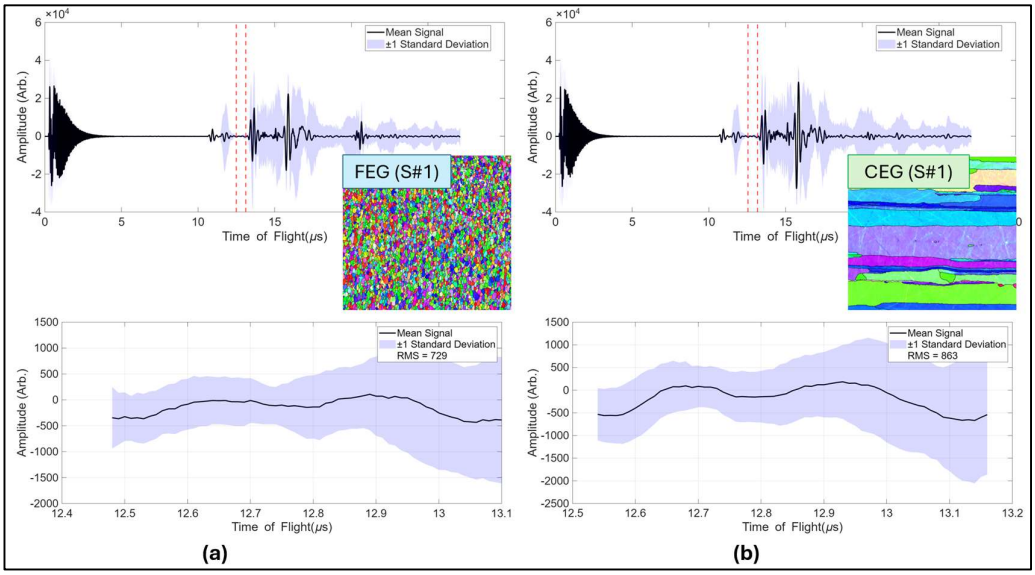


Figure 74. LCR backscatter for Sample #1 (Region B) [101]

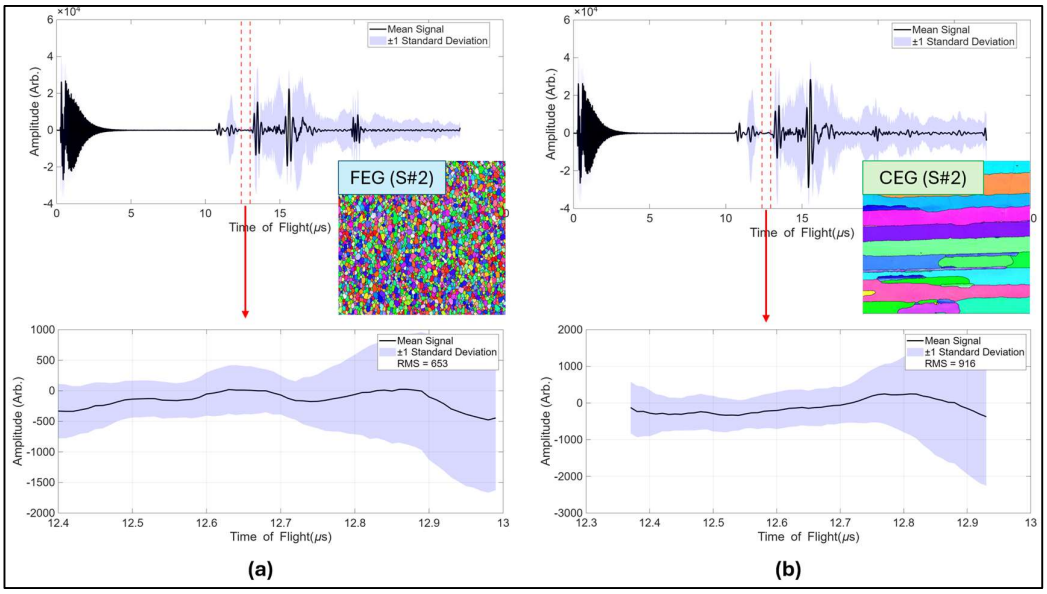


Figure 75. LCR backscatter for Sample #2 (Region B) [101]

It is noted that the Region B ToF windows for FEG and CEG are not always identical (

Table 7 and Table 8); because RMS depends on window length, this can influence the absolute RMS values. However, the observed FEG–CEG contrast (higher RMS in CEG) remains consistent across both samples and repeated acquisitions, indicating that the trend is not an artefact of minor window-length differences. In Figure 74 and Figure 75, the shaded bands visualise the spread of the backscatter response across the FMC transmit–receive paths ($\boldsymbol{T_i R_j}$) within each acquisition and are included to illustrate path-to-path variability (descriptive dispersion), rather than to imply inferential statistical significance.

7.2.8 FFT

7.2.8.1 Frequency-domain processing and spectral metrics

For frequency-domain analysis, each time-domain waveform was energy-normalised prior to FFT computation by dividing the signal by the square-root of the sum of squared amplitudes. From the normalised spectra, the centre frequency $\boldsymbol{f_c}$(amplitude-weighted mean frequency) and the −6 dB bandwidth $\mathbf{BW_{-6dB}} = \boldsymbol{f_{high}} - \boldsymbol{f_{low}}$ were extracted, where $\boldsymbol{f_{low}}$ and $\boldsymbol{f_{high}}$ denote the half-amplitude points around the dominant peak. For LCR measurements, spectra are reported over 0–10 MHz because spectral content above this range is negligible in the present configuration.

The present FFT analysis characterises relative spectral redistribution through centre frequency and bandwidth; it is not a direct frequency-dependent attenuation measurement. Determining a spectral attenuation coefficient would require a spectral-ratio calculation between signals acquired over controlled propagation distances.

7.2.8.2 LCR FFT

The LCR spectra show a consistent dependence on microstructural state (Figure 76 and Figure 77). For Sample #1, the CEG region exhibits a lower centre frequency (3.99 MHz) than the FEG region (4.07 MHz), together with a narrower −6 dB bandwidth (2.89 MHz vs 2.99 MHz). For Sample #2, the same trend is observed: centre frequency decreases from 4.07 MHz (FEG) to 4.04 MHz (CEG) and the −6 dB bandwidth narrows from 2.92 MHz to 2.85 MHz. These shifts indicate modest but repeatable spectral redistribution in the CEG condition, consistent with stronger frequency-selective damping along the near-surface LCR propagation layer in the elongated, textured microstructure.

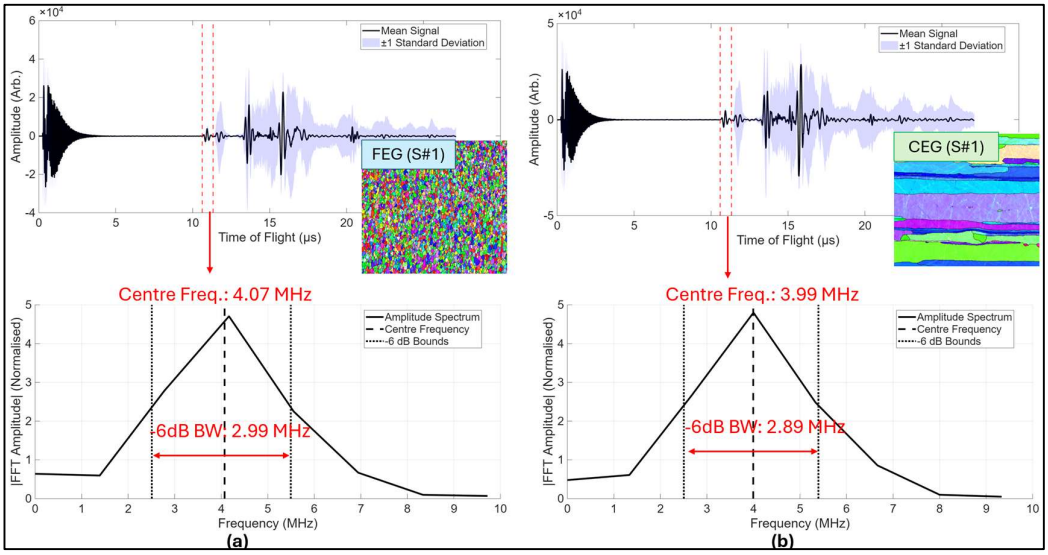


Figure 76. LCR energy-normalised FFT spectra for Sample #1 (0–10 MHz), with extracted centre frequency and −6 dB bandwidth indicated [101]

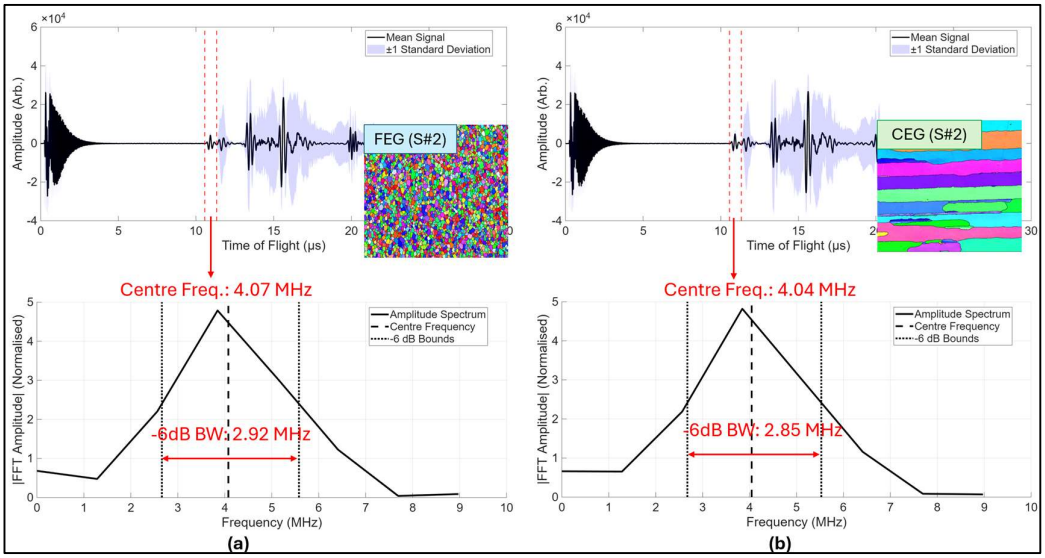


Figure 77. LCR energy-normalised FFT spectra for Sample #2 (0–10 MHz), with extracted centre frequency and −6 dB bandwidth indicated [101]

These trends are consistent with stronger frequency-dependent scattering and damping in the CEG region. The result is a redistribution of spectral energy toward lower frequencies, coupled with suppression of the high-frequency tail. By comparison, equiaxed grains with weaker texture preserve broader bandwidth and a shallower high-frequency decay. The near-surface LCR configuration may accentuate these effects because the sampled region contains the microstructural contrast identified by EBSD. However, the measured spectral shifts were modest and should be interpreted as relative indicators of microstructural variation rather than calibrated measurements of grain morphology or texture.

7.3 Summary of Results: Microstructural Control of LCR Attenuation and Observable Separation

7.3.1 Microstructural Length Scale and LCR Attenuation

The FEG region consists of ultrafine equiaxed grains (1–3 μm) with largely random crystallographic orientation and high grain boundary density, whereas the CEG region contains elongated grains with characteristic dimensions of 200–600 μm and increased anisotropy correlation length.

For a longitudinal velocity of 6400 m/s at 5 MHz, the LCR wavelength in aluminium is approximately 1.3 mm. The nondimensional parameter governing scattering is:

$$ka = \frac{2\pi a}{\lambda} \qquad (14)$$

Equation 31 Definition of the nondimensional scattering parameter ka, relating characteristic microstructural length scale $a$to ultrasonic wavelength λ.

where *a* is characteristic grain dimension and *λ* is wavelength.

For FEG (1–3 μm), $\boldsymbol{ka} \ll \mathbf{1}$, placing the material deep within the long-wavelength (Rayleigh-type) regime. Elastic stiffness fluctuations are extremely fine relative to the wavelength, and the wavefield experiences statistical averaging over many grains. The medium therefore behaves quasi-homogeneously at the LCR scale.

For CEG (200–600 μm), grains represent 15–50% of the wavelength. Although still smaller than λ, the scattering cross-section increases substantially, and forward phase perturbations become significant. The larger elastic heterogeneity per grain promotes cumulative phase decoherence and enhanced attenuation.

The attenuation contrast observed in *Figure 67* and *Figure 68* is therefore primarily controlled by microstructural length scale relative to wavelength, rather than grain boundary density. A boundary-count model would predict higher attenuation in FEG, which is inconsistent with both classical scattering theory and the present measurements. Scattering strength increases with grain size and stiffness contrast, not simply with interface density [141, 142, 144, 155].

7.3.2 Effect of Morphology and Anisotropy Correlation

Building on the directional velocity response discussed alongside Figure 59 and Figure 60, grain morphology also influences scattering, attenuation and phase coherence along the ultrasonic propagation path. The FEG microstructure exhibits short anisotropy correlation length with largely uncorrelated orientation fluctuations. Phase perturbations remain small and statistically cancelling along the propagation path.

In contrast, the elongated CEG structure increases anisotropy correlation length along the growth direction. Orientation clustering and direction-dependent velocity fluctuations promote coherent accumulation of phase errors as the LCR wave propagates parallel to the surface. Because LCR waves travel over relatively long surface-parallel distances, even moderate velocity variations accumulate, resulting in measurable amplitude loss and increased attenuation.

The higher attenuation observed in CEG is therefore attributed to:

- Grain dimensions representing a significant fraction of the ultrasonic wavelength
- Increased elastic stiffness fluctuation per grain
- Enhanced anisotropy correlation due to elongation and local texture
- Cumulative phase decoherence along the LCR path

Conversely, the ultrafine FEG region behaves effectively as a homogenised elastic medium at the LCR wavelength scale.

The attenuation contrast observed in Figure 67 and Figure 68 is therefore primarily controlled by microstructural length scale relative to wavelength, rather than grain boundary density.

7.3.3 Observable-Level Separation and PAURS+

Table 9 summarises the FEG-to-CEG response obtained from pulse-echo ToF, attenuation and backscatter, together with the LCR ToF, attenuation, backscatter and frequency-domain measurements. Rather than implying strict decoupling, the table is intended as a comparative summary of the dominant observable trends identified throughout the Results section. Under the present stress-relieved conditions, the data indicate a consistent contrast in physical sensitivity between ToF and amplitude-based metrics, particularly for the LCR configuration.

The main observations are as follows:

- Pulse-echo ToF exhibits appreciable microstructure sensitivity, indicating that its direct use for RS quantification would require microstructural calibration or compensation.
- LCR ToF shows substantially smaller FEG-to-CEG variation than pulse-echo ToF under the present conditions, supporting its interpretation as a stress-dominant observable with relatively weak microstructural influence in the aluminium samples examined here.
- LCR attenuation and backscatter RMS show clear and consistent FEG-to-CEG contrast in both samples, while FFT spectral descriptors (centre frequency and −6 dB bandwidth) exhibit modest but repeatable FEG-to-CEG shifts; together these trends indicate sensitivity to grain-scale scattering, heterogeneity, and anisotropy.
- Pulse-echo attenuation and backscatter RMS also show microstructural contrast, but with lower consistency and weaker discrimination than the corresponding LCR metrics.

Table 9. Summary of all results

Output	Observable	FEG to CEG Change (Pulse Echo)		FEG to CEG Change (LCR)	
		Sample#1	Sample#2	Sample#1	Sample#2
Predominantly stress-dominant observable	ToF (Backwall-to-backwall *ΔToF* for Path-span ΔToF difference for LCR)	2,350 ns to 2,580 ns	2,580 ns to 2,730 ns	98 ns to 106 ns	101 ns to 105 ns
Predominantly microstructure-dominant observable	Attenuation	0.54 dB to 1.1 dB	0.14 dB to 1.84 dB	1.49 dB to 2.09 dB	1.62 dB to 2.38 dB
	Backscatter RMS (Region B for LCR)	2230 to 2370	2580 to 4830	729 to 863	653 to 916
	LCR frequency-domain response	Minimal difference	Minimal difference	Centre freq.: 4.07 MHz to 3.99 MHz −6 dB BW: 2.99 MHz to 2.89 MHz vs	Centre freq.: 4.07 MHz to 4.04 MHz −6 dB BW: 2.92 MHz to 2.85 MHz vs

Taken together, the LCR results support the premise that multiple observables extracted from the same FMC acquisition can exhibit different relative sensitivities. Under the present macroscopically stress-relieved conditions, LCR path-span ToF showed limited variation between the FEG and CEG regions,

while attenuation and backscatter produced clearer microstructural contrast. The frequency-domain results were considered separately after verification of the spectral-processing procedure.

The conceptual structure of this observable-level separation is summarised in *Figure 78*, which illustrates the distinct physical pathways through which each observable is expected to respond primarily to stress or microstructure. Interpreted jointly, these results provide a physically grounded route toward future simultaneous stress and microstructure assessment from the same LCR dataset, without changing wave mode, transducer configuration, or inspection geometry. Although this work does not perform combined inversion or direct stress reconstruction, it establishes the observable-level evidence required to motivate such a framework and provides the physical basis for PAURS+.

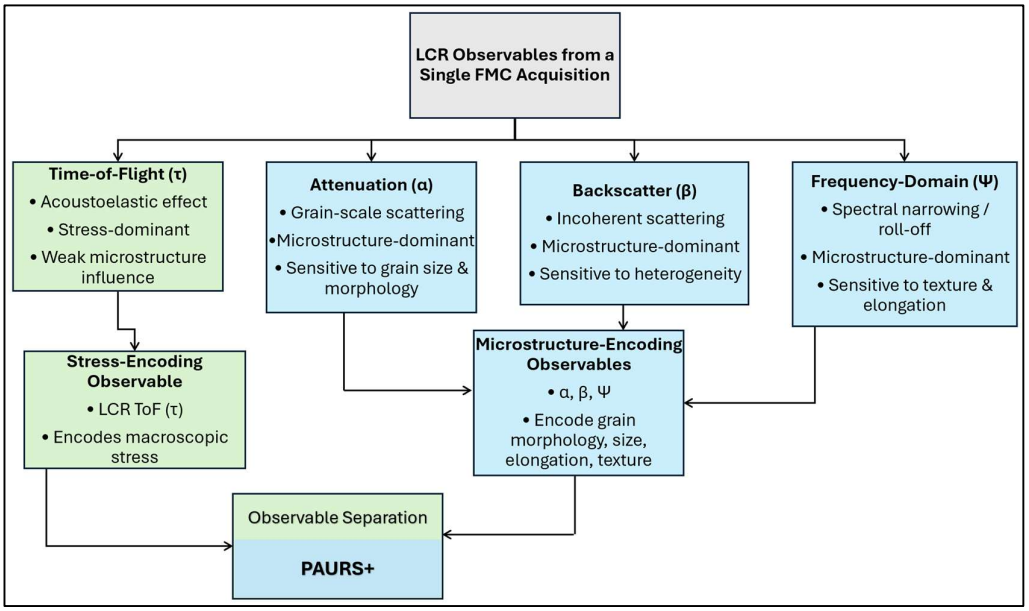


Figure 78. Conceptual map of LCR observables and their roles within PAURS+. ToF (τ) encodes stress, whereas attenuation (α), backscatter (β) and frequency-domain metrics (Ψ) encode microstructure. [101]

The results presented here do not aim to rank or quantify the relative influence of individual microstructural parameters. Rather, they demonstrate that phased-array LCR measurements contain multiple observables that respond differently when the microstructural state is altered under controlled, stress-relieved conditions. In this early-stage study, attenuation, backscatter, and frequency-domain features show clear qualitative sensitivity to the transition from FEG to CEG, while the LCR path-span *ΔToF* metric exhibits comparatively weak variation at the scale of a few nanoseconds. This contrast indicates that LCR measurements encode both stress-related and microstructure-related information within the same dataset. Establishing quantitative sensitivity, uncertainty bounds, and statistical robustness for each observable requires dedicated experiments

with controlled variation of individual microstructural parameters and is therefore beyond the scope of the present work.

7.4 Conclusions

This study evaluates the relative microstructural sensitivities of phased-array LCR measurements using stress-relieved AFSD aluminium containing FEG and CEG regions. The results show that the measured LCR characteristics respond differently to the investigated microstructural conditions. The principal experimental findings of this study are:

1. LCR ToF as a predominantly stress-sensitive observable under the present macroscopic stress-relieved conditions: Across transmit–receive paths and measurement frames, the FEG–CEG LCR *ΔToF* remained very small (of order a few nanoseconds), whereas pulse-echo ToF differences were two orders of magnitude larger. Under nominally stress-relieved conditions at the macroscopic scale, LCR ToF exhibits substantially weaker microstructural dependence than pulse-echo ToF, while pulse-echo ToF remains strongly influenced by microstructure due to through-thickness averaging.
2. Microstructural contrast in amplitude-based measurements: LCR attenuation and backscatter RMS were consistently higher in CEG than in FEG. These trends are consistent with increased scattering and path-integrated signal loss in the coarse elongated microstructure.
3. The complementary behaviour observed in this study, in which LCR path-span ToF exhibited limited microstructural variation while LCR attenuation and backscatter showed clearer contrast, provides an initial basis for microstructure-aware interpretation using a single phased-array acquisition.

The results were obtained on stress-relieved aluminium with AFSD-type microstructures; extension to other alloys, textures, and processing routes requires further validation. The acoustoelastic coefficient was probed only preliminarily for microstructure dependence and was not determined via full tensile calibration. Quantitative microstructural descriptors (e.g., grain size distributions, aspect ratios, and texture indices) were not yet integrated into inversion.

From a theoretical standpoint, this work contributes an observable-level interpretation framework that links distinct ultrasonic measurements to dominant physical mechanisms in stressed polycrystalline media. Rather than proposing a new wave-propagation model, the study establishes how acoustoelastic effects, scattering, and anisotropy manifest preferentially in different LCR observables, providing a physically grounded basis for multi-field interpretation from a single phased-array dataset.

Future work should focus on (i) joint inversion of RS and microstructure from the LCR descriptor set $(\boldsymbol{\tau}, \boldsymbol{\alpha}, \boldsymbol{\beta}, \boldsymbol{\Psi})$ with uncertainty propagation across FMC paths and frames; (ii) frequency scaling and controlled use of mode-converted windows to enhance microstructural contrast where statistically

robust; (iii) generalisation to additional alloys and AM/weld microstructures with correlation to quantitative EBSD; and (iv) calibration against established stress-measurement techniques to confirm quantitative stress recovery with microstructure-aware correction, ultimately enabling in-process, robotic deployment.

Chapter 8: Discussion

8.1 Findings across the three studies

This thesis accomplishes its main goal throughout the three studies. This is the development and validation of PAURS as a non-destructive, automation-compatible approach for RS measurements in AM components.

The most important outcome is that PAURS consistently reproduced the principal features of the RS distributions observed using the reference methods. These are the locations of the peak tensile stress and the shape of the peak RS region associated with the HAZ. Chapter 5 demonstrates that PAURS can reproduce the expected RS distribution in WAAM Ti-6Al-4V but only establishes feasibility in one material and geometry. In Chapter 6, the validation shifts from assessing whether PAURS can measure the RS distribution to evaluating its ability to detect RS redistribution, which is particularly useful in manufacturing systems where peening is utilised in situ. Finally, in Chapter 7, the justification for using ToF measurements from Chapters 5 and 6 for heterogeneous materials is discussed, as the non-ToF observables are more sensitive to microstructure.

A second outcome is the PAURS' repeatable methodology. FMC improves the diagnostic value of PAURS by increasing path redundancy and allowing path-to-path consistency to be evaluated. This is crucial because acoustoelastic ToF shifts are small and sensitive to variations in couplant thickness and contact between the transducer and the sample.

Finally, the microstructure case study enables a better analysis of the results of previous studies. This supports the notion that LCR ToF is mainly sensitive to stress, whereas attenuation, backscatter, and the frequency domain are more sensitive to microstructure. These relative differences in observable sensitivity provide a basis for microstructure-aware interpretation

In combination, the findings of the studies show that PAURS can work in certain circumstances. PAURS is most reliable when the desired output is the distribution of subsurface RS, the location of tensile peaks, the area of the high-stress HAZ region, or the change in RS resulting from mitigation methods. PAURS is weaker when the requirements are absolute through-thickness RS measurements or a benchmark measurement independent of calibration transferability. Thus, PAURS should be considered a deployable comparative and process-monitoring method rather than a substitute for all well-established RS techniques.

8.2 Validation

It is difficult to carry out a direct quantitative comparison of the validation since the various RS methods have different penetration depths. While PAURS measures a path-averaged LCR in order to sample the shallow subsurface, XRD focuses on near-surface or surface areas, and CM involves destructively reconstructing a cut plane stress component. For these reasons, the thesis mainly validates PAURS on the basis of the shape of the distribution, the position of the peak, the stress gradient or the HAZ width, and also on its sensitivity to the stress distribution.

This explains the differences in magnitude observed in comparisons. In the WAAM Ti-6Al-4V feasibility study, PAURS and CM report the same RS distribution with a central tensile peak at the LCR penetration depth, but different peak magnitudes. This difference is consistent with differences in depth and averaging, and with the fact that CM reconstructs a cut-plane field, whereas PAURS reports a shallow-subsurface path average.

The strongest evidence of process sensitivity was obtained from the peening study where a significant drop in PAURS is observed after inter-pass peening. XRD and CM provide complementary evidence of redistribution, although the sample conditions and measured volumes differ. Such an agreement is essential in evaluating in-process mitigation. So, these three studies clearly show the importance of considering both sample regions and deployability when comparing validation results. Table 10 summarises the methods carried out throughout this thesis and their respective properties.

Table 10 Comparison of RS measurement methods relevant to this thesis, summarised from the reviewed literature [6, 20–22, 25, 27–30, 36–40, 45–49, 53, 55, 63, 156, 157] and the three studies

Method	Type		Sampled Region	Main Sensitivity	Main Limitation	Resolution/ averaging	Deployability
Contour Method (CM)	Destructive		Full cut-plane	Stress normal to the cut plane	Destructive, not repeatable on the same sample	Dense surface measurement plus FE reconstruction	Low
X-ray Diffraction (XRD)	Non-destructive		Surface/near-surface	Elastic lattice strain	Limited penetration depth	Local surface spot or mapped surface points	Medium-to-high, equipment dependent
Conventional LCR ultrasonics	Non-destructive		Near-surface/subsurface path average	Stress-induced velocity ToF change	Coupling, temperature, calibration, texture, and path averaging effects	Typically, only a small number of paths, often two, so limited averaging and limited ability to detect unstable paths	High, simple and portable
PAURS	Non-destructive		Near-surface/ subsurface path average	Stress-induced ToF change with phased-array outlier removal	The system needs to be calibrated, the signal quality has to be controlled, and the results must be analysed in a way that is aware of the microstructure.	Scan step sets spatial sampling; FMC provides 64 paths per position for redundancy and QC	High, compatible with automation

Due to differences among these RS measurement methods, there are four main points of agreement in RS measurements that enable validation. This is shown in Figure 79.

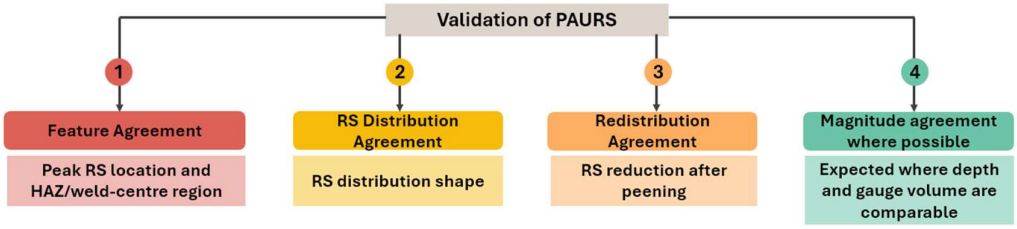


Figure 79 The four main agreements between PAURS and validation methods

The first agreement considers the measurement features, such as the location of Peak RS and the HAZ region. The second agreement concerns the overall shape of the RS distribution. The third agreement considers the behaviour and redistribution of RS with mitigation methods such as inter-pass peening. The final agreement is the magnitude agreement, which is only possible if PAURS and the chosen validation method can be directly compared. These four main agreements allow comparison among different RS methods whilst accounting for their properties, such as penetration depth, sensitivity, and resolution.

8.3 PAURS against diffraction and modelling

PAURS is not meant to replace diffraction, CM or modelling. The main strength lies in bridging the gap between accurate benchmark measurements and real-world in situ assessments. Diffraction and CM are useful for qualification confidence, but PAURS provides robust measurements that strengthen mitigation validation and adaptive control for WAAM going forward. Its main strength is the connection between accurate benchmark measurements and real-world in situ evaluations. Although diffraction and CM are helpful for qualification confidence, PAURS provides reliable measurements that will support future mitigation validation and adaptive control for WAAM.

8.4 Limitations

Among the three studies, the main limitation of PAURS is that it is a shallow-subsurface RS method and does not directly measure through-thickness RS in thick sections. This is a trade-off that enables deployability and repeatability. Where deep internal information is required, PAURS should be paired with an occasional benchmark method such as CM, particularly during early qualification.

Also, the main factors affecting measurements in PAURS are coupling and scan variability. The thesis contribution is that this is managed through FMC. This enables multi-path averaging, differential timing correction, and outlier rejection, reducing variability in the investigated laboratory measurements. Operation at elevated manufacturing temperatures was not demonstrated and would require temperature compensation.

Microstructure remains the main risk in heterogeneous AM materials. The PAURS+ study is therefore not an individual microstructure study; it is important for providing the analysis necessary to defend

the earlier PAURS measurements. In Chapters 5 and 6, the RS calculation relies on LCR ToF. Chapter 7 supports this choice by showing that ToF is the ultrasonic observable most appropriate for RS calculation. At the same time, attenuation, backscatter and frequency-domain metrics should be treated primarily as indicators of microstructural variation. This reduces the risk that PAURS results for WAAM samples are interpreted based on observables dominated by microstructure rather than by stress.

Together, the studies demonstrate that PAURS has developed from a feasible phased-array LCR measurement concept into an experimentally evaluated methodology with potential for automated deployment for subsurface RS assessment. The thesis, however, does not claim that PAURS replaces diffraction, CM, or modelling. Instead, it positions PAURS as the method that enables repeated, non-destructive, automation-compatible assessment of RS distribution, where the key industrial decision is whether a process or mitigation strategy has produced an acceptable stress distribution.

8.5 Future Work

Future research might involve reversing the PAURS arrangement so as to examine the components from the side onto which the material has been deposited. This approach would improve the ability to detect stresses in the deposited wall and in the region where the deposited layer meets the substrate. In order to carry out such a procedure, a specially designed wedge or holder would be needed to take account of the wall's shape, the surface roughness and the conditions for probe contact. The measurements taken from both the deposited side and the substrate side could then be compared in order to study the stress distribution at various effective depths.

Further validation is required across a wider range of materials, geometries and manufacturing conditions. The present work focused mainly on WAAM Ti-6Al-4V and AFSD AA7075. Future studies should evaluate PAURS in other alloys and manufacturing processes, including welded components, while independently varying component thickness, deposition strategy and RS mitigation treatment. This would establish the extent to which the measurement procedure and uncertainty are transferable between applications.

The accuracy of stress measurement can be improved by using a reference specimen which is produced by annealing or some other established stress-relief technique. Although the original material used in the first PAURS studies provided a steady baseline, it had not been independently confirmed to have zero RS. In future calibration work, the baseline from the original material should be compared with that from an annealed reference, and the RS in both instances should also be measured. By doing this, it will be possible to determine any offset associated with the reference, and thus the accuracy of the PAURS values can be improved.

The acoustoelastic calibration should also be investigated more systematically. Future experiments could examine the effects of material texture, propagation direction, loading and unloading behaviour, frequency and probe configuration on the measured coefficient. Calibration using separate specimens from the deposited, heat-affected and parent-material regions would help determine whether one coefficient can represent the complete component or whether region-specific calibration is required.

Further work is needed to quantify the effective LCR interrogation depth and spatial sensitivity of each phased-array path. Experiments using specimens with controlled stress gradients, machined reflectors or independently measured depth profiles could be combined with numerical modelling to produce configuration-specific depth-sensitivity functions. Measurements at several frequencies could then be used to investigate stress variation with depth rather than assigning each frequency a single nominal penetration depth.

The FMC processing workflow might be extended by means of formal uncertainty propagation and by incorporating an automated classification of path quality. Future algorithms should combine waveform similarity, signal quality, zero-crossing stability and path-to-path consistency without rejecting any paths simply because their calculated stress differs from the average. The influences of interpolation, the choice of temporal window, coupling correction and reference selection should all be considered by propagating them into uncertainty limits that are dependent on position for the final stress profile.

PAURS+ requires further controlled experiments before stress and microstructure can be quantified independently. Samples should be produced with systematic variations in grain size, aspect ratio and crystallographic texture while maintaining a controlled macroscopic stress state. Complementary tests should then vary applied stress while maintaining consistent microstructure. Correlation with EBSD and other microstructural measurements would allow the relative sensitivities of ToF, attenuation, backscatter and verified frequency-domain descriptors to be quantified.

A longer-term objective is the development of a joint stress and microstructure interpretation framework. Rather than assigning each ultrasonic observable exclusively to one physical field, a calibrated model could estimate the probability that a measured change arises from stress, microstructure or experimental variability. This would require larger datasets, uncertainty-aware modelling and validation against compatible reference measurements.

Finally, PAURS should be developed towards automated and in-process deployment. A robotic inspection system could control probe position, contact pressure, couplant application and scanning speed while acquiring FMC data during selected stages of manufacture. Repeated measurements during deposition, inter-pass peening, unclamping and post-process treatment would allow the evolution and redistribution of RS to be monitored. Initial deployment should focus on controlled laboratory trials before progressing to industrial components and manufacturing environments.

Chapter 9: Conclusions

This thesis addresses the need for a non-destructive, repeatable and potentially automation-compatible method for assessing shallow-subsurface RS distributions in WAAM Ti-6Al-4V components. It presents the development, refinement and evaluation of PAURS, in which phased-array LCR measurements are used to estimate the longitudinal RS component from stress-induced ToF variation.

PAURS functions in a different measurement domain from the reference techniques mentioned in this thesis. While CM provides a two-dimensional cross-sectional view of the stress component normal to the chosen cut plane, it is destructive and cannot be carried out more than once on the same component. XRD provides localised, direction-specific measurements of the surface or near-surface region but has a penetration depth that is much shallower than that of PAURS. Rather than replacing either of these techniques, PAURS supplements CM and XRD by enabling repeatable, path-averaged measurements in a shallow subsurface area.

Comparisons between PAURS, CM and XRD were therefore interpreted according to the stress component, measurement depth, gauge volume and spatial resolution represented by each technique. Exact agreement was not expected because the methods sampled different material regions. Greater emphasis was placed on the overall RS distribution, the location of tensile and compressive regions, peak position and changes associated with processing or mitigation.

The studies carried out using WAAM found that PAURS was able to reproduce the main features of the longitudinal RS distribution in the Ti-6Al-4V components under examination. The results showed that there was a high tensile stress below the deposited wall and that this had been caused by the redistribution following inter-pass peening. The agreement with CM and XRD was most accurate regarding the general shape of the stress profile and the position of the peak, not concerning the precise stress values.

The first feasibility study of PAURS referred to the parent material as a basis of comparison. Since this area had not been annealed and had not been independently verified to have zero RS, the PAURS values should be understood as stresses relative to the parent material reference and might therefore include an unknown common offset. Nevertheless, this parent material did provide a consistent reference against which to evaluate spatial variations throughout the component. In order to achieve accurate absolute stress measurements, a stress-relieved reference that had been verified would be required.

FMC was an important development within PAURS because it increased the number of available transmitter-receiver paths. This additional information supported path comparison, averaging, identification of unstable signals and assessment of path-to-path variability. Differential processing also reduced timing contributions common to selected paths, including coupling and wedge delays.

However, FMC did not remove systematic effects shared across the dataset. The final measurements remained dependent on the acoustoelastic calibration, parent-material datum, temperature, couplant condition, wedge positioning, waveform selection and local material response. FMC should therefore be regarded as an important reliability and quality-assessment capability within the investigated PAURS configuration, rather than as a universal solution to every source of ultrasonic RS uncertainty.

The PAURS+ study extended the methodology by examining the relative sensitivity of different ultrasonic observables to controlled microstructural variation. Under the macroscopically stress-relieved conditions investigated, the LCR path-span ToF showed comparatively limited variation between the fine equiaxed and coarse elongated microstructures. Attenuation and backscatter produced clearer microstructural contrast, indicating that the same phased-array acquisition contains observables with different dominant physical sensitivities.

The results support an interpretation that takes the microstructure into account, but they do not show a complete or universal separation of stress and microstructure. LCR ToF should be considered mainly stress-sensitive only in the circumstances that have been studied, whereas measurements based on amplitude give complementary evidence of material heterogeneity. Further controlled calibration is necessary before stress and microstructure can be reconstructed separately and quantitatively from a single dataset.

PAURS is therefore best positioned for applications requiring repeated assessment of shallow-subsurface RS distributions, particularly the identification of stress gradients, peak regions and changes following mitigation. It is not currently a replacement for CM when a cross-sectional stress map is required or for XRD when local near-surface lattice strain is the measurement objective. Its principal advantage is the ability to provide non-destructive, repeatable and potentially automated measurements in locations where destructive sectioning or repeated diffraction measurements may be impractical.

The next steps involve combining PAURS with automated scanning, the use of controlled probe pressure and the application of couplant in a consistent manner. It will also be necessary to establish standard operating procedures for selecting the wedge, carrying out acoustoelastic calibration, verifying the reference datum, extracting the ToF values, assessing the quality of the path and reporting the uncertainty. However, further validation for other materials, geometries, frequencies and types of

inspection surface will have to take place before the method can be routinely transferred between different manufacturing applications.

The main conclusions from this thesis are:

- PAURS provided non-destructive and repeatable measurements of the shallow-subsurface longitudinal RS distribution in the investigated WAAM Ti-6Al-4V components.
- CM gave a more comprehensive view of the distribution of cross-sectional stress, while XRD offered measurements that were localised near the surface.
- • PAURS was able to reproduce the main RS profile, the location of the peak, and the redistribution associated with the manufacturing and peening conditions under investigation, even though the exact magnitudes differed because of variations in the sampling regions and reference conditions.
- The parent material used in the initial study was a reference datum rather than a verified stress-free condition. The reported PAURS values should therefore be interpreted relative to that datum.
- FMC increased data redundancy and supported path comparison, averaging and signal-quality assessment, but did not eliminate systematic uncertainty associated with calibration, coupling, temperature, reference selection or microstructure.
- PAURS+ provided evidence that LCR ToF, attenuation and backscatter exhibit different relative sensitivities to the investigated microstructural transition. This supports microstructure-aware interpretation but not complete quantitative separation of stress and microstructure.
- PAURS is best positioned as a complementary, automation-compatible approach with potential for future manufacturing-stage monitoring, rather than as a replacement for CM or XRD.

The thesis as a whole presents PAURS as a methodology that is still in development and provides a plausible path to achieving automated shallow-subsurface RS assessment in WAAM; its future use in an industrial context will rely on better absolute referencing, the quantification of uncertainty, additional validation with regard to materials and geometry, and the ongoing development of interpretation that takes microstructure into account.

References

1. DebRoy, T., Wei, H.L., Zuback, J.S., Mukherjee, T., Elmer, J.W., Milewski, J.O., Beese, A.M., Wilson-Heid, A., De, A., Zhang, W.: Additive manufacturing of metallic components – Process, structure and properties. Prog. Mater. Sci. 92, 112–224 (2018). https://doi.org/10.1016/j.pmatsci.2017.10.001

2. Frazier, W.E.: Metal Additive Manufacturing: A Review. J. Mater. Eng. Perform. 23, 1917–1928 (2014). https://doi.org/10.1007/s11665-014-0958-z

3. Ngo, T.D., Kashani, A., Imbalzano, G., Nguyen, K.T.Q., Hui, D.: Additive manufacturing (3D printing): A review of materials, methods, applications and challenges. Compos. B Eng. 143, 172–196 (2018). https://doi.org/10.1016/j.compositesb.2018.02.012

4. Williams, S.W., Martina, F., Addison, A.C., Ding, J., Pardal, G., Colegrove, P.: Wire + Arc Additive Manufacturing. Materials Science and Technology. 32, 641–647 (2016). https://doi.org/10.1179/1743284715Y.0000000073

5. Wang, F., Williams, S., Colegrove, P., Antonysamy, A.A.: Microstructure and Mechanical Properties of Wire and Arc Additive Manufactured Ti-6Al-4V. Metallurgical and Materials Transactions A. 44, 968–977 (2013). https://doi.org/10.1007/s11661-012-1444-6

6. Withers, P.J., Bhadeshia, H.K.D.H.: Residual stress. Part 2 – Nature and origins. Materials Science and Technology. 17, 366–375 (2001). https://doi.org/10.1179/026708301101510087

7. Withers, P.J.: Residual stress and its role in failure. Reports on Progress in Physics. 70, 2211–2264 (2007). https://doi.org/10.1088/0034-4885/70/12/R04

8. Kandil, F., Lord, J., Fry, A., Grant, P.: A Review of Residual Stress Measurement Methods -A Guide to Technique Selection. (2001)

9. Fry, A.T.: A review of residual stress measurement methods A guide to technique selection. (2001)

10. Bastola, N., Jahan, M.P., Rangasamy, N., Rakurty, C.S.: A Review of the Residual Stress Generation in Metal Additive Manufacturing: Analysis of Cause, Measurement, Effects, and Prevention. Micromachines (Basel). 14, 1480 (2023). https://doi.org/10.3390/mi14071480

11. Totten, G.E.., Howes, M.A.H.., Inoue, Tatsuo.: Handbook of residual stress and deformation of steel. ASM International (2002)

12. Martina, F., Roy, M.J., Szost, B.A., Terzi, S., Colegrove, P.A., Williams, S.W., Withers, P.J., Meyer, J., Hofmann, M.: Residual stress of as-deposited and rolled wire+arc additive manufacturing Ti–6Al–4V components. Materials Science and Technology. 32, 1439–1448 (2016). https://doi.org/10.1080/02670836.2016.1142704

13. Mishurova, T., Sydow, B., Thiede, T., Sizova, I., Ulbricht, A., Bambach, M., Bruno, G.: Residual Stress and Microstructure of a Ti-6Al-4V Wire Arc Additive Manufacturing Hybrid Demonstrator. Metals (Basel). 10, 701 (2020). https://doi.org/10.3390/met10060701

14. Hönnige, J.R., Colegrove, P.A., Ahmad, B., Fitzpatrick, M.E., Ganguly, S., Lee, T.L., Williams, S.W.: Residual stress and texture control in Ti-6Al-4V wire + arc additively manufactured intersections by stress relief and rolling. Mater. Des. 150, 193–205 (2018). https://doi.org/10.1016/j.matdes.2018.03.065

15. Martina, F., Roy, M.J., Szost, B.A., Terzi, S., Colegrove, P.A., Williams, S.W., Withers, P.J., Meyer, J., Hofmann, M.: Residual stress of as-deposited and rolled wire+arc additive manufacturing Ti–6Al–4V components. Materials Science and Technology. 32, 1439–1448 (2016). https://doi.org/10.1080/02670836.2016.1142704

16. Mishurova, T., Sydow, B., Thiede, T., Sizova, I., Ulbricht, A., Bambach, M., Bruno, G.: Residual Stress and Microstructure of a Ti-6Al-4V Wire Arc Additive Manufacturing Hybrid Demonstrator. Metals (Basel). 10, 701 (2020). https://doi.org/10.3390/met10060701

17. Xian, G., Pan, J., Lee, J., Kang, N.: Weakening the Anisotropic Property and Refining Prior-β Grains via Hammer Peening Treatment During Wire Arc Additively Manufacturing of Ti-6Al-4V. Metals (Basel). 14, 1261 (2024). https://doi.org/10.3390/met14111261

18. Hönnige, J.R., Davis, A.E., Ho, A., Kennedy, J.R., Neto, L., Prangnell, P., Williams, S.: The Effectiveness of Grain Refinement by Machine Hammer Peening in High Deposition Rate Wire-Arc AM Ti-6Al-4V. Metallurgical and Materials Transactions A. 51, 3692–3703 (2020). https://doi.org/10.1007/s11661-020-05781-6

19. Neto, L., Williams, S., Ding, J., Hönnige, J., Martina, F.: Mechanical Properties Enhancement of Additive Manufactured Ti-6Al-4V by Machine Hammer Peening. Presented at the (2020)

20. Withers, P.J., Bhadeshia, H.K.D.H.: Residual stress. Part 1 – Measurement techniques. Materials Science and Technology. 17, 355–365 (2001). https://doi.org/10.1179/026708301101509980

21. Schajer, G.S.: Relaxation Methods for Measuring Residual Stresses: Techniques and Opportunities. Exp. Mech. 50, 1117–1127 (2010). https://doi.org/10.1007/s11340-010-9386-7

22. Schajer, G.S., Prime, M.B.: Use of Inverse Solutions for Residual Stress Measurements. J. Eng. Mater. Technol. 128, 375–382 (2006). https://doi.org/10.1115/1.2204952

23. Prime, M.B.: The two-way relationship between residual stress and fatigue/fracture. In: Conference Proceedings of the Society for Experimental Mechanics Series. pp. 19–23. Springer New York LLC (2018)

24. Bueckner, H.F.: The Propagation of Cracks and the Energy of Elastic Deformation. J. Fluids Eng. 80, 1225–1229 (1958). https://doi.org/10.1115/1.4012657

25. Prime, M.B.: Cross-Sectional Mapping of Residual Stresses by Measuring the Surface Contour After a Cut. J. Eng. Mater. Technol. 123, 162–168 (2001). https://doi.org/10.1115/1.1345526

26. Prime, M.B., Hill, M.R.: Residual Stress Mapping in Welds Using the Contour Method. (2002)

27. Schajer, G.S., Whitehead, P.S.: Hole-drilling method for measuring residual stresses. Morgan & Claypool Publishers (2018)

28. Schajer, G.S., Altus, E.: Stress Calculation Error Analysis for Incremental Hole-Drilling Residual Stress Measurements. J. Eng. Mater. Technol. 118, 120–126 (1996). https://doi.org/10.1115/1.2805924

29. Ammar, M., Shirinzadeh, B., Lai, K., Wei, W.: On the Sensing and Calibration of Residual Stresses Measurements in the Incremental Hole-Drilling Method. Sensors. 21, 7447 (2021). https://doi.org/10.3390/s21227447

30. Santus, C., Neri, P., Romoli, L., Cococcioni, M.: Residual Stress Determination with the Hole-Drilling Method on FDM 3D-Printed Precurved Specimen through Digital Image Correlation. Applied Sciences. 14, 3992 (2024). https://doi.org/10.3390/app14103992

31. Prevey, P.S.: X-RAY DIFFRACTION RESIDUAL STRESS TECHNIQUES. (1986)

32. Stacey, A., Macgillivary, H.J., Webster, G.A., Webster, P.J., Ziebeck, K.R.A.: MEASUREMENT OF RESIDUAL STRESSES BY NEUTRON DIFFRACTION. (1985)

33. Li, C., Jacques, S.D.M., Chen, Y., Daisenberger, D., Xiao, P., Markocsan, N., Nylen, P., Cernik, R.J.: A synchrotron X-ray diffraction deconvolution method for the measurement of residual stress in thermal barrier coatings as a function of depth. J. Appl. Crystallogr. 49, 1904–1911 (2016). https://doi.org/10.1107/S1600576716013935

34. Em, V., Ivan, K., Woo, W., Mikula, P.: Neutron Diffraction Measurements of Residual Stresses for Ferritic Steel Specimens over 80 mm Thick. Metals (Basel). 14, 638 (2024). https://doi.org/10.3390/met14060638

35. Mo, F., Sun, G., Li, J., Zhang, C., Wang, H., Chen, Y., Liu, Z., Yang, Z., Li, H., Yang, Z., Pang, B., Huang, Y., Tian, Y., Gong, J., Chen, B., Peng, S.: Recent Progress of Residual Stress Distribution and Structural Evolution in Materials and Components by Neutron Diffraction Measurement at RSND. Quantum Beam Science. 2, 15 (2018). https://doi.org/10.3390/qubs2030015

36. AKITA, K., SUZUKI, H.: Residual Stress Measurement by Neutron Diffraction. Radioisotopes. 59, 741–750 (2010). https://doi.org/10.3769/radioisotopes.59.741

37. Luo, J., Li, N., Wang, X., Liu, C.: 同步辐射X射线衍射技术在残余应力分析中的应用.

38. Laurence, R.C., Canelo-Yubero, D., Maawad, E., Faria, G.A., Staron, P., Schell, N., Ramadhan, R.S., Cabeza, S., Paecklar, A., Pirling, T., Poncela, M.S., Martinez, J.M., Slim, M.F., Buslaps, T., Withers, P.J., Roy, M.: Determination of Residual Stress in Additively Manufactured 316L Stainless Steel Benchmark Parts Through Synchrotron X-Ray Diffraction and Neutron Diffraction. Strain. 61, (2025). https://doi.org/10.1111/str.70005

39. Toupin, R.A., Bernstein, B.: Sound Waves in Deformed Perfectly Elastic Materials. Acoustoelastic Effect. J. Acoust. Soc. Am. 33, 216–225 (1961). https://doi.org/10.1121/1.1908623

40. Pao, Y.-H., Gamer, U.: Acoustoelastic waves in orthotropic media. J. Acoust. Soc. Am. 77, 806–812 (1985). https://doi.org/10.1121/1.392384

41. Hellier, C.J.: Handbook of Nondestructive Evaluation, Second Edition. McGraw-Hill Education, New York (2013)

42. Kim, K., Ee, J.-H., Kim, K., Kim, U.-R., Lee, J.: Mechanical Snell's Law. Journal of the Korean Physical Society. 76, 281–285 (2020). https://doi.org/10.3938/jkps.76.281

43. Jain, A., Swaminathan, M.: Physics of ultrasound. (2015)

44. Geľatko, M., Hatala, M., Vandžura, R., Botko, F.: Longitudinal critically refracted (L_{CR}) ultrasonic wave for residual stress measurement. IOP Conf. Ser. Mater. Sci. Eng. 1199, 012060 (2021). https://doi.org/10.1088/1757-899X/1199/1/012060

45. Hwang, Y.-I., Kim, G., Kim, Y.-I., Park, J.-H., Choi, M.Y., Kim, K.-B.: Experimental Measurement of Residual Stress Distribution in Rail Specimens Using Ultrasonic LCR Waves. Applied Sciences. 11, 9306 (2021). https://doi.org/10.3390/app11199306

46. Leon-Salamanca, T., Bray, D.F.: Residual stress measurement in steel plates and welds using critically refracted longitudinal (LCR) waves. Research in Nondestructive Evaluation. 7, 169–184 (1996). https://doi.org/10.1007/BF01606385

47. Yang, S., Wang, M., Yang, L.: Investigation of Uncertain Factors on Measuring Residual Stress with Critically Refracted Longitudinal Waves. Applied Sciences. 9, 485 (2019). https://doi.org/10.3390/app9030485

48. Liu, H., Li, Y., Li, T., Zhang, X., Liu, Y., Liu, K., Wang, Y.: Influence factors analysis and accuracy improvement for stress measurement using ultrasonic longitudinal critically refracted (LCR) wave. Applied Acoustics. 141, 178–187 (2018). https://doi.org/10.1016/j.apacoust.2018.07.017

49. Lai, H.-H., Yan, D.-H., Chang, W.-J., Chung, K.-H., Xing, L.-X., Chang, W.-T., Wu, W.: Effects of factors from practical workpieces on ultrasonic LCR method stress measurement. Discover Applied Sciences. 6, 335 (2024). https://doi.org/10.1007/s42452-024-06003-z

50. Braconnier, D., Yoon, B.-S., Lee, H.-J.: Developments in Ultrasonic Phased Array Inspection I Understanding of Key Number in Phased Array. In: Understanding of Key Number in Phased Array. 8th International Conference on NDE in Relation to Structural Integrity for Nuclear and Pressurised Components (2012)

51. Moles, M.: Ultrasonic phased array. The NDT Technician. 11, 1–5 (2012)

52. Komura, I., Nagai, S., Kashiwaya, H., Mori, T., Arii, M.: Improved ultrasonic testing by phased array technique and its application. Nuclear Engineering and Design. 87, 185–191 (1985). https://doi.org/10.1016/0029-5493(85)90107-4

53. Drinkwater, B.W., Wilcox, P.D.: Ultrasonic arrays for non-destructive evaluation: A review, (2006)

54. Drinkwater, B.W., Wilcox, P.D.: Ultrasonic arrays for non-destructive evaluation: A review. NDT & E International. 39, 525–541 (2006). https://doi.org/https://doi.org/10.1016/j.ndteint.2006.03.006

55. Holmes, C., Drinkwater, B.W., Wilcox, P.D.: Post-processing of the full matrix of ultrasonic transmit–receive array data for non-destructive evaluation. NDT & E International. 38, 701–711 (2005). https://doi.org/10.1016/j.ndteint.2005.04.002

56. Mohammadi, M., Fesharaki, J.J.: Determination of acoustoelastic/acoustoplastic constants to measure stress in elastic/plastic limits by using LCR wave. NDT & E International. 104, 69–76 (2019). https://doi.org/10.1016/j.ndteint.2019.04.003

57. Castellano, A., Fraddosio, A., Marzano, S., Daniele Piccioni, M.: Some advancements in the ultrasonic evaluation of initial stress states by the analysis of the acoustoelastic effect. In: Procedia Engineering. pp. 1519–1526. Elsevier Ltd (2017)

58. Deputat, J.: Application of the acoustoelastic effect in measurements of. residual stresses. Archives of Acoustics. 15, 57–68 (2014)

59. Bray, D.E., Tang, W.: Evaluating stress gradients in steel plates and bars with the LCR ultrasonic wave Subsurface stress evaluation in steel plates and bars using the L CR ultrasonic wave. (1997)

60. Mohammadi, M., Fesharaki, J.J.: Determination of acoustoelastic/acoustoplastic constants to measure stress in elastic/plastic limits by using LCR wave. NDT & E International. 104, 69–76 (2019). https://doi.org/10.1016/j.ndteint.2019.04.003

61. Walker, J., Mills, B., Javadi, Y., MacLeod, C., Sun, Y., Taraphdar, P.K., Ahmad, B., Gurumurthy, S., Ding, J., Sillars, F.: Study of Residual Stress Using Phased Array Ultrasonics in Ti-6AL-4V Wire-Arc Additively Manufactured Components. Sensors. 24, 6372 (2024). https://doi.org/10.3390/s24196372

62. Osipovich, K.S., Panfilov, A.O., Chumaevskii, A. V., Semenchuk, V.M., Kushnarev, Yu. V., Moskvichev, E.N., Gurianov, D.A., Kolubaev, E.A.: Influence of ultrasound on evolution of the Ti-6Al-4V alloy microstructure during wire-feed electron-beam additive manufacturing. Russian Physics Journal. (2026). https://doi.org/10.1007/s11182-026-03654-w

63. Kolimi, I.Z., Marteau, J., Bouvier, S., Auguste, P., Lefebvre, F.: Residual Stress and Microstructural Uniformity in Large-Scale Ti-6Al-4V Fabricated via Additive Friction Stir Deposition. J. Manuf. Sci. Eng. 148, (2026). https://doi.org/10.1115/1.4071166

64. Javadi, Y., Mills, B., MacLeod, C., Lines, D., Abad, F., Lotfian, S., Mehmanparast, A., Pierce, G., Brennan, F., Gachagan, A., Mineo, C.: Phased Array Ultrasonic Method for Robotic Preload Measurement in Offshore Wind Turbine Bolted Connections. Sensors. 24, 1421 (2024). https://doi.org/10.3390/s24051421

65. Mills, B., Walker, J., Javadi, Y., MacLeod, C.N., Alipooramirabad, H., Reid, M., Paradowska, A.: Residual stress analysis in robotically welded plates using phased array ultrasonics with validation through neutron diffraction and hole-drilling methods. International Journal of Pressure Vessels and Piping. 216, 105518 (2025). https://doi.org/10.1016/j.ijpvp.2025.105518

66. Walker, J., Mills, B., Javadi, Y., MacLeod, C., Sun, Y., Ahmad, B., Williams, S., Ding, J., Tamimi, S.: Inter-pass peening for residual stress control in additive manufacturing: validation using ultrasonic, X-ray and contour method. Mater. Des. 260, 115247 (2025). https://doi.org/10.1016/j.matdes.2025.115247

67. Wang, W., Zhang, J., Wilcox, P.D.: Metallic material microstructure grain size measurements from backscattering signals in ultrasonic array data sets. NDT & E International. 149, 103251 (2025). https://doi.org/10.1016/j.ndteint.2024.103251

68. Zhang, J., Song, Y., Li, X., Zhong, C.: Comparison of Experimental Measurements of Material Grain Size Using Ultrasound. J. Nondestr. Eval. 39, 30 (2020). https://doi.org/10.1007/s10921-020-00675-4

69. Gurmesa, F., Lemu, H., Adugna, Y., Harsibo, M.: Residual Stresses in Wire Arc Additive Manufacturing Products and Their Measurement Techniques: A Systematic Review. Applied Mechanics. 5, 420–449 (2024). https://doi.org/10.3390/applmech5030025

70. Williams, S.W., Martina, F., Addison, A.C., Ding, J., Pardal, G., Colegrove, P.: Wire + Arc Additive Manufacturing. Materials Science and Technology. 32, 641–647 (2016). https://doi.org/10.1179/1743284715Y.0000000073

71. Ding, J., Colegrove, P., Mehnen, J., Ganguly, S., Sequeira Almeida, P.M., Wang, F., Williams, S.: Thermo-mechanical analysis of Wire and Arc Additive Layer Manufacturing process on large multi-layer parts. Comput. Mater. Sci. 50, 3315–3322 (2011). https://doi.org/10.1016/j.commatsci.2011.06.023

72. Szost, B.A., Terzi, S., Martina, F., Boisselier, D., Prytuliak, A., Pirling, T., Hofmann, M., Jarvis, D.J.: A comparative study of additive manufacturing techniques: Residual stress and microstructural analysis of CLAD and WAAM printed Ti–6Al–4V components. Mater. Des. 89, 559–567 (2016). https://doi.org/10.1016/j.matdes.2015.09.115

73. Szost, B.A., Terzi, S., Martina, F., Boisselier, D., Prytuliak, A., Pirling, T., Hofmann, M., Jarvis, D.J.: A comparative study of additive manufacturing techniques: Residual stress and microstructural analysis of CLAD and WAAM printed Ti–6Al–4V components. Mater. Des. 89, 559–567 (2016). https://doi.org/10.1016/j.matdes.2015.09.115

74. Ahmad, B., Zhang, X., Guo, H., Fitzpatrick, M.E., Neto, L.M.S.C., Williams, S.: Influence of Deposition Strategies on Residual Stress in Wire + Arc Additive Manufactured Titanium Ti-6Al-4V. Metals (Basel). 12, 253 (2022). https://doi.org/10.3390/met12020253

75. Gurmesa, F.D., Lemu, H.G.: Literature Review on Thermomechanical Modelling and Analysis of Residual Stress Effects in Wire Arc Additive Manufacturing. Metals (Basel). 13, 526 (2023). https://doi.org/10.3390/met13030526

76. Boruah, D., Dewagtere, N., Ahmad, B., Nunes, R., Tacq, J., Zhang, X., Guo, H., Verlinde, W., De Waele, W.: Digital Image Correlation for Measuring Full-Field Residual Stresses in Wire and Arc

Additive Manufactured Components. Materials. 16, 1702 (2023). https://doi.org/10.3390/ma16041702

77. Hosseinzadeh, F., Kowal, J., Bouchard, P.J.: Towards good practice guidelines for the contour method of residual stress measurement. The Journal of Engineering. 2014, 453–468 (2014). https://doi.org/10.1049/joe.2014.0134

78. Chen, Y., Sun, H., Li, Z., Wu, Y., Xiao, Y., Chen, Z., Zhong, S., Wang, H.: Strategy of Residual Stress Determination on Selective Laser Melted Al Alloy Using XRD. Materials. 13, 451 (2020). https://doi.org/10.3390/ma13020451

79. Luo, Q., Yang, S.: Uncertainty of the X-ray Diffraction (XRD) sin2 ψ Technique in Measuring Residual Stresses of Physical Vapor Deposition (PVD) Hard Coatings. Coatings. 7, 128 (2017). https://doi.org/10.3390/coatings7080128

80. Fitzpatrick, M.E., Fry, A.T., Holdway, P.: NPL Good Practice Guide no. 52: determination of residual stresses by x-ray diffraction. (2002)

81. Olson, M.D., DeWald, A.T., Prime, M.B., Hill, M.R.: Estimation of Uncertainty for Contour Method Residual Stress Measurements. Exp. Mech. 55, 577–585 (2015). https://doi.org/10.1007/s11340-014-9971-2

82. Acevedo, R., Sedlak, P., Kolman, R., Fredel, M.: Residual stress analysis of additive manufacturing of metallic parts using ultrasonic waves: State of the art review. Journal of Materials Research and Technology. 9, 9457–9477 (2020). https://doi.org/10.1016/j.jmrt.2020.05.092

83. dos Santos, , Auteliano A., Bray, D.E.: Comparison of Acoustoelastic Methods to Evaluate Stresses in Steel Plates and Bars. J. Press. Vessel Technol. 124, 354–358 (2002). https://doi.org/10.1115/1.1484114

84. Zhu, Y., Zhao, H., Song, C., Hu, B.: The Measurement of Acoustoelastic Constant to evaluate Stress by UsingUltrasonic Waves. J. Phys. Conf. Ser. 1486, 072057 (2020). https://doi.org/10.1088/1742-6596/1486/7/072057

85. Hwang, Y.-I., Lee, H., Kim, Y.-I., Kim, K.-B.: Methodology for Mapping the Residual Stress Field in Serviced Rails Using LCR Waves. J. Nondestr. Eval. 41, 63 (2022). https://doi.org/10.1007/s10921-022-00895-w

86. Man, C.-S.: Effects of Crystallographic Texture on the Acoustoelastic Coefficients of Polycrystals. Nondestructive Testing and Evaluation. 15, 191–214 (1998). https://doi.org/10.1080/10589759908952872

87. Chen, H., Wang, X., Han, X., Zheng, F., Yan, W.: Ultrasonic Non-Destructive Detection Method for Residual Stress in Rotary Forging Aluminum Alloy Plates. Materials. 17, 2528 (2024). https://doi.org/10.3390/ma17112528

88. Chaki, S., Ke, W., Demouveau, H.: Numerical and experimental analysis of the critically refracted longitudinal beam. Ultrasonics. 53, 65–69 (2013). https://doi.org/10.1016/j.ultras.2012.03.014

89. Djerir, W., Boutkedjirt, T., Ourak, M., Halimi, R., Rezzoug, A., Rekbi, F.M.L., Allag, A.: Numerical and Experimental Evaluation of the Critically Refracted Longitudinal Waves (LCR) Beam Profile Generated by a Transducer. Russian Journal of Nondestructive Testing. 59, 654–664 (2023). https://doi.org/10.1134/S1061830923600272

90. Liu, Y., Liu, E., Chen, Y., Wang, X., Sun, C., Tan, J.: Study on Propagation Depth of Ultrasonic Longitudinal Critically Refracted (LCR) Wave. Sensors. 20, 5724 (2020). https://doi.org/10.3390/s20195724

91. Xu, Q., Wang, H.: Sound Field Modeling Method and Key Imaging Technology of an Ultrasonic Phased Array: A Review. Applied Sciences. 12, 7962 (2022). https://doi.org/10.3390/app12167962

92. Holmes, C., Drinkwater, B.W., Wilcox, P.D.: Advanced post-processing for scanned ultrasonic arrays: Application to defect detection and classification in non-destructive evaluation. Ultrasonics. 48, 636–642 (2008). https://doi.org/10.1016/j.ultras.2008.07.019

93. Svilainis, L., Dumbrava, V.: Analysis of the interpolation techniques for time-of-flight estimation. Ultrasound. 63, 25–29 (2008). https://doi.org/10.5755/j01.u.63.4.17082

94. Yang, F., Shi, D., Lo, L.-Y., Mao, Q., Zhang, J., Lam, K.-H.: Auto-Diagnosis of Time-of-Flight for Ultrasonic Signal Based on Defect Peaks Tracking Model. Remote Sens. (Basel). 15, 599 (2023). https://doi.org/10.3390/rs15030599

95. Park, S.-H., Choi, S., Song, D.-G., Jhang, K.-Y.: Microstructural Characterization of Additively Manufactured Metal Components Using Linear and Nonlinear Ultrasonic Techniques. Materials. 15, 3876 (2022). https://doi.org/10.3390/ma15113876

96. Yeoh, W.Y., Lan, B., Lowe, M.J.S.: Investigation of the influence of macrozones in titanium alloys on the propagation and scattering of ultrasound. Proceedings of the Royal Society A: Mathematical, Physical and Engineering Sciences. 479, (2023). https://doi.org/10.1098/rspa.2023.0176

97. Wan, T., Naoe, T., Wakui, T., Futakawa, M., Obayashi, H., Sasa, T.: Effects of Grain Size on Ultrasonic Attenuation in Type 316L Stainless Steel. Materials. 10, 753 (2017). https://doi.org/10.3390/ma10070753

98. Dobrovolskij, D., Schladitz, K.: Simulation of Ultrasonic Backscattering in Polycrystalline Microstructures. Acoustics. 4, 139–167 (2022). https://doi.org/10.3390/acoustics4010010

99. Markja, I., Dhoska, K., Elezi, D., Moezzi, R., Petru, M.: Effect of the Grain Sizes on the Ultrasonic Propagation and Attenuation on Different Types of Steels Microstructure During Non-Destructive Testing. Annales de Chimie - Science des Matériaux. 45, 329–334 (2021). https://doi.org/10.18280/acsm.450408

100. Heat Treatment of Wrought Aluminum Alloy Parts, (2002)

101. Javadi, Y., Mills, B., Samuel, J., Showell, D., Walker, J., Azam, S., Tamimi, S., Mohseni, E., Macleod, C.: Toward Isolation of Microstructural and Residual-Stress Contributions in Phased-Array LCR Ultrasonics, (2026)

102. Ahmad, B., Fitzpatrick, M.E.: Minimization and Mitigation of Wire EDM Cutting Errors in the Application of the Contour Method of Residual Stress Measurement. Metallurgical and Materials Transactions A. 47, 301–313 (2016). https://doi.org/10.1007/s11661-015-3231-7

103. Naveed, N.: Guidelines to select suitable parameters for contour method stress measurements. Archives of Mechanics. 72, 39–58 (2020). https://doi.org/10.24423/aom.3378

104. Javadi, Y., Hutchison, A., Zimermann, R., Singh, J., Mohseni, E., Rahimi, S., Mehnen, J., Macleod, C., Pierce, G., Tant, K., Gachagan, A.: Feasibility study of residual stress measurement using phased array ultrasonic method Feasibility study of residual stress measurement using phased array ultrasonic method FEASIBILITY STUDY OF RESIDUAL STRESS MEASUREMENT USING PHASED ARRAY ULTRASONIC METHOD. (2022)

105. Bray, D.E.: Current directions of Ultrasonic Stress Measurement Techniques

106. Sattari-Far, I., Javadi, Y.: Influence of welding sequence on welding distortions in pipes. International Journal of Pressure Vessels and Piping. 85, 265–274 (2008). https://doi.org/10.1016/j.ijpvp.2007.07.003

107. Mills, B., Javadi, Y., Macleod, C.N.: Compensating Couplant Effects in Phased-Array Ultrasonic ToF Sensing for Residual Stress. Sensors. 26, 3975 (2026). https://doi.org/10.3390/s26133975

108. Abbasi, Z., Ozevin, D.: Acoustoelastic Coefficients in Thick Steel Plates under Normal and Shear Stresses. Exp. Mech. 56, 1559–1575 (2016). https://doi.org/10.1007/s11340-016-0186-6

109. Hamelin, C.J., Muránsky, O., Smith, M.C., Holden, T.M., Luzin, V., Bendeich, P.J., Edwards, L.: Validation of a numerical model used to predict phase distribution and residual stress in ferritic steel weldments. Acta Mater. 75, 1–19 (2014). https://doi.org/10.1016/j.actamat.2014.04.045

110. Chan, S.Y., Pooja, C., Dennise, T.A., Keegan, L.: Evaluation of Measurement Uncertainty for Residual Stress Measurements using X-Ray Diffraction. (2017)

111. Javadi, Y., Hutchison, A., Zimermann, R., Lines, D., Sweeney, N.E., Vasilev, M., Mohseni, E., Vithanage, R.K.W., MacLeod, C.N., Pierce, G., Mehnen, J., Gachagan, A.: Development of a Phased Array Ultrasonic System for Residual Stress Measurement in Welding and Additive Manufacturing. In: Volume 4B: Materials and Fabrication. American Society of Mechanical Engineers (2022)

112. Javadi, Y., Mills, B., Leilabadi, P.P., Nicolson, E., Lotfian, S., Zimermann, R., Abad, F., Mehmanparast, A., Macleod, C., Pierce, G., Lines, D., Brennan, F., Mehnen, J., Gachagan, A.: Phased Array Ultrasonic Testing of Offshore Wind Bolted Flange Connections. (2023)

113. Mills, B., Javadi, Y., Abad, F., Lotfian, S., MacLeod, C., Mehmanparast, A., Pierce, G., Gachagan, A.: Inspection of wind turbine bolted connections using the ultrasonic phased array system. Heliyon. 10, (2024). https://doi.org/10.1016/j.heliyon.2024.e34579

114. Javadi, Y., Hutchison, A., Zimermann, R., Singh, J., Mohseni, E., Rahimi, S., Mehnen, J., Macleod, C., Pierce, G., Tant, K., Gachagan, A.: Feasibility study of residual stress measurement using phased array ultrasonic method Feasibility study of residual stress measurement using phased array ultrasonic method FEASIBILITY STUDY OF RESIDUAL STRESS MEASUREMENT USING PHASED ARRAY ULTRASONIC METHOD. (2022)

115. Ramuhalli, P., Good, M.S., Diaz, A.A., Anderson, M.T., Watson, B.E., Peters, T.J., Dixit, M., Bond, L.J.: Ultrasonic Characterization of Cast Austenitic Stainless Steel Microstructure: Discrimination between Equiaxed- and Columnar-Grain Material ? An Interim Study. , Richland, WA (United States) (2009)

116. Lavarello, R.J., Ghoshal, G., Oelze, M.L.: On the estimation of backscatter coefficients using single-element focused transducers. J. Acoust. Soc. Am. 129, 2903–2911 (2011). https://doi.org/10.1121/1.3557036

117. Rokhlin, S.I., Sha, G., Li, J., Pilchak, A.L.: Inversion methodology for ultrasonic characterization of polycrystals with clusters of preferentially oriented grains. Ultrasonics. 115, 106433 (2021). https://doi.org/10.1016/j.ultras.2021.106433

118. Liu, Y., Van Pamel, A., Nagy, P.B., Cawley, P.: Investigation of ultrasonic backscatter using three-dimensional finite element simulations. J. Acoust. Soc. Am. 145, 1584–1595 (2019). https://doi.org/10.1121/1.5094783

119. Lin, J.J., Lv, Y.H., Liu, Y.X., Xu, B.S., Sun, Z., Li, Z.G., Wu, Y.X.: Microstructural evolution and mechanical properties of Ti-6Al-4V wall deposited by pulsed plasma arc additive manufacturing. Mater. Des. 102, 30–40 (2016). https://doi.org/10.1016/j.matdes.2016.04.018

120. Hicks, C., Tamimi, S., Sivaswamy, G., Pimentel, M., McKegney, S., Fitzpatrick, S.: Hybrid manufacturing approach for landing gear applications: WAAM Ti–6Al–4V on forged Ti–5Al–5Mo–5V–3Cr. Journal of Materials Research and Technology. 30, 6596–6608 (2024). https://doi.org/10.1016/j.jmrt.2024.05.088

121. Sun, R., Li, L., Zhu, Y., Guo, W., Peng, P., Cong, B., Sun, J., Che, Z., Li, B., Guo, C., Liu, L.: Microstructure, residual stress and tensile properties control of wire-arc additive manufactured 2319 aluminum alloy with laser shock peening. J. Alloys Compd. 747, 255–265 (2018). https://doi.org/10.1016/j.jallcom.2018.02.353

122. Javadi, Y., Hutchison, A., Zimermann, R., Singh, J., Mohseni, E., Rahimi, S., Mehnen, J., Macleod, C., Pierce, G., Tant, K., Gachagan, A.: Feasibility study of residual stress measurement using phased array ultrasonic method Feasibility study of residual stress measurement using phased array ultrasonic method FEASIBILITY STUDY OF RESIDUAL STRESS MEASUREMENT USING PHASED ARRAY ULTRASONIC METHOD. (2022)

123. Bray, D.E., Tang, W.: Subsurface stress evaluation in steel plates and bars using the LCR ultrasonic wave. Nuclear Engineering and Design. 207, 231–240 (2001). https://doi.org/10.1016/S0029-5493(01)00334-X

124. Sun, J., Pan, Y., Liu, Y., Kuang, F., Lu, R., Lu, X.: Strength–ductility synergy strategy of Ti6Al4V alloy fabricated by metal injection molding. International Journal of Minerals, Metallurgy and Materials. 32, 1641–1654 (2025). https://doi.org/10.1007/s12613-024-3023-4

125. Shao, H., Cai, L., Shan, D., Wang, K., Li, L., Zhang, G., Zhao, Y.: Microstructure and high strength–ductility synergy of Ti–6Al–4V alloy induced by joule heat treatment. J. Mater. Sci. 53, 16609–16617 (2018). https://doi.org/10.1007/s10853-018-2794-2

126. Rossini, N.S., Dassisti, M., Benyounis, K.Y., Olabi, A.G.: Methods of measuring residual stresses in components. Mater. Des. 35, 572–588 (2012). https://doi.org/10.1016/j.matdes.2011.08.022

127. Francis, J.A.: Measurement, modelling and mitigation of residual stress. Materials Science and Technology. 32, 1409–1410 (2016). https://doi.org/10.1080/02670836.2016.1232476

128. Zimermann, R., Mohseni, E., Vasilev, M., Loukas, C., Vithanage, R.K.W., Macleod, C.N., Lines, D., Javadi, Y., Espirindio E Silva, M.P., Fitzpatrick, S., Halavage, S., Mckegney, S., Pierce, S.G., Williams, S., Ding, J.: Collaborative Robotic Wire + Arc Additive Manufacture and Sensor-Enabled In-Process Ultrasonic Non-Destructive Evaluation. Sensors. 22, 4203 (2022). https://doi.org/10.3390/s22114203

129. Ahmad, B., Zhang, X., Guo, H., Fitzpatrick, M.E., Neto, L.M.S.C., Williams, S.: Influence of Deposition Strategies on Residual Stress in Wire + Arc Additive Manufactured Titanium Ti-6Al-4V. Metals (Basel). 12, 253 (2022). https://doi.org/10.3390/met12020253

130. Neto, L., Williams, S., Davis, A.E., Kennedy, J.R.: Effect of Machine Hammer Peening Conditions on β Grain Refinement of Additively Manufactured Ti-6Al-4V. Metals (Basel). 13, 1888 (2023). https://doi.org/10.3390/met13111888

131. Neto, L., Williams, S., Davis, A.E., Kennedy, J.R.: Effect of Machine Hammer Peening Conditions on β Grain Refinement of Additively Manufactured Ti-6Al-4V. Metals (Basel). 13, 1888 (2023). https://doi.org/10.3390/met13111888

132. Williams, S.W., Martina, F., Addison, A.C., Ding, J., Pardal, G., Colegrove, P.: Wire + Arc Additive Manufacturing. Materials Science and Technology. 32, 641–647 (2016). https://doi.org/10.1179/1743284715Y.0000000073

133. Srivastava, S., Garg, R.K., Sharma, V.S., Sachdeva, A.: Measurement and Mitigation of Residual Stress in Wire-Arc Additive Manufacturing: A Review of Macro-Scale Continuum Modelling Approach. Archives of Computational Methods in Engineering. 28, 3491–3515 (2021). https://doi.org/10.1007/s11831-020-09511-4

134. Francis, J.A., Bhadeshia, H.K.D.H., Withers, P.J.: Welding residual stresses in ferritic power plant steels. Materials Science and Technology. 23, 1009–1020 (2007). https://doi.org/10.1179/174328407X213116

135. White, G.: Fatigue Behavior of (BS 1470 N8-0) Aluminum Alloy and (BS 1501–510) Nickel Steel Double-Fillet and Tee-Butt Welds (Subject to Bending). J. Test. Eval. 20, 180–189 (1992). https://doi.org/10.1520/JTE11711J

136. Javadi, Y., Sweeney, N.E., Mohseni, E., MacLeod, C.N., Lines, D., Vasilev, M., Qiu, Z., Mineo, C., Pierce, S.G., Gachagan, A.: Investigating the effect of residual stress on hydrogen cracking in multi-pass robotic welding through process compatible non-destructive testing. J. Manuf. Process. 63, 80–87 (2021). https://doi.org/10.1016/j.jmapro.2020.03.043

137. Kartal, M.E., Liljedahl, C.D.M., Gungor, S., Edwards, L., Fitzpatrick, M.E.: Determination of the profile of the complete residual stress tensor in a VPPA weld using the multi-axial contour method. Acta Mater. 56, 4417–4428 (2008). https://doi.org/10.1016/j.actamat.2008.05.007

138. Hönnige, J., Seow, C.E., Ganguly, S., Xu, X., Cabeza, S., Coules, H., Williams, S.: Study of residual stress and microstructural evolution in as-deposited and inter-pass rolled wire plus arc additively manufactured Inconel 718 alloy after ageing treatment. Materials Science and Engineering: A. 801, 140368 (2021). https://doi.org/10.1016/j.msea.2020.140368

139. Withers, P.J., Turski, M., Edwards, L., Bouchard, P.J., Buttle, D.J.: Recent advances in residual stress measurement. International Journal of Pressure Vessels and Piping. 85, 118–127 (2008). https://doi.org/10.1016/j.ijpvp.2007.10.007

140. Egle, D.M., Bray, D.E.: Measurement of acoustoelastic and third-order elastic constants of rail steel. J. Acoust. Soc. Am. 59, S32–S32 (1976)

141. Stanke, F.E., Kino, G.S.: A unified theory for elastic wave propagation in polycrystalline materials. J. Acoust. Soc. Am. 75, 665–681 (1984). https://doi.org/10.1121/1.390577

142. Arguelles, A.P., Turner, J.A.: Ultrasonic attenuation of polycrystalline materials with a distribution of grain sizes. J. Acoust. Soc. Am. 141, 4347–4353 (2017). https://doi.org/10.1121/1.4984290

143. Bai, X., Tie, B., Schmitt, J.-H., Aubry, D.: Finite element modeling of grain size effects on the ultrasonic microstructural noise backscattering in polycrystalline materials. Ultrasonics. 87, 182–202 (2018). https://doi.org/10.1016/j.ultras.2018.02.008

144. Papadakis, E.P.: Ultrasonic Attenuation and Velocity in Three Transformation Products in Steel. J. Appl. Phys. 35, 1474–1482 (1964). https://doi.org/10.1063/1.1713652

145. Bray, D.E., Junghans, P.: Application of the LCR ultrasonic technique for evaluation of post-weld heat treatment in steel plates. NDT & E International. 28, 235–242 (1995). https://doi.org/10.1016/0963-8695(95)00020-X

146. Bray, D., Dennis, R.: Test Repair Weld Revised Weld Residual Stress and Creep Damage Assessments. (2011)

147. Javadi, Y., Pirzaman, H.S., Raeisi, M.H., Najafabadi, M.A.: Ultrasonic inspection of a welded stainless steel pipe to evaluate residual stresses through thickness. Mater. Des. 49, 591–601 (2013)

148. Ramuhalli, P., Good, M.S., Diaz, A.A., Anderson, M.T., Watson, B.E., Peters, T.J., Dixit, M., Bond, L.J.: Ultrasonic Characterization of Cast Austenitic Stainless Steel Microstructure:

Discrimination between Equiaxed- and Columnar-Grain Material ? An Interim Study. , Richland, WA (United States) (2009)

149. Liu, Y., Tian, Q., Guan, X.: Grain Size Estimation using phased array ultrasound attenuation. NDT & E International. 122, 102479 (2021). https://doi.org/10.1016/j.ndteint.2021.102479

150. Zhang, J., Song, Y., Li, X., Zhong, C.: Comparison of Experimental Measurements of Material Grain Size Using Ultrasound. J. Nondestr. Eval. 39, 30 (2020). https://doi.org/10.1007/s10921-020-00675-4

151. Luo, Z., Wang, H., Zhang, S., Li, F., Jin, S.: A phased array ultrasonic-based enhanced strategy of critically refracted longitudinal (LCR) wave technique. NDT & E International. 133, 102765 (2023). https://doi.org/10.1016/j.ndteint.2022.102765

152. Luo, Z., Li, F., Wang, H., Zhang, X., Li, Y., Jin, S.: Ultrasonic evaluation of early-stage hygrothermal aging damage for anisotropic composites based on PA-LCR technology. NDT & E International. 156, 103470 (2025). https://doi.org/10.1016/j.ndteint.2025.103470

153. McNelley, T.R., Swaminathan, S., Su, J.Q.: Recrystallization mechanisms during friction stir welding/processing of aluminum alloys. Scr. Mater. 58, 349–354 (2008). https://doi.org/10.1016/j.scriptamat.2007.09.064

154. Lavarello, R.J., Ghoshal, G., Oelze, M.L.: On the estimation of backscatter coefficients using single-element focused transducers. J. Acoust. Soc. Am. 129, 2903–2911 (2011). https://doi.org/10.1121/1.3557036

155. Bu, Y., Liu, X., Turner, J.A., Song, Y., Li, X.: Grain size evaluation with time-frequency ultrasonic backscatter. NDT & E International. 117, 102369 (2021). https://doi.org/10.1016/j.ndteint.2020.102369

156. Lodh, A., Thool, K., Samajdar, I.: X-ray Diffraction for the Determination of Residual Stress of Crystalline Material: An Overview. Transactions of the Indian Institute of Metals. 75, 983–995 (2022). https://doi.org/10.1007/s12666-022-02540-6

157. Sumana, Kumar, A.: TOTAL FOCUSING METHOD BASED ULTRASONIC PHASED ARRAY IMAGING IN THICK STRUCTURES. J. Nondestruct. Eval. Diagn. Progn. Eng. Syst. 1–16 (2021). https://doi.org/10.1115/1.4050802